Prediction of extreme wave-structure interactions for multi-columned structures in deep water

James Robert Grice

University College

A thesis submitted in partial fulfilment of the requirements for the degree of Doctor of Philosophy at the University of Oxford

January 2013

Department of Engineering Science
University of Oxford
Parks Road
Oxford
OX1 3PJ

Prediction of extreme wave-structure interactions for multi-columned structures in deep water

James Robert Grice

A thesis submitted in partial fulfilment of the requirements for the degree of Doctor of Philosophy at the University of Oxford

University College

January 2013

ABSTRACT

With a continuing and rising demand for hydrocarbons, the energy companies are installing infrastructure ever further offshore, where such infrastructure is often exposed to extreme waves. This thesis explores some aspects of wave-structure interaction, particularly the maximum water surface elevation increase in severe storms due to these local interactions.

The effects on wave-structure interactions of column cross-sectional shape are investigated using linear and second-order wave diffraction theory. For multi-column structures, the excitation of locally resonant wave modes (near-trapping) is studied for several column cross-sectional shapes, and a simple method for estimating the surface elevation mode shape is given. The structure of the quadratic transfer functions for second-order sum wave elevation is investigated and an approximation assuming these QTFs are flat perpendicular to the leading diagonal is shown to be adequate for the first few lowest frequency modes.

NewWave-type focused wave groups can be used as a more realistic model of extreme ocean waves. A Net Amplification Factor based on the NewWave model is given as an efficient tool for finding the incident frequencies most likely to cause a violent wave-structure interaction and where these violent responses are likely to occur. Statistics are collected from Monte Carlo type simulations of random waves to verify the use of the Net Amplification Factor. Going beyond linear calculations, surface elevation statistics are collected to second-order and a 'designer' wave is found to model the most extreme surface elevation responses. A 'designer' wave can be identified at required levels of return period to help to understand the relative size of harmonic components in extreme waves.

The methods developed with a fixed body are then applied to an identical hull which is freely floating, and the responses between the fixed and moving cases are compared. The vertical heave motion of a semi-submersible in-phase with the incident wave crests is shown to lead to a much lower probability of water-deck impact for the same hull shape restrained vertically. The signal processing methods developed are also applied to a single column to allow comparison with experimental results. Individual harmonic components of the hydrodynamic force are identified up to at least the fifth harmonic. Stokes scaling is shown to hold even for the most violent interactions. It is also shown that the higher harmonic components of the hydrodynamic force can be reconstructed from just the fundamental force time history, and a transfer function in the form of a single phase and an amplitude for each harmonic. The force is also reconstructed well to second-order from the surface elevation time history using diffraction transfer functions. Finally, possible causes of damage to a platform high above mean water level in the North Sea are investigated.

ACKNOWLEDGEMENTS

I would very much like to thank Prof. Rodney Eatock Taylor and Prof. Paul Taylor for their excellent supervision. Their experience and enthusiasm have given me guidance and insight throughout my DPhil and I am very grateful to be able to share my thoughts and ideas with persons of such high expertise in the field of Ocean Engineering. I consider myself extremely lucky to have had the guidance of not one but two mentors and I am very proud of the work that their endless support has helped me to achieve.

I would like to thank Dr. Liang Sun for sharing his extensive experience in the use of DIFFRACT and helping me find my feet in the early days of my project. His help and advice was greatly appreciated throughout my research and his swift responses to queries on the intricacies of DIFFRACT were always most welcome.

I would like to thank Dr. Colin Grant and Dr. Richard Gibson for being so welcoming during my internship at BP p.l.c. and for sharing their knowledge and experience. I very much enjoyed my time with them and the rest of the Sub-Sea and Offshore Structures team and came away having learnt a lot about the oil industry. Dr. Dan Walker has also been a great help, offering advice and guidance on both my research and my career throughout the DPhil.

I would also like to acknowledge the financial support of the Engineering and Physical Sciences Research Council and BP p.l.c. without whom this project would not have been possible.

Finally, I would like to thank my family and friends for all their endless support, Univ. for giving me a home all these years in Oxford, UCBC for all the wonderful memories and lifelong friends, and Jen, for everything.

Table of Contents

Notation

g	Gravitational acceleration, 9.81 ms^{-2}
η	Wave surface elevation
k	Wavenumber
ν	Deep water wavenumber
λ	Wavelength
ω	Angular frequency
f	Frequency
T	Period
S	Spectral energy density
H_s	Significant wave height
ϕ	Diffraction coefficient
ψ	Phase
F	Force
x_0, y_0	Location of NewWave focus point
t_0	Time of NewWave focus
X, Y	Position relative to focus point $(x - x_0, y - y_0)$
τ	Time relative to focus time $(t - t_0)$
β	Incident wave direction, positive anticlockwise from x-axis
θ_j	Column angle, positive anticlockwise from x-axis
a	Radius of circular column
b	Width of vertical plate
d	Water depth
h	Centre-centre column half spacing
r/a	Normalised radius of curvature for intermediate column
$\text{P}(x > x')$	Probability that x is greater than x'
σ	Standard deviation
γ	JONSWAP peak enhancement factor
ρ	Unit-amplitude autocorrelation factor
A	Wave crest amplitude
A_{max}	Maximum wave crest amplitude
α_J	JONSWAP scaling coefficient
n	Spectral component index
N	Number of spectral components
N_K	Keulegan-Carpenter number

A_m^k	Matrix of coefficients used to find near-trapped modes in the method of Linton and Evans (1990)
H_n	Hankel function
J_n, Y_n	Bessel functions
N_c	Number of columns
M	Number of terms the infinite series is truncated to in the method of Linton and Evans (1990)
ξ	Normalised wave amplitude, $\xi = \alpha/m_0^{1/2}$
α	Most probable extreme wave amplitude in N_w waves
N_w	Number of waves
m_0	Total energy of the spectrum
a_n, b_n	Real and imaginary amplitude components of random surface elevation spectra
z_n	Random number with zero mean and unit variance for generating a_n and b_n
$N_{spectra}$	Number of random spectra generated
$R(x, y)$	Net Amplification Factor
LTFs/QTFs	Linear / Quadratic Transfer Functions
MWL	Mean Water Level
f_0	Fundamental frequency
F_h	Hydrodynamic force
F_L	Linear force component
F_{LH}	Hilbert transform of the linear force component
ζ	Damping coefficient
Q	Quality factor - describes shape of a spectral peak

Sub- and superscripts

$_i$	Incident
$_s$	Scattered
$_R$	Response
$_p$	Peak spectral energy component
$_P$	Potential second-order terms
$_Q$	Quadratic second-order terms
$^{(1)}$	Linear
$^{(2)}$	Second-order
$^{(2+)}$	Second-order sum
$^{(2-)}$	Second-order difference

Chapter 1

Introduction

1.1 Background

When one looks at the number of natural disasters in recent years, it is not hard to argue that extreme weather is becoming more frequent and perhaps more intense. At the time of submission for this thesis, people across the Caribbean and up the east coast of the USA are still trying to rebuild their lives after Hurricane Sandy. Much of the world's untouched oil and gas resources are situated offshore, and so oil and gas production infrastructure must be developed ever further from the coast, mostly in areas exposed to extreme waves. The global energy demand is ever increasing and, in spite of investment in renewable energy, it is widely accepted that demand for fossil fuels will continue to grow for many years. The summary of the Douglas-Westwood (2012) World Floating Production Market Forecast 2013-2017 states that the money spent on floating production systems between 2013 and 2017 will double compared to the previous five years, with a prediction of $91bn. It also predicts that 63 % of the money spent on floating production systems will be in deep water. With energy companies being forced ever further from the coast, and with more instances of extreme weather, the number of hazards created by operating structures offshore is increasing.

The extreme storm conditions to which new structures will be exposed and the structures' ability to withstand them are important design criteria for new offshore facilities. As infrastructure is developed further offshore, the increase in water depth below a struc-

ture limits the methods of installation and attachment to the seabed that are economically feasible. In water depths greater than ca. 500 m, structures fixed directly to the seabed become impractical and, instead, floating structures such as tension leg platforms (TLPs), semi-submersibles, spars, and FPSOs are used. These floating structures consist of several large, closely spaced columns piercing the surface of the water, rather than the single towers and steel jackets found in shallower water. The interaction effects of extreme waves with these large offshore structures can lead to violent upwelling and runup on the surface piercing structural elements.

Upwelling, the local modification of an incident surface wave due to the presence of a structure, and runup, the local modification on the solid surface of a free surface piercing structure, can cause significant amplification relative to the undisturbed incident wave, and so must be considered during design. These phenomena can lead to green-water impact on the deck of offshore platforms, creating a risk for both personnel and equipment. Extreme wave impact has resulted in both loss of life and damage to oil and gas production facilities for many years (Kaiser et al. (2008), Rigworld (2013)). Although such incidents are rare, and they may not often cause massive structural failure, the loss of life and loss of revenue from production downtime clearly needs to be minimised. Despite these known risks, there are still gaps in the understanding of wave-structure interactions and in the prediction of water surface elevation around arrays of surface-piercing columns which need to be researched.

Energy companies have been model-testing their offshore structures during the design phase for forty years or more. Some of the most important criteria evaluated in testing are how often water-deck impact will occur, where on the deck the impacts will be most likely to occur, and which sea states lead to these extreme events. Even now the accepted method is to simply generate a few hundreds or thousands of random waves, collect statistics of their interactions with the structure model, and extrapolate out to longer return periods. This is a rather crude method which makes no attempt to understand the physics behind these extreme events. Often, the only simulations used prior to model testing to gain an idea of how the model will behave in extreme sea states are linear diffraction solutions to monochromatic incident waves. Monochromatic waves are clearly not an accurate repre-

sentation of extreme storm waves, and it is clear that the use of linear diffraction theory will not give accurate predictions of extreme wave-structure interactions. DNV (Det Norske Veritas) offshore standard OS-C201, Section D500 discussed the design of air gap in offshore structures. It states that "Analysis undertaken to check air gap should be calibrated against relevant model test results when available. Such analysis should take into account: wave and structure interaction effects, wave asymmetry effects, global rigid body motions (including dynamic effects), effects of interacting systems (e.g. mooring and riser systems), and maximum and minimum draughts". No guidance is given in this section on methods of numerical simulation, model testing, or the calibration between simulations and model tests. DNV Classification Note 30.6 gives detailed guidance on reliability analysis of marine structures and the use of statistical extrapolation techniques to predict extreme wave elevations. There is no discussion of looking at the physics of extreme waves and the relative significance of the harmonic components. The aim of this research is to improve our understanding of the conditions that lead to extreme events, and the relative size of the individual harmonics that make up these events. Perturbation expansions and more accurate extrapolations may then be used to predict the probability of water-deck impact.

1.2 Literature Review

1.2.1 Linear diffraction

Wave-structure interaction is in general a fully non-linear, three-dimensional problem. However, it can be approximated by low order models if certain assumptions and simplifications are appropriate. Linear diffraction theory makes the usual assumptions of the flow being frictionless, incompressible, and irrotational. If the characteristic dimension of a body, such as column diameter, can be considered large relative to the amplitude of the surface elevation, then it can be assumed that viscous effects will be minimal. There will be some viscous effects such as vortices shed around sharp corners but it can be assumed that diffraction will be the dominant effect. The Keulegan-Carpenter number characterises the ratio of inertial and viscous forces for bluff objects in oscillatory flow. It is found using the equation:

$$N_K = \frac{VT}{L} \tag{1.1}$$

where N_K is the Keulegan-Carpenter number, V is the amplitude of the oscillation flow velocity, T is the period of the oscillation, and L is the characteristic length of the body. For a sinusoidal component this is also equal to $N_K = \frac{2\pi A_0}{L}$, where A_0 is the oscillation motion amplitude of particles in the fluid. Assuming a characteristic length equal to the average Thunder Horse column diameter, $L = 24.68$ m, and an oscillation motion amplitude equal to a severe storm significant wave height of $H_s = 14$ m, the Keulegan-Carpenter number is $N_K = 3.56$.

Hogben et al. (1977) discussed the estimation of fluid loading on offshore structures in various flow regimes. Figure 1 in Hogben et al. (1977) plots the dominant flow regimes for values of N_K between 0 and 40 and for values of Reynold's number, R_e, between 10^4 and 10^7. For $N_K < 5$ inertia forces dominate and for $N_K > 25$ drag forces dominate. $5 < N_K < 25$ represents a transition zone where both inertia and viscous forces should be considered. For N_K to enter this transition zone with the average Thunder Horse geometry a significant wave height greater than 19.6 m would be needed. For extreme storms in the Gulf of Mexico an $H_s > 19.6$ m is beyond the range that should be investigated. After hurricanes Ivan and Katrina, API raised the design H_s values across the Gulf of Mexico with the highest being 15.8 m, Berek et al. (2007). This means that potential flow calculations can be used to model the wave-structure interactions with viscous forces considered negligible. Potential flow uses this assumption of inviscid flow to simplify the equations governing wave surface elevation, giving a more easily calculated yet accurate approximation of the surface elevation due to diffraction effects.

Within the restrictions of these assumptions, Laplace's equation can be solved in the fluid domain with a scalar velocity potential. This velocity potential can then be expressed as a superposition of linear and higher order components through a perturbation expansion. The velocity potential solutions at each order contribute to the boundary conditions at higher orders, and so these must be solved sequentially from the first-order up.

A perturbation expansion approach of this kind was used for wave-wave self interactions by Stokes (1847) but it was almost 100 years later that linear solutions to the diffraction problem were first derived by Havelock (1940). Havelock found an analytical solution for the diffraction of regular incident waves by a single cylinder in water with infinite depth. This was extended to finite water depth by McCamy and Fuchs (1954). Thorough reviews of analytical and numerical approaches to linear diffraction were given by Yeung (1982) and Mei (1989).

1.2.2 Non-linear diffraction

Linear theory is a poor approximation to the behaviour of extreme storm waves. Understanding the physics behind the interaction of extreme focused wave groups with offshore structures ultimately requires a fully nonlinear analysis. An understanding of the key features of nonlinear interactions can be gained through the use of a perturbation expansion procedure, such as that of Stokes (1847), to extend linear diffraction theory to a second-order approximation. Second-order diffraction theory is made more complicated compared to first-order by the addition of an inhomogeneous free surface boundary condition. Many of the initial attempts to solve the second-order diffraction theory were incomplete because the free surface boundary conditions were inconsistently satisfied, as shown by Chakrabarti (1978).

It was shown by Lighthill (1979) and Molin (1979) that, when finding second-order forces only, one does not have to directly solve for the second-order potential in the Stokes expansions. A transformation by Green's second identity of the contribution from an integration of the second-order potential on the submerged body surface allows the direct calculation of the second-order diffraction potential to be avoided. Lighthill (1979) used the addition of a double frequency pressure distribution, derived from the first-order solution but at twice the linear frequency, to solve for the second-order body force. Molin (1979) found that second-order diffracted waves could be split into two components: those travelling with the linear waves, 'phase locked waves', and those travelling independently, 'free waves'. Solutions must be found for both of these components to satisfy the inhomogeneous and homogeneous

boundary conditions respectively.

Eatock Taylor and Hung (1987) used the Green's second identity transformation technique to find a semi-analytical solution for the second-order forces from regular waves incident on a single cylinder extending to the seabed. Kim and Yue (1990) presented results for second-order forces on such a single cylinder in bichromatic waves and Moubayed and Williams (1995) presented equivalent second-order force results on arrays of multiple columns using the interaction theories of Linton and Evans (1990).

If surface elevations are required as well as forces, complete solutions for the second-order velocity potential must be found. Kim and Yue (1989) used numerical solutions based on Green's functions to satisfy the second-order boundary conditions, but Kriebel (1990) presented an analytical solution for the second-order velocity potential caused by interactions of monochromatic waves with a large vertical cylinder. Kriebel (1990) found that for steep wave interactions with the cylinder, the maximum second-order runup greatly exceeded predictions made by linear theory. Kriebel (1992) presented the results of a series of experiments to confirm this, with the second-order predictions being much closer to the measured runup than the linear predictions. Chau and Eatock Taylor (1992) solved the second-order velocity potential for a single vertical cylinder in monochromatic regular waves, in a computer code named DIFFRACT, and this analysis was extended to truncated cylinders and bichromatic waves by Huang and Eatock Taylor (1996a, 1996b). Lee and Newman (1994) built on the authors' previous work of Lee et al. (1991) and Newman and Lee (1992) to extend their application of an efficient panel code (WAMIT) to find the complete second-order solution on arbitrary 3D bodies. This included fixed and moving bodies with monochromatic and bichromatic incident waves. The second-order code described in their work was based on the first-order panel code of Korsemeyer et al. (1988).

Second-order diffraction theory was extended from regular waves to unidirectional focused wave groups by Eatock Taylor and Fonquernie (2001). Eatock Taylor and Fonquernie (2001) first applied second-order theory to wave-wave interactions for a focused wave group and then used a semi-analytical second-order diffraction method to extend this theory to the second-

order scattering of a NewWave (see Section 1.2.5) focused wave group by a vertical circular cylinder. Buldakov et al. (2004) then studied the second-order diffraction of a directionally spread focused wave group by a single circular cylinder. It was found that the scattering of directionally spread focused wave groups based on a JONSWAP spectrum (see Section 1.2.4) was qualitatively similar to the diffraction of a unidirectional focused wave group in the same sea state, with a small reduction in surface elevation amplitude that increased for larger spread angles.

Zang et al. (2006) looked at the effects of second-order wave diffraction in runup around the bow of a ship-shaped body with a unidirectional incident focused wave group. The Oxford code DIFFRACT was extended so that its quadratic boundary element method could be used with unidirectional and bidirectional bichromatic incident waves. The results for runup with a unidirectional incident focused wave group were shown to have a significant second-order component and, when compared with experimental measurements at Imperial College, excellent agreement was found. Zang et al. (2009) examined the importance of nonlinear components in wave-structure interactions by comparing numerical and experimental results for the diffraction of steep waves by a circular cylinder in shallow water. It was shown that the second-order numerical solution for both wave runup and the spectrum of the response surface elevation matched experimental results well and that the linear solution was a poor approximation.

Numerical solutions to fully nonlinear diffraction were developed using both finite element (FE) and boundary element (BE) methods. Wu and Eatock Taylor (1995) made a comparison between the FE and BE methods and found that, although the BE method only requires surface mesh discretisation compared to the FE method needing the whole flow domain, the BE method needed significantly more computational resources. This is due to the effect of matrix structure on storage requirements. The BE method usually leads to fully populated matrices, with storage and calculation times therefore being proportional to the square of the number of nodes. The FE method usually leads to banded matrices and so the relationship between problem size and storage or calculation times is closer to being linear. Büchman et al. (2000) compared second-order and fully nonlinear time-domain BE methods

for finding runup on a vertical bottom-seated circular cylinder in waves and current. It was shown that for low Froude number, low wave steepness cases the second-order model was an accurate and fast alternative to the fully nonlinear method. However, at higher steepness and Froude numbers the fully nonlinear method was more accurate.

Ma et al. (2001a, 2001b) detailed a methodology for finding a solution to 3D wave-structure interaction problems with fixed bodies using an FE method, and then verified their results on cases with one or two vertical cylinders. Kim et al. (2006) investigated runup on cylinders in very steep Stokes waves, also using an FE method (based on Hamilton's principle) to discretise the fluid domain. An alternative approach based on the BE method was used by Boo (2002) and Ferrant (2003) for simulations of three-dimensional wave diffraction. Ferrant (2003) compares two methods of solving for non-linear wave diffraction by 3D surface piercing structures in the time domain. Both methods are based on a BE method solution of the boundary value problem in the time domain, with the first using a second-order diffraction model and the second using a fully non-linear diffraction model without any approximation in time for the non-linear boundary conditions. Bai and Eatock Taylor (2006, 2007, 2009) used the BE method to look at three-dimensional wave diffraction around surface-piercing structures, including interactions between fully nonlinear waves and fixed or floating structures in a wave tank.

Wu and Eatock Taylor (2003) studied the feasibility of combining the FE and BE methods in a coupled approach for 2D nonlinear diffraction and this was extended to 3D in Eatock Taylor et al. (2005). Eatock Taylor et al. (2005) noted that the FE method was superior away from the body, where the domain is regular, and that the BE method was preferable closer to the body with the complications of a moving mesh. Combining the strengths of both methods in a coupled approach was shown to have many advantages over implementations of the approaches individually.

Ducrozet et al. (2010) discussed developments on an efficient fully nonlinear potential flow model for simulating 3D wave-wave and wave-structure interactions. Bingham and Zhang (2007) and Engsig-Karup et al. (2009) presented the high order finite difference scheme

OceanWave3D on which this fully nonlinear potential flow model is based. It uses a fully nonlinear Mixed Euler-Lagrange formulation with a BE method solution for the boundary integral equation part of the problem.

1.2.3 Diffraction from arrays of bodies

Wave-structure interaction with an array of bodies is far more complicated than an isolated body. When a wave is incident on a body in an array, the scattered wave produced will subsequently be re-scattered by all adjacent bodies. In calculating the velocity potential, both the diffraction of the incident field by each body and the multiple scattering effects of the adjacent bodies in the array must be taken into account. Usually, the total wave field is split into a component for the incident potential and a component for the general potential of a body describing the waves radiating away from it.

Possible methods to solve the wave-structure interaction problem include treating the array of bodies as a single unit, an iterative method involving multiple reflections between the bodies, and a direct matrix method involving the approximation that each scattered wave acts as a plane wave at the adjacent bodies. The first method is difficult to perform for large arrays, and the second, as developed by Twersky (1952), quickly becomes unmanageable as the number of interacting wave components increases rapidly with the number of bodies in the array. The third method, the direct matrix method, was originally devised by Spring and Monkmeyer (1974) but was then extended and improved by Simon (1982) and McIver and Evans (1984). Kagemoto and Yue (1986) combined the second and third solutions to give an exact algebraic method for calculating the wave hydrodynamics of a multi-body structure using the diffraction properties of individual bodies only, which required far fewer resources than a full diffraction solution.

Eatock Taylor and Sincock (1989) investigated the linear diffraction effects for the case of a tension leg platform in regular waves and found that for a linear solution the wave heights in the vicinity of the structure could be increased by up to a factor of two due to the wave-structure interactions. Linton and Evans (1990) used a simplified expression for

the first order velocity potential local to a cylinder and greatly improved the direct matrix method developed by Spring and Monkmeyer (1974). Maniar and Newman (1997) extended this method to look at loading on linear arrays of bottom-mounted circular cylinders, finding unusually large loads for near-resonant modes at critical frequencies.

These near-resonant modes correspond to the phenomenon of near-trapping. This is a near-resonant local response excited by waves of a certain frequency interacting with arrays of vertical surface-piercing columns and other geometries, including single bodies. Each near-trapping frequency is associated with a mode of strong local free surface oscillation which decays slowly to infinity due to wave radiation. These modes can be excited by incident linear free waves of a near-trapping frequency, higher order interactions with a response frequency equal to a near-trapped frequency or through forced excitation by non-linear waves with many linear incident wave components. Near-trapping is associated with the phenomenon of trapped modes although, unlike pure trapped modes, near-trapping is not connected to non-uniqueness in the frequency domain solution for a real frequency. Trapped modes in linearised water-wave theory for cylinders in the centre of a channel were discovered by Ursell (1951) and further investigated by Jones (1953). These trapped modes were then first proven mathematically by Callan et al. (1991). Much work has since been carried out on pure trapping, with many key papers written by Evans, Linton, Ursell, and McIver. Kagemoto et al. (2002) investigated the trapped mode phenomena for linear arrays of circular cylinders experimentally and found that the surface amplifications at the predicted trapped mode frequencies were significantly lower than expected. Kagemoto et al. suggested that this difference in surface amplification was probably due to viscous dissipation in the boundary layers around the cylinder walls.

Work has been carried out on the near-trapping phenomenon for many years, particularly by Linton and Evans (1993), Evans et al. (1994), and Evans and Porter (1997), which extended the analysis of Linton and Evans (1990) for arrays of an arbitrary number of bottom-mounted circular cylinders equispaced around the circumference of a circle. Evans and Porter (1997) found that the largest forces on arrays of multiple cylinders were associated with a standing wave forming within the array.

The work of Evans and Porter (1997) was motivated by that of Maniar and Newman (1997) which showed that large forces were experienced on cylinders close to the centre of a linear array for incident waves at a frequency close to a predicted trapped mode. Pure trapped modes with real excitation wavenumbers are most often associated with infinite periodic linear arrays of columns. In other geometries, near-trapped modes can be identified with complex excitation wavenumbers near the real axis which can be excited in physical situations by the real component of this theoretical trapped mode wavenumber. Evans et al. (1994) and Davies and Pamovski (1998) showed that near-trapped modes existed for a wide range of column cross-sections.

Finding the excitation frequencies of a near-trapped mode can be difficult numerically and the methods available to identify these scattering frequencies were discussed by Meylan and Gross (2003). Hazard and Lenoir (1993) and Hazard and Lenoir (2002) studied the scattering frequencies for arbitrary 2D bodies in water. Meylan and Eatock Taylor (2009) showed that one can approximate the solution in the time domain near the singularities associated with a near-trapped mode of water-waves scattered by bodies and produce a modal shape associated with the near-trapped mode.

Both Huang and Eatock Taylor (1996c) and Malenica (1997) independently developed similar semi-analytical approaches to the solution of second-order diffraction of monochromatic incident waves by an array of four circular cylinders. This was then extended by Malenica et al. (1999). Ohl et al. (2001a) investigated the diffraction of regular waves by an array of four closely spaced bottom-seated circular cylinders. Surface elevation results were compared between physical experiments and linear diffraction theory and a good match was found for incident waves of low steepness. Second- and third-order terms were estimated from the experimental results near a second-order near-trapped mode excitation and comparisons were made with the semi-analytical second-order diffraction approach of Malenica et al. (1999). Ohl et al. (2001b) then extended this analysis to irregular waves, focused wave groups, and random seas. Linear diffraction theory was found to work well with focused wave groups for linearised extreme events.

Walker and Eatock Taylor (2005) looked at modelling the excitation of near-trapped modes in linear arrays of circular cylinders and the diffraction of NewWave groups by arrays of closely spaced columns. Walker et al. (2008) investigated linear and second-order diffraction of monochromatic waves and NewWave focused wave groups by an array of four circular cylinders using the semi-analytical second-order diffraction approach of Malenica et al. (1999). The considerations needed when predicting the minimum air-gap for a structure were discussed.

In terms of readily accessible software in Oxford, there are two codes which might be used. WAMIT is a state of the art program capable of analysing wave-structure interactions to second-order. It is managed by WAMIT Inc, founded by Prof. J N. Newman and Dr. Chang-Ho Lee in 1999, and has since been licensed to over 100 industrial and research organisations worldwide. It uses the Boundary Integral Equation Method (BIEM) and is able to solve to second-order wave-structure interaction problems for monochromatic, bichromatic, and bidirectional waves. For full details of the theoretical basis for WAMIT see Lee and Newman (2004) or the many other publications cited on the Wamit Inc. website (www.wamit.com). DIFFRACT is another program capable of analysing wave-structure interactions to second-order for monochromatic, bichromatic, and bidirectional waves. It was initially developed by Prof. R. Eatock Taylor and Dr. F.P. Chau using the BE method and has been greatly extended and improved over the years. For more details on DIFFRACT, see Section 2.1.1.

1.2.4 CFD simulations

An alternative method of modelling non-linear wave interactions with offshore structures is computational fluid dynamics (CFD). This is particularly useful for modelling the post-breaking phase of violent interactions as potential flow methods cannot model breaking waves. CFD calculations can require far greater computational resources than a potential flow calculation in the same conditions, but with modern advances in hardware this is becoming more viable for frequent use and CFD is capable of taking into account viscous effects and the mixing of fluid and air.

There are several different methods available for solving the Navier-Stokes equations in fluid dynamics calculations which can be split into three groups: those using a moving grid (Lagrangian method), those using a fixed grid (Eulerian), and those without a grid. The fully non-linear Boundary Element Method discussed earlier is part of the Lagrangian moving grid group. The governing equations are solved along the boundaries of the grid cells and boundary conditions are applied at the current location of the boundaries for each calculation in time. The Eulerian moving grid group includes CFD methods such as Volume of Flow (VoF), Level Set (LS), and Contained Interpolation Profile (CIP). The grid used in Eulerian calculations is either stationary or can move in a certain prescribed manner to allow for changes in the interface.

Volume of Flow method

The VoF method is an advection scheme which means that it is a numerical method for tracking the position of the fluid-air interface but does not solve all of the governing equations itself. The VoF method solves all the governing equations except the free surface boundary condition and so another algorithm must be used alongside the VoF method. The VoF method was based on earlier Marker and Cell methods and developed by Noh and Woodward (1976) and Hirt and Nichols (1981). It uses a scalar fraction function, C, that describes the amount of fluid in a cell. If a cell is only air then $C = 0$, if a cell is only water $C = 1$, and if the water-air phase cuts across the cell then C is a discontinuous function jumping from 1 to 0 at the point of the interface. This fraction function is then combined with the local flow velocity, v, to give the equation:

$$\frac{\delta C}{\delta t} + v.\nabla C = 0 \tag{1.2}$$

Recent work using the VoF method include Kleefsman et al. (2004), which used a local height function to modify the VoF method for more accurate modelling of the free surface flow. This method was validated against experimental results for a dam break and published

photographic experimental results for water entry and exit of 2D objects. The results show that the modified VoF method gives accurate results for the presented cases. Jacobsen et al. (2012) discussed a new method in OpenFoam for modelling wave generation which, when combined with the VoF scheme in OpenFoam, is shown to accurately model the propagation and breaking of waves. Huang and Lin (2012) used a VoF scheme with a numerical model based on the Reynolds-Averaged Navier-Stokes (RANS) equations to simulate the propagation and breaking of focused wave groups. The results are validated against experimental results and other methods of simulation with very good agreement.

Level Set method

The level set method is a numerical technique for tracking interfaces developed in the 1980s by Osher and Sethian, see Osher and Sethian (1988). The LS method has been used in a wide range of fields, including CFD, and further work on the LS method by Osher and Sethian are discussed in Sethian (1999) and Osher and Fedkiw (2002). A disadvantage of the LS method is that it is poor on mass conservation. An improvement to this was made in Enright et al. (2002) by combining the Eulerian LS method with a Lagrangian marker particle scheme. Lagrangian marker particles are used to rebuild the level set in under-resolved areas resulting in a smooth geometrical description of the interface. The conservation of mass with this combined method was shown to be comparable with VoF methods and the interface resolution was shown to be comparable with purely Lagrangian schemes. Wang et al. (2009) made improvements to the combined particle level set method of Enright et al. (2002) with a modified interface reconstruction scheme. Several examples are used to validate the method and show the improved results, including a 3D drop impact into a liquid pool. However, the loss of mass is still greater than combined level set volume of flow (CLSVOF) methods, see Wang et al. (2008).

Constrained Interpolation Profile Method

The constrained interpolation profile method was developed by Yabe (Yabe et al. (2001)) to model the interactions of materials of all phases in one algorithm. It was based on the cubic-interpolated pseudo-particle method (Takewaki et al. (1985), Takewaki et al. (1987), Yabe et al. (1991)) and it is a semi-Lagrangian method developed to treat incompressible fluids in a compressible fluid framework. This simultaneous treatment of both compressible and incompressible flows with high density ratios allows the interaction of a gas with liquids and solids. Governing equations including continuity of mass and Navier-Stokes equations are solved on a Cartesian grid using a finite difference method.

Hu and Kashiwagi (2004) discussed the use of the constrained interpolation profile method to model extremely non-linear free-surface flows, including violent wave-body interactions. Results from several validation examples were presented and compared with experimental data with good agreement. For the example of forced heaving with a wedge-type float in a 2D numerical wave tank, the hydrodynamic force predictions were found to be similar in accuracy to using the Boundary Element Method when compared to the experimental data. Yang and Qiu (2012) used the constrained interpolation profile method to model 3D water entry problems, comparing the numerical results with experimental data. The validation results showed good agreement with experimental data and were shown to be an improvement over potential flow methods for the cases presented with a sphere and cusped body.

Smoothed Particle Hydrodynamics method

The smoothed particle hydrodynamics method is a gridless scheme as it models individual particles upon which the governing equations are solved rather than at points on a grid. The computational elements are not grid cells but instead they are moving points in space where samples are taken of computational data for the fluid. This method has benefits over many grid based methods such as conservation of mass. Each particle represents a finite

amount of mass and no particles are lost during the simulation. This means that mass conservation is guaranteed without any extra calculation. It also only performs calculations in the region occupied by the water and not the empty space representing air. The SPH method was originally developed for use in astrophysics by Gingold and Monaghan (1977) and Lucy (1977). It has since been modified and applied in many diverse applications. In fluid dynamics Monaghan (1988) gave a derivation of the equations and several examples of their application for modelling compressible gas flows. This was extended for use with solitary waves propagating on a shallow beach by Monaghan and Kos (1999), for breaking waves in shallow water and around ships in Tulin and Landrini (2000), and for modelling fluid motion generated by impact with Monaghan et al. (2003). More recently, Imhsen et al. (2010) improved the handling of boundaries and introduced adaptive time-stepping to Predictive-Corrective Incompressible SPH (PCISPH, see Solenthaler and Pajarola (2009)) for accurate rigid body interactions and Macklin and Müller (2013) made further improvements to allow the simulation of incompressible flows with bigger time increments. However, it is still not possible to perform simulations in real time.

1.2.5 Collection of experimental data

The collection and analysis of experimental data for extreme wave behaviour and wave-structure interactions has been carried out for many decades and is still very important for both further research into extreme waves and for validating numerical simulation methods. Chapter 7 of this thesis discusses some experimental results for the interaction of focused wave groups with a vertical surface-piercing column. There are very few published results for experiments investigating the interaction of focused wave groups with structures. A short summary is given in this section of these published experimental results and others which are relevant to the experiment discussed in Chapter 7 (see Zang et al. (2010)) or to work discussed elsewhere in this thesis such as the interaction of extreme waves with closely spaced columns.

Previous experimental work using focused wave groups to model extreme waves in flumes and basins include Rapp and Melville (1990), Baldock et al. (1996), Johannessen and Swan

(2001), and Ning et al. (2009). Rapp and Melville (1990) discussed extensively laboratory tests that they carried out on breaking waves in open ocean. They exploited the dispersion of deep-water waves to generate a single breaking wave group, allowing the direct effects of the breaking to be confined to a limited region of the wave channel. Although these experiments were carried out before the work on focused wave groups of Tromans et al. (1991) and Jonathan and Taylor (1997), the results are similar to the use of NewWave as a control signal. Baldock et al. (1996) investigated the effect of nonlinear wave-wave interactions on unidirectional focused wave groups and introduced the method of inverting wave groups in paired crest and trough focused wave groups to investigate the structure of the wave groups. Johannessen and Swan (2001) then extended this work to spread sea wave groups and presented a method based on the use of pairs of inverted focused wave groups to separate the odd and even harmonic components of the free surface elevation. More recently Ning et al. (2009) discussed extensive experimental tests on the propagation of focused wave groups along a wave flume with comparisons against numerical solutions using a higher order BEM. The numerical simulations were shown to match up well with the experimental results and the effects of second- and third-order wave-wave interactions on the focus point and the shape of the focused wave group were discussed.

Hunt et al. (2002) presented experimental results on the interaction of focused wave groups with a planar beach and sea wall using steep focused wave groups based on the NewWave model. Pairs of experiments were run with crest and trough focused wave groups which when added or subtracted were used to separate the free and bound wave components of the surface elevation data. Borthwick et al. (2006) presented measurements of the water particle kinematics for focused wave groups interacting with a planar beach. Pairs of crest and trough focused wave groups and a symmetry based separation method was again used to isolate components of the measured kinematics. Zang et al. (2006) compared numerical simulations with experimental data on the interactions of focused wave groups with a ship shaped body. Excellent agreement was found between the numerical and experimental results and the second-order wave-structure were shown to be significant.

Kagemoto et al. (2002) discussed experimental results for the interaction of monochro-

matic head waves with a row of fifty identical vertical truncated cylinders. The wave periods used were selected to excite a trapped mode and the surface elevations around the row of columns were then compared with numerical simulations. After some modifications to the code excellent agreement was found between the experimental and numerical results. Morris-Thomas and Thiagarajan (2004) looked at the interaction of monochromatic waves with a single vertical cylinder and isolated the first, second, and third harmonics of the measured surface elevation to investigate the relative sizes of these harmonics. Walker (2006) discussed results from model tests on the interaction of monochromatic waves with a four-column, gravity-based structure. Comparisons of the experimental results with numerical solutions showed that linear theory is insufficient for predicting violent wave-structure interactions as it underestimates the response. Much better agreement was shown when comparing numerical results to second-order with the experimental data.

1.2.6 Ocean storm wave spectra

Various idealised spectra could be used to model ocean waves. One of the simplest is that proposed by Pierson and Moskowitz (1964), which was obtained from measurements of waves in the North Atlantic Ocean. It is based on the concept of a fully developed sea, which assumes there is enough time and space for the wind driven waves to reach equilibrium. After analysis of data collected from the North Sea, Hasselmann et al. (1973) came up with a modification to the Pierson-Moskowitz (PM) spectrum. Their analysis found that the wave spectrum was never fully developed and, instead, non-linear wave-wave interactions continued indefinitely. A peak enhancement factor was used to modify the PM spectrum to improve the fit with their data. This was named the JONSWAP spectrum after the project name, Joint North Sea Wave Observation Project. The PM spectrum is given by the following equation:

$$S_{PM}(\omega) = \frac{5}{16} H_s^2 \frac{\omega_p^4}{\omega^5} \exp\left[-\frac{5}{4}\left(\frac{\omega_p}{\omega}\right)^4\right] \tag{1.3}$$

The JONSWAP spectrum is then given by

$$S_J(\omega) = A_\gamma \, S_{PM}(\omega) \, \gamma^r \tag{1.4}$$

$$r = \exp\left[-\frac{(\omega - \omega_p)^2}{2\sigma^2\omega_p^2}\right] \tag{1.5}$$

where ω_p is the peak frequency, γ is the peak enhancement factor (typically taken as $\gamma = 3.3$ for winter storms in the North Sea), $A_\gamma = 1 - 0.287\ln(\gamma)$, and $\sigma = 0.07$ for $\omega \leq \omega_p$ or 0.09 for $\omega > \omega_p$. For $\gamma = 1$ the JONSWAP spectrum reduces to the PM spectrum.

1.2.7 NewWave theory

Extreme storm waves are generally assumed to be statistical extremes in rough random seas, occurring randomly but very infrequently. Due to their randomness, the position or time of their occurrence cannot be predicted but the expected shape when they do occur can be. This is effectively the average shape of extreme wave crests in a given sea state. The rarity of their occurrences means random wave tests must be run for a very long time to capture a near-extreme event.

As mentioned above, regular waves are not representative of an extreme wave crest and so focused wave groups are often used to model the average shape. A focused wave group occurs when a set of wave components focus at a single position in space and time. Tromans et al. (1991) discussed how the average shape of an extreme wave with maximum elevation A_{Max} in a linear random Gaussian sea state can be described by a focused wave group. This model became known as NewWave. Tromans et al. demonstrated that the use of a 'designer' wave in the study of interactions with extreme waves can remove lengthy time domain calculations without sacrificing accuracy. Tromans et al. (1991) discussed the use of computationally intensive time domain simulations to find the maximum expected wave-structure interactions in a given time domain as an alternative to the use of sea states modelled using deterministic, monochromatic, periodic wave theory. These lengthy time domain simulations produced much more accurate results than the deterministic, monochromatic method as the periodic wave used in this approach often overestimates wave kinematics and therefore fluid load.

Lindgren (1970) and Boccotti (1983) showed that the average shape of a large crest, both temporally and spatially, is a scaled autocorrelation function in a linear random model of the ocean surface. This idea allowed a 'designer' wave to be used by Tromans et al. (1991) to ensure the accuracy of the time domain simulations mentioned earlier while avoiding the lengthy calculations required with that method. When many of the independent sinusoidal components found in a NewWave focused wave group come into phase, an extreme crest forms due to superposition. The unit-amplitude autocorrelation function is the Fourier transform of the wave energy spectrum and is given by:

$$\rho(\tau) = (1/\sigma^2) \int_0^\infty S(\omega) \cos(\omega\tau) d\omega \tag{1.6}$$

where σ is the standard deviation, ω is the linear angular frequency, and $S(\omega)$ is the wave energy spectrum. Taking into account spatial dependencies and discretising the function into the sum of N sinusoidal components leads to NewWave for a unidirectional wave group being:

$$\eta(X, Y, \tau) = (\frac{A_{Max}}{\sigma^2}) \sum_{n=1}^{N} S(\omega_n) \Delta\omega \, \cos(k_n(X \cos\beta + Y \sin\beta) - \omega_n \tau) \tag{1.7}$$

where β is the direction of propagation, (x_0, y_0, t_0) is the occurrence of the largest crest, $X = x - x_0$, $Y = y - y_0$, $\tau = t - t_0$, A_{Max} is the linear crest amplitude, and k_n is the wavenumber of the n^{th} wave component. Section 3.3 will show a derivation of the maximum expected amplitude for a given number of waves which will be used as A_{Max}. The angular frequency is related to k_n by the linear dispersion equation for waves on intermediate and deep water, with d being the water depth:

$$\omega_n^2 = k_n g \tanh(k_n d) \tag{1.8}$$

A comparison was made by Jonathan and Taylor (1997) between large non-linear crests from time series recorded offshore in the North Sea and equivalent predictions by the NewWave model. The largest non-linear crests from the measured time series were linearised and then compared with the NewWave profile. The agreement was excellent, showing that

NewWave is a reasonable model for large offshore wave crests.

The NewWave model discussed above uses the common assumption that extreme ocean waves can be modelled as having crests of infinite length and constant height perpendicular to the propagation direction. In real life, extreme storm waves have crests of a finite width and their three-dimensional structure is described by short-crested wave theory. The assumption of modelling waves as being planar with constant height is a good approximation because storm waves typically have incident periods of 12-15 s with wavelengths between 220-350 m. A large offshore structure will have a typical column spacing of around 80 m, which is fairly small compared to the peak wavelength. It therefore seems reasonable to assume that the crest height will be relatively constant across the width of the structure for an extreme wave.

A well-known and much studied example of an extreme wave is the Draupner New Year wave, see Adcock et al. (2011). However, its structure appears to be rather unusual as it appears that it arose in a (strongly) crossing sea state, which is fairly unusual for extreme sea states on the open ocean. The research presented in this thesis will focus on unidirectional waves and will therefore not make comparisons with the Draupner wave.

1.2.8 Linear random field statistics

It is generally accepted that regular waves are not a realistic model for extreme storm conditions. Instead, focused wave groups (as discussed above) or random seas should be used. Instead of treating an extreme wave as a deterministic event, as with the focused wave group analysis, the maximum expected free surface elevation may be calculated from the number of observed waves and the energy in their spectra. Statistical theory can show (Longuet-Higgins (1952), Dean and Dalrymple (1991)) that if the sea surface is composed of N statistically independent sinusoidal frequency components close to a mean frequency value, ω, forming a slowly varying surface elevation envelope, $B(t)$, then for a large number N, the probability of a wave crest amplitude being greater than or equal to an arbitrary wave crest amplitude, A', is given by the Rayleigh distribution with standard deviation, σ:

$$P(A \geq A') = e^{(-\frac{1}{2}(A'/\sigma)^2} \tag{1.9}$$

Ohl et al. (2001b) used random wave statistics in the prediction of linear diffracted free surface elevations around square arrays of four circular cylinders. Tayfun (1980) investigated narrow-banded non-linear sea waves, finding a simplified probabilistic description in the form of an amplitude modulated Stokes wave (Stokes (1847)) with a mean frequency and random phase. This is used to show that the wave heights are Rayleigh distributed as for the linear case but that the crests are non-Rayleigh. Tayfun and Fedele (2007) developed a second-order narrow-band approximation predicting the theoretical expected structure of large non-linear waves. Mori and Janssen (2006) took the analysis to beyond second-order, finding a weakly non-Gaussian theory for predicting the occurrence probability of freak waves and an estimate for the deviation from the usual Gaussian theory.

1.2.9 Second-order random field statistics

There are several methods of combining the statistics of both linear and second-order responses in a given sea state to find the probability of the water surface reaching a given level. These methods include those discussed by Tromans (see Gibson et al. (2007)), Winterstein (see Jha and Winterstein (2000)) and Naess (see Naess (1985)). The Tromans method incorporates a fully non-linear wave model into a spectral response surface method for broadbanded, unidirectional, deep-water sea states. All of the calculations are performed in the probability domain, avoiding lengthy time-domain simulations. A probability density function (pdf) is defined for the linear components of the wave surface elevation on the open ocean in a storm of specified properties, without the structure present. A transfer function is found to account for the presence of the structure, relative to open ocean, and its effect on wave surface elevation. This transfer function is then applied to the open ocean surface elevation pdf to transform it into a pdf describing the response surface elevation. Then a numerical search is carried out in probability space to find the Fourier representation of the most probable time history for the specified level of system response. This is a first-order reliability FORM method. For more information see Tromans et al. (1992).

Both the Winterstein and Naess methods express extreme responses in terms of a second-order Volterra series (including a linear and a quadratic term). Much work has been done on models such as these including, but certainly not limited to, Vinje (1983), Langley (1987), Naess (1985), and Naess (1990). The Winterstein method then uses water-depth dependent analytic formulae to predict the skewness and kurtosis of nonlinear random waves and the statistics of wave elevation and crest heights with specified return periods are then predicted by fitting a Hermite model to the first four moments of the response history, see Winterstein (1988), Jha and Winterstein (2000) and Winterstein and Sweetman (2001).

The Naess method finds the mean level upcrossing frequency of the second-order stochastic Volterra series and then asymptotic expressions are used to obtain closed-form solutions to the extreme-value problem (see Naess (1990), Naess and Karlsen (2004), and Naess et al. (2006)). This work was extended by Naess et al. (2008) to allow the efficient use of Monte Carlo simulations in the prediction of extreme responses for nonlinear floating offshore structures. Finally, a brute force method is also possible using linear transfer functions (LTFs) and QTFs calculated by software such as DIFFRACT or WAMIT. Jha and Winterstein (2000) suggested that one of the reasons for nonlinear ocean waves not entering common ocean engineering practice could be because of the 'cumbersome need for time-domain simulation of second-order waves' and that they used this as the motivation for the development of alternative methods. A brute force approach is generally considered to be impractical for regular use, but useful for validating any other method used.

1.3 Project Summary

The ultimate aim of the research will be to develop a screening method, based on numerical modelling, to assess the incidence and violence of possible water projection close to such diffracting structures. The methods will be developed so that they may be applied to any offshore structure, but this research will look mainly at a single semi-submersible geometry.

Scaled model tests in wave tanks are expensive and time-consuming, and so a viable alternative computational method would be a great aid to the design process. Reliable

predictions of sea states likely to cause violent wave-structure interactions could be used to target model testing to specific cases, minimising the time needed and maximising the usefulness of any results collected in the improvement of air-gap predictions. An alternative testing method would also allow modifications and iterations of the design to be made and tested faster, and at less cost. This project will aim to bring together the tools discussed in the literature review and to build on them to develop a screening method for use in the design of offshore structures. To be useful to the industry, the proposed numerical screening to be developed must be proven to be an accurate model of wave-structure interactions which takes into account both linear and second-order interaction effects. An incident wave field with a realistic spectrum for waves in severe storms should be used, such as Pierson-Moskowitz (Pierson and Moskowitz (1964)) or JONSWAP (Hasselmann et al. (1973)).

Instead of modelling storm conditions by deterministic, monochromatic, periodic wave theory using the elevation and period of a suitable extreme crest for the design location, Tromans et al. (1991) created a probabilistic focused wave group analysis (NewWave). This 'designer' wave models the sea as a set of independent sinusoidal components of random amplitude and removes the lengthy calculations required in the previous approach, minimising computation time while preserving accuracy. Extreme waves are random occurrences, and as such their position and time of occurrence cannot be predicted. However, NewWave effectively predicts the average shape of an extreme wave crest whenever it does occur in a given sea state. This is an efficient and accurate method of simulating extreme storm waves, and has been verified as the average shape of severe waves measured offshore: see Jonathan and Taylor (1997), Taylor and Williams (2004).

When designing a structure with an array of large surface-piercing columns, such as semi-submersible rigs and concrete gravity-based structures, diffraction effects must be included in any analysis conducted. When designing the air-gap, diffraction effects will be a major factor, along with mean water level and maximum incident wave crest amplitude. The air-gap is the vertical distance between the underside of the deck and the extreme wave crest beneath. It must be sufficiently large to prevent water strike on the deck, but must also be minimised to keep the centre of gravity as low as possible and to prevent excessive wind-

loading on the vertical surfaces of the platform. Accurately predicting the maximum height of vertical water projection and optimising structural configurations to minimise this height will be of particular interest to the offshore industry.

Using NewWave theory to model the shape of extreme wave crests, linear diffraction theory as developed by Linton and Evans (1990) can then be used to predict the interaction of extreme storm waves with arrays of cylindrical bottom-seated columns. For more complicated geometry a numerical diffraction code, DIFFRACT, will be used. DIFFRACT utilises the boundary element method to find a second-order solution to the three-dimensional water-wave diffraction problem (Eatock Taylor and Chau (1992)). A thorough examination will be made of how structure geometry affects the diffraction of storm waves at both first- and second-order, accounting for the cross-sectional shape of columns and their placement relative to others in an array. Understanding the relationship between structure geometry and wave-structure interactions is important when assessing the reliability of numerical surface elevation predictions based on simplified models of the structure being designed.

A possible cause of large runup and upwelling is a phenomenon known as near-trapping. This comprises near-resonant hydrodynamic responses that occur theoretically in arrays of surface-piercing bodies at certain frequencies dependent on the structure geometry (Evans and Porter (1999)). Diffraction of extreme waves by arrays of surface-piercing structures will be discussed for a variety of configurations. The investigation into how column geometry affects the diffraction of incident waves will focus on the incident sea states associated with near-trapped modes.

Statistical tools will be presented for more accurate extrapolation of simulation results to first- and second-order, with the aim of improving predictions of water-deck impact. The investigation of the effects of geometry on wave-structure interactions and the use of statistical tools in accurately predicting extreme events will be compared for both fixed and moving models. Although the structures under investigation such as TLPs and semi-submersibles are all floating in deep water, their anchoring systems vary greatly and have a large effect on the body motions possible. TLPs are restricted in their vertical motion due

to the nature of the system of stiff tendons, and so a fixed model may be more appropriate than a floating model when it comes to finding the diffraction solutions for them. Fixed and floating models will be compared to see if this has a significant effect on the prediction of wave-structure interactions.

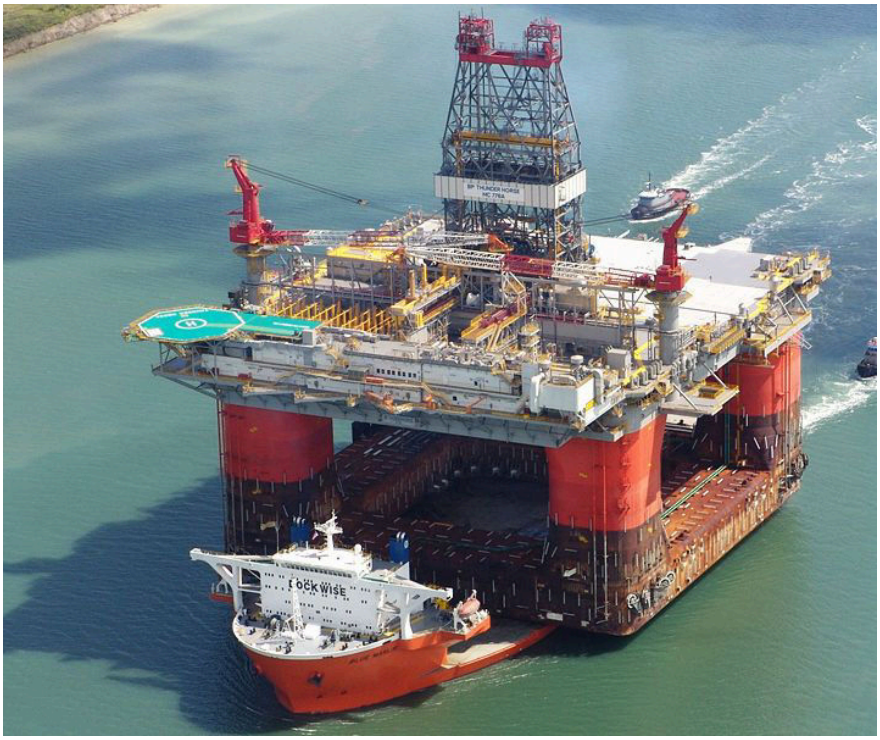

Figure 1.1: The Thunder Horse platform being transported to the Gulf of Mexico.

The structure serving as the main focus of the results presented here is BP's Thunder Horse semi-submersible. Thunder Horse is fairly typical of many semi-submersibles in its geometry, but it is one of the largest of its kind, with a displacement of almost 130000 tons and a deck area of over 12000 m^2. Figure 1.1 shows the Thunder Horse platform being transported to its current mooring in the Gulf of Mexico before its installation, and gives an excellent view of the structure's now-submerged geometry.

It has been stated that the aim of this research is to improve our understanding of the interactions between extreme waves and arrays of closely spaced surface-piercing columns. However, the positioning of columns close to others makes the wave-structure interactions far more complicated than for a single isolated column. Before one can understand the

physics behind interactions with multiple columns, one must first be confident of predicting interactions with a single column. The author participated in conducting experiments to measure the interaction of focused wave groups with a single column in medium depth water. Analysis of the results from these experiments will be included to ensure the behaviour around isolated columns is understood.

Many of the methods and techniques discussed in this research can be applied to both single and multiple columns and so the large set of data recorded in the single column experiments provides a valuable opportunity for testing these methods against physical data rather than just simulations. It also allows an investigation into the relative sizes of harmonic components well above second-order. DIFFRACT is limited to second-order and so it is important to look at whether the first two harmonics are enough to give a good approximation of extreme wave-structure interactions or whether higher order calculations would be necessary. Finally, some data were obtained for damage to a large TLP due to wave impact in a storm. The methods presented in this research will be applied to this real life example to see if the cause of the damage can be better understood.

1.4 Project Objectives

Building on the research outlined in the literature review, the objectives of the research described here are as follows:

1. Use linear water wave diffraction theory to investigate the effect of column geometry on wave-structure interactions.
2. Use linear wave diffraction theory to investigate wave-structure interactions with arrays of multiple columns.
3. Investigate the phenomenon of near-trapping with monochromatic linear excitation and square arrays of closely spaced columns. Study the effect on near-trapping of perturbing the structure geometry.
4. Use NewWave theory to more accurately model extreme waves. Compare wave-structure interactions for NewWave wave groups with monochromatic regular waves.
5. Discuss statistical methods of predicting extreme linear wave-structure interactions. Find the largest expected linear surface elevation magnifications due to wave-structure interactions.

6. Validate these statistical tools through the use of random sampling of a sea state spectrum in Monte Carlo type simulations and the collection of statistics on the generated random wave events.

7. Extend the use of water wave diffraction theories to second-order and compare these second-order wave-structure interactions to earlier linear results.

8. Compare second-order excitation of near-trapped modes with earlier linear results. Investigate whether linear calculations can be used to say anything useful about the more computationally intensive second-order responses at the same response frequency.

9. Collect statistics of response at second-order using Monte Carlo type simulations of random spectra. Investigate the relative size of first- and second-order response components. Predict the maximum expected surface elevation to second-order in a typical storm for the structure under study.

10. Investigate the structure of QTFs and determine whether flat approximations of QTF matrices can be used to minimise lengthy calculations.

11. Apply the methods described to a moving body and compare the results with an equivalent fixed model. Assess the importance of modelling structure motions in the prediction of wave-deck impact.

12. Analyse experimental data from focused wave group interactions with a single column to improve our understanding of the physics behind extreme wave-structure interactions. Investigate the feasibility of reconstructing body forces from surface elevation data in the vicinity of the column, as these are far more easily acquired than body forces for actual structures.

13. Use the methods described above to investigate a case of damage due to wave-structure interactions for a large multi-column structure in the North Sea.

14. Assess the practicality of using diffraction solutions in the design stage of future offshore structures to minimise expensive wave tank testing. Make recommendations for further work to build on the research described in this thesis.

1.5 Synopsis

The project objectives listed above are discussed in the following chapters:

Chapter 2 looks at the linear interactions of regular monochromatic waves with fixed structures. The effect of column geometry on diffraction about an isolated column is investigated, as given in Objective 1, along with the interactions due to closely spaced columns in

an array from Objective 2. Objective 3 called for the study of the near-trapping phenomenon with first-order excitations and an investigation into how symmetry perturbation can affect this, both of which are also studied in Chapter 2.

Chapter 3 looks at Objectives 4, 5, and 6, which called for the use of NewWave focused wave groups as more accurate models of extreme storm waves. Statistical tools are developed for predicting the maximum expected wave-structure interactions and these are then validated through the collection of statistics with randomly sampled Monte Carlo type simulations.

Objectives 7 and 8 are investigated in Chapter 4 with the extension of diffraction theory for monochromatic waves to second-order. Second-order diffraction results are compared with linear results at the same response frequency to see if linear calculations can be used to predict the more computationally intensive second-order calculations. Second-order excitation of near-trapped modes are investigated with a comparison of the mode shapes arising from first- and second-order excitation.

Chapter 5 extends the statistical methods of Chapter 3 to second-order and compares the results to the linear equivalent, for Objective 9. Predictions are made of the maximum expected wave-structure interactions in a typical storm and these predictions are then compared to the linear results from Chapter 3. QTF structure and their approximation are then discussed, as required for Objective 10.

Chapter 6 applies the methods discussed in the previous chapters to a now freely floating model and compares the results to those for an equivalent fixed structure. The importance of modelling body motions on water-deck impact is investigated, as stated in Objective 11.

Chapter 7 studies Objective 12 and analyses experimental data for interactions of focused wave groups with an isolated column. This is used to improve our understanding of wave-structure interactions and to verify some of the methods used for multiple columns earlier in the thesis. Chapter 8 aims to satisfy Objective 13 and improve our understanding of damage due to water-deck impact on a floating structure in the North Sea.

Chapter 9 then discusses the final objective of assessing whether diffraction solutions and numerical simulations can be used effectively to minimise expensive water-tank testing. Recommendations for the use of these methods and further work to build on this research will also be proposed.

Chapter 2

Linear diffraction

2.1 Introduction

This chapter looks at first-order diffraction of regular waves by single and multiple columns. The results presented here were generated using the numerical diffraction code DIFFRACT (discussed below). Solutions calculated by DIFFRACT have been thoroughly validated against published data and the first section of this chapter presents some of these verifications. Diffraction of incident regular waves by a single bottom-seated column is then studied, with particular care taken to investigate the effect of column cross-sectional shape on the diffracted wave field. As mentioned earlier, the majority of models used in this research were based on the geometry of BP p.l.c.'s Thunder Horse semi-submersible.

The analysis for isolated columns is then extended to arrays of two and four columns, with comparisons made between the three sizes of arrays (one, two, and four columns). The near-trapping phenomenon is studied for square arrays of four bottom-seated columns. The effect of column cross-section on near-trapping is investigated, as is the effect of perturbing the symmetry of the array by moving the location or changing the size of one of the four columns. Finally, more accurate models of Thunder Horse are used with comparisons made between arrays of bottom-seated columns, truncated columns in deep water, and columns connected by pontoons in deep water.

Only linear results are presented in this chapter. Further linear results are discussed in

Chapter 3, which presents data on diffraction of NewWave focused wave groups and statistical tools for the prediction of extreme wave-structure interactions. Second-order results are presented in Chapters 4 and 5, which discuss the structure of second-order QTFs and second-order statistics of response respectively. Figure 2.1 shows a schematic of the basic array geometry in plan view to illustrate the parameters used to describe the models under study. The columns are numbered clockwise from the top right quadrant; wave propagation direction, β, is measured relative to the x-axis; and each column angle, θ_i, is measured positive anti-clockwise from the x-axis.

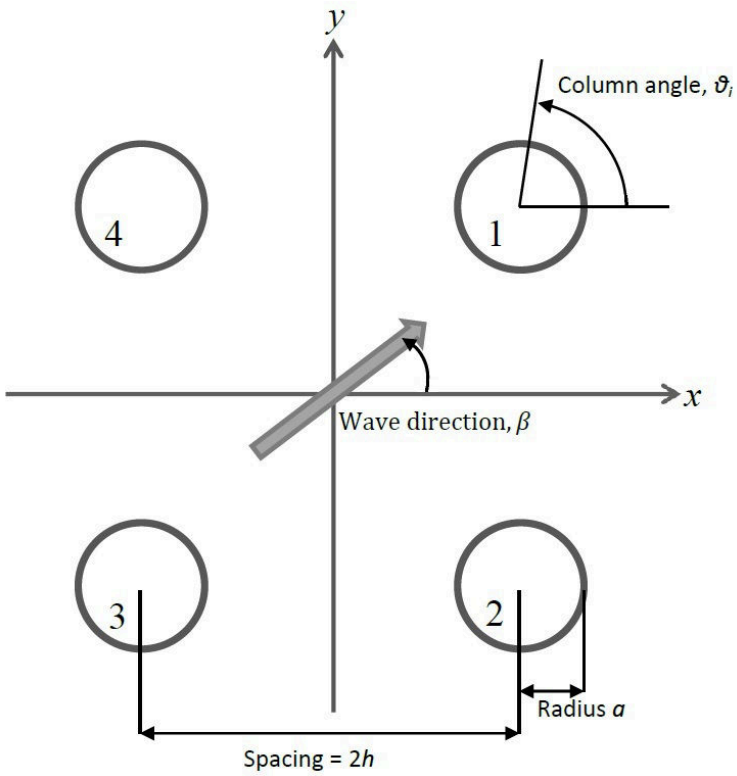

Figure 2.1: Schematic of array geometry and parameter definitions.

2.1.1 DIFFRACT

DIFFRACT is a CFD program for analysing first- and second-order wave-structure interaction problems using a higher-order Boundary Element Method. DIFFRACT approximates the first- and second-order velocity potentials in a Stokes' expansion for monochromatic or bichromatic and unidirectional or bidirectional seas. These can be incident on a single body

or arrays of bodies of arbitrary shape, both fixed and floating. The meshes used in the analysis consist of eight noded quadrilateral elements generated using a commercial mesh generating package called Gambit. This software is part of Fluent Inc. (www.ansys.com) and allows high quality meshes on arbitrary geometries.

The use of quadratic, rather than linear, elements on the solid bodies, and also on the free surface mesh for linear outer surface elevation and any second-order calculations, allows much smoother numerical solutions across the elements. It also enables satisfactory solutions to be obtained with far fewer elements than linear panels. Chau (1989) and Eatock Taylor and Chau (1992) describe the methodology behind DIFFRACT, with further details of the extension to floating bodies and to bichromatic waves in the final BOFCOS programme report by Eatock Taylor and Chamberlain (1993). For a definition of the quadratic transfer function (QTF) used, see Kim and Yue (1990). Further extension of the code in 2005 allowed bidirectional bichromatic waves to be analysed and a full second-order diffraction analysis to be carried out by modifying the code to include a second-order difference frequency term. The REBASDO progress report by Zang et al. (2003) details modifications to include free surface elevations in the output and the 2006-2009 SAFE OFFLOAD project added further features, see Eatock Taylor et al. (2008).

Hydrodynamic wave forces on the structure and free surface elevations both on and around the structure can be calculated to first- and second-order in addition to first-order motions of floating bodies. When calculating first-order forces and runup on the body, meshes are required for the cross-section of the body where it pierces the surface and the outer surface of the body. For surface elevations around the body and second-order forces or surface elevations, a mesh is also required of the surrounding outer free surface. Where appropriate, one or two planes of symmetry can be used to reduce computational times, and structures can be single or multiple bodies. The use of automatic mesh generation along with a GUI interface allows for much easier user implementation than previous versions of DIFFRACT.

2.2 Validation

It is obviously of great importance to validate against published data any code used to produce results, both analytical or numerical. DIFFRACT has been thoroughly validated for isolated columns and arrays at first and second-order, as discussed previously in Section 2.1.1. However, due to the importance of the accuracy of DIFFRACT solutions to this thesis, it seemed prudent to test the code against published data or a validated analytical solution for surface elevation around arrays of closely spaced columns. Two of the validation tests performed are presented here with comparisons between DIFFRACT and analytical solutions. The analytical solutions presented in this section were found by implementing the method of Evans and Porter (1997) which is described in the appendix to their paper.

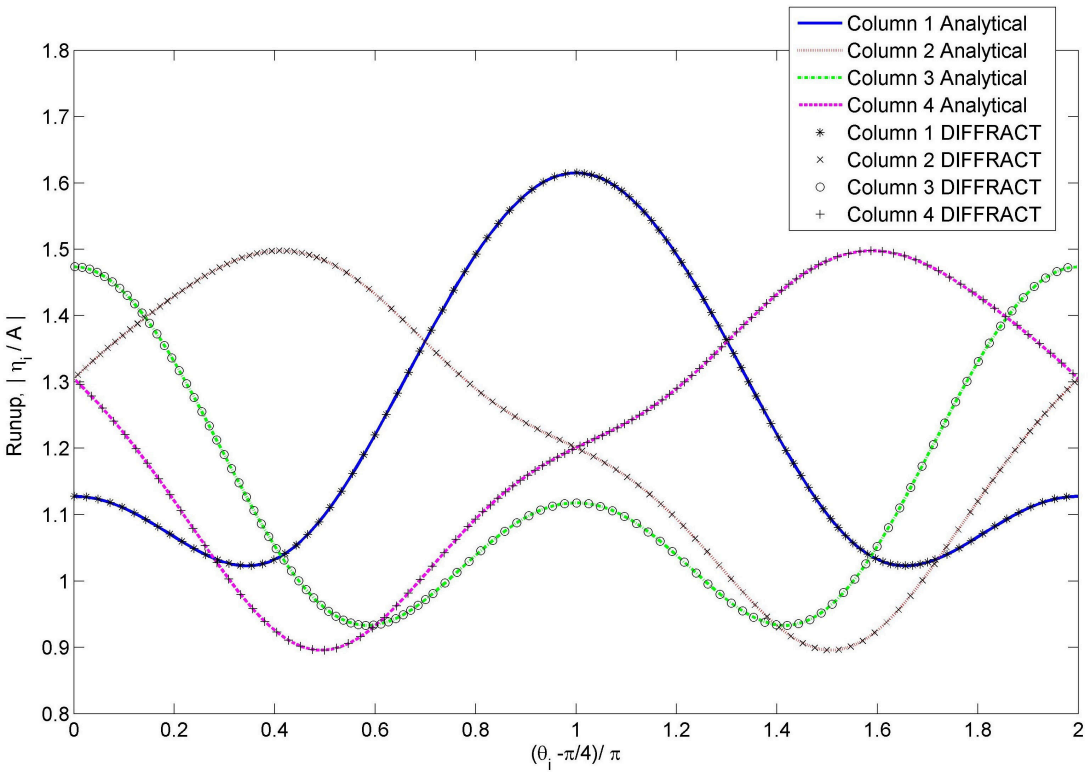

Figure 2.2: Non-dimensional first-order runup around a square array of four circular columns. $2h = 4a$, $d = 3a$, $ka = 0.468$, $\beta = 45°$. The lines show the analytical solution, the markers show DIFFRACT numerical solutions.

The first comparison is for the free surface runup around a square array of four circular columns, with the geometry and incident wave based on a solution presented by Malenica

et al. (1999). The column radius is a, the centre-to-centre spacing is $2h = 4a$, the water depth is $d = 3a$, the non-dimensional wavenumber is $ka = 0.468$, and the wave direction is $\beta = 45°$. Malenica et al. (1999) presented a solution to second-order but in this section only the first-order results are compared. See Chapter 4 for the second-order comparison.

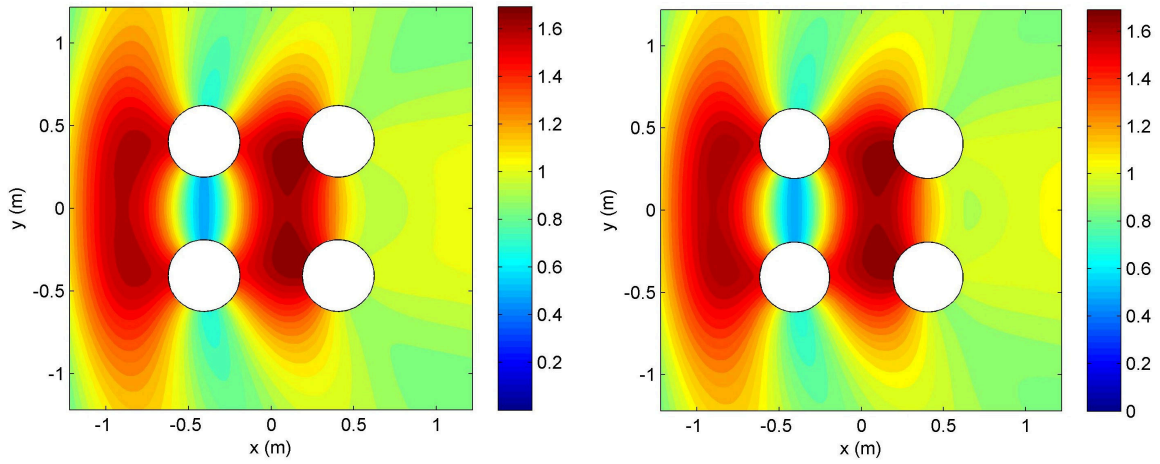

(a) Analytical solution (b) DIFFRACT solution

Figure 2.3: Magnitude of the non-dimensional linear surface elevation around a square array of four circular columns. $a = 0.203$ m, centre-to-centre spacing $2h = 4a$, $ka = \pi/6$, and $\beta = 0°$.

Figure 2.2 plots both analytical and DIFFRACT solutions for the magnitude of the non-dimensional runup around each column. The runup for each column is plotted against θ_i, where i represents the current column number, with Column 1 positioned at $(2a, 2a)$ and the other three columns numbered clockwise from this. θ_i is measured positive anti-clockwise from the x-axis (see Figure 2.1). The analytical and DIFFRACT solutions match up extremely well.

The second comparison is for the free surface elevation local to another square array of circular columns. This time the geometry and incident wave used are chosen to match the array analysed by Ohl et al. (2001a) where the column radius $a = 0.203$ m, centre-to-centre spacing is $2h = 4a$, wavenumber $ka = \pi/6$, water depth $d = 2$ m, and wave direction $\beta = 0°$. Figure 2.3 shows contour plots of the magnitude of the total surface elevation around the array, non-dimensionalised by dividing by the incident wave amplitude, A, for both analytical

and DIFFRACT solutions. The numerical and analytical solutions presented show excellent agreement again, both with each other and also with Ohl et al. (2001a).

2.3 Single columns

2.3.1 Column shape

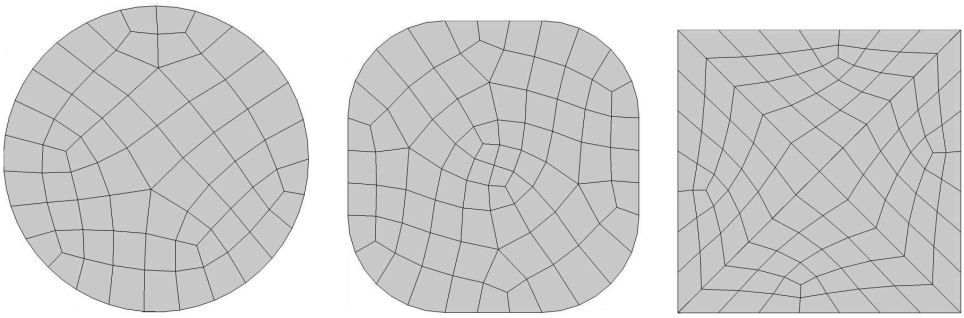

(a) Circular (b) Intermediate (c) Square

Figure 2.4: Column cross-sections, all with equal cross-sectional area (shown approximately to scale): (a) circular, (b) intermediate, and (c) square.

We now move onto new results. Three different column cross-sections were investigated (Figure 2.4): Circular (C), Square (S), and Intermediate (I), where the intermediate case is a square column with rounded edges and normalised radius of curvature, $r/a = 0.62$. Each column shape has the same cross-sectional area, and wavenumbers are normalised by the radius of the circular column, a. In all figures the wave direction, β, is given as the angle of incidence with the x-axis ($\beta = 0°$ moves from left to right, $\beta = 90°$ moves from bottom to top). Figure 2.5 shows two plots of maximum possible runup amplification against wavenumber for single bottom-seated columns with regular incident waves of unit amplitude, A, a water depth of $d/a = 2.43$, wave directions $\beta = 0° \ \& \ 45°$, and a wavenumber range of $ka = 0$ - 8.5. This extends beyond the range of practical interest for a typical storm wave spectrum but is used to illustrate the asymptotic behaviour.

The grey dotted line shown in both plots represents the maximum possible runup amplification on the circular column relative to the incident wave amplitude, A. This begins at 1 for very long waves with a wavenumber close to zero, rises to an asymptote of 2 for very short waves, and has small oscillations about the general trend. As the wavenumber increases, the wavelength eventually becomes small compared to the column diameter and the column can

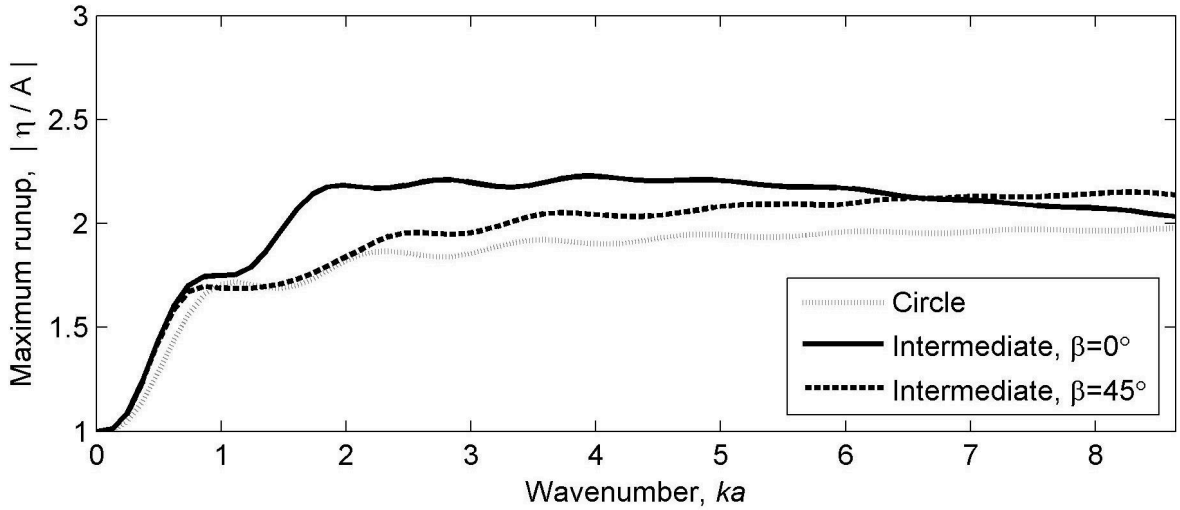

(a) Maximum |runup/A| against wavenumber, ka, for single C & I columns

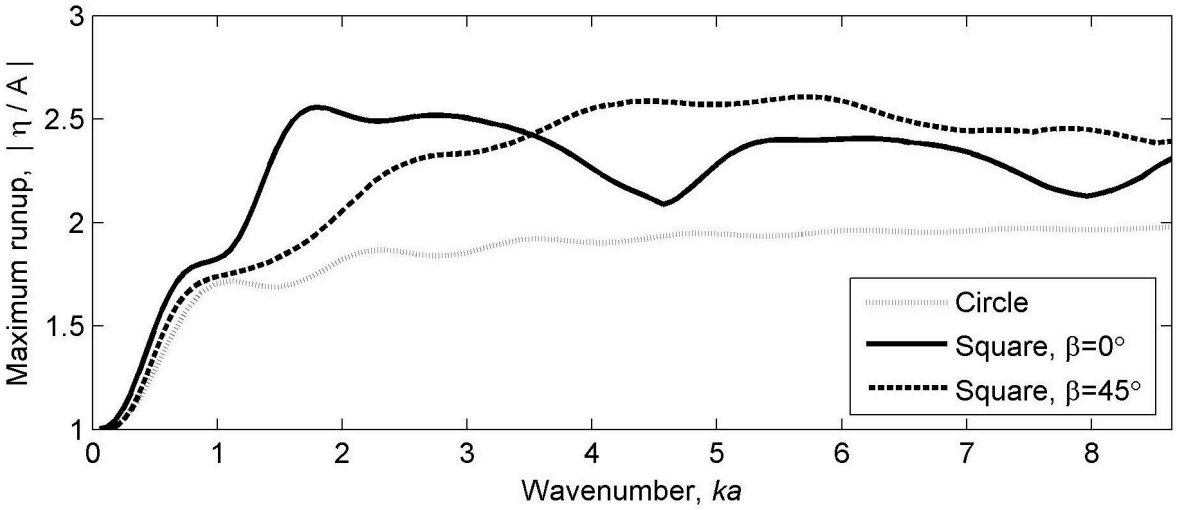

(b) Maximum |runup/A| against wavenumber, ka, for single C & S columns

Figure 2.5: Maximum |runup/A| vs. wavenumber for ka = 0-8.5 (where a is the circular radius) on (a) single circular (C) and intermediate (I) shaped columns and (b) single circular (C) and square (S) shaped columns.

eventually be locally approximated as an infinite vertical wall. The amplification for normal incidence is then the sum of the incident and reflected waves, giving the asymptote of 2.

The solid and dashed lines in Figure 2.5(a) show the maximum possible runup amplification at any point on the intermediate column for wave directions of $\beta = 0^\circ$ and $\beta = 45^\circ$ respectively (where $\beta = 0^\circ$ is positive along the x-axis and perpendicular to a flat face). For the case of an intermediate geometry column with $\beta = 0^\circ$, the maximum runup increases with wavenumber faster than for the circular column, first reaching an amplification of 2.18 at $ka = 1.974$. It then slowly asymptotes down to a value of 2, with small oscillations about the trend. For the intermediate geometry column with $\beta = 45^\circ$ case, the maximum runup

increases only a little faster than for the circular case. The maximum value reached, 2.15, is not as high as that of the $\beta = 0^\circ$ case, 2.23.

The solid and dashed lines in Figure 2.5(b) show the maximum possible runup at any point on the square column for wave directions of $\beta = 0^\circ$ and $\beta = 45^\circ$ respectively. For the square $\beta = 0^\circ$ case, the maximum runup increases with wavenumber faster than for the other two column shapes, reaching a maximum amplification of 2.56 at $ka = 1.79$. Again there is a slow asymptote, but this time to a slightly higher asymptotic value and with large oscillations about the trend. This will be discussed in Section 2.3.2. For the square $\beta = 45^\circ$ case, the runup amplification increases more slowly than for the square $\beta = 0^\circ$ case but reaches a slightly higher maximum value of 2.61. The oscillations about the asymptotic trend are smaller than those of the square $\beta = 0^\circ$ case.

2.3.2 Fresnel diffraction effects

The maximum $|\eta/A|$ on the non-circular columns is higher than for the circular case because of Fresnel diffraction effects (MacLaurin, 1909). Columns with angular corners placed perpendicular to incident regular waves have oscillations about the mean surface elevation across the leading face. Figure 2.6 shows runup for three cases: semi-analytical results for a vertical flat plate of width $2b$ positioned perpendicular to the flow (solid line), DIFFRACT results for a thin vertical wall of width $2b$ and thickness $0.1b$ (dashed line), and DIFFRACT results for a vertical circular column of diameter $2b$ (dotted line). The circular column is centred at the origin, and the plate and wall are aligned along the y-axis. Flow is along the x-axis, perpendicular to the flat plate and wall. The equations used for runup on the sharp edged plate are based on the analysis in Molin et al. (2006), which uses an eigenfunction expansion of the flow around a vertical plate at the centre of a wave tank (here taken to be very wide). The runup on the circular column is plotted against position on the y-axis.

The figures show that in each case there is a mean runup value of approximately 2. However, they also show that for both the plate and wall there is significant variation across their width and runup in excess of the asymptote. As the wavenumber increases, this runup

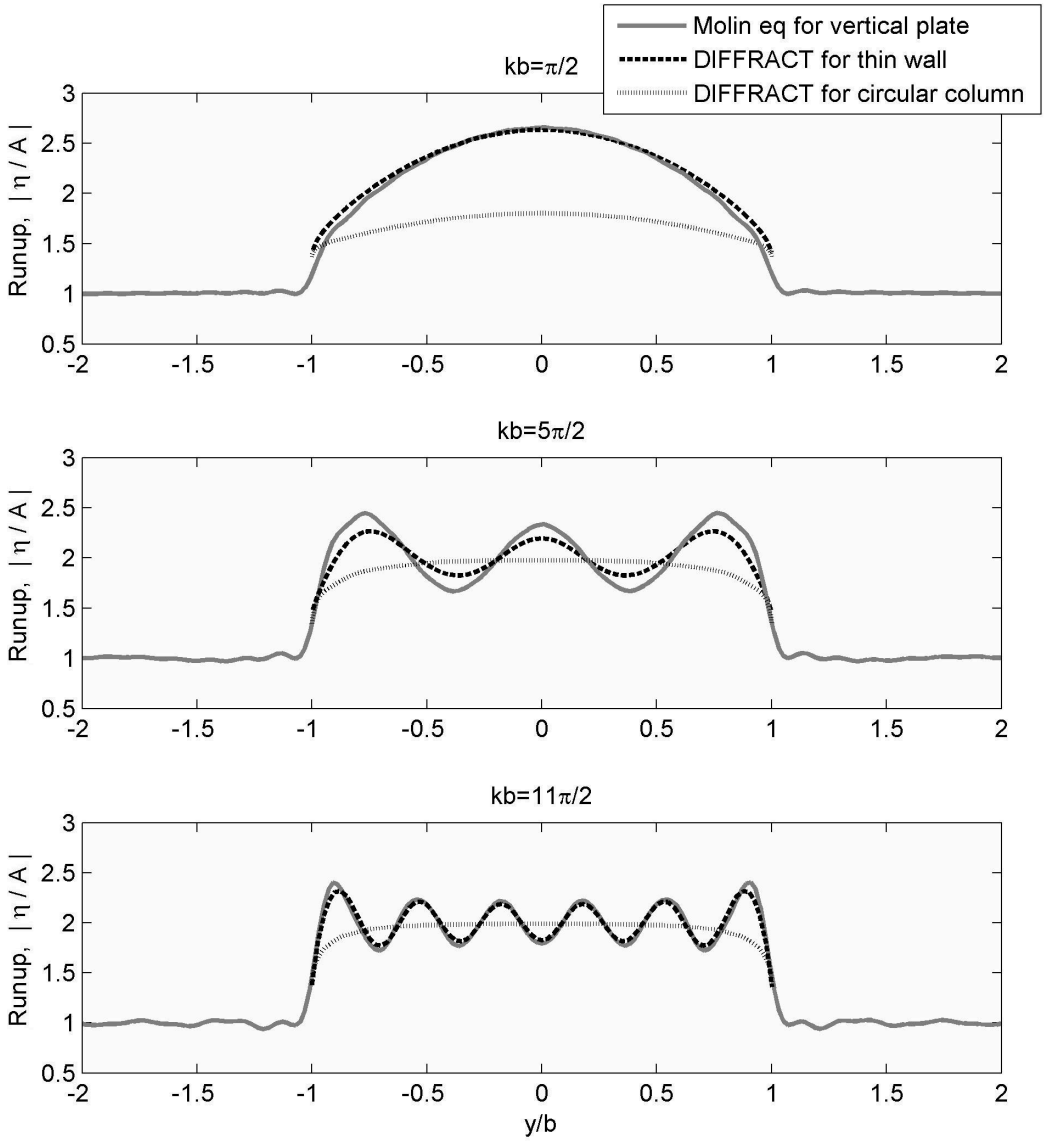

Figure 2.6: Runup on a flat vertical plate of width $2b$ (solid line), on a thin vertical wall of width $2b$ (dashed line), and on a circular column of diameter $2b$ (dotted line) for $kb = \pi/2$, $5\pi/2$, and $11\pi/2$.

variation seems to decrease in amplitude. The oscillations seen across the plate are not present for the circular cylinder. Previous work by Molin et al. (2005) showed that first-order effects similar to those shown on the plate were also present on a square column. The DIFFRACT results in Figure 2.6 for a thin wall are very similar to those for a vertical plate. Some differences are to be expected due to the finite thickness of the wall but the results are close enough to suggest that the use of DIFFRACT for such thin rectangular structures is reasonable.

Figure 2.7 shows two plots of runup versus wavenumber. Figure 2.7(a) shows maximum

runup anywhere on the surface of the body against wavenumber for three different cases: analytical results for a vertical plate in a channel as mentioned above (solid line), DIFFRACT results for a thin wall (dashed line), and DIFFRACT results for a square column (dotted line). The incident wave direction is perpendicular to the flat face in each case. All cases have an asymptote which is greater than 2, the value seen with a single circular column. This suggests that the Fresnel diffraction effects have a minimum oscillation amplitude which is greater than zero. Figure 2.7(b) shows runup at the centre for the three cases used in Figure 2.7(a). These asymptote to a value of 2, as expected, since the Fresnel oscillation peaks localise towards the edges with increasing wavenumber.

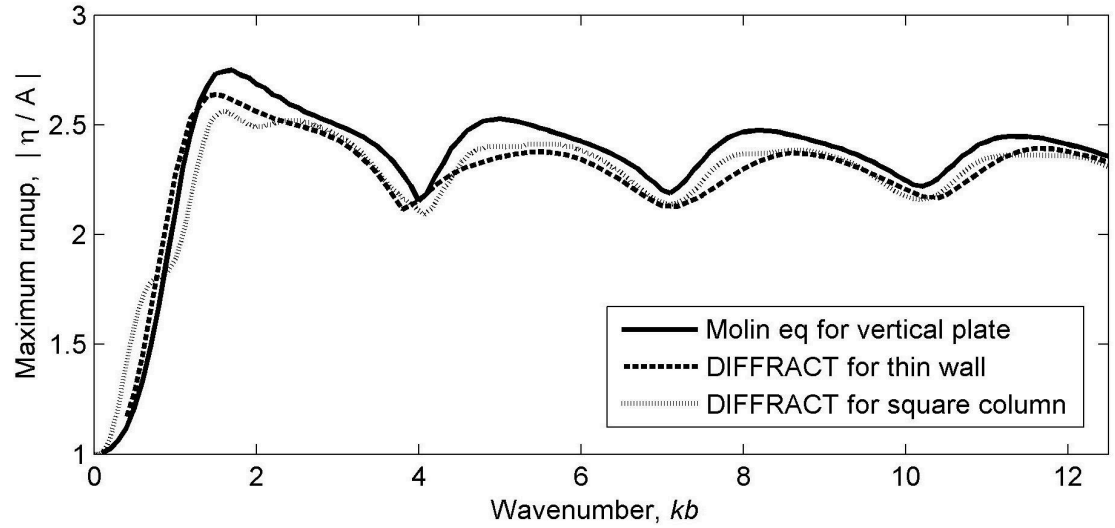

(a) Maximum |runup/A| against wavenumber, kb

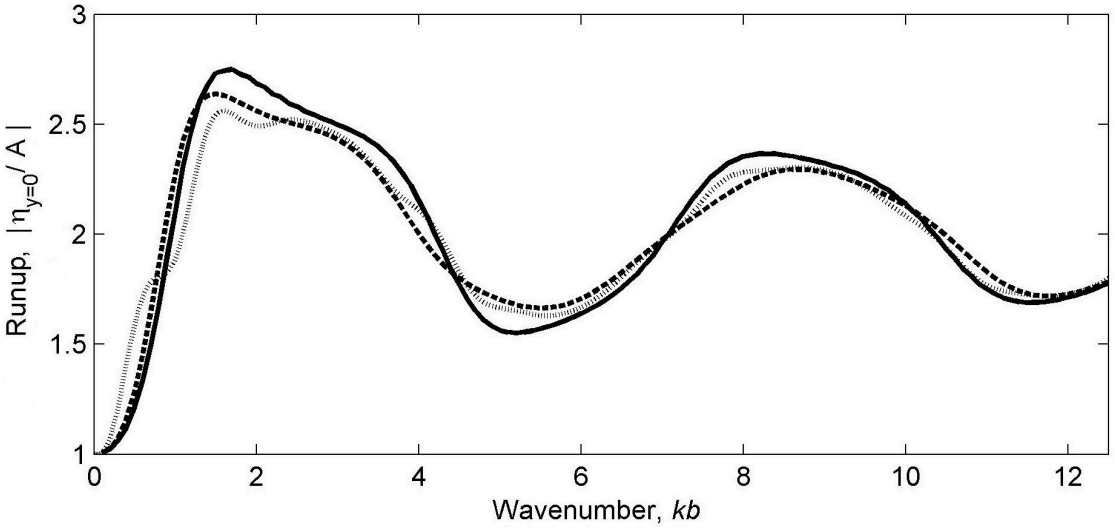

(b) |runup$_{y=0}$/A| at centre against wavenumber, kb

Figure 2.7: (a) Maximum |runup/A| against wavenumber, kb, and (b) |runup$_{y=0}$/A| at the centre against wavenumber, both shown on a flat vertical plate (solid line), on a thin vertical wall (dashed line), and on a square column (dotted line), all of width $2b$ with $\beta = 0\,^{\circ}$.

As wavenumber increases, the oscillation patterns seen in Figure 2.6 become less spread out along the wall with the pattern becoming more compact at the sharp corners. There is also a decrease in amplitude with wavenumber until a limiting value is reached. This behaviour is similar to the Gibbs phenomenon found in signal processing. The Gibbs phenomenon describes the difficulty of approximating a periodic discontinuous function with a finite series of continuous cosine and sine terms. At the discontinuity, the approximation contains large oscillations which can overshoot the signal being approximated. As the number of terms in the Fourier series increases, the width and height of the oscillations both decrease. However, the amplitude of the overshoot does not decay to zero, it instead reaches a minimum oscillation amplitude of 8.95 % of the discontinuity height. The similarities between Fresnel diffraction and the Gibbs phenomenon are in behaviour only. The Fresnel diffraction effects describe a real physical process whereas the Gibbs phenomenon describes a problem occurring when approximating a discontinuous function with a finite series of continuous sine and cosine terms. There is simply a useful analogy between the two where a continuous periodic function (incident ocean waves or a finite sum of sine and cosine terms) is disturbed by a singularity (a sharp cornered obstacle or a discontinuity in the function to be approximated) and the result is an imperfect fit with oscillations about the target function.

2.3.3 Upwelling in the surrounding field

It has been shown that runup on a single column is highly dependent on the body cross-sectional shape. Field plots demonstrate that the cross-section can cause significant changes to the diffracted field for a distance of several diameters out from the column. Figures 2.8(a-c) show comparisons of field plots around the previously discussed circular, intermediate, and square columns for a regular wave with $\beta = 0^\circ$ and $ka = 1.831$ ($T = 5.215$ s). This wavenumber was selected as corresponding to one of the near-trapping frequencies identified in Section 2.5, but also lying in the range of ka values that show a large difference between the runup on the isolated columns having these three different shapes.

The variation in column shape causes little difference in the general surface elevation pat-

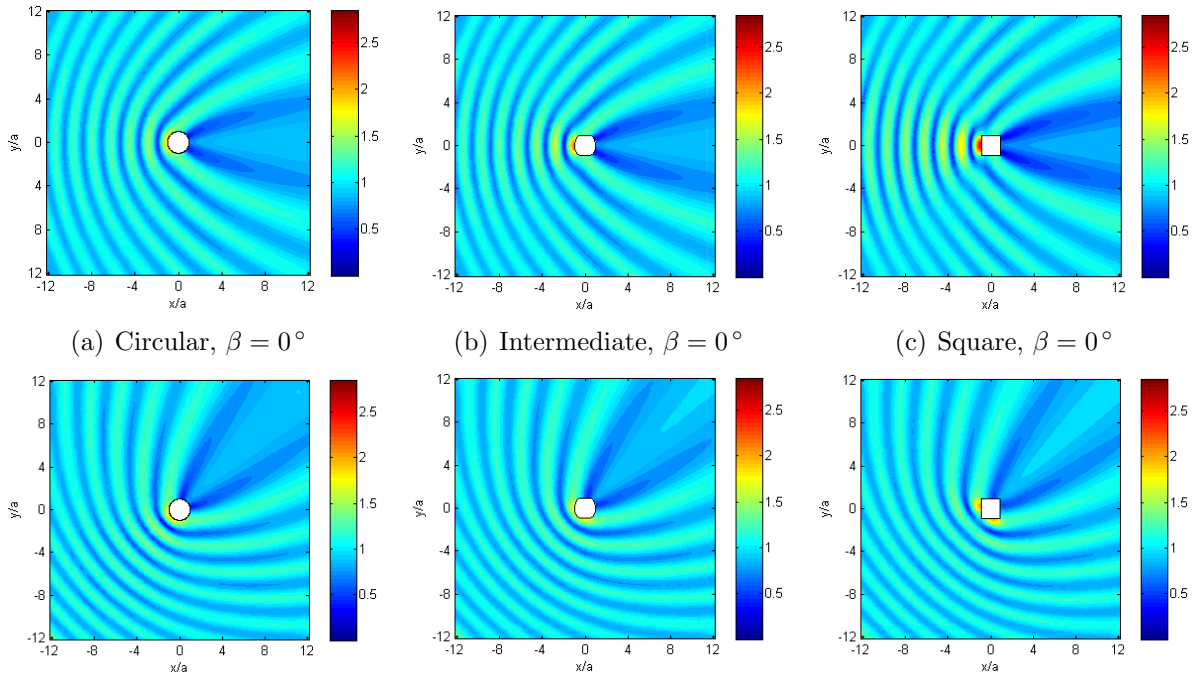

(a) Circular, $\beta = 0°$ (b) Intermediate, $\beta = 0°$ (c) Square, $\beta = 0°$

(d) Circular, $\beta = 45°$ (e) Intermediate, $\beta = 45°$ (f) Square, $\beta = 45°$

Figure 2.8: Total surface elevation amplitude around single bottom-seated circular, intermediate, and square columns for regular incident waves with $ka = 1.831$ ($T = 5.215$ s), and $\beta = 0°$ in (a-c), $\beta = 45°$ in (d-f).

tern for either wave direction. However, the amplitudes within the general pattern are modified with notably higher runup on the non-circular columns for the $\beta = 0°$ wave direction. There are maximum values of 1.86, 2.17, and 2.56 for the circular, intermediate, and square cases respectively, giving a 38 % increase between the circular and square columns. There is also increased amplification for several diameters' distance upstream. For the $\beta = 45°$ wave direction (Figures 2.8(d-f)), there is reduced runup on the intermediate column relative to the circular case and the square column has a smaller increase than for the $\beta = 0°$ case. The location of the maximum runup on the intermediate and square column cases was not on the leading edge but to the sides on the adjacent flat faces. There are also areas of reduced amplification upstream and increased elevation downstream relative to the circular case.

Table 2.1 shows maximum surface elevation amplification in several cases for a regular incident wave with $ka = 1.831$ ($T = 5.215$ s) in each. There are three wave directions: $\beta = 0°$, $30°$, and $45°$, and four column shapes: circular, intermediate, square with a flat face perpendicular to $\beta = 0°$, and rotated square with a flat face perpendicular to $\beta = 45°$. Results are also given for arrays of two and four columns, which are discussed in the next

β	Shape	$\lvert\eta_{Max}/A\rvert$ by array:		
		One	Two	Four
0	Circular	1.86	2.05	2.17
	Intermediate	2.17	2.39	2.49
	Square	2.56	2.77	2.77
	Rotated Square	1.99	2.11	2.29
30	Circular	1.86	2.00	2.12
	Intermediate	1.99	2.22	2.23
	Square	2.32	2.58	2.57
	Rotated Square	2.32	2.71	2.92
45	Circular	1.86	2.13	2.84
	Intermediate	1.79	2.13	2.66
	Square	1.99	2.25	2.85
	Rotated Square	2.56	2.84	3.49

Table 2.1: Maximum $|\eta/A|$ for circular, intermediate, square, and rotated square columns in arrays of one, two or four columns with $ka = 1.831$ ($T = 5.215$ s) and $\beta = 0°$, $30°$, and $45°$.

section.

2.4 Multiple columns

The results from the previous section show that cross-sectional shape affects the diffraction patterns caused by a single column in regular waves. What is of more interest to us is the effect of column shape on the interaction of waves with arrays of multiple columns. Two groups of columns in simple arrays are studied in this section and compared with the single columns discussed previously. For each of the column cross-sections used there is a single pair of columns equally spaced either side of the x-axis and an array of four columns in a square formation. The dimensions used in the four column array are typical for a semi-submersible platform, with a centre-to-centre spacing between adjacent columns of $2h/a = 6.71$ in water of depth $d/a = 2.43$. A summary of the single column results discussed earlier is shown in the first column of Table 2.1.

Figure 2.9 shows field plots around pairs of columns, which have the four cross-sections discussed above. The conditions are unit-amplitude, regular, incident waves of wavenumber $ka = 1.831$ ($T = 5.215$ s) and $\beta = 0°$, with waves approaching through the left side of

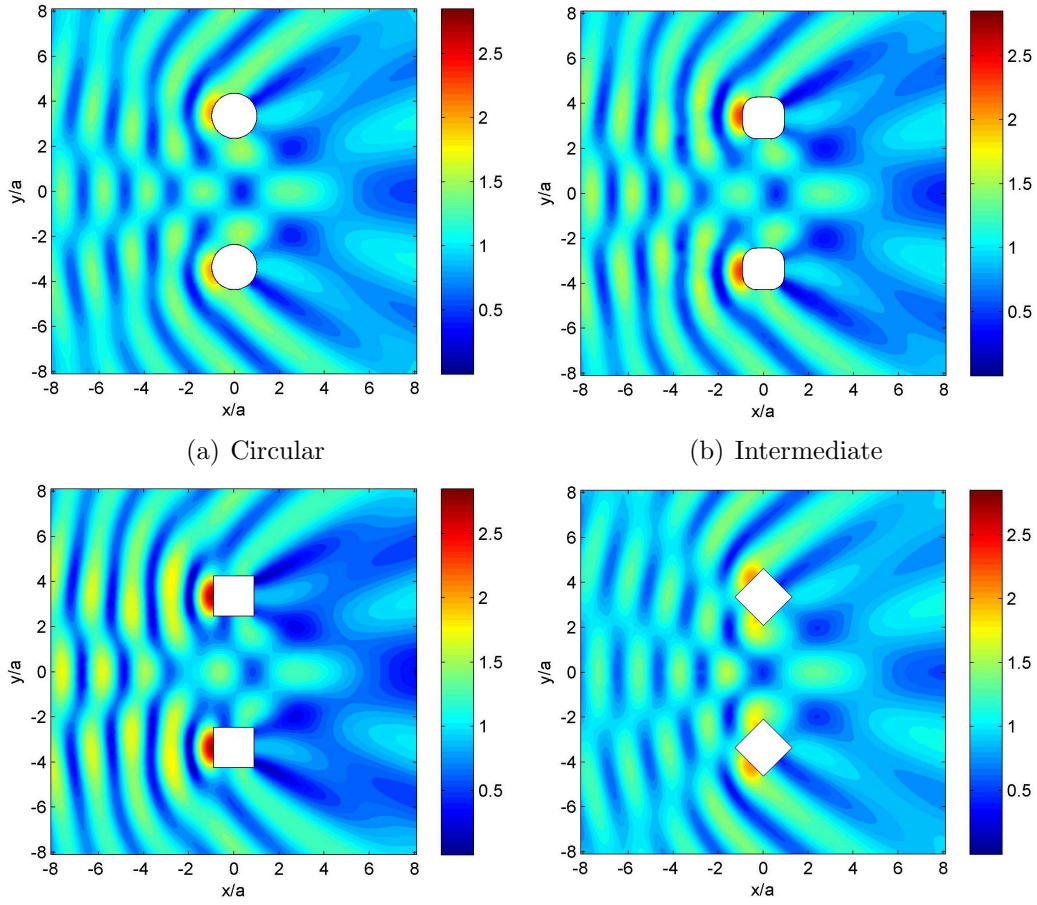

(a) Circular (b) Intermediate

(c) Square (d) Rotated Square

Figure 2.9: Total surface elevation amplitude around pairs of bottom-seated circular, intermediate, square or rotated square columns for regular incident waves with $\beta = 0°$ and $ka = 1.831$ ($T = 5.215$ s).

the figure. As with the single column case, changing the cross-section of the columns has relatively little effect on the general shape of the diffraction pattern. There is obvious sheltering downstream and three main lines of amplification upstream, with the largest amplifications occurring on the surface of the columns. Changing the shape of the column does lead to a change in the maximum $|\eta/A|$ amplification, as shown in Table 2.1. It is important to note that the interaction of the two columns leads to a higher maximum amplification in every case relative to the equivalent single column.

Table 2.1 shows that for the $\beta = 0°$ case the two square columns have a maximum surface amplification of 2.77, which is an 8 % increase relative to the single square column case and a 35 % increase relative to the pair of circular columns. For the intermediate $\beta = 0°$ case, the presence of a second column causes a 10 % increase relative to the single column. Interestingly, for the cases with two columns and $\beta = 45°$ the maximum values

for the intermediate and circular columns are now equal, unlike for a single column where the circular case is higher. The increase from single to two columns at $\beta = 45°$ is 19 % for the intermediate and only 13 % for the square column shape. The largest amplification for a single column or pair of columns is 2.84, with a pair of rotated square columns and $\beta = 45°$. These values all show that the interactions between columns are definitely affected by column shape, and this should therefore be taken into account when designing a new structure.

Figure 2.10 shows field plots around square arrays of four bottom-seated columns with the four column shapes discussed above, unit amplitude regular incident waves, a wavenumber of $ka = 1.831$ ($T = 5.215$ s), and $\beta = 0°$ and $45°$. The presence of four closely spaced columns leads to far more complicated diffraction patterns than those shown previously and usually higher maximum surface amplifications. For the $\beta = 0°$ case, the circular column array has a large peak at its centre and a second smaller one between the leading two columns. For the intermediate shaped columns the upstream peak becomes slightly larger than the central peak and this effect is magnified in the square column case. The presence of the downstream square columns does not raise the maximum surface amplification relative to the two column case but does cause increased amplification for several column diameters in front of the upstream pair. The four rotated square columns have a maximum amplification of 2.29, which is only a little larger than the circular case with 2.17 (see Table 2.1).

For the $\beta = 45°$ case there is a distinct change in the position of the maximum surface amplification, from the upstream edge of the downstream column in the circular case to the inside edges of the middle two columns for the square case. There are also decreases in amplification upstream of the leading column from the circular to intermediate to square column cases. The rotated square column case has peaks on the leading edges of the downstream and central columns, along with the downstream edge of the upstream column. With a value of 3.49, the maximum surface amplification for the array of four rotated square columns is by far the highest of all cases studied at this wavenumber.

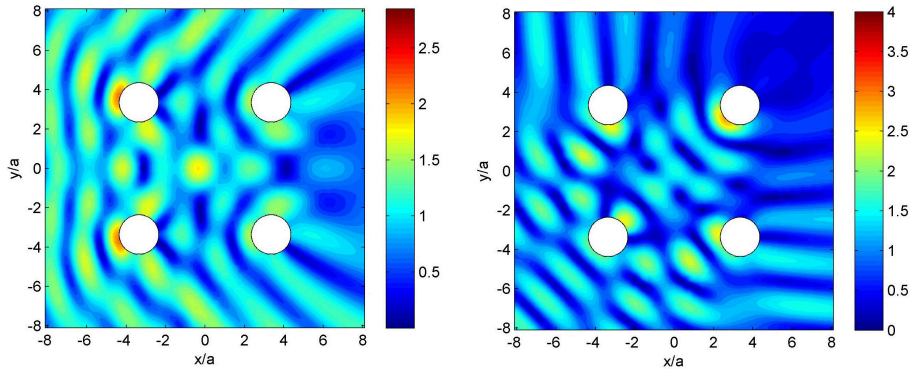

(a) Circular, $\beta = 0\,^\circ$ (b) Circular, $\beta = 45\,^\circ$

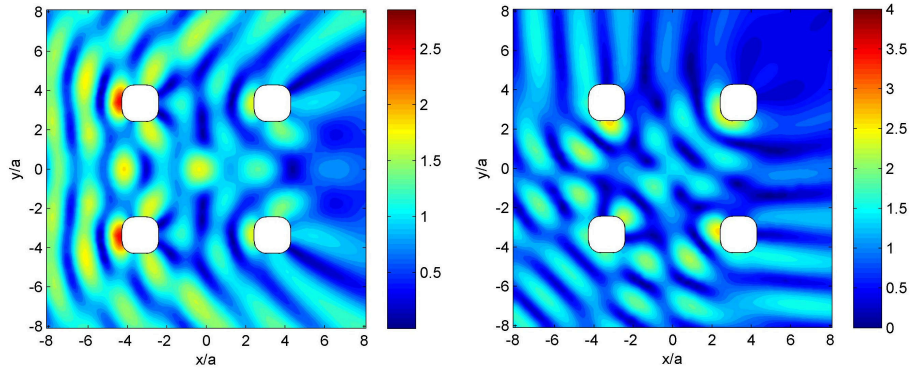

(c) Intermediate, $\beta = 0\,^\circ$ (d) Intermediate, $\beta = 45\,^\circ$

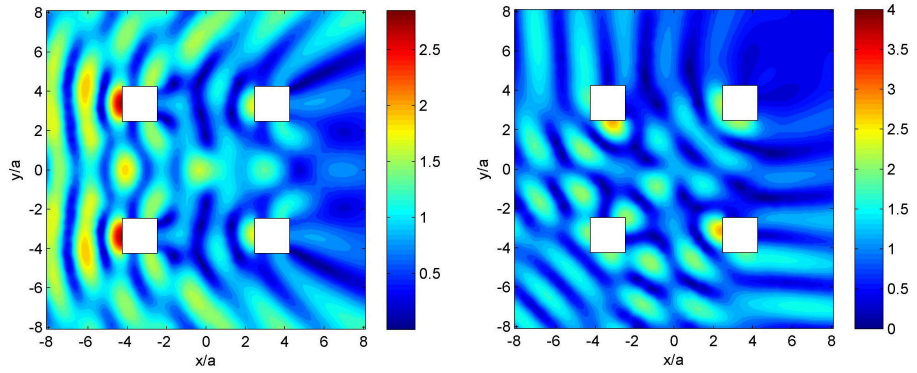

(e) Square, $\beta = 0\,^\circ$ (f) Square, $\beta = 45\,^\circ$

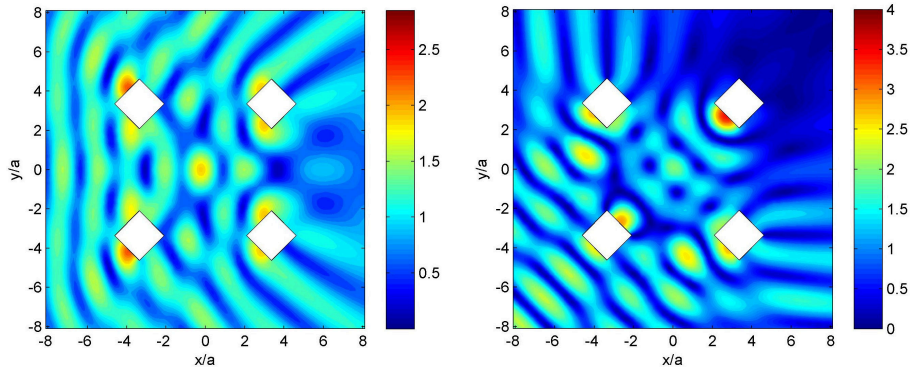

(g) Rotated Square, $\beta = 0\,^\circ$ (h) Rotated square, $\beta = 45\,^\circ$

Figure 2.10: Total surface elevation around square arrays of four bottom-seated circular, intermediate, square or rotated square columns for regular incident waves with $ka = 1.831$ ($T = 5.215$ s). $\beta = 0\,^\circ$ for (a),(c),(e), and (g) and $\beta = 45\,^\circ$ for (b),(d),(f), and (h).

2.5 Near-trapping

Near-trapped modes are near-resonant responses excited by waves of the appropriate frequency interacting with structures such as arrays of vertical surface piercing columns, see Evans and Porter (1997). Each near-trapped frequency is associated with a mode of strong local free surface oscillation in time which radiates energy rather weakly to infinity. These modes can be excited either by incident free waves of a near-trapped frequency or through forced excitation by non-periodic wave groups via the interaction of many linear incident wave components.

The method of Linton and Evans (1990) was used to find the theoretical near-trapped frequencies for the case of four bottom-seated vertical circular columns with radius $a =$ 12.34 m, depth 30 m, and centres located at $(\pm 41.42 \text{ m}, \pm 41.42 \text{ m})$. These dimensions are typical of the columns of a large semi-submersible platform. An analytical solution for this simplified structure can provide a useful starting point when analysing a more realistic model, for which a numerical solution must be found. Complex trapped wavenumbers can be predicted by finding when the determinant of the coefficient matrix system, which is based on the truncated infinite series, is close to zero. For a full analysis of the linear problem see the solution in Linton and Evans (1990); however, some key equations are presented here.

For N_c cylinders, N_c+1 polar coordinate systems are used: (r, θ) as the global coordinate system centred at the origin and then N_c local coordinate systems, one for each of the cylinders, with the origin of (r_j, θ_j) located at the centre of the j^{th} cylinder, (x_j, y_j).

The potential due to scattering from cylinder j is given by

$$\phi_S^j = \sum_{n=-\infty}^{\infty} A_n^j Z_n^j H_n(kr_j) e^{in\theta_j} \tag{2.1}$$

where A_n^j are complex coefficients to be found, a_j is the radius of cylinder j, $Z_n^j = J_n^{'}(ka_j)/H_n^{'}(ka_j)$, $H_n(kr_j)$ is the Hankel function: $H_n(kr_j) \equiv J_n(kr_j) + iY_n(kr_j)$, $J_n \,\&\, Y_n$ are the usual Bessel functions, and $J_n^{'}$ is the derivative of J_n etc.

The total potential at any point can then be found from the above equation using Graf's addition theorem:

$$\begin{aligned}\phi &= \phi_I + \sum_{j=1}^{N_c} \phi_S^j \\ &= e^{ikr\cos(\theta-\beta)} + \sum_{j=1}^{N_c}\sum_{n=-\infty}^{\infty} A_n^j Z_n^j H_n(kr_j) e^{in\theta_j}\end{aligned} \tag{2.2}$$

where β is the wave heading relative to the x-axis. An infinite series of equations for the coefficients A_m^k can be obtained by specifying that the total diffracted wave field satisfies the conditions of no flow through the solid surface of each cylinder:

$$A_m^k + \sum_{j=1\neq k}^{N_c}\sum_{n=-\infty}^{\infty} A_n^j Z_n^j H_{n-m}(kR_{jk}) e^{i(n-m)\alpha_{jk}} = -I_j e^{im(\pi/2-\beta)} \tag{2.3}$$

for $k = 1, ..., N_c$; $-\infty \leq m \leq \infty$ where $I_j = e^{ik(x_j\cos\beta + y_j\sin\beta)}$ is a phase factor associated with cylinder j, $R_{jk} = \sqrt{(x_k - x_j)^2 + (y_k - y_j)^2}$ and α_{jk} is the angle defined positive anticlockwise from the positive x-axis to the line joining the centres of cylinders j and k. This infinite series must be truncated outside the range $-M \leq m \leq M$ to allow numerical computation. Solving a truncated set of these equations gives a general solution and these A_m^k values can then be used to give the wave elevation at any point.

The transfer function from incident wave to scattered free surface elevation is then

$$H(x, y, t) = Re(\eta(x, y)e^{-i\omega t})/A \tag{2.4}$$

where $\eta(x, y) = A\phi(x, y)$ and A is the amplitude of the incident wave.

When the determinant of the coefficient matrix system based on the truncated infinite series above is close to zero, the free surface amplitudes can become large close to the cylinders. By plotting contours of the modulus of the complex determinant of this matrix system on axes showing the real and imaginary wavenumber values, the locations of zero values can be found. This is shown in Figure 2.11 with the zeros easily identifiable. The exact values of the near-trapping frequencies can be found using the function 'fminsearch'

in Matlab (2010) and initial values estimated from the contour plot in Figure 2.11.

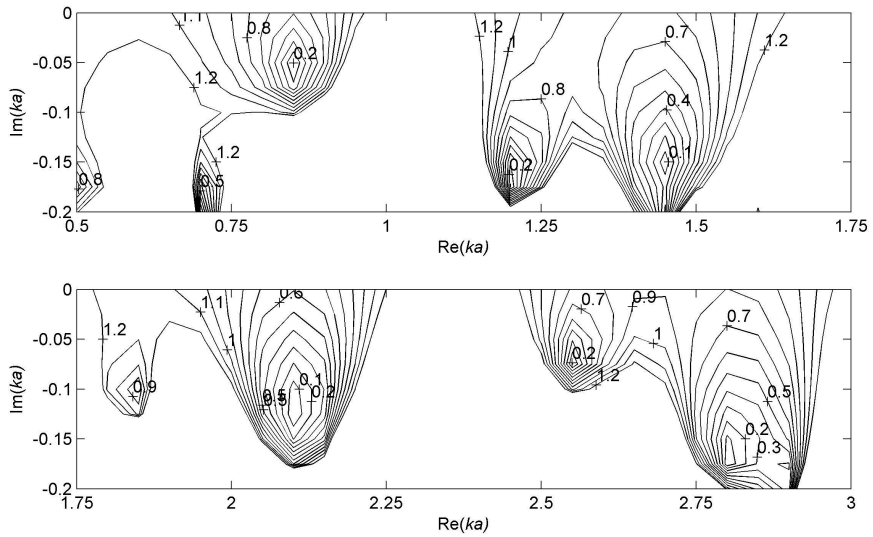

Figure 2.11: Contours of the modulus of the determinant of the matrix of A coefficients.

These near-trapping wavenumbers are shown in Table 2.2 with columns showing the real and imaginary parts of the wavenumber normalised by column radius and the associated peak period for the typical semi-submersible dimensions given above. The real parts of these complex wavenumbers are the wavenumbers of near-trapped response modes, and if the imaginary part were zero it would be a case of pure trapping. The size of the imaginary part gives a measure of the wave damping due to radiation to infinity. Therefore, the closer the imaginary part is to zero, the closer to pure-trapping the mode becomes and very large responses can be predicted to have rather weak radiation leaking outwards to infinity.

For the geometry analysed there are 13 near-trapped modes with a wavenumber less than 0.3 m^{-1}. For wavenumbers greater than this, the maximum possible elevation is too small to be of practical interest. The mode with the longest wavelength is at Re(ka)= 0.324 and for the geometry used this corresponds to an excitation period of 12.38 s. This is of interest as storm waves on the open ocean typically have $T_p = 12 - 15$ s, which means that this mode could be excited linearly. The other modes are unlikely to be excited linearly in a typical storm; however, they could be excited by higher order responses. A second-order

Re(ka)	Im(ka)	T (s)
0.324	-0.1605	12.380
0.521	-0.1936	9.789
0.711	-0.2002	8.330
0.858	**-0.0600**	**7.582**
1.209	-0.1697	6.408
1.447	-0.1475	5.865
1.831	-0.1176	5.215
2.106	-0.1201	4.851
2.558	**-0.0724**	**4.409**
2.798	-0.1686	4.210
2.895	-0.1903	4.138
3.298	-0.1023	3.882
3.561	-0.1678	3.732

Table 2.2: Near-trapped wavenumbers for the array of four bottom-seated circular columns.

sum response for $T_p = 14$ s waves could lead with frequency doubling to an excitation at $T_p = 7$ s. The two near-trapped modes with the smallest Im(ka), shown in bold in Table 2.2, have corresponding peak periods of 7.582 and 4.409 s. A small imaginary part of the wavenumber indicates a particularly large response. As mentioned above, these two modes are unlikely to be excited linearly due to their small peak period; however, frequency doubling and tripling of typical storm waves suggests that the $T = 7.582$ s mode could be excited as a large second-order response and the $T = 4.409$ s mode could be excited as a large third-order response. Second-order analysis of near-trapped modes for similar geometries will be addressed in Chapter 4.

Near-trapped modes are excited by particular incident wave directions. Figure 2.12(a) concerns runup on a square array of four circular bottom-seated columns. The columns are numbered clockwise starting from the quadrant where both x and y are positive. The maximum |runup/A| on each column is plotted against wave direction, β, and can be used as an indication of which wave directions will excite a near-trapped mode. They are, however, a starting point only; for example, if a near-trapped mode caused a point of maximum amplification in the centre of the array, then looking only at runup could miss it. Allowing for this, Figure 2.12(a) still strongly suggests that there is an excitation direction at $\beta = 45°$ with high runup on all four columns. There are also other potential excitation directions

with peaks in runup amplification on one or more columns at $\beta = 10°$, $20°$, $70°$, and $80°$, although these may be less significant.

Figure 2.12(b) shows a plot similar to Figure 2.12(a) but for a square array of four square bottom-seated columns. There are some obvious differences relative to the circular case. The largest excitation direction is no longer at $\beta = 45°$ but instead there is a pair of excitation directions at $\beta = 43°$ and $47°$. Also, as β tends to $0°$ or $90°$ the two leading columns have a much larger runup amplification than for the circular case, as is expected from the previously shown field plots of square versus circular columns.

The majority of results presented in this research are with wave directions along lines of

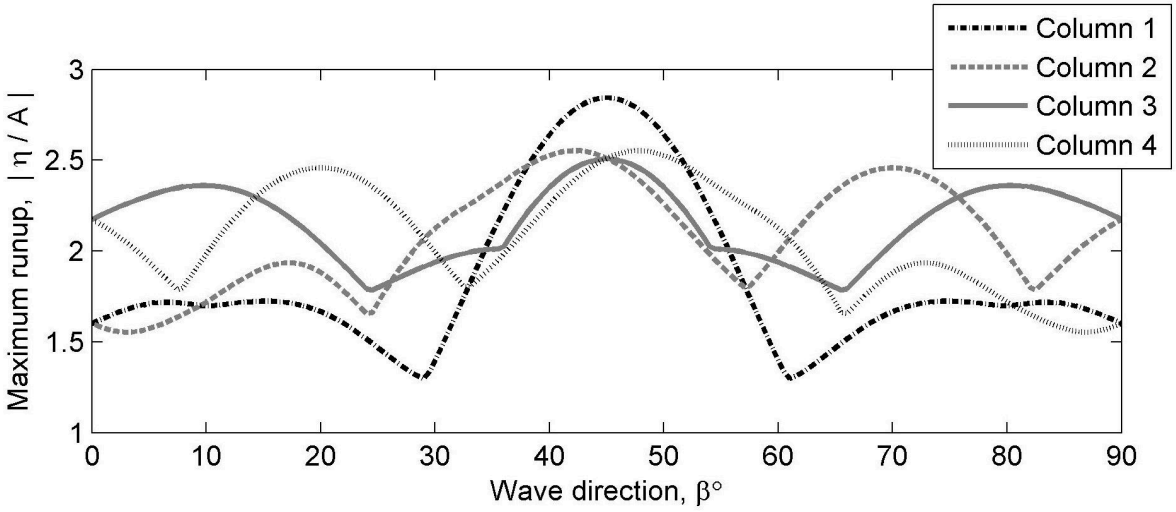

(a) Circular columns

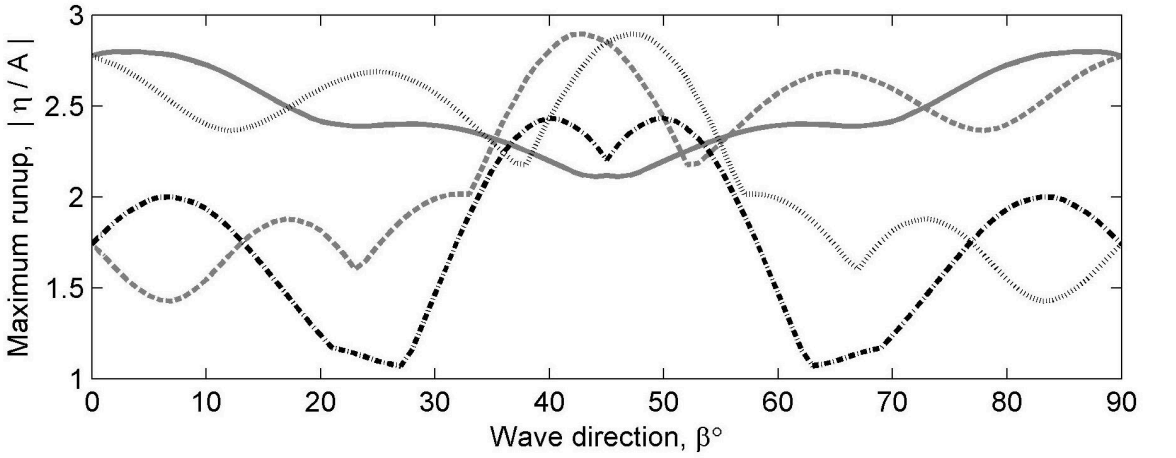

(b) Square columns

Figure 2.12: Maximum |runup/A| on arrays of four bottom-seated columns for $\beta = 0 - 90°$ and $ka = 1.831$ ($T = 5.215$ s).

symmetry in the structure, e.g. $\beta = 0°$ and $45°$. Other directions were also investigated but due to limited space in this thesis only limited examples are shown. It is unsurprising given the symmetry of the structure and the nature of near-trapping that the most violent and interesting responses were usually excited by an incident wave direction along a line of symmetry.

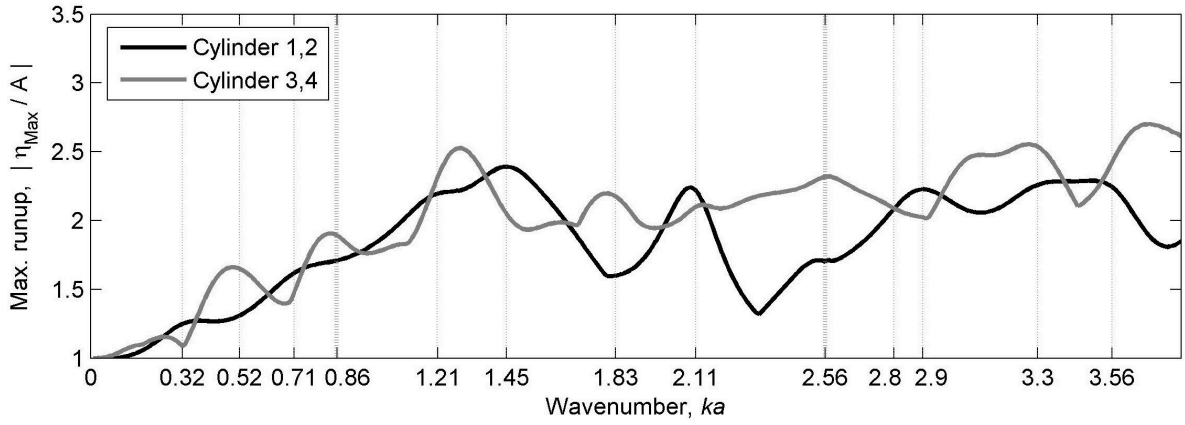

(a) $\beta = 0°$

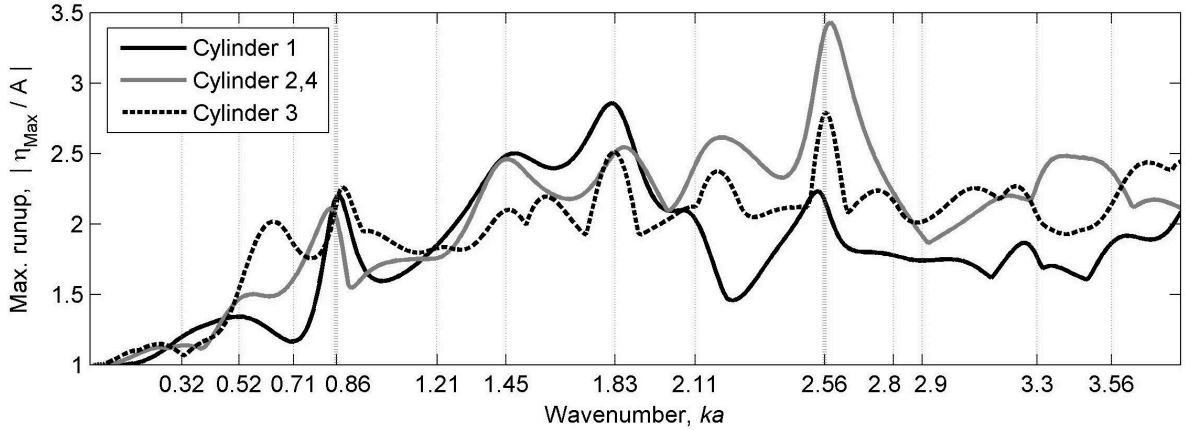

(b) $\beta = 45°$

Figure 2.13: Maximum runup vs. ka for each cylinder with $\beta = 0°$ and $45°$.

For the four circular columns, Figure 2.13 shows the maximum runup around each column for ka = 0-3.8, where k is wavenumber and a is column radius. The vertical lines show the theoretical near-trapped frequencies for an array of circular columns with the bold vertical lines representing the two near-trapped modes with the smallest imaginary part of the wavenumber. In general, the peaks and the theoretical near-trapping frequencies match up well. The most well defined peaks are for $ka = 0.858$ and 2.558, which are also the near-

trapping frequencies with the smallest imaginary part. These plots look at the maximum runup for each column but it is also interesting to look at individual points. Some points of interest were found by taking the location of the maximum elevation at several of the peaks in Figure 2.13. These include $\theta_3 = 7\pi/8$ on Column 3 for a $\beta = 0°$ wave direction, and $\theta_4 = 13\pi/8$ on Column 4 and the leading edge of the rear column ($\theta_1 = 5\pi/4$ on Column 1) for a $\beta = 45°$ wave direction. The runup was found across the whole range of ka values at these locations. By comparing the surface elevation peaks at these locations with the theoretical near-trapped frequencies, one can gain an idea of which modes have little or no effect for each wave direction without the more lengthy full field surface elevation calculations.

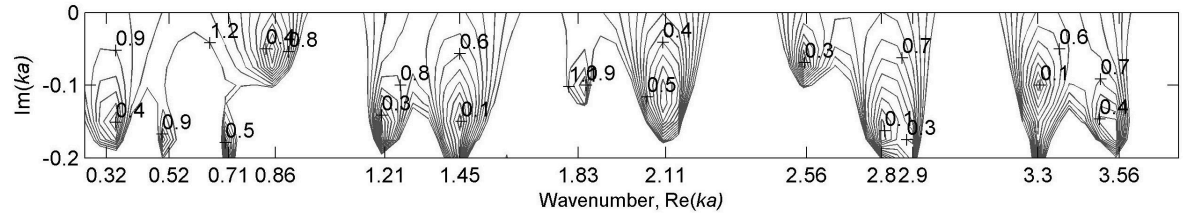

(a) Contours of the modulus of the determinant of the matrix of A coefficients

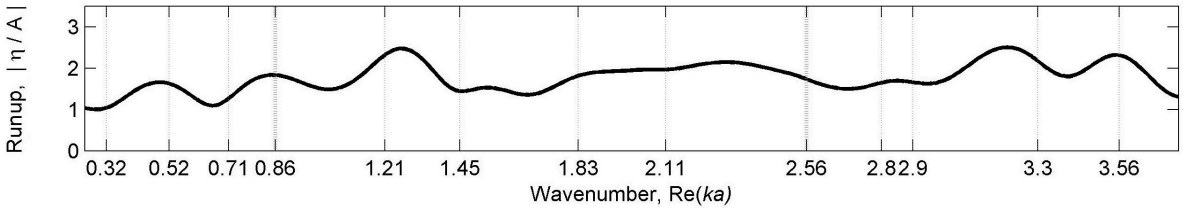

(b) Runup on Column 3 at $\theta_3 = 7\pi/8$ for $\beta = 0°$

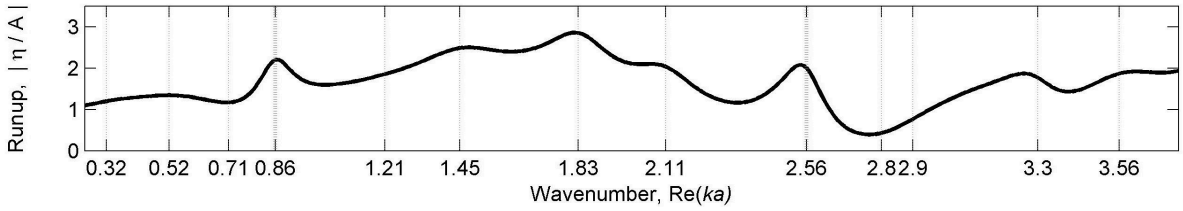

(c) Runup on Column 1 at $\theta_1 = 5\pi/4$ for $\beta = 45°$

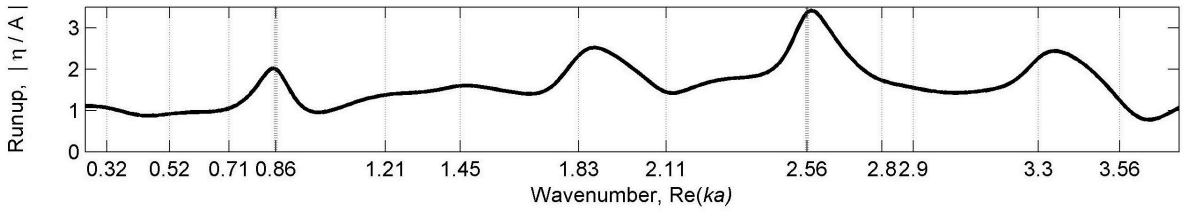

(d) Runup on Column 4 at $\theta_4 = 13\pi/8$ for $\beta = 45°$

Figure 2.14: Near-trapping zero locations and runup vs. ka at $\beta = 0°$, $\theta_3 = 7\pi/8$, and $\beta = 45°$, $\theta_1 = 5\pi/4$ and $\theta_4 = 13\pi/8$.

Figure 2.14 shows runup versus ka for three cases plotted below the contours from Figure 2.11. The dotted vertical lines again show the predicted near-trapped wavenumbers, lining up with the zeros of the contours in Figure 2.14(a). The peaks in runup match up fairly well with the near-trapped frequencies. The highest of all the peaks is at $ka = 2.57$ on Column 4 with an amplification value of 3.41. This is obviously very close to the predicted wavenumber of $ka = 2.558$ and an extremely high amplification for a linear response. Not all of the theoretical near-trapping frequencies give rise to enhanced response in each of these plots. This is to be expected because each near-trapping mode requires specific wave directions for it to be excited (see Figure 2.12), and, even when excited, the amplifications may not be local to the areas under analysis here.

Having established that runup can be a useful starting point when studying the near-trapped modes for a structure, it can also be used to look at how the shape of columns affects the near-trapped modes. Figure 2.15 shows the maximum runup amplification vs. wavenumber for square arrays of four bottom-seated columns. The three plots represent wave directions of $\beta = 0°$, $30°$, and $45°$. For each wave direction, the four column shapes discussed previously (circular, intermediate, square, and rotated square) were analysed. The peaks do not always match up exactly with a predicted near-trapped frequency. Near-trapped modes are properties of the structure geometry and are unrelated to the incident wave. When excited by an incident wave, the response can be expected to reflect the characteristics of both the incident wave and the excited near-trapped mode. In addition to this, a near-trapped mode minimises the total energy radiated out to infinity for the whole structure, which does not necessarily correspond to the maximum runup at an individual location within the array.

For the first four near-trapped modes, the figures show that at each wave direction there is little difference in runup between the four column shapes. This is because the incident waves have a wavelength sufficiently large compared to the column widths that their shape has negligible effect. As the incident wavelength decreases, the shape of the columns becomes more important and the plots begin to diverge. At the first near-trapped mode with a small imaginary part, $ka = 0.858$ ($T = 7.582$ s), column shape has not yet begun to have a

noticeable effect on the surface amplification. The plots for all three wave directions show a distinct peak, with a |runup/A| value of around 2. The $\beta = 45°$ case gives a slightly larger value than the others.

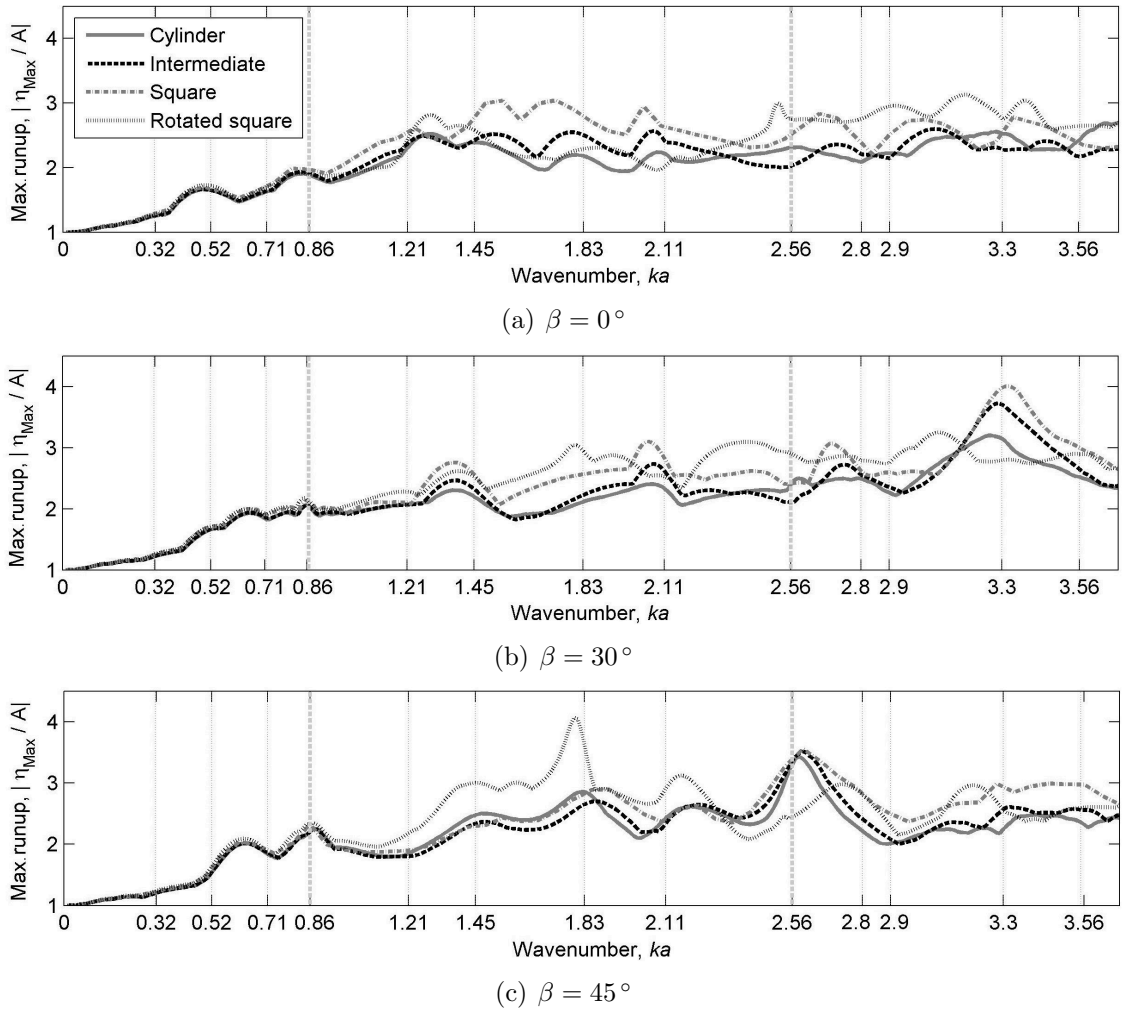

(a) $\beta = 0°$

(b) $\beta = 30°$

(c) $\beta = 45°$

Figure 2.15: Maximum |runup/A| vs. wavenumber, ka, for four bottom-seated circular, intermediate, square or rotated square columns with $\beta = 0°$, $30°$, and $45°$.

At the second near-trapped mode with a small imaginary part, $ka = 2.558$ ($T = 4.409$ s), the surface amplification is now affected by column shape. For $\beta = 45°$ there are large peaks in the circular, intermediate, and square cases of amplitude around 3.4. However, the rotated square case shows almost no peak at that wavenumber. For $\beta = 30°$ there is a small peak at $ka = 2.558$ in the circular case but not for the other column shapes studied. For $\beta = 0°$ there is a small, broad peak centred at $ka = 2.558$ in the circular case, and a narrow peak in the rotated square case. The intermediate and square column cases have no peak at this value of ka.

The largest amplification value shown in Figure 2.15 is 4.07 and is for the rotated square columns with a wave direction of $\beta = 45°$ and a wavenumber of $ka = 1.789$. For linear diffraction this is a huge amplification. For the typical semi-submersible geometry studied, $ka = 1.789$ corresponds to a peak period of 5.3 s. This is much smaller than the normal range of storm peak periods, 12-15 s, and so would probably not be linearly excited by a large wave. However, with frequency doubling or tripling there could be severe second- or third-order effects. If one looks back to Figure 2.5(b), the peak in runup on a single square column for a wave direction perpendicular to a flat face is at $ka = 1.789$ with an amplification of 2.56. For the four rotated square columns case this large amplification is compounded by a near-trapped mode (for circular columns at $ka = 1.831$) leading to the maximum amplification of 4.07 mentioned above. Interestingly, the amplification at $ka = 1.789$ for the other three column shapes is much lower, with values around 2.8 in each case. It is also interesting to compare this maximum amplification with the results in Table 2.2 for the case of four rotated square columns, $\beta = 45°$, and $ka = 1.831$. In Table 2.2 the ka value of 1.831 is for a near-trapped mode in the circular column array, and is only 2.35 % higher than the ka value of 1.789 which gives the peak $|\text{runup}/A|$ value of 4.07 for four rotated square columns and $\beta = 45°$. A 2.35 % rise in ka leads to a 16.6 % fall in the maximum $|\text{runup}/A|$ value from 4.07 to 3.49, which shows how narrow the peak is.

The next largest peak is at $ka = 3.38$, $\beta = 30°$ with square columns and an amplification of 3.98. Unlike the previous example, at this wavenumber the circular, intermediate, and square cases all have a large, distinct near-trapped mode but the rotated square case does not.

2.6 Near-trapped mode shapes

The near-trapping phenomenon has just been discussed along with methods of finding the associated near-trapped modes for a given structure. This section looks at methods of finding the shape of the trapped standing wave pattern that forms within the array when one of the theoretical near-trapped modes is excited. Initially, linear excitations are studied for the typical semi-submersible geometry discussed earlier, but second-order excitations are looked

at in Chapter 4.

2.6.1 Mode shape approximation

A method of approximating the shape of response for a near-trapped mode is presented here. After using the method of Linton and Evans (1990) to identify the near-trapped frequencies for a given structure, the associated mode shapes can be approximated using their symmetric and antisymmetric properties. The surface elevation within and around the bottom-seated column array is calculated using the analytical method of Linton and Evans (1990) for a unit-amplitude, regular wave train, incident from a single excitation direction. The incident field is then stripped away to leave the scattered surface response. This is repeated for the same case but with the opposite incident wave direction. To save computation time, the previously calculated scattered elevation field can simply be mirrored. Next, if the mode shape is symmetric, the two scattered elevation fields from opposing directions are superimposed. If antisymmetric, the same method is used except one subtracts the two scattered fields rather than adding. If rotational symmetry is present then this method can be applied for appropriate pairs of opposing wave directions. Finally, the average of the combined field is taken to give the symmetric or antisymmetric components of the near-trapped mode response.

Figure 2.16 shows stage one of the above method for a near-trapped mode with wavenumber $ka = 1.209$ ($T = 6.408$ s), wave direction $\beta = 0°$, and $A = 10.8$ m. It plots the real and imaginary components, and the modulus of these, of the total surface elevation for a unit-amplitude, regular wave with the given sea state incident on the array from the left. Figure 2.17 then shows stage two, plotting the real and imaginary components, and the modulus of these, of the scattered surface elevation, having stripped away the incident field from the total elevation.

Once this scattered field has been mirrored (or the method repeated for the opposite incident direction), the two scattered fields can be added or subtracted before being averaged to find the symmetric or antisymmetric components of the mode shape respectively. This is

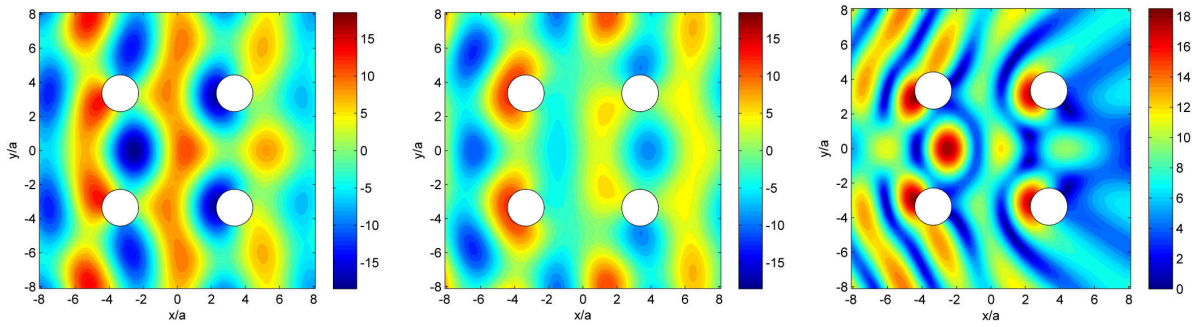

(a) Real (b) Imaginary (c) Modulus

Figure 2.16: Total surface elevation for a regular incident wave with four bottom-seated circular columns and $ka = 1.209$ ($T = 6.408$ s), $\beta = 0°$.

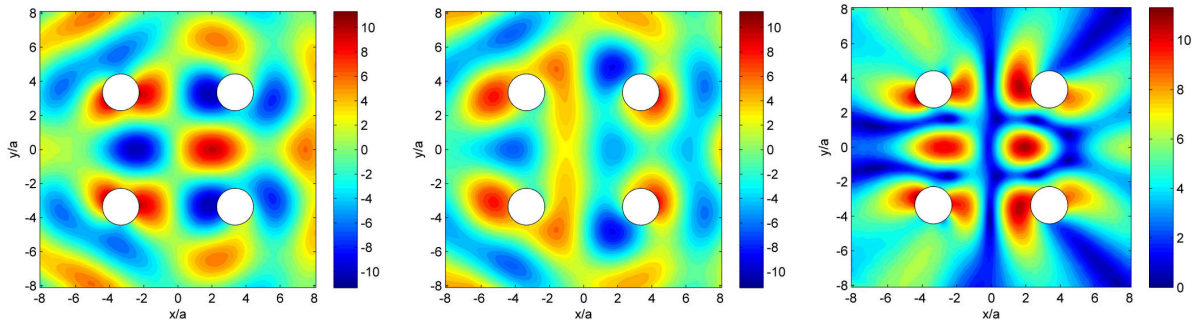

(a) Real (b) Imaginary (c) Modulus

Figure 2.17: Scattered surface elevation for a regular incident wave with four bottom-seated circular columns and $ka = 1.209$ ($T = 6.408$ s), $\beta = 0°$.

illustrated by Figure 2.18, which compares the modulus of the symmetric and antisymmetric components of the mode shape for $ka = 1.209$ ($T = 6.408$ s), $\beta = 0°$. Figure 2.18(a) shows the antisymmetric component and Figure 2.18(b) shows the symmetric component, both found using this method. Figure 2.18(a) clearly shows the mode shape with a complex excitation pattern. In contrast, Figure 2.18(b) shows almost no response within the array. Thus the mode shape is antisymmetric about the centre of the array in the x-direction, but symmetric in the y-direction. This will be looked at further in Section 2.6.3.

The method presented above can be applied to each predicted near-trapped mode, regardless of excitation being first- or second-order. The modes should be viewed as a mixture of both standing waves and outward propagating radiation. Within the array the mixture is mostly standing wave, and outside the array it is mostly radiation. These outward propagating components correspond to the radiation damping of the mode. The size of the imaginary part of the predicted near-trapped wavenumber indicates the amount of damping within the

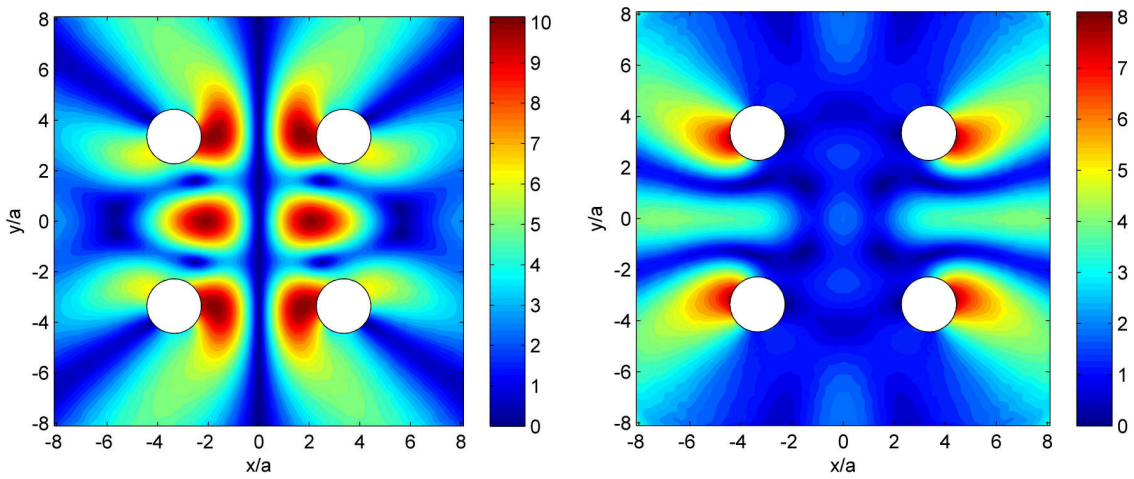

(a) Antisymmetric (b) Symmetric

Figure 2.18: Comparison of symmetric and antisymmetric diffraction patterns for first-order excitation of a near-trapped mode with four bottom-seated circular columns and $\omega = 0.980$ rad/s ($T = 6.408$ s), $\beta = 0°$.

mode.

2.6.2 Eigenvalue method

An alternative and more sophisticated method of predicting the response shape at a near-trapped mode is discussed in Section 3 of Meylan and Eatock Taylor (2009). An eigen analysis is performed on a set of equations describing the wave-structure interactions, which are found using the analytical method of Evans and Porter (1997). The resulting eigenvectors are then used with the corresponding eigenvalue to evaluate the surface elevation around the structure for a near-trapped mode. These field plots are used to validate the approximate method discussed in the previous section.

Figure 2.19 plots the predicted mode shape for a complex wavenumber of $ka = 2.5576+0.07239$i. This is the expected mode shape associated with the near-trapped mode using the complex wavenumber as predicted earlier in Section 2.5. Figures 2.19(a-c) show the real and imaginary components, and the modulus of these, of the mode shape response respectively. However, DIFFRACT can only analyse wave-structure interactions for real wavenumbers. Figure 2.20 therefore shows the equivalent eigen analysis mode shape response using only the real part of the wavenumber for the near-trapped mode. This allows a more accurate comparison between the two methods. Comparing these plots with those of Figure 2.24, obtained using

the method described in Section 2.6.1, shows a good match between the two methods with just a phase difference. There are some differences in the radiating pulses outside the array, but within the centre they are very close.

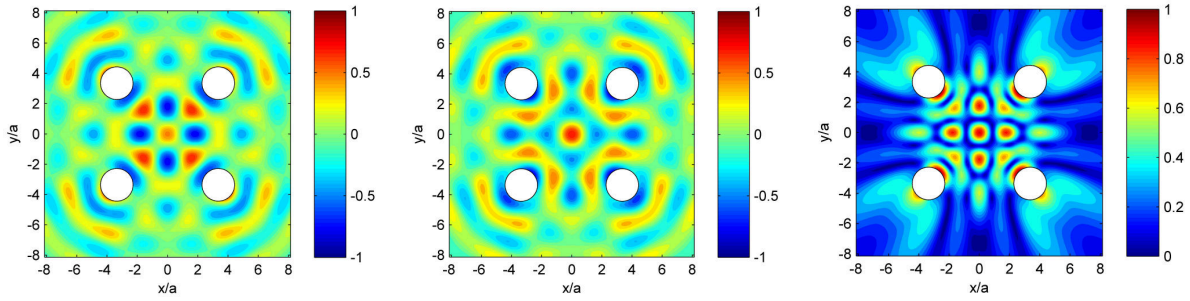

(a) Real (b) Imaginary (c) Modulus

Figure 2.19: Mode shape (using method of Meylan and Eatock Taylor (2009)) for a near-trapped mode with four bottom-seated circular columns and $ka = 2.5576+0.07239\text{i}$.

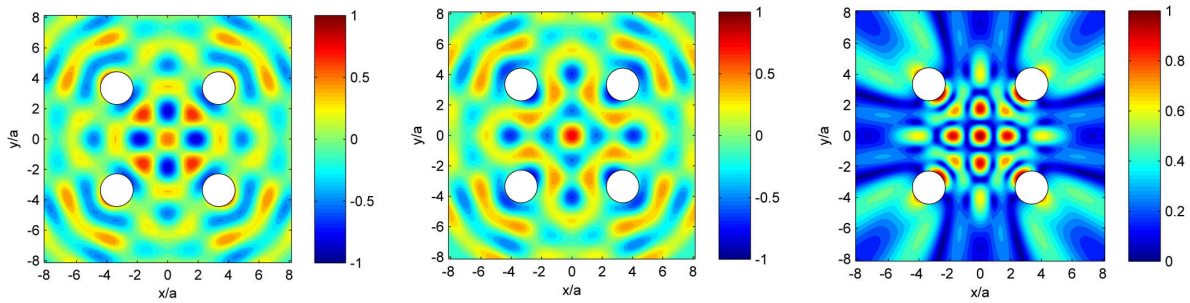

(a) Real (b) Imaginary (c) Modulus

Figure 2.20: Mode shape (using method of Meylan and Eatock Taylor (2009)) for a near-trapped mode with four bottom-seated circular columns and $ka = 2.5576$ ($T = 4.409$ s).

2.6.3 Linear mode shapes

Figure 2.21 shows the real and imaginary components, and the modulus of these, of the antisymmetric components of the mode shape for $ka = 1.209$ ($T = 6.408$ s), $\beta = 0°$. This mode is fairly complex, showing six peaks within the array arranged in a 3x2 rectangular formation with the long face perpendicular to the excitation direction. There is a line of symmetry along the x-axis, and a line of anti-symmetry along the y-axis. The peaks each oscillate sinusoidally, 180° out of phase with the adjacent peaks. Pulses can be seen radiating

from the array, with the same symmetry as the standing wave within the array.

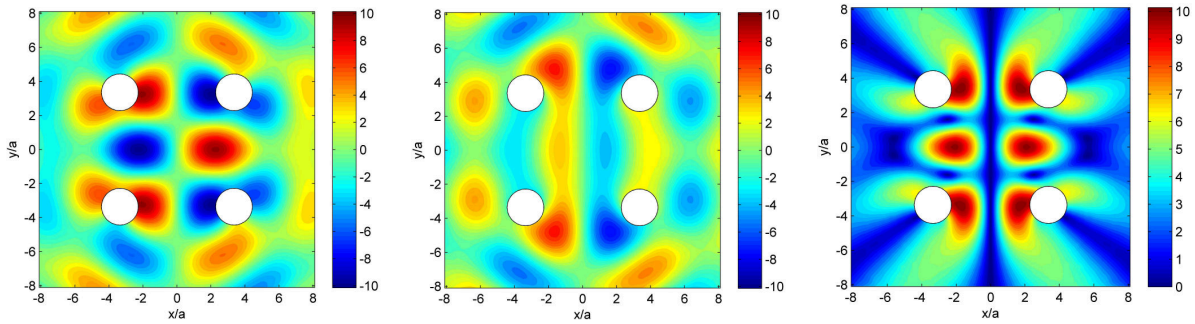

(a) Real (b) Imaginary (c) Modulus

Figure 2.21: Antisymmetric components of the response for a near-trapped mode with four bottom-seated circular columns and $ka = 1.209$ ($T = 6.408$ s), $\beta = 0°$.

Figure 2.22 shows the real and imaginary components, and the modulus of these, of the symmetric components of the mode shape for $ka = 1.209$ ($T = 6.408$ s), $\beta = 0°$. This shows almost no response within the array. It instead shows the runup outside the columns caused by reflection of the incident waves rather than excitation of a near-trapped mode. The fact that there is a small response in the centre shows that this method is approximate and that modes other than at the incident frequency can also be excited to some extent.

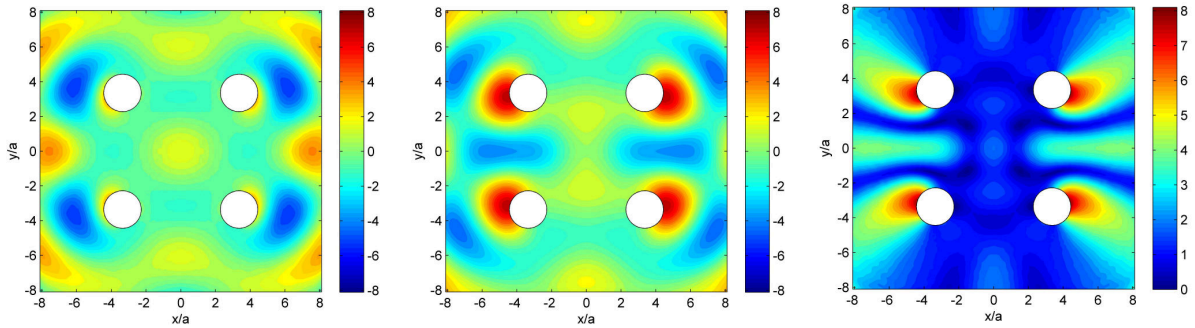

(a) Real (b) Imaginary (c) Modulus

Figure 2.22: Symmetrical components of the response for a near-trapped mode with four bottom-seated circular columns and $ka = 1.209$ ($T = 6.408$ s), $\beta = 0°$.

As mentioned earlier, a small imaginary part of the near-trapped mode wavenumber suggests that there is low damping and therefore a higher chance of a large response. Figures

2.23 and 2.24 show the responses to the two modes with the smallest imaginary wave components, $ka = 0.858$ ($T = 7.582$ s), $\beta = 45°$ and $ka = 2.558$ ($T = 4.409$ s), $\beta = 45°$ respectively, as highlighted in bold in Table 2.2. Both responses were found using the approximate method and show first-order excitation field plots of the real and imaginary components of the response, and the modulus of these.

Figure 2.23(a) shows a ($\mp\pm$) oscillating pattern within the array, with two lines of symmetry (at $\pm 45°$), and two lines of anti-symmetry (at $0°$ and $90°$). At a 1/4 cycle in time after maximising the elevation peaks, the surface elevation within the array is uniformly very close to zero, Figure 2.23(b). This is a node of the pattern in time. In contrast, outside the array, crests and troughs can be seen with the same symmetry as the internal standing wave pattern, these being the radiated part of the wave field. Of course, because of the symmetry, this mode can only be excited by incoming waves with crests hitting the array in a diagonal direction.

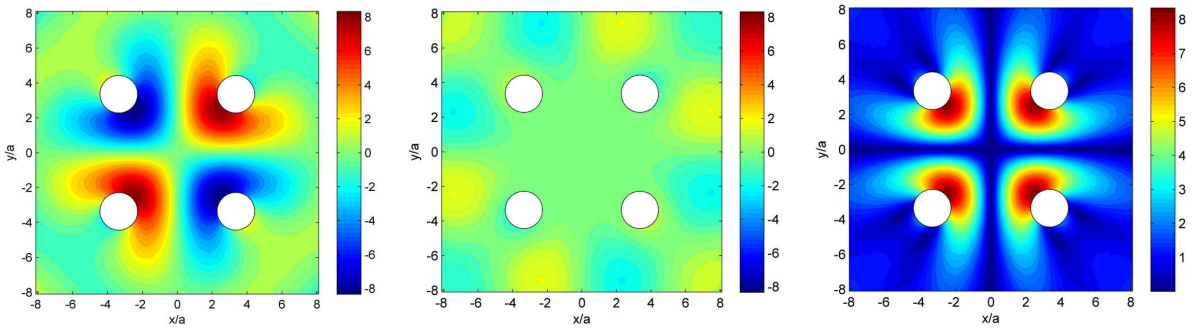

(a) Real (b) Imaginary (c) Modulus

Figure 2.23: Mode shape for a near-trapped mode with four bottom-seated circular columns and $ka = 0.858$ ($T = 7.582$ s), $\beta = 45°$.

Figure 2.24 shows the real and imaginary components, and the modulus of these, of the mode shape for a much higher near-trapped mode with a wavenumber of $ka = 2.558$ ($T = 4.409$ s) but with the same array and diagonal excitation wave directions as above. This mode shape is far more complex than the previous case. When excited by a regular incident wave, the central peak oscillates vertically. Figure 2.24(a) shows the mode response when this central peak is at a maximum. The runup peaks on the inside edges of the four columns

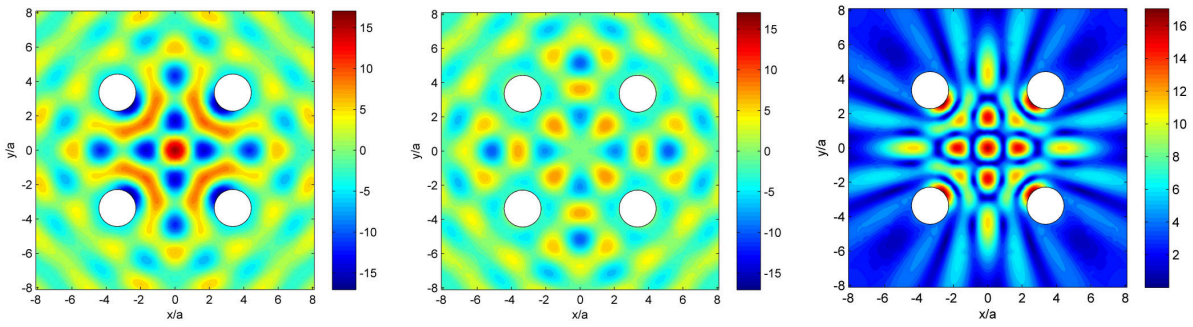

(a) Real (b) Imaginary (c) Modulus

Figure 2.24: Mode shape for a near-trapped mode with four bottom-seated circular columns and $ka = 2.558$ ($T = 4.409$ s), $\beta = 45°$.

also oscillate sinusoidally, in phase as a group, but 167° out of phase with the central peak. Immediately surrounding the central peak there is a circle of eight alternating peaks and troughs, which again oscillate in phase as a group but 153° out of phase with the central peak. There is some sloshing between adjacent peaks and troughs in the ring surrounding the central peak. This ring also interacts with the central peak and the four runup peaks on the inside edges of the four columns. During these oscillations and interactions, pulses of peaks and troughs are radiated out from the array between the columns in four diverging patterns along the axes and waves are radiated along the four diagonal directions. Although this mode has four planes of symmetry, it is most efficiently excited by plane waves diagonally incident on the array.

The results shown so far are linear, and most typical storm waves would not have enough spectral energy at these frequencies to significantly linearly excite the modes discussed. However, second-order sum interactions for typical storm waves with periods around 12-15 s could lead to large responses at several of the modes investigated. Assuming for now that there is at least some correlation between the linear and second-order mode shape, the complexity of the spatial structure in the near-trapped modes and their proximity in frequency lead to the possibility of water projection to high levels, at a variety of positions, both within and around the column array in a random sea. Second-order sum interactions at these near-trapped modes will be discussed in Chapters 4 and 5.

2.7 Symmetry perturbation

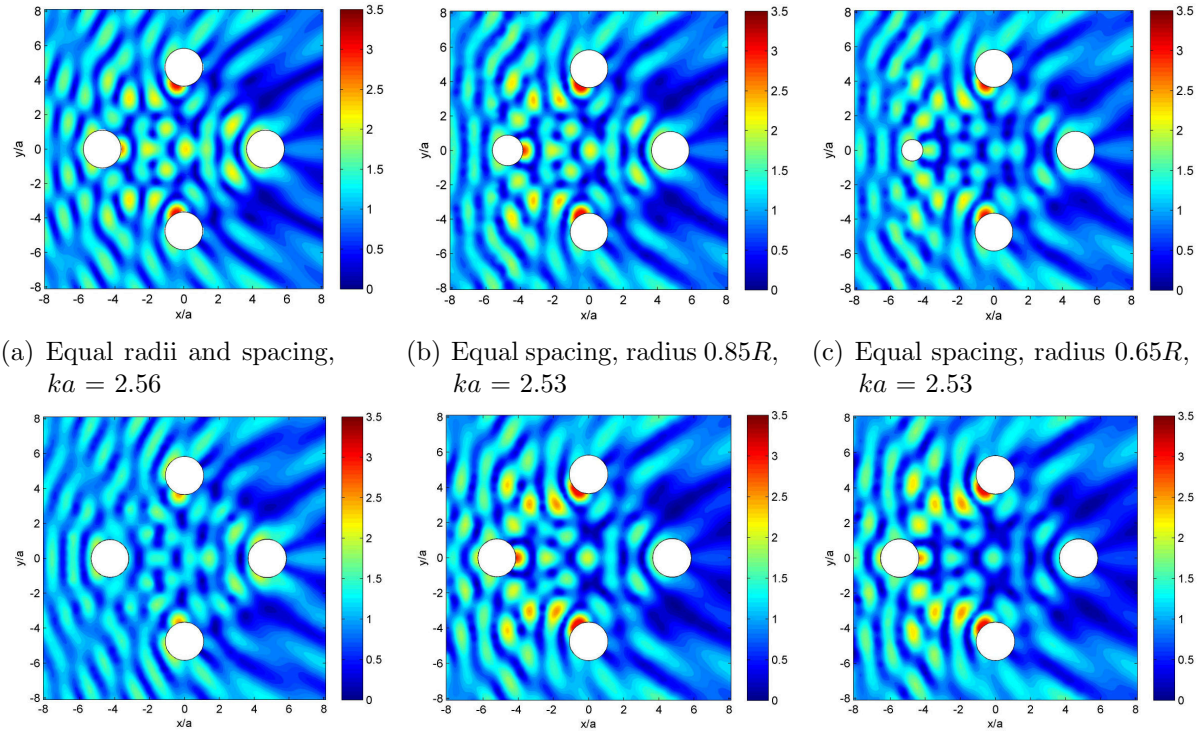

(a) Equal radii and spacing, $ka = 2.56$

(b) Equal spacing, radius $0.85R$, $ka = 2.53$

(c) Equal spacing, radius $0.65R$, $ka = 2.53$

(d) Equal radii, offset $-0.1h$, $ka = 2.63$

(e) Equal radii, offset $+0.1h$, $ka = 2.47$

(f) Equal radii, offset $+0.15h$, $ka = 2.43$

Figure 2.25: Total surface elevation around an array of four columns with the symmetry broken by offsetting a column or reducing its radius.

Figure 2.25 examines how reliant near-trapping is on there being exact symmetry in the layout of the column array. All the plots shown in Figure 2.25 are field plots of surface elevation amplification for a regular incident wave with four bottom-seated circular columns and $\beta = 0°$. Figure 2.25(a) has a symmetric layout with $ka = 2.558$ ($T = 4.409$ s) and all column diameters and spacings equal. Figures 2.25(b) & 2.25(c) have equal column centre-to-centre spacings, but the diameter of the leading column is reduced by 15 % and 35 % respectively. The reduction in diameter leads to a change in the near-trapped wavenumber to $ka = 2.53$ in both cases. The arrays in Figures 2.25(d), 2.25(e), & 2.25(f) all have equal column diameters, but the leading column-centre to array-center spacing is changed by -10 %, +10 %, and +15 % respectively. The difference in spacing also leads to a change in near-trapped wavenumber, with ka values of 2.63, 2.47, and 2.43 respectively. These near-trapped wavenumbers were again found using the method of Linton and Evans (1990).

The symmetric case, 2.25(a), has a maximum amplification of 3.33, located on the inside

edge of the two central columns. Cases 2.25(b) & 2.25(c) have maximum values of 3.46 and 3.14 respectively, with few changes to the general diffraction pattern. The peaks upstream of the central columns are slightly increased in case 2.25(b), and there is reduced amplification in the centre of the array for 2.25(c) with a series of peaks along the x-axis upstream of the array. Case 2.25(d), with the leading column moved closer to the array by 10 %, has a greatly reduced maximum amplification of 2.55. The diffraction pattern is still fairly similar to the fully symmetric case, but all the peaks are reduced in height and are generally more uniform across the field. For cases 2.25(e) & 2.25(f), the maximum amplifications are 3.42 and 3.53 respectively, with a very similar general pattern to the symmetric case apart from some reduction to the amplification within the centre of the arrays.

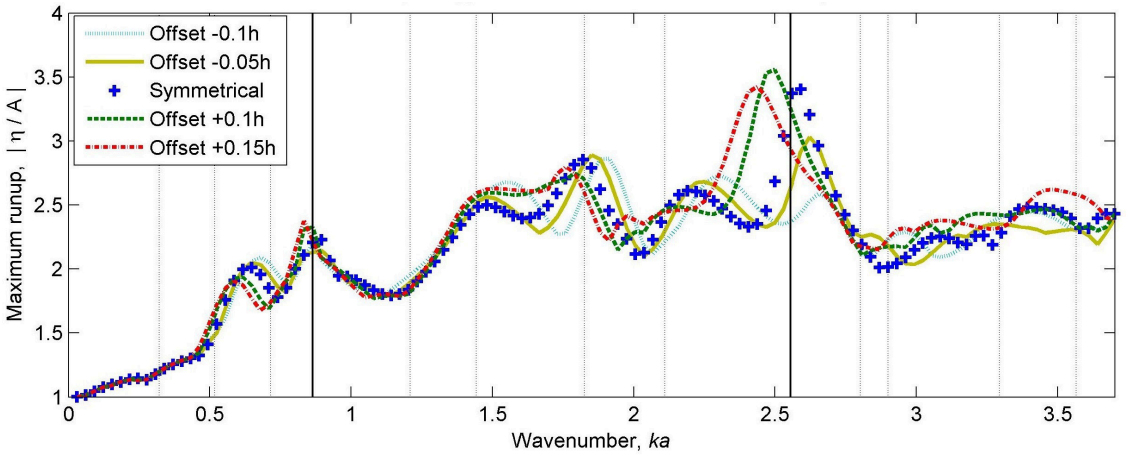

Figure 2.26: Maximum |runup/A| on all four columns vs. ka in an array of four circular columns with one column offset to break up the symmetry. Wave direction $\beta = 45°$.

Figure 2.26 shows plots of maximum |runup/A| vs. ka for arrays of four circular columns with the symmetry broken by offsetting one of the columns. The leading column for a $\beta = 45°$ wave direction is moved along the diagonal and the offsets are given in terms of the distance to the array centre, which is h for the symmetric case. The figure shows that increasing the distance of one of the columns from the array centre causes a reduction in the excitation wavenumber of near-trapped modes, but causes little change to the maximum |runup/A| for each peak. The reduction in the excitation wavenumber is to be expected because for a $\beta = 45°$ wave direction one of the dominant dimensions is the diagonal column spacing. If this spacing is increased then it is logical that the peak excitation will occur at

a longer wavelength and hence a reduced wavenumber. An interesting result is that when this diagonal spacing is reduced, the near-trapped mode near $ka = 2.558$ ($T = 4.409$ s) has a greatly reduced amplitude. For an offset of $0.05h$ towards the centre, the peak amplitude reduces from 3.41 to 3.03 and the peak wavenumber increases from $ka = 2.59$ to 2.62. When the offset is extended to $0.1h$, the peak is replaced with two smaller peaks of amplitude 2.72 and 2.58 with wavenumbers $ka = 2.31$ and $ka = 2.65$ respectively.

This analysis shows that causing some reduction in symmetry can both increase and decrease the maximum elevation amplification caused by near-trapping. A reduction in maximum amplification could obviously prove advantageous when designing a structure to minimise water-deck impact. This coupled with a general reduction across the centre of the array as seen in case 2.25(d) is of particular interest for semi-submersible oil platforms, as the drilling equipment and risers are generally located there. However, only a single near-trapped mode has been looked at in this section. For a reduction in symmetry as shown in 2.25(d) to be useful it would have to be investigated across all near-trapped modes to ensure that there was no increase in amplification for a mode not discussed here. Any reduction in amplification would also have to be weighed against the increased complexity of designing and fabricating an asymmetric structure.

2.8 The effect of water depth

Depth dependence is an important consideration when numerically solving wave-structure interaction problems. The equations governing the hydrodynamics are dependent on water depth, particularly at second-order; consequently, the time required for these equations to be solved is also related to the depth. For deep water calculations such as those in the Thunder Horse case, where the semi-submersible floats in water 1920 m deep, one must find a balance between accurate results and minimising computation time.

This section shows an example of the type of investigation needed to find an optimum depth. Since computation time increases with depth, one must find the minimum depth where convergence occurs and the results become depth independent. Table 2.3 contains

first- and second-order calculations for a simplified Thunder Horse geometry over a range of water depths. Results were found at each depth for a regular incident wave of amplitude 1 m with wave direction $\beta = 45°$ and period $T = 14$ s ($\lambda = 306$ m), which is typical of a storm wave. The columns in the table show water depth, linear body force, linear surface elevation, second-order sum body force, and second-order potential sum elevation respectively. Forces are given in Newtons, and elevations are given at the centre of the array in metres.

Depth (m)	$F^{(1)}$ (N)	$\eta^{(1)}$ (m)	$F^{(2+)}$ (N)	$\eta_P^{(2+)}$ (m)
50	7.827E+06	1.163E+00	5.661E+04	5.856E-02
100	7.720E+06	1.130E+00	6.398E+04	2.633E-02
150	7.675E+06	1.127E+00	6.568E+04	2.230E-02
200	7.667E+06	1.128E+00	6.592E+04	2.171E-02
250	7.666E+06	1.128E+00	6.598E+04	2.162E-02
300	7.666E+06	1.128E+00	6.599E+04	2.160E-02
350	7.665E+06	1.128E+00	6.600E+04	2.159E-02
400	7.665E+06	1.128E+00	6.600E+04	2.159E-02
450	7.665E+06	1.128E+00	6.600E+04	2.159E-02
500	7.665E+06	1.128E+00	6.600E+04	2.159E-02
1000	7.665E+06	1.128E+00	6.600E+04	2.159E-02

Table 2.3: Depth dependence of DIFFRACT calculation for forces and surface elevations to first- and second-order.

It is clear from Table 2.3 that all four variables are converged to four significant figures by a depth of 350 m. Any depth greater than this will increase the calculation time and yet give the same result to a reasonable degree of accuracy. This is an example of how water depth can affect the results, but the convergence depth of 350 m found here is a guide rather than a rule. Frequency must also be taken into account and a similar investigation to that above, but for an incident wave of period $T = 10$ s, shows convergence at a smaller depth. This is to be expected as a smaller period means a higher wavenumber and so $tanh(kd) \to 1$ will occur at a smaller depth. Conventionally it is assumed to be deep water if the depth is greater than half of the wavelength, λ.

2.9 Multiple columns with pontoons

There are three models under study in this section. All three models are based on the dimensions of the Thunder Horse semi-submersible but are simplified to different degrees. Models 1 and 2 are not connected by pontoons and so the number of nodes on the body surface is greatly reduced, along with the associated DIFFRACT computation times. All three models approximate Thunder Horse as having two planes of symmetry. DIFFRACT is able to use one or two planes of symmetry to reduce computation times and so the mesh only needs to cover one quadrant of the simplified structure. Model 1 is the simplest with four bottom-seated columns of an average Thunder Horse cross-section in 30 m depth water. Model 2 looks at the effect of water depth on calculations with the same columns as in Model 1, but now the columns are truncated at a draft of 30 m, in water of 350 m depth. Model 3 is the closest to Thunder Horse with columns of the average Thunder Horse cross-section, pontoons of height 11.52 m, and an overall draft of 30 m. The water depth is 350 m as with Model 2. Figure 2.27 shows example meshes for the models discussed here. Figure 2.27(a) shows the mesh used in Model 1 with water depth 30 m, Figure 2.27(b) shows the mesh used in Model 2 with draft 30 m, a base and water depth 350 m, and Figure 2.27(c) shows Model 3.

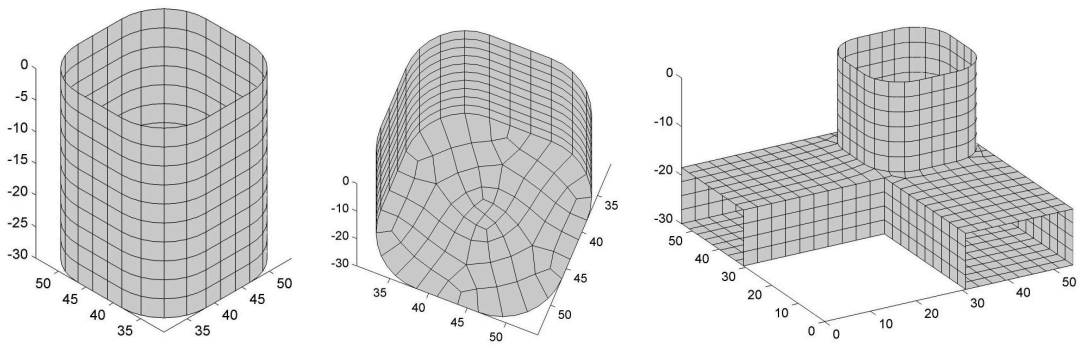

(a) Model 1 (b) Model 2 (c) Model 3

Figure 2.27: Example meshes for the models used in this section. View of (b) is from beneath to show the meshed base for use in deep water.

Figure 2.28 shows the modulus of the linear surface elevation amplification. Figures 2.28(a-c) are for Models 1-3 respectively, all with wavenumber $ka = 1.831$ ($T = 5.215$ s,

$\lambda = 42.5$ m) and wave direction $\beta = 45°$, which corresponds to one of the near-trapping frequencies identified in Section 2.5. At first glance they seem identical; however, there are some small differences, which are shown more clearly in Figure 2.29. Figures 2.29(a) & 2.29(b) show the modulus of the scattered fields around Models 1 and 3 respectively, normalised by incident amplitude, A. Figure 2.29(c) shows the difference between these two plots, $|\eta_{S,3}| - |\eta_{S,1}|$.

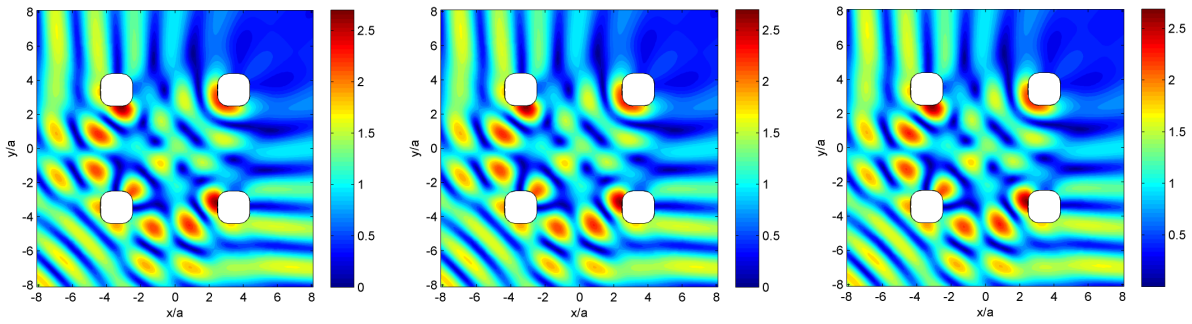

(a) Model 1 (b) Model 2 (c) Model 3

Figure 2.28: Modulus of the total surface elevation around the three Thunder Horse models of varying simplification. $ka = 1.831$ ($T = 5.215$ s), $\beta = 45°$.

Figures 2.29(a) & 2.29(b) show the pattern of the standing wave that forms within the array. Energy is lost to infinity as pulses are radiated out from the near-trapped standing wave. These are shown by the drawn out peaks that begin on the edges of the array and smear outwards. More discussion on near-trapped mode shapes is given in Chapter 4. The maximum amplitude of the difference shown in Figure 2.29(c) is 0.084, which is only 3% of the maximum amplitude in the scattered elevation plots of Figures 2.29(a) & 2.29(b). The difference in overall magnitude of surface amplification is relatively small within the array (up to 0.05) and almost zero downstream in the sheltered zone. The increased water depth and addition of pontoons clearly makes little impact on sheltering effects from the array for these incident waves. There are a series of obvious geometric patterns radiating out from the array upstream and to the sides. The alternating peaks and troughs in these patterns show that the reflections and radiated pulses are offset between Figures 2.29(a & b). They are spaced equally for the two models and are very small in amplitude about the mean elevation, but a peak in 2.29(a) straddles both a peak and trough in 2.29(b).

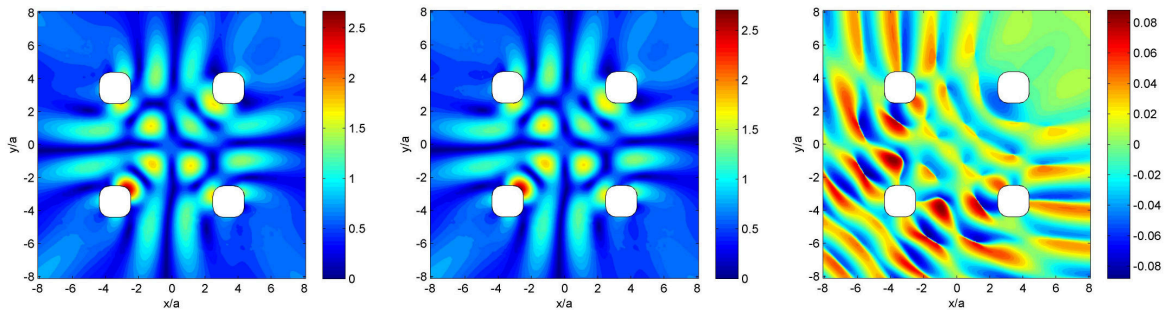

(a) $|\eta_{S,1}|$, Model 1 (b) $|\eta_{S,3}|$, Model 3 (c) $|\eta_{S,3}| - |\eta_{S,1}|$, Models 3-1

Figure 2.29: Scattered surface elevation around (a) Model 1, and (b) Model 3. (c) shows the difference between these two. $ka = 1.831$ ($T = 5.215$ s), $\beta = 45°$.

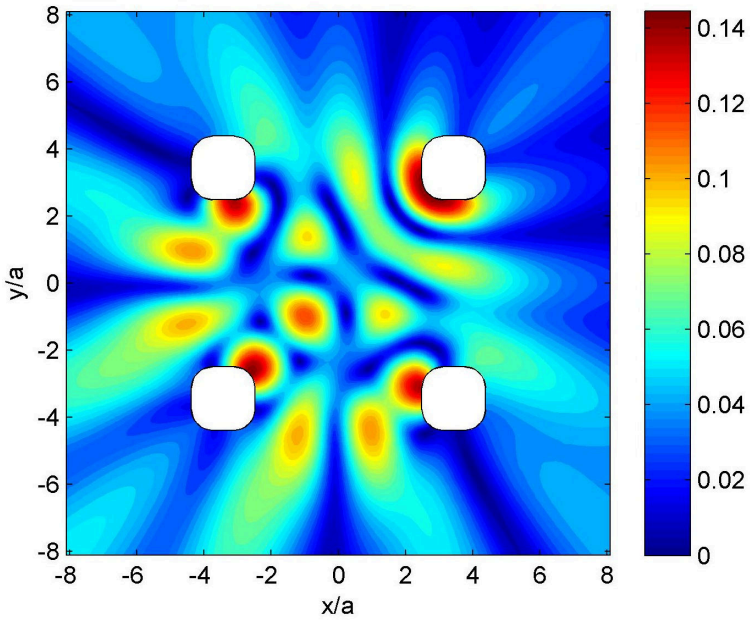

Figure 2.30: Magnitude of the difference in scattered surface elevation between Models 3 & 1 for an incident wave of $ka = 1.831$ ($T = 5.215$ s), $\beta = 45°$.

Figure 2.30 again shows the difference between Models 1 and 3 for an incident wave of $ka = 1.831, \beta = 45°$, but this time the modulus of the difference, $|\eta_{S,3} - \eta_{S,1}|$, is plotted rather than the difference in amplitudes, $|\eta_{S,3}| - |\eta_{S,1}|$. The peaks in this plot are highest within the array and tend to be located at the same positions as the peaks in the scattered surface plots, Figures 2.29(a) & 2.29(b). Since Figure 2.29(c) showed that there was little difference in amplitude within the array for the two models, the peaks shown in Figure 2.30 must represent a phase difference. Figure 2.30 shows that there is a difference of up to 0.142 m between the scattered surface elevations for Models 1 and 3, which is just over 5% of the peak value.

These figures show that the surface elevation amplification around Model 3 has some

differences when compared to the simpler Model 1. However, these differences are small relative to the peak amplification value for the wave conditions used ($ka = 1.831, \beta = 45°$). These differences are very dependent on the incident wavelength. An example is now given for a near-trapped mode with a lower wavenumber $ka = 0.858$ ($T = 7.582$ s, $\lambda = 89.8$ m), and wave direction again $\beta = 45°$. Figure 2.31 shows the total and scattered surface elevations for unit regular incident waves with these conditions. Figures 2.31(a) & 2.31(b) were calculated with Model 1, and Figures 2.31(c) & 2.31(d) with Model 3. The differences between the two models are now much greater, as expected.

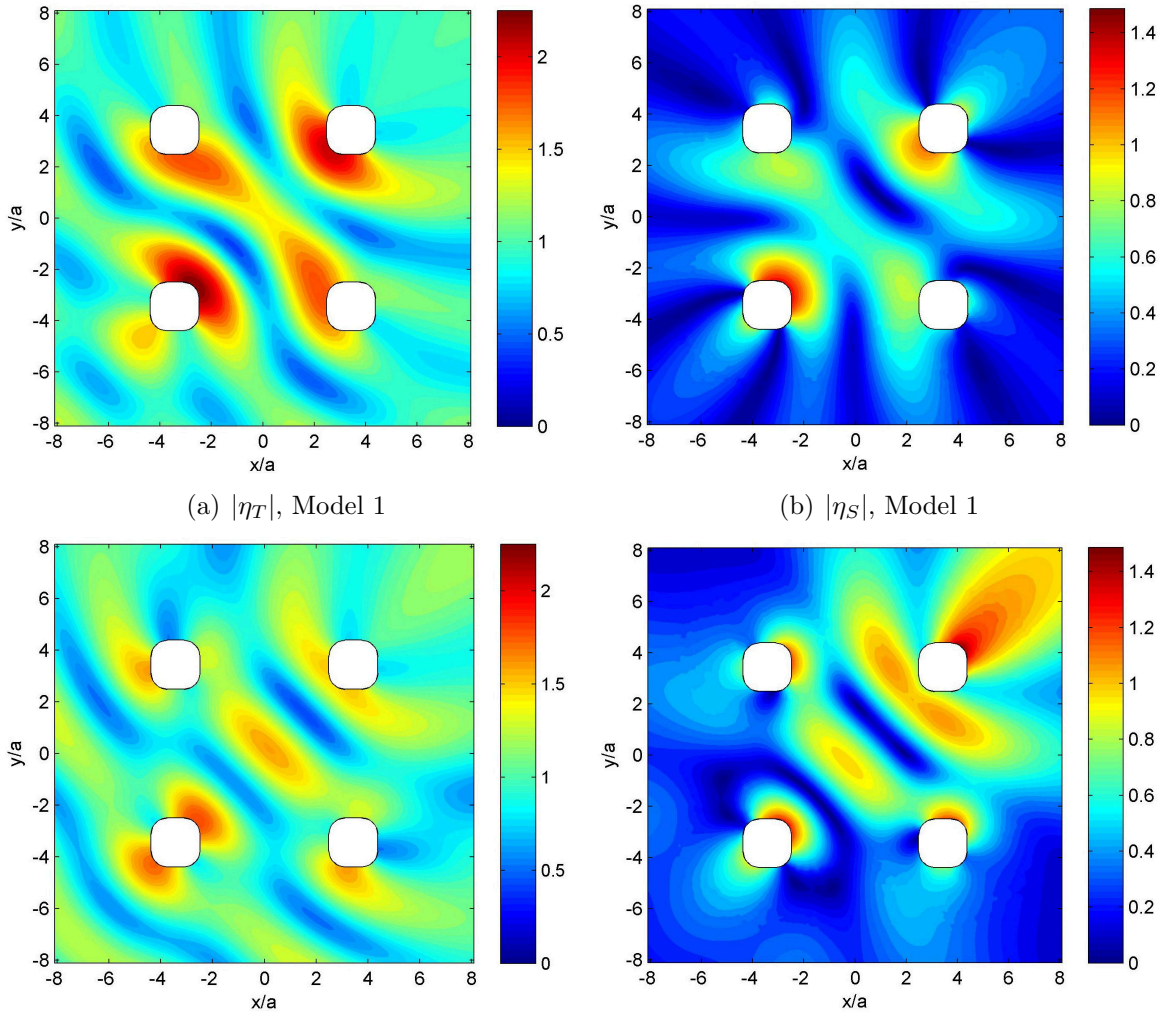

(a) $|\eta_T|$, Model 1

(b) $|\eta_S|$, Model 1

(c) $|\eta_T|$, Model 3

(d) $|\eta_S|$, Model 3

Figure 2.31: Amplitude of total surface elevation, η_T, and scattered surface elevation, η_S, around Models 1 and 3 for an incident wave of $ka = 0.858$ ($T = 7.582$ s), $\beta = 45°$.

2.10 Conclusions

Conclusions drawn from the results presented in this chapter are briefly summarized below.

- Fresnel diffraction effects at sharp corners can greatly increase the maximum runup and upwelling around a column.
- Column cross-sectional shape can have a large effect on both the position and amplitude of maximum surface elevation around isolated and multiple columns.
- Interaction between multiple columns leads to higher surface elevations than for an isolated column of the same cross-section in the same sea state.
- The near-trapping phenomenon is observed in arrays of columns with near-resonant modes occurring at frequencies and wave-directions dependent on column geometry.
- For symmetric column layouts, symmetry and anti-symmetry can be used to estimate near-trapped mode shapes.
- Perturbing the symmetry of an array of columns can have a large effect on the position and amplitude of surface elevation around the array.

Chapter 3

Linear statistics of response

3.1 Introduction

The previous chapter introduced a variety of methods for analysing how ocean waves interact with offshore structures and discussed the importance of structure geometry in these interactions. For clarity in the wide range of topics discussed, the incident waves in the previous chapter were simple regular waves. Regular waves require minimal computation and allow simple explanations of concepts but are poor models of actual storm waves. To model storm waves one can use random wave simulations or focused wave groups. NewWave focused wave groups were discussed in the literature review and introduced as a far more efficient alternative to random wave simulations. NewWave focused wave groups give the average expected shape of an extreme wave event as a compact group of several periods. A good representation of the largest events found in several hours worth of random time histories can therefore be reproduced in just a few periods by a NewWave group.

Section 3.2 compares the diffraction of NewWave groups with regular waves, where the wave groups are based on a JONSWAP spectrum with a peak frequency equal to that of the regular wave. Section 3.3 then looks at the use of statistical tools such as NewWave in more detail. These statistical tools are applied to Thunder Horse to find the expected size of extreme crests for this structure and to help improve our understanding of the physics behind extreme waves in the presence of structures in general. Section 3.4 uses the brute

force calculation of random wave statistics to validate the tools introduced earlier in this chapter.

3.2 Diffraction of NewWaves

In Chapter 2, regular waves were used to look at mode shapes and the effect of column geometry on wave-structure interactions. All their energy is present at a single frequency whereas the energy in NewWave wave groups is distributed across a range of frequencies governed by a spectrum, in this case a JONSWAP spectrum. The diffraction of this NewWave group is different from the regular wave because a number of near-trapped modes will be excited simultaneously to various degrees. This section compares diffraction of a regular wave with that of a NewWave where the peak frequency of the NewWave spectrum is equal to the regular wave frequency. The peak wavenumber used is $k_p a = 1.831$ ($T_p = 5.215$ s), to coincide with one of the near-trapped modes identified earlier, and the tail of the spectrum is cut off at three times the peak frequency. A cutoff at three times the peak frequency causes a less than 1 % loss of spectral energy relative to a cutoff of $10\omega_p$, while reducing the computation time required.

Figure 3.1(a) shows the modulus of the total surface elevation for a unit incident regular wave at the peak wavenumber and $\beta = 45^\circ$ (waves propagating across the diagonal from bottom left to top right). The Thunder Horse Model 3 was used, and the results for this model with the regular wave case were first discussed in Chapter 2 for Figure 2.28. Figure 3.1(b) then shows the modulus of the total surface elevation for a unit-amplitude incident NewWave focused at the centre of the array with $\beta = 45^\circ$. The total surface elevation for the incident NewWave has a maximum amplitude of 1.99, which is greatly reduced from that of the regular wave, 2.69. The distribution of wave energy across a spectrum of frequencies leads to a blurring of the diffraction pattern. The near-trapped mode associated with the peak frequency dominates, but there are also several other near-trapped modes that are excited to some extent which will interfere with the dominant diffraction pattern, both constructively and destructively over time.

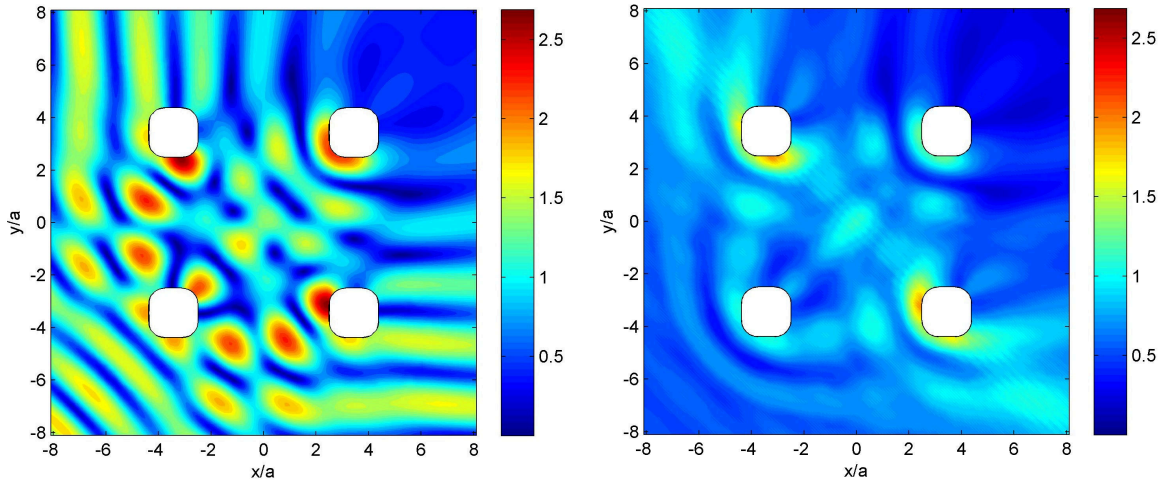

(a) Regular incident wave

(b) NewWave incident wave group

Figure 3.1: (a) Modulus of the total surface elevation for an incident regular wave and (b) an equivalent plot for an incident NewWave, both for $k_p a = 1.831$ ($T = 5.215$ s) and $\beta = 45\,^\circ$ with unit amplitude.

The incident NewWave group used in Figure 3.1(b) has a distinct focus point, chosen to be at the centre of the array as a starting point. The location of the focus point is a major factor in the maximum amplitude possible at each point across the field. To provide a more direct comparison between regular waves and focused wave groups for a given sea state one would have to find the maximum amplitude at each point in the field for all possible focus points rather than just a single location. This would be very time consuming to calculate each NewWave individually and so statistical tools are needed that will avoid such lengthy calculations and still provide useful information about maximum expected projections across the whole field. The next section looks at the statistics of linear response and introduces methods of analysis to minimize computation time.

3.3 Statistics of linear response

This section addresses the following problem: We know that on the open sea, wave crest amplitudes are approximately Rayleigh distributed, and that the average shape of a wave around a large crest tends to the scaled autocorrelation function (NewWave). What is the equivalent result near a multi-column structure for which near-trapped local modes of surface response are possible?

Hence, we are interested in two pairs of localised wave groups:

Pair 1

(a) The average shape of a large wave crest at a point on the open sea.

(b) The interaction of this wave group with the structure.

Pair 2

(c) The average shape of a large wave crest at a point close to the structure, looking at the one-in-N_w wave surface response with the structure present for the same storm as in (a).

(d) The incoming wave group which maximises this response and what it looks like in the absence of the wave-structure interaction.

We find a simple reciprocity result between wave groups (b) and (d).

Extreme storm waves are statistical outliers in rough, random seas which occur randomly and very infrequently. Due to their randomness, the position or time of their occurrence cannot be predicted but the expected shape when they do occur can be. Regular waves are not representative of an extreme wave and so, instead, this average shape of extreme crests in a given sea state can be modelled by a focused wave group. A focused wave group arises when a set of wave components focuses at a single position in space and time. Tromans et al. (1991) discussed how the average shape of an extreme wave with maximum elevation A_{Max} in a linear random Gaussian sea state can be described by a focused wave group.

This has become known as NewWave and is used to model the irregular shape of ocean waves as a set of independent sinusoids of random amplitude. It can be shown mathematically (see Boccotti (1983)) that for a linear random model of the ocean surface, the average shape of a large crest, both temporally and spatially, is a scaled autocorrelation function. A comparison was made by Jonathan and Taylor (1997) between large, non-linear crests from time series recorded offshore in the North Sea and equivalent predictions by the NewWave model. The largest non-linear crests from the measured time series were linearised and then compared with the NewWave profile. The agreement was excellent, showing that NewWave is a reasonable model for large offshore wave crests. For an example of an undisturbed NewWave wave group in the open ocean with a typical peak period of $T_p = 12$ s see Figure 3.2. A summary of the equations used in this analysis is now presented. For more detailed

derivations see Tromans et al. (1991), Newman (1977) Section 6.20, and Ochi (1973).

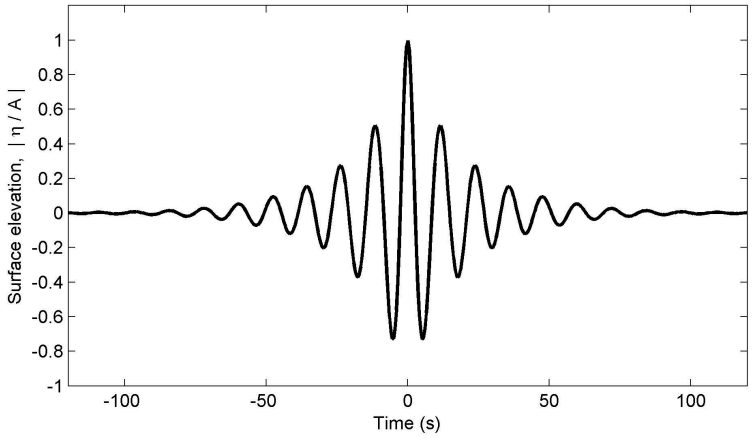

Figure 3.2: Time history at the focus point of a NewWave wave group in open ocean normalised by the maximum amplitude, A, with peak period $T_p = 12$ s.

First-order diffraction theory can be used along with linear superposition to combine the diffracted wave field for each incident wave component of fixed amplitude according to the incident spectrum. JONSWAP spectra are used, see Hasselmann et al. (1973), with near-trapped frequencies from the regular wave analysis in Section 2.5 chosen as interesting values for the peak frequency in each spectrum.

By superposition of monochromatic, deterministic, plane waves, a double integral can be derived to give the surface elevation for general wave motions as:

$$\eta(x,y,t) = Re \int_0^\infty \int_0^{2\pi} A(\omega,\beta) e^{ik(\omega)(x\cos\beta + y\sin\beta) - i\omega t} d\beta d\omega \tag{3.1}$$

where $\eta(x,y,t)$ is the surface elevation, ω is angular frequency, k is wavenumber, β is the angle of incidence relative to the x-axis, and $A(\omega,\beta)$ is wave amplitude. In this case the wave amplitude is complex, with the real and imaginary parts both normally distributed and functions of frequency and wave propagation direction. When $A(\omega,\beta)$ is a random variable, this equation can be used to represent a spectrum of ocean waves (Newman (1977) p256, Eq. 59).

The randomness of ocean waves means that when dealing with their extremes, a proba-

bilistic method must be used to predict the probability distribution of the maximum wave amplitude. Instead of the complex variable used above, A will be taken as consisting of a random amplitude distribution and a random phase angle uniformly distributed between 0 and 2π. The commonly used JONSWAP spectra have a fairly narrow peak in frequency and so it can be assumed that the individual waves follow a Rayleigh distribution in amplitude (and wavelength). The normalised probability density function for the wave amplitude is therefore

$$p(\xi) = \xi e^{-\xi^2/2} \tag{3.2}$$

where $\xi = \alpha/m_0^{1/2}$ is the normalised wave amplitude and m_0 is the total energy of the spectrum, $S(\omega_n)$.

$$m_0 = \sum_{n=0}^{\infty} S(\omega_n)\Delta\omega \tag{3.3}$$

For a single wave, the cumulative probability of its amplitude being less than $\alpha = \xi(m_0)^{1/2}$ is given by

$$P(\xi) = \int_0^{\xi} p(\xi')d\xi' = 1 - e^{-\xi^2/2} \tag{3.4}$$

Therefore for N_w statistically independent waves, the probability that the amplitude, α, will be exceeded at least once is

$$1 - P^{N_w} = 1 - (1 - e^{-\xi^2/2})^{N_w} \tag{3.5}$$

This can then be used to find the probability density of the largest value in N_w waves. Finding when its derivative is zero leads to an expression for the most probable extreme wave amplitude in N_w waves as

$$\alpha = (2m_0 \log N_w)^{1/2} = \left(2 \log N_w \sum_n S(\omega_n)\Delta\omega\right)^{1/2} \tag{3.6}$$

For rare waves (large N_w), Ochi (1973) showed that the probability of exceeding Equation 3.6 is 0.632. One may think that for extreme wave amplitudes a more conservative criterion

should be taken. However, this research is interested in the likely extreme wave amplitude at the peak of a storm in an extreme sea state. What is important is the combined probabilities of both the sea state occurring and the wave amplitude being exceeded within N_w waves at the storm peak. If a sea state with a long return period of say 100 years is used then the criterion given in Equation 3.6 is reasonable. Of course, with any assessment for a real project, the aim of applying probability theory is to ensure that the overall risk to the installation over its design life is less than some acceptable level (perhaps 10^{-6}). Then the response statistics for every storm to be expected over this design life need to be combined. This derivation of the long term probability distribution is outside the work of this thesis, as it requires in depth knowledge of the variation of storm severity over the multi-decade lifetime of the installation.

As mentioned earlier, there are two pairs of localised wave groups under study. Both cases involve interactions of a wave group with an array of bottom-seated columns. The presence of a structure will cause each wave component to be scattered and the phase of each scattered wave component will be dependent partly on the component's wavenumber. A wave group that would be focused in open seas (defined by an instant when all the phase angles are zero, so all the crests add) would no longer be focused with a structure present. The amplitude and phase of each spectral component is modified by its respective diffraction coefficient, $\phi_n(x, y)$. In this section this is calculated using the method of Linton and Evans (1990) and only arrays of four bottom-seated circular columns are looked at so analytical expressions can be used. The methods are applied to more complex structures later using $\phi_n(x, y)$ calculated by the more computationally intensive numerical solver DIFFRACT.

For the first case, a NewWave-type solution in the open ocean, the notation η_a represents the average time history for a large wave crest at a point on the open sea. When this wave group is incident on the array of four circular columns, the surface elevation time history in response is given by η_b. For this first pair with an incident NewWave-type solution, the expected maximum incident amplitude, α_I, is given as in Equation 3.6 using the incident spectrum, $S = S_I$, and the number of waves, $N_w = 1000$. For a storm with peak period $T_p = 12 - 15$ s, $N_w = 1000$ corresponds to around four hours.

The second case of interest is the average shape of the largest responses with a structure present in a random sea. The statistics discussed can be applied to both an incident NewWave spectrum and the response spectrum where wave-structure interactions are taken into account. Applying these statistics to the response spectrum gives a NewWave-type solution in response and the maximum expected response for a given sea state and geometry. The total wave field is used as a starting point to find the average shape of a large crest with the structure present, whereupon the incident wave field required to cause this can be inferred. To maximise the wave-structure interaction, a probabilistic NewWave solution in response is found, η_c. To find this, the diffraction coefficient, $\phi_n(x, y)$, is now modifying the energy density spectrum rather than the amplitude spectrum and so the relationship is squared, not linear. This leads to a new maximum expected wave amplitude of α_R.

$$\alpha_R(x,y) = \left(2\log N_w \sum_n S_R(\omega_n)\Delta\omega\right)^{\frac{1}{2}} = \left(2\log N_w \sum_n |\phi_n(x,y)|^2 S_I(\omega_n)\Delta\omega\right)^{\frac{1}{2}} \tag{3.7}$$

3.3.1 Net Amplification Factor

The maximum expected amplitude can now be found for both cases of interest given an incident spectrum and the number of observed waves, N_w. However, since extreme wave-structure interactions are of most interest, the incident spectrum and NewWave focus location should be chosen to maximise the responses. The local energy density for the total diffracted field can be given in terms of the local energy density for the incident field at frequency ω_n as the following equation:

$$S_R(\omega_n) = S_I(\omega_n).|\phi_n(x,y,\omega_n)|^2 \tag{3.8}$$

The ratio of amplitudes for the total diffracted and incident fields, given by Equation 3.6 with the appropriate spectra, can be used to give a Net Amplification Factor, R:

$$R(x,y) = \frac{\alpha_R(x,y)}{\alpha_I} = \sqrt{\frac{\left(\sum_n |\phi_n(x,y)|^2 S(\omega_n)\Delta\omega\right)}{\left(\sum_n S(\omega_n)\Delta\omega\right)}} \tag{3.9}$$

This gives a composite magnification of surface elevation in the vicinity of the structure for all possible NewWaves consistent with the same sea state. The sea states used here are JONSWAP spectra with a near-trapped frequency as the spectrum peak frequency. The Net Amplification Factor can be plotted across the whole field and will immediately show all points that pose a risk of large upwelling or runup. Once these points of interest have been identified, the time histories discussed earlier can be calculated.

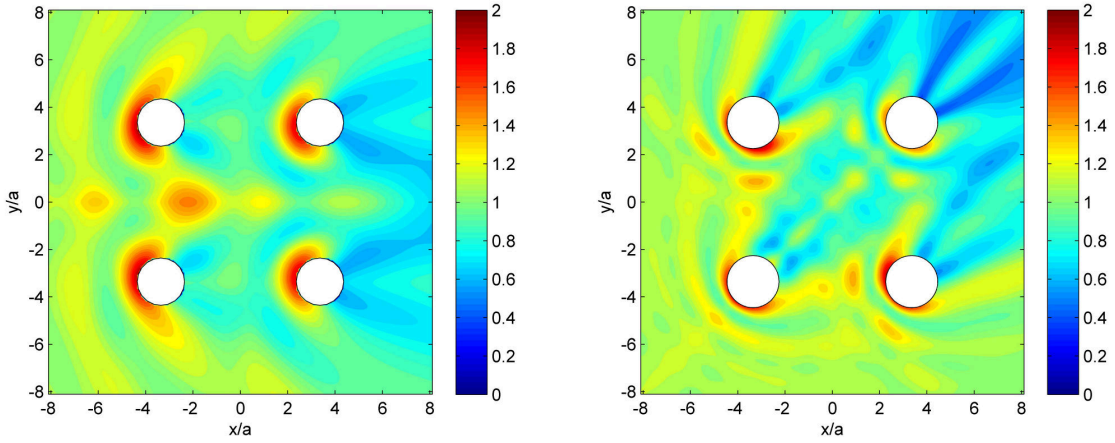

(a) $\beta = 0^\circ$ and $k_p a = 1.209$ (b) $\beta = 45^\circ$ and $k_p a = 2.558$

Figure 3.3: Net Amplification Factor around an array of four bottom-seated circular columns for (a) $\beta = 0^\circ$, $k_p a = 1.209$ ($T_p = 6.408$ s) and (b) $\beta = 45^\circ$, $k_p a = 2.558$ ($T_p = 4.409$ s).

Figure 3.3 shows field plots of the Net Amplification Factor for an array of four circular bottom-seated columns in water of depth 30 m, with the typical semi-submersible geometry discussed previously. The wavenumbers and wave directions used correspond to near-trapped frequencies identified in Section 2.5, where Figure 3.3(a) is for $k_p a = 1.209$ ($T_p = 6.408$ s), $\beta = 0^\circ$ and Figure 3.3(b) is for $k_p a = 2.558$ ($T_p = 4.409$ s), $\beta = 45^\circ$. Both figures show that the points of highest amplification are caused by runup on the columns. It is interesting to see that immediately in front of these peak areas there is a band where the maximum amplification is below 1. There are also very clear sheltering effects downstream of each of the columns for both cases. Some points of substantial upwelling are evident along the x-axis in Figure 3.3(a), but Figure 3.3(b) shows far less upwelling within the array. However, the $k_p a = 2.558$ ($T_p = 4.409$ s), $\beta = 45^\circ$ case does have fairly significant upwelling directly in

between the columns, reaching amplifications of almost 1.5 (see Table 3.1).

A point of note is that the maximum amplification in a NewWave solution for $k_p a = 1.209$, $\beta = 0°$, with a value of 1.885, is lower than for a regular wave of $ka = 1.209$, $\beta = 0°$, with a value of 2.313. For $k_p a = 2.558$, $\beta = 45°$ the maximum value of 1.897 is much lower than for a regular wave of $ka = 2.558$, $\beta = 45°$ with 3.328. One would expect to see some reduction as the near-trapped condition is specific to a single frequency which becomes only a single (although large) component out of many in a NewWave solution. One can understand the much larger reduction for the $\beta = 45°$ cases by looking back to Figure 2.15 and the Q-factor of the peaks. The Q-factor or quality factor is a dimensionless parameter describing the shape of a spectral peak by relating the bandwidth at 3dB to the peak frequency, $Q = f_p/\Delta f$. A high Q peak is therefore tall and narrow, a low Q peak is broad and flat. A NewWave centred on a high Q near-trapped peak would have a smaller maximum elevation than one centred on a low Q peak of similar maximum value. The peak in maximum runup versus wavenumber near $ka = 2.558$ for four circular columns is a tall narrow peak. The majority of the NewWave components will be much lower than at $k_p a$. However, with the $\beta = 0°$ cases there is a much broader peak near $ka = 1.209$ with the maximum runup being fairly consistent over a large range of ka values. This results in both NewWave cases shown having a similar maximum amplification despite the regular wave peak surface elevation for $ka = 2.558$, $\beta = 45°$ being very high.

To show the runup in more detail, a polar plot of the Net Amplification Factor can be plotted for each column, see Figure 3.4. Each polar plot represents the net amplification around a separate column and they are drawn in the same positions as the columns. The angle on each polar plot is the angle around each column, with zero being along the positive x-axis in the direction of propagation of the incident wave field. The magnitude plotted at each angle on the polar plot is the Net Amplification Factor at that angle on the respective column. The largest values are just upstream of the leading columns and slightly towards the middle of the array rather than on the columns' leading edges. There is also a small peak at the downstream side of each polar plot. This is due to the flow of water following the contours of the column around each side and then meeting at the rear and superimposing.

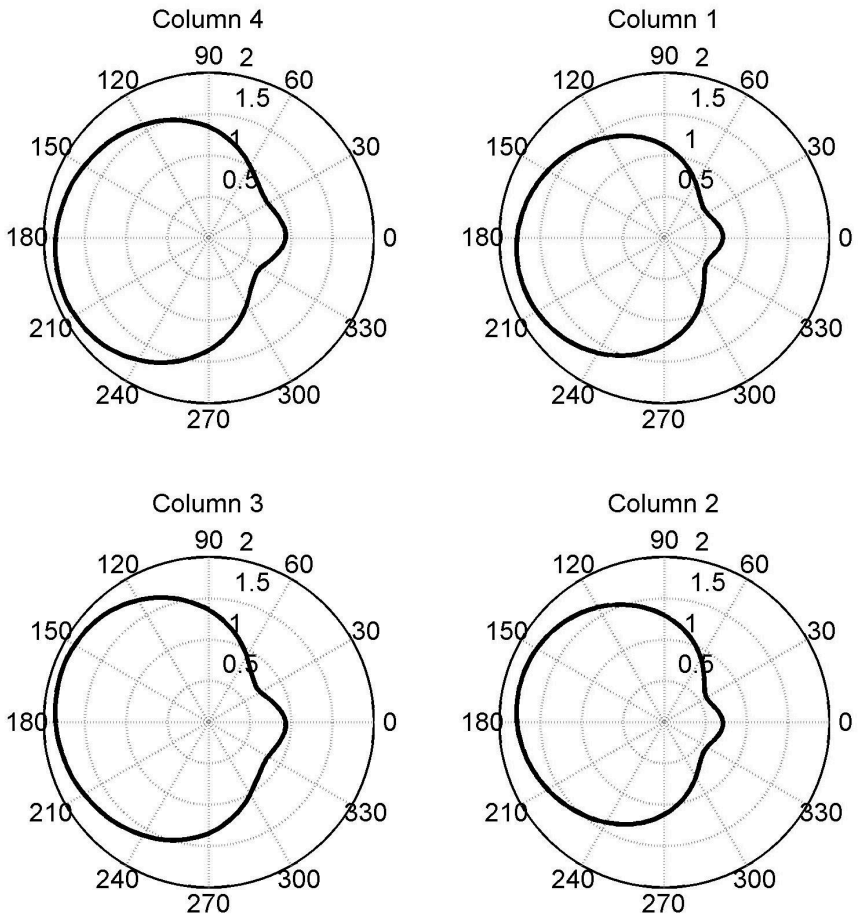

Figure 3.4: Net Amplification Factor runup on each column in an array of four circular columns with $\beta = 0°$ and $k_p a = 1.209$ ($T_p = 6.408$ s).

Figure 3.5 shows the sensitivity of the Net Amplification Factor to peak frequency. It shows field plots of the Net Amplification Factor for an array of four circular bottom-seated columns in water of depth 30 m, with the typical semi-submersible geometry discussed previously and wave direction $\beta = 0°$. The peak angular frequencies used in the JONSWAP spectra for the plots are varied by ± 10 % and ± 20 % about $\omega_p = 0.980$ Hz, which is the near-trapped frequency used as the peak in Figure 3.3(a) ($k_p a = 1.209$). The general patterns shown are very similar to Figure 3.3(a) with fairly small changes to the maximum NAF values and some smearing out of the response pattern away from the centre frequency. The largest differences are reduced sheltering downstream of the array and reduced peaks along the x-axis for $\omega_p \pm 20$ % , Figures 3.5(a) & 3.5(d).

Having found where to focus the NewWave wave groups to obtain the maximum expected response, the four time histories discussed previously can be calculated. When the maximum expected incident amplitude is combined with a discretised form of Equation 3.1 and a focus

$\Delta\omega_p$	-20 %	-10 %	0	10 %	20 %
k_pa	0.7740	0.9795	1.209	1.4633	1.7414
R_{Max}	1.715	1.791	1.885	1.816	1.8741

Table 3.1: Maximum Net Amplification Factor for the array of four bottom-seated circular columns with corresponding peak frequency and wavenumber.

point of (x_0, y_0, t_0), Equation 3.10 can be derived for an undisturbed focused NewWave wave group. In this equation ω_n is the angular frequency of the n^{th} spectral component, k_n is the wavenumber of the n^{th} spectral component, β is the angle of incidence with the x-axis, $X = x - x_0$, $Y = y - y_0$, and $\tau = t - t_0$. When at the focus location $x = x_0$ and $y = y_0$, so $X = 0$ and $Y = 0$. If also $t_0 = 0$ then $\text{Re}\{e^{ik_n(X\cos\beta + Y\sin\beta) - i\omega_n\tau}\}$ reduces to simply: $\cos(\omega_n t)$. Equation 3.11 gives the time history for case (b), the array response to the incident NewWave from case (a). It is very similar to Equation 3.10, differing only in the diffraction coefficient modifying the numerator. Equation 3.12 gives the time history for case (c), a NewWave-type solution in response, and is also similar to Equation 3.10; however, the incident spectra in both the numerator and denominator are modified by $|\phi_n(x,y)|^2$ and the maximum amplitude has changed. Finally, Equation 3.13 gives the time history for case (d), the incident wave time history required to cause a maximum response with the structure present but now with the structure absent.

$$\eta_a(x,y,t) = \alpha_I \frac{\sum_n S_I(\omega_n)\Delta\omega Re\Big\{e^{ik_n(X\cos\beta + Y\sin\beta) - i\omega_n\tau}\Big\}}{\sum_n S_I(\omega_n)\Delta\omega} \tag{3.10}$$

$$\eta_b(x,y,t) = \alpha_I \frac{\sum_n S_I(\omega_n)\Delta\omega Re\Big\{\phi_n(x,y)e^{ik_n(X\cos\beta + Y\sin\beta) - i\omega_n\tau}\Big\}}{\sum_n S_I(\omega_n)\Delta\omega} \tag{3.11}$$

$$\eta_c(x,y,t) = \alpha_R \frac{\sum_n |\phi_n(x,y)|^2 S_I(\omega_n)\Delta\omega Re\{e^{ik_n(X\cos\beta + Y\sin\beta) - i\omega_n\tau}\}}{\sum_n |\phi_n(x,y)|^2 S_I(\omega_n)\Delta\omega} \tag{3.12}$$

$$\eta_d(x,y,t) = \alpha_R \frac{\sum_n |\phi_n(x,y)|^2 S_I(\omega_n)\Delta\omega Re\Big\{\phi_n^{-1}(x,y)e^{ik_n(X\cos\beta + Y\sin\beta) - i\omega_n\tau}\Big\}}{\sum_n |\phi_n(x,y)|^2 S_I(\omega_n)\Delta\omega} \tag{3.13}$$

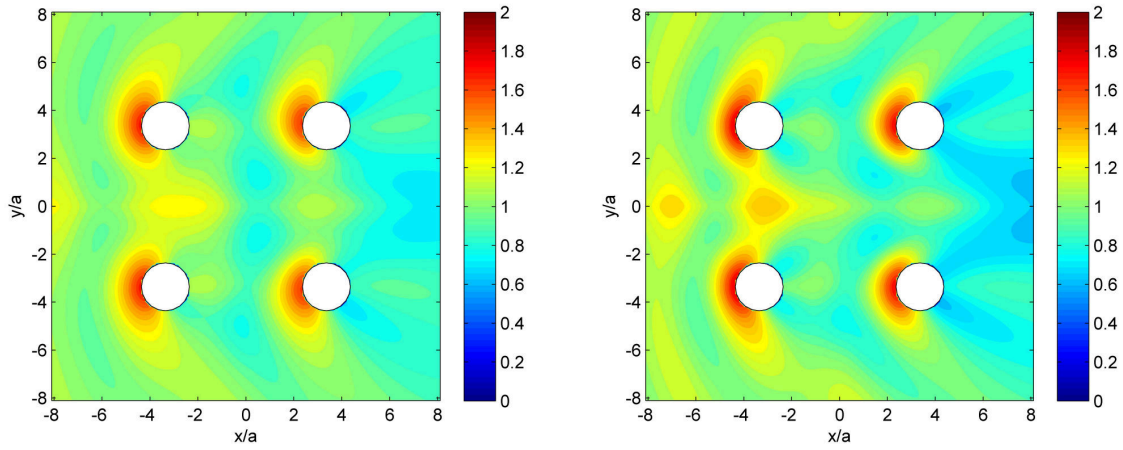

(a) $k_p a = 0.7740$, $\omega_p - 20$ %

(b) $k_p a = 0.9795$, $\omega_p - 10$ %

(c) $k_p a = 1.4633$, $\omega_p + 10$ %

(d) $k_p a = 1.7414$, $\omega_p + 20$ %

Figure 3.5: Net Amplification Factor around an array of four bottom-seated circular columns for $\beta = 0°$ with peak frequency perturbed by ± 10 % and ± 20 % relative to Figure 3.3(a) to investigate sensitivity to peak frequency. (a) $k_p a = 0.7740$, (b) $k_p a = 0.9795$, (c) $k_p a = 1.4633$, and (d) $k_p a = 1.7414$.

3.3.2 Incident NewWave wave group - Pair 1

Figure 3.6(a) and 3.6(b) shows two time histories normalised by α_I for the first NewWave solution mentioned above, the most probable shape associated with a one-in-N_w extreme linear crest in the open sea. Figure 3.6(a) shows an undisturbed, open ocean NewWave wave group, case (a), plotting Equation 3.10 for $k_p a = 1.209$ ($T_p = 6.408$ s) and $\beta = 0°$. It is a typical time history for a NewWave with a very compact wave group just a few periods long and a tall central peak at focus when all the linear components come into phase. Figure 3.6(b) shows case (b), the deterministic response elevation time history when this NewWave is now incident on an array of four circular columns, plotting Equation 3.11 at the same location as Figure 3.6(a). The focus point of the incident wave corresponds to the leading

edge of the upstream columns. There is a rapid rise over a similar number of periods to Figure 3.6(a) but the amplitude rises faster as wave energy is absorbed by the array. The peak amplitude is reached approximately two periods earlier than in the undisturbed case. After the peak there is a much slower fall in amplitude than Figure 3.6(a) because there are near-trapped effects within the obstacle array and energy is radiated only slowly by this mode.

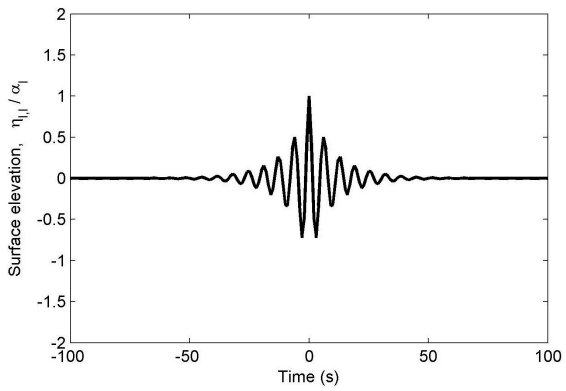

(a) Pair 1: Undisturbed NewWave

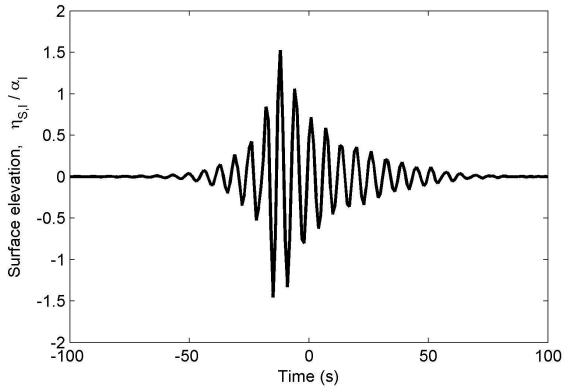

(b) Pair 1: Array response due to incident NewWave

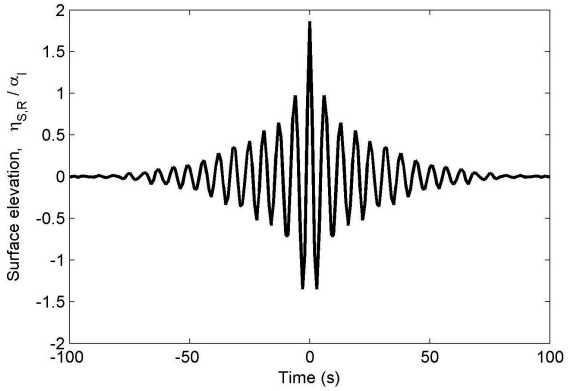

(c) Pair 2: NewWave in response

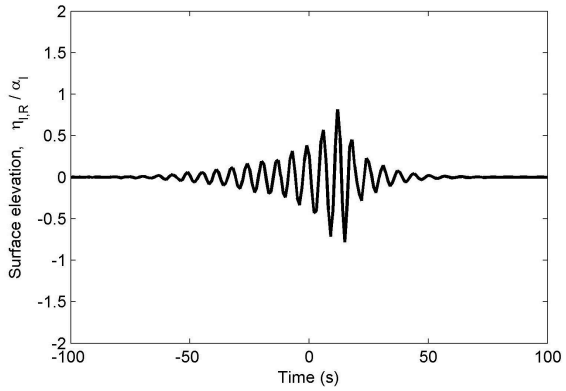

(d) Pair 2: Incident wave group required to cause maximum NewWave in response

Figure 3.6: Time histories at the focus point of a NewWave wave group with $k_p a = 1.209$ ($T_p = 6.408$ s) and $\beta = 0^\circ$ for (a) Pair 1, average shape of a large wave crest at a point on the open sea, (b) Pair 1, the surface elevation after interaction of this wave group with a square array of four bottom-seated circular columns, (c) Pair 2, total surface elevation for a maximum expected NewWave in response, $\eta_c(x_0, y_0, t)$, on the array of four columns, and (d) Pair 2, incident wave group, $\eta_d(x_0, y_0, t)$, that leads to the maximum expected response with the structure. All cases normalised by α_I

3.3.3 NewWave-type solution with a structure present - Pair 2

The surface elevation for a maximum expected NewWave in response, case (c), is given by Equation 3.12, now the one-in-N_w extreme surface elevation with the structure in place. These time histories are taken from the leading edge of the upstream column as the previous two cases were, and the maximum crest elevation in case (c) is 1.87 times greater than the NewWave in the open ocean, case (a). Apart from the magnitude of the maximum expected response, what is also of interest is the incident wave group that is required to cause it, case (d). The incident surface elevation for a maximum NewWave in response is given by Equation 3.13. This can be found from Equation 3.12 by using the diffraction coefficient, remembering that it is again the amplitude that is being modified, not the energy density spectrum, hence a linear relationship.

Figures 3.6(c) and 3.6(d) plot two time histories for the case of a NewWave in response, both normalised by α_I. Figure 3.6(c) is a plot of case (c), the actual NewWave in response that leads to a maximum expected wave-structure interaction and Figure 3.6(d) is case (d), the incident wave time history required to cause a maximum response but with the structure absent.

Now, if $\phi_n(x,y)^*$ is the complex conjugate of the diffraction coefficient, $\phi_n(x,y)$, then the square of the modulus is given by $|\phi_n(x,y)|^2 = \phi_n(x,y).\phi_n(x,y)^*$. This means that in the numerator of Equation 3.13, $|\phi_n(x,y)|^2/\phi_n(x,y)$ is equivalent to simply $\phi_n(x,y)^*$. If we now compare Equation 3.13, case (d), with Equation 3.11, case (b), the numerators are complex conjugates. The wave amplitude, α, and the denominator, m_0, are both real numbers which means that the phase is determined by the numerator only. This results in a case of reciprocity in time with the shape of the time histories being a mirror image about the focus time (Ohl et al. (2001b)). There is also a scaling factor between the two time histories of $(\alpha_R/m_{0,R})/(\alpha_I/m_{0,I})$. Figure 3.7 shows the time histories of $\eta_b(x_0,y_0,t)$ and $\eta_d(x_0,y_0,-t)$, where the incident elevation for a maximum expected NewWave in response is plotted against $-t$, not t, to show that apart from a single constant scaling factor the two time histories are identical and mirrored about the focus time t_0. The scaling factor for this

example is 1.87 and the solid green line shows that when scaled by 1.87, $\eta_b(x_0, y_0, t)$ and $1.87\eta_d(x_0, y_0, -t)$ are identical.

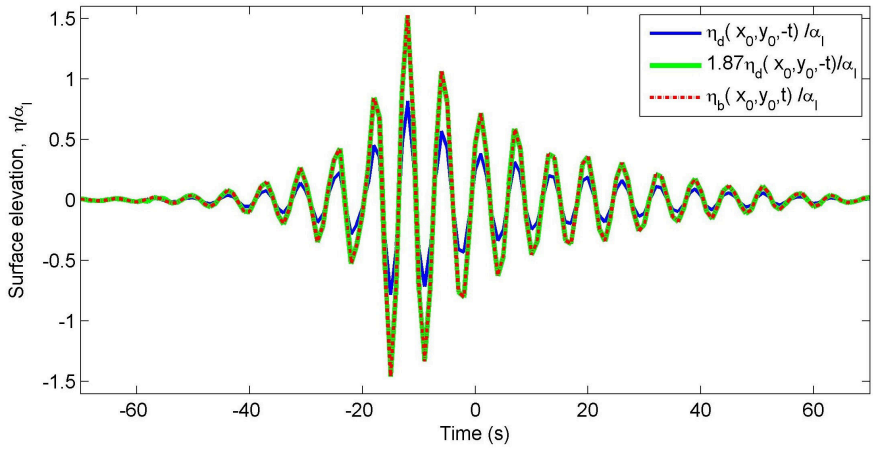

Figure 3.7: Time histories of the surface elevation for the response to an incident NewWave $\eta_b(x_0, y_0, t)$ (solid blue line) and scaled by 1.87 (green line), and the incident wave group leading to a maximum NewWave in response mirrored in time, $\eta_d(x_0, y_0, -t)$ (dashed line), all normalised by α_I with $k_p a = 1.209$ ($T_p = 6.408$ s) and $\beta = 0°$.

3.4 Validation

The previous section discussed the use of probabilistic tools to predict the maximum expected surface elevation for a given sea state. This section aims to validate these probabilistic methods though the brute force calculation of a large number of wave-structure interactions. Brute force calculations such as Monte-Carlo type simulations are generally considered impractical for regular use but they are ideal for verifying the methods of the previous section as they allow statistics to be collected and compared to the predicted results.

3.4.1 Generating random spectra

A series of long random realisations of the surface elevation are required, with each one based on the same user defined sea state. Sea surface elevation is assumed to be a stationary Gaussian random process with zero mean. The random time series are generated by forming random spectra, and then using the inverse FFT to take a Fourier sum of all the components. In the method presented here (based on Section 4.3 of Kernot (1995)), the amplitudes of

each of the Fourier components are also random variables with Gaussian distributions and zero means. Two sets of coefficients are used, a_n and b_n, where $n = 1 : N/2$ and N is the length of the signal being generated. The surface elevation is then given by the equation

$$\eta(t) = \Sigma_{n=1}^{N/2}(a_n \cos(\omega_n t) + b_n \sin(\omega_n t)) \tag{3.14}$$

where ω_n is the angular frequency of the n^{th} component. The variance of the Fourier coefficients, a and b, is based on the one sided power spectrum, $S(\omega_n)$, for the desired sea state:

$$\sigma_n^2 = S(\omega_n)d\omega \tag{3.15}$$

A random number generator is used to produce a set of Gaussian distributed random numbers, z_n, with zero mean and unit variance. These are then scaled up using the standard deviation given by the target sea state:

$$a_n = z_n.\sqrt{S(\omega_n)d\omega} \tag{3.16}$$

The square root is due to the fact that the JONSWAP spectrum, S, represents the power spectrum. The amplitude components, a_n and b_n, are used in the surface elevation spectrum (where b_n is also generated by Equation 3.16, but a different random number z_n). The power spectrum has a squared relationship with elevation. Once this surface elevation spectrum has been generated, an inverse FFT is then used to find the associated time history. Since all the manipulation occurs in the frequency spectrum, the method requires modest computation time to generate the spectra. One can also pad the design spectrum with zeros to produce longer time histories for each random spectrum generated.

3.4.2 Validating random spectra

When using statistics collected from the random spectra to validate results from the previous section, it is important to confirm that they are being generated correctly. One must be confident that the random incident spectra generated have the desired characteristics of the

target sea state before one begins the lengthy computations to collect statistics from them. A large set of 10000 spectra was generated based on a sea state with a JONSWAP spectrum, $H_s = 10.8$ m, and $T_p = 17$ s (see Figure 3.8 for the original smooth spectrum).

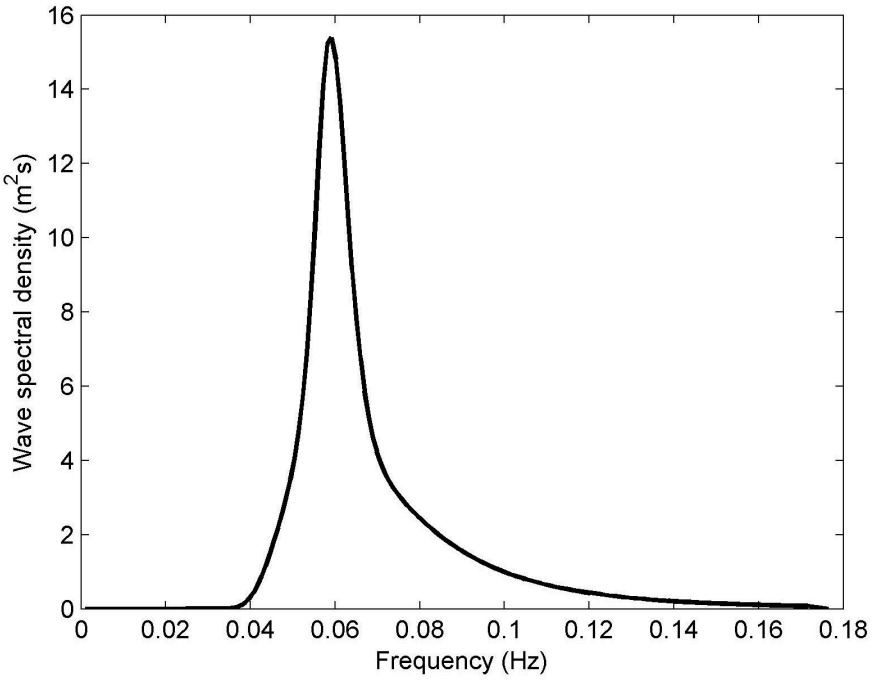

Figure 3.8: JONSWAP spectrum vs. frequency with $H_s = 10.8$ m and $T_p = 17$ s.

Each of the 10000 spectra was generated using the above method and, for each spectrum produced, an inverse FFT was used to find the associated surface elevation time history. The first validation to be made was to check that the correct spectral information was conserved. The autocorrelation was found for each of the time histories and then averaged across the ensemble. This ensemble averaging meant that any noise in the data was minimised without reducing the temporal resolution. The average autocorrelation can then be compared to a NewWave focused wave group produced from the same parent JONSWAP spectrum as used in the random spectra generation. The results are shown in Figure 3.9 scaled to unit amplitude and there is a very good match between the two. The two signals do diverge slightly further away from the focus point (due to sample variability in an ensemble of realisations) but overall the spectral content of the random spectra set is correct.

The next validation to be made, once the spectral content has been confirmed, is the

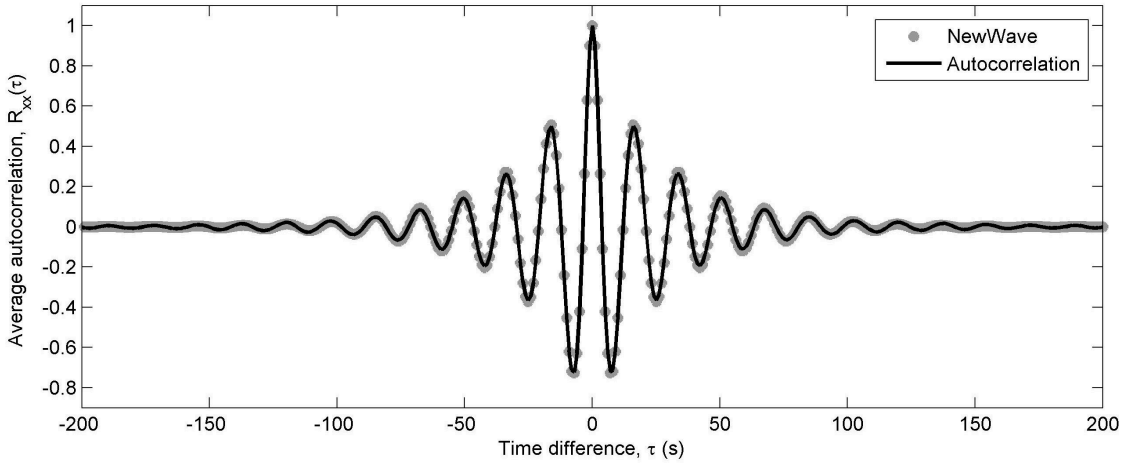

Figure 3.9: The average autocorrelation for the set of random elevation time histories (black line) and a NewWave focused wave group (grey markers) based on the JONSWAP spectrum used to generate the random time histories.

amplitude. H_s was calculated for each of the 10000 random spectra by finding the mean square value of the associated time histories. A normal distribution was fitted to the calculated H_s values with a mean of $\mu = 10.7669$ and a standard deviation of $\sigma_{ND} = 0.8559$. If multiple sets of 10000 spectra were calculated and the mean H_s found for each set, these mean H_s values would be distributed with a standard deviation closely approximated by $\sigma_{ND}/(N_{spectra})^{\frac{1}{2}} = 0.8559/(10000)^{\frac{1}{2}} = 0.0086$. The ensemble mean of the 10000 H_s values was found to be $H_{s,mean} = 10.8009$, which, given a target H_s of 10.8, is within the accuracy expected for a set of 10000 spectra. Figure 3.10(a) shows a histogram of the significant wave heights. The black line plots the normal distribution fitted to these values and shows a good approximation for the distribution. This is emphasized in Figure 3.10(b) which plots the cumulative probability distributions of the H_s values (grey line) and the normal distribution (black line) with an excellent match between the two.

Figure 3.11(a) shows a histogram of the individual wave crest amplitudes across the whole ensemble, based on the maximum value between each zero up-crossing, with over 800,000 values. Ochi (1998), Section 3.2.1 shows that if one assumes that a sea state can be approximated by a narrow-banded random process then the wave amplitude obeys a Rayleigh distribution. Given the sharp peak shown in Figure 3.8 and the high concentration of spectral energy about the peak frequency, it seems a reasonable assumption to approximate this JONSWAP spectrum as narrow-banded. The black line in Figure 3.11(a) plots a Rayleigh

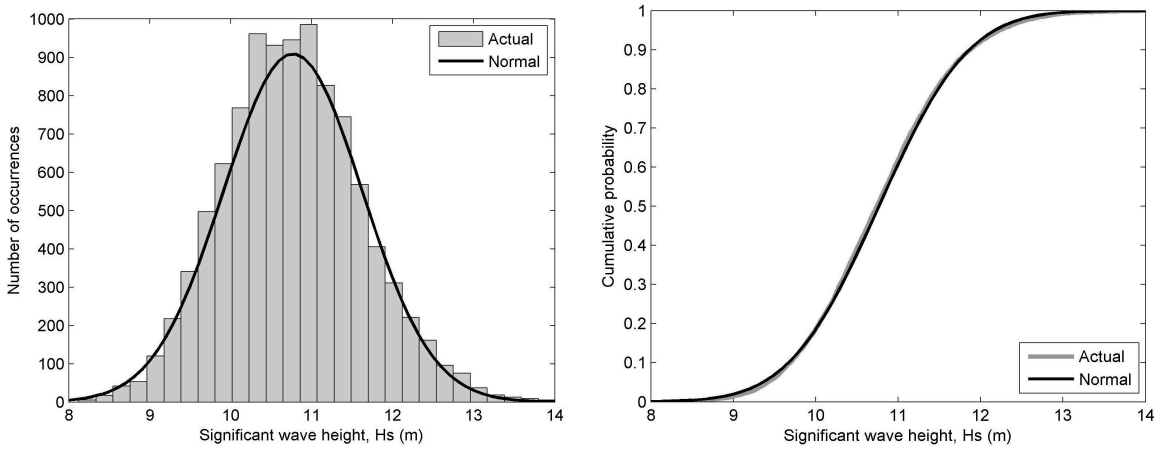

(a) Histogram of H_s (b) Cumulative probability distribution

Figure 3.10: Significant wave height, H_s, for all 10000 random spectra. (a) shows a histogram of H_s with a fitted normal distribution (black), (b) shows the CDFs of the fitted normal distribution in black and the H_s values in grey.

distribution that has been fitted to the wave crest amplitudes with a value of $\sigma = 2.6749$ (see Equation 3.2). The cumulative probability distributions are plotted in Figure 3.11(b) with the wave crest amplitudes in grey and the Rayleigh distribution in black. Both plots in Figure 3.11 show that the Rayleigh distribution fits the data well for wave heights above 3.5 m but underestimates the probability below this. It confirms that the random time series are behaving as expected and that taking JONSWAP spectra as narrow-banded is a reasonable approximation for the larger waves in the sea state.

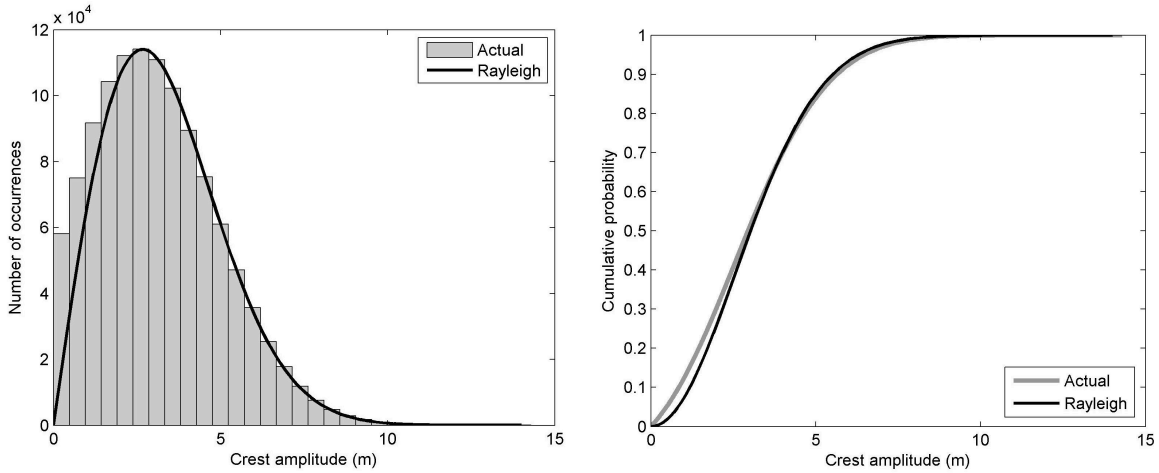

(a) Histogram of wave crest amplitudes (b) Cumulative probability distribution

Figure 3.11: Wave crest amplitudes for all 10000 random spectra. (a) shows a histogram of H_s with a fitted Rayleigh distribution (black), (b) shows the CDFs of the fitted Rayleigh distribution in black and the wave crest amplitudes in grey.

3.4.3 Surface elevation time histories

Once one is satisfied that large sets of random spectra can be generated for a given sea state, surface elevation time histories can be found using inverse FFTs. For the open ocean this is all that is required but in the vicinity of a structure the spectra must first be modified by linear transfer functions (LTFs). Sets of 10000 random spectra were produced, each with an associated time history of length 1033 s and a sampling frequency of 1.983 Hz. An FFT calculation in Matlab is more efficient for signals where the number of components is a power of 2. The number of components for each double sided spectrum (both positive and negative frequency components) was chosen to be 2048 to allow matrices of a size easily computed on a standard laptop. The time histories were therefore 1033 s long because 1024 frequency components were used and the time history duration is equal to $2048 \div 1.983$. For each of these spectra, the total linear response in the presence of a Thunder Horse like structure was also found by modifying the incident spectra. For interactions with a Thunder Horse type structure, a symmetric array of four columns with the average Thunder Horse cross-section connected by pontoons was used. This was introduced as Model 3 in Section 2.9 and the transfer functions were found using DIFFRACT. By calculating the response both in open ocean and in the vicinity of a structure one can find the change in surface elevation caused by the presence of the structure.

NewWave in open ocean

A further check to confirm that the results are reliable is to compare the largest events in a random sea to a NewWave focused wave group. NewWave has been shown to be an accurate model for the average extreme crest surface elevation and so by identifying the largest crests in a large set of random time histories and averaging over these crests at each point in time, the resulting mean surface elevation should be very close to a NewWave based on the sea state spectrum. A set of 10000 random spectra were generated based on a JONSWAP spectrum with a peak period of 17 s and a significant wave height of 10.8 m.

Figure 3.12(a) shows a comparison between the average surface elevation for the largest 500 crests and an ideal NewWave in the same sea state with the amplitudes matched at time

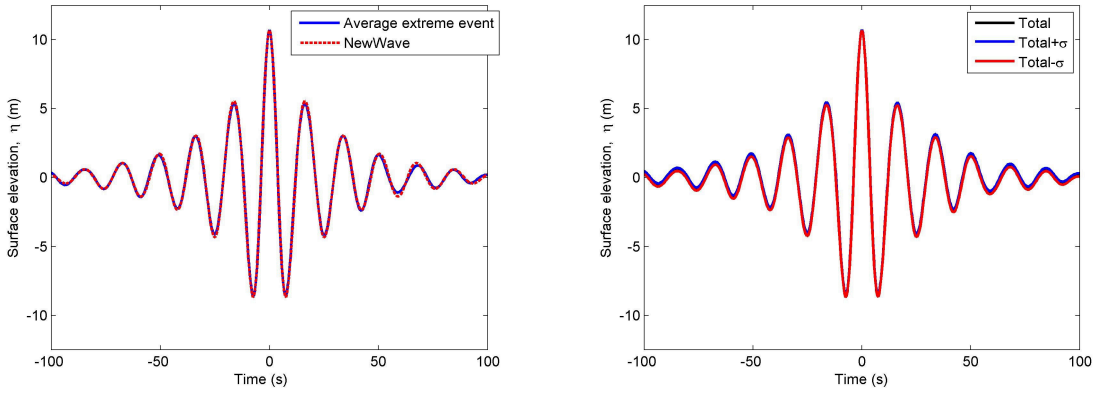

(a) Top 500 crests

(b) Error bars

Figure 3.12: (a) Average surface elevation for the largest 500 peaks in open ocean with $H_s = 10.8$ m and (b) the associated one STD error bars for the mean elevation.

$t = 0$ s. The results are very close to the ideal NewWave with only small deviations several periods away from the focus point. These small deviations are to be expected due to the uncertainty introduced by the random spectra used. To confirm that these small deviations are within the expected tolerance, one can find the standard deviation of the mean surface elevation and plot error bars one standard deviation either side of the mean. At each point in time the standard deviation was found for the 500 surface elevations being averaged over. This standard deviation of the individual crest elevation was divided by $\sqrt{500}$ to give the standard deviation of the mean, which was then added or subtracted from the average crest elevation to give the error bars. These error spreads are shown in Figure 3.12(b) and suggest that the method used to produce the random time histories is working correctly.

Error spreads

An additional check can be carried out by looking at the standard deviation of the 500 surface profiles being averaged rather than for the mean. The same data set of random spectra as the last section was used with $H_s = 10.8$ m and $T_p = 17$ s. One of the definitions of significant wave height is $H_s = 4\sigma$, where σ is the standard deviation of the surface elevation. Since a value of $H_s = 10.8$ m was chosen, the standard deviation of the surface elevation should tend to 2.7 m. Figure 3.13 plots the surface elevation with the one standard deviation error bars either side. The error spreads tend towards 2.7002 m as one moves further from the focus point at time $t = 0$ s. Close to the focus time the standard deviation

becomes very small. This is because the largest crests have been deliberately isolated and aligned to allow a comparison between the average crest elevation and a NewWave group. If random waves were incident on a structure and a similar figure plotted for the total scattered surface profiles at a point close to the structure then the error bars would tend to a larger value due to the H_s being locally increased by the diffraction effects of the structure.

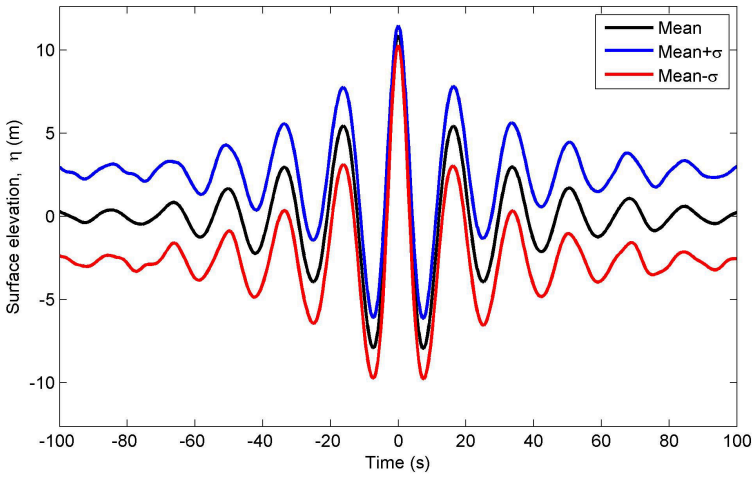

Figure 3.13: Error boundaries for the surface elevations being averaged in open ocean with $H_s = 10.8$ m.

3.4.4 NAF - Validation

In Section 3.3.1 the Net Amplification Factor was introduced as a useful tool in extreme wave analysis. The purpose is to help find the locations expected to give the largest responses in the vicinity of a structure in a particular sea state and show how large those responses are likely to be for a given number of waves. The examples shown in Section 3.3.1 were for the simple model of four bottom-seated circular columns. This allowed quick and cheap calculations for an approximation of the structure being examined to establish the methods discussed. However, a more accurate model should be used to both confirm that an approximation such as this gives reasonable results and also to look at the situation in more detail. Figure 3.14 compares field plots of the NAF for both the simple (Figure 3.14(a)) and more realistic (Figure 3.14(b)) models for a JONSWAP sea state with the spectral peak coinciding with a near-trapped mode of $k_p a = 1.209$ ($T_p = 6.408$ s), $\beta = 0°$. The figures show that

the change in geometry and increase in water depth between the two models causes only small changes to the overall pattern of the NAF plot. There are some differences in the amplitudes of peaks and troughs between the two figures and some squaring of the patterns due to the change in column shape. Most of the peaks are in the same location except for a peak along the x-axis just upstream of the array which has moved slightly closer to the array for the more realistic model. Overall, the simple model allows a good approximation for less computation time. However, to ensure accurate results the more complex model will be used for the rest of this chapter.

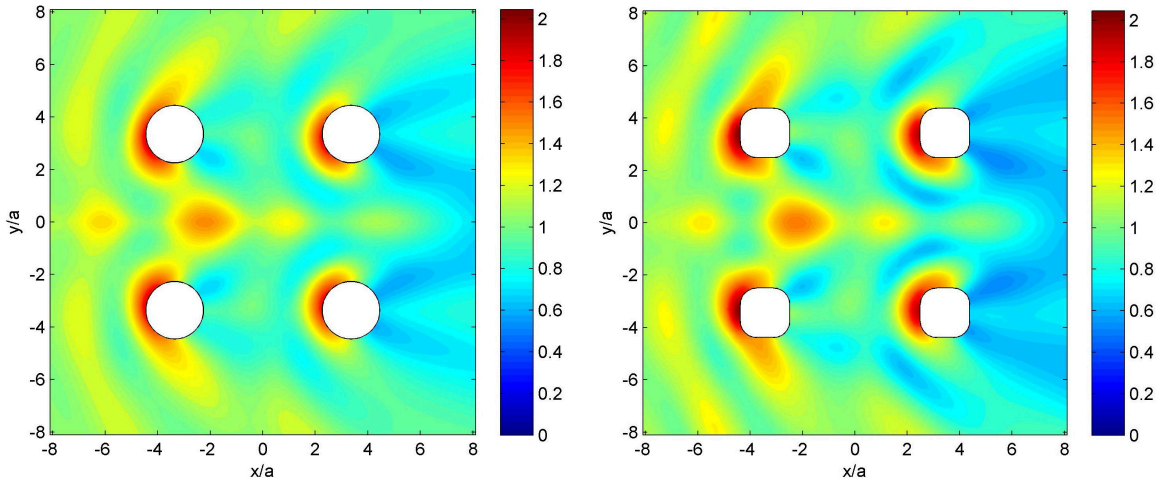

(a) Bottom-seated circular columns

(b) Realistic deep water model

Figure 3.14: Net Amplification Factor for (a) simple and (b) realistic Thunder Horse models for $k_p a = 1.209$ ($T_p = 6.408$ s), $\beta = 0°$.

The derivation of the NAF has already been described in a previous section but it is prudent to validate it as useful for predicting violent wave-structure interactions. One method of validating the NAF is to generate a large set of random spectra (as discussed earlier in this section) based on the same overall sea state as for the NAF. These random spectra can then be used to generate time histories for the surface elevation, both in the presence of the structure using the DIFFRACT LTFs and in open ocean without the need of transfer functions. The time histories can then be combined into two large data sets (with and without the structure) and the largest events identified in each. By comparing the largest extreme events with and without the structure and repeating this across the field, a brute

force statistical simulation of the NAF can be made.

A set of 100 random linear time histories, each of length 1033 s, were generated using the Monte Carlo type method for a sea state with $k_p a = 1.209$ ($T_p = 6.408$ s), $\beta = 0°$. LTFs were then used to modify the random spectra and find the associated time histories at a location in the vicinity of the structure. For each time history, the zero upcrossings were identified and used to find the crest and trough for each period. The crests were then combined into a single data set and sorted into height order. The average was taken of the largest 500 crests and the process was repeated at each location across the field. Finally, the random time histories were used without any modification by an LTF to find the largest 500 crests in open ocean. This was then used to normalise the average extreme crest elevation with the structure present, allowing a direct comparison with the analytical NAF. For the sea state mentioned above, Figure 3.15(a) shows the NAF and Figure 3.15(b) shows the results of the Monte Carlo type method. It is clear that there are few differences between the two plots, even though the NAF method takes far less computation time. On a computer with a 2.2GHz processor, 8Gb RAM and Windows 7 64-bit, the Monte Carlo type method takes around 4000 s to produce 100 time histories, each of length 1033 s at locations on a 4 m grid over a 200x200 m area. The equivalent NAF calculation takes just 43 s on the same computer with almost identical results.

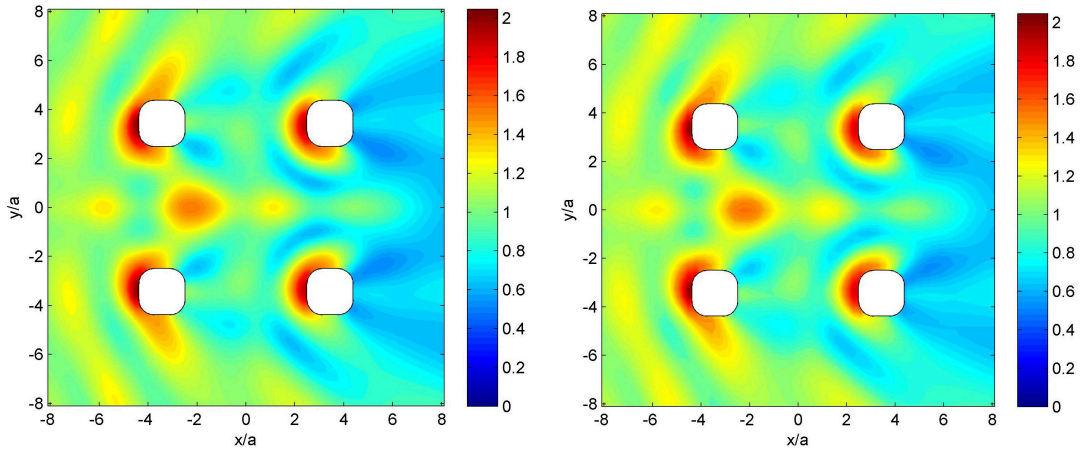

(a) NAF (b) Average extreme crest amplification

Figure 3.15: (a) Net Amplification Factor and (b) average Monte Carlo crest amplification for $k_p a = 1.209$ ($T_p = 6.408$ s), $\beta = 0°$.

3.5 Conclusions

Conclusions drawn from the results presented in this chapter are briefly summarized below.

- Diffraction of an incident random wave record gives rather different results from a regular wave chosen to match the spectral peak frequency, with reduced maximum amplitude and several near-trapped modes being excited simultaneously in the random field.

- A Net Amplification Factor independent of time or H_s can be plotted across the field around a structure to show the locations expected to give the largest linear surface motion.

- There is a simple reciprocity between the deterministic response to a NewWave group incident on a structure and the incident wave group leading to a NewWave solution in response with the structure present.

- Random surface elevations can be generated efficiently by applying diffraction transfer functions in the frequency domain and then taking an inverse FFT to find the associated time history.

- Collection of random statistics for surface elevations, both with and without a structure present, has been used to verify the use of the Net Amplification Factor to predict locations of large responses.

Chapter 4

Second-order diffraction

4.1 Introduction

Chapter 2 looked at the linear diffraction of regular waves by single and multiple columns of several different cross-sections. This work is now extended to second-order to investigate the effect on quadratic transfer functions (QTFs) of column shape and proximity to other columns, along with a study of the distribution of QTFs with frequency for a given structure. Equation 4.1 shows the linear response elevation to two incident waves with amplitude A_i m, angular frequency ω_i rad/s, and phase ψ_i rad, where $i = 1, 2$ and b_i is the linear transfer function at frequency ω_i. The second-order response components are then given in Equation 4.2 with the QTFs for the potential sum term b_{PS}, quadratic sum term b_{QS}, potential difference term b_{PD}, and quadratic difference term b_{QD}. Quadratic terms refer to the simple local product of two first-order incident wave components. Potential terms arise from the inhomogeneous equations at second-order and refer to the interactions between pairs of incident frequency components that give rise to wave components at the output frequencies. Sum terms refer to response at a frequency equal to the sum of the incident frequencies, $\omega_R = \omega_i + \omega_j$, (i.e. double the incident frequency for the self-interaction) and the difference terms refer to a response at $\omega_R = \omega_i - \omega_j$.

$$\eta_R^{(1)} = b_1\eta_1 + b_2\eta_2 = b_1 A_1 e^{-i(\omega_1 t + \psi_1)} + b_2 A_2 e^{-i(\omega_2 t + \psi_2)} \tag{4.1}$$

$$\eta_R^{(2)} = (b_{PS} + b_{QS})A_1A_2e^{-i((\omega_1+\omega_2)t+\psi_1+\psi_2)} + (b_{PD} + b_{QD})A_1A_2e^{-i((\omega_1-\omega_2)t+\psi_1-\psi_2)} \quad (4.2)$$

Firstly, a description of the issues faced when meshing structures for second-order analysis is given. This is followed by some validation simulations to confirm that accurate and converged results were produced. Having established that second-order results can be reliably obtained, the investigation from Chapter 2 into the effect of structure geometry on the diffraction of incident waves is extended to second-order. Field plots of QTFs for arrays of four bottom-seated columns are then used to find the mode shapes excited by second-order interactions. These second-order mode shapes are compared with the equivalent mode shape from first-order excitation.

Finally, the structure of QTFs in the frequency domain is investigated to see if reliable results are given when QTF approximation methods are used to minimise computation time.

4.2 Meshing and convergence

Ensuring convergence of second-order simulations is essential for accurate results and yet there is no fixed method or software to guarantee this. Similar issues are faced when using DIFFRACT as with other second-order codes, such as the industry standard code WAMIT. There are many parameters that affect whether convergence is reached, along with the design of the mesh itself. To aid in the design of meshes for use with DIFFRACT, the commercial mesh generating software Gambit is used. This makes it easier to keep the elements within the mesh as close as possible to being square. Elongated or skewed cells can lead to the Jacobian used in the numerical procedure becoming ill-conditioned. The resolution of the mesh must be fine enough to allow at least several cells per output wavelength for the highest frequency response component.

DIFFRACT requires that the nodes on the body water-line must only be shared with

two quadrilateral cells on the outer surface (see Figure 4.1), and the body surface mesh is limited to a maximum number of nodes (around 5000 for a Windows 7 64-bit system with 6Gb RAM). To help minimise the number of nodes needed to mesh a structure, one can use up to two planes of symmetry so that only a quarter of the body would then have to be meshed. For complex structures such as Thunder Horse, this maximum number of body cells can still be restrictive for second-order analysis at higher frequencies even with the use of symmetry. The radius of the outer free surface mesh also affects convergence.

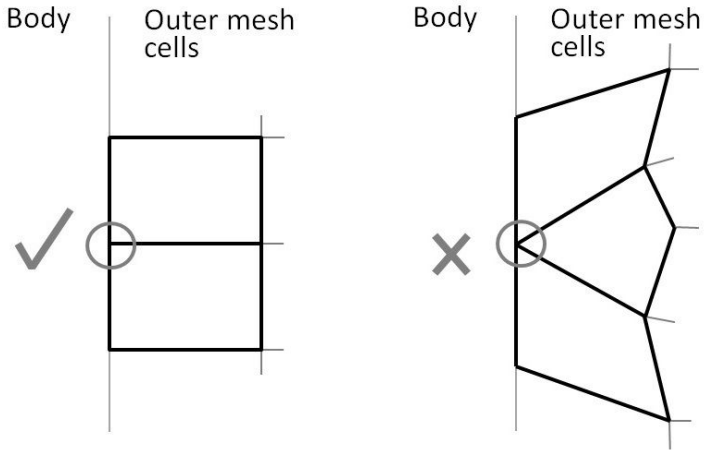

(a) Two cells, acceptable (b) Three cells, unacceptable

Figure 4.1: Acceptable and unacceptable sharing of nodes on the body surface between (a) two and (b) three cells respectively.

Two guidelines to help judge the size needed for a given frequency were suggested by Chau (1989) and Kernot (1995). Chau (1989) recommended an outer radius of at least double the water depth for a fixed diffracting body and Kernot (1995) found that the outer radius should be at least as large as the longest wavelength. Second-order analysis of bichromatic waves in deep water can therefore be problematic, particularly when the pair of frequencies is far from the leading diagonal. If a high frequency is paired with a low frequency then the mesh resolution must be fine enough to cope with the small wavelength of the sum response and the outer radius should be longer than the wavelength of the low frequency component. This can lead to meshes with large numbers of cells which can make convergence testing very time consuming.

As there is no fixed method for ensuring convergence, one must run a large number of tests with varying meshes and DIFFRACT parameters to ensure that convergence is achieved. It was found that for the Thunder Horse Model 3 structure discussed earlier, convergence could not be found for incident angular frequencies above 1.1 rad/s. For JONSWAP spectra with a cutoff at double the peak frequency, this limits the range of peak frequencies to excite at second-order the lowest four near-trapped modes. A cutoff at double the peak frequency causes a less than 5 % loss of spectral energy compared to a cutoff at ten times the peak frequency while greatly reducing the number of QTF calculations required. Extensive convergence tests were carried out and the author is confident that the results presented are accurate. Some examples of the convergence tests carried out are given below.

The example results given are for the pair of frequencies $(1.0725, 0.8259)$ rad/s ($(T_1, T_2) = (5.858, 7.608)$ s) with $\beta = 45°$. There are many different parameters that affect whether convergence is reached or not including body mesh cell size (bc), outer surface mesh cell size (oc), and outer surface mesh radius (r_m). Figure 4.2 shows convergence tests on (a) the body mesh cell size, (b) the outer surface mesh cell size, and (c) the outer surface mesh radius. In each case several meshes are used to calculate the response for the pair of incident waves discussed. The responses for all the meshes are then plotted to show how much variation there is between the different meshes used.

Figure 4.2(a) plots the potential sum QTFs along the x-axis for the pair of unit amplitude incident waves and three different meshes on the body. The blue line represents a body mesh with average cell width 5 m, the red line a body mesh with average cell width 4 m, and the green line a body mesh with average cell width 3 m. The outer surface meshes for all three cases have an outer radius of 500 m and an average cell width of 5 m. The three different body meshes give very similar results for this pair of incident waves, with a slightly larger gap between the blue and red lines than between the red and green lines. This shows that with an average body cell width of 3 m convergence has been reached to a satisfactory level, with minimal improvements from a finer mesh not worth the extra calculation time.

Figure 4.2(b) plots the potential sum QTFs along the x-axis for the same pair of unit-

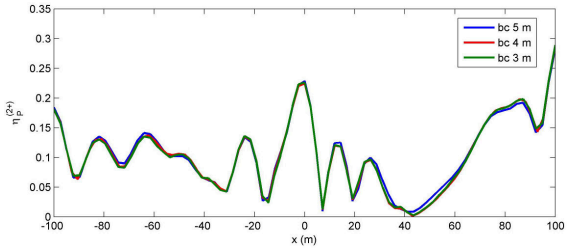

(a) Body cell varies, outer surface cell 5 m, outer radius 500 m

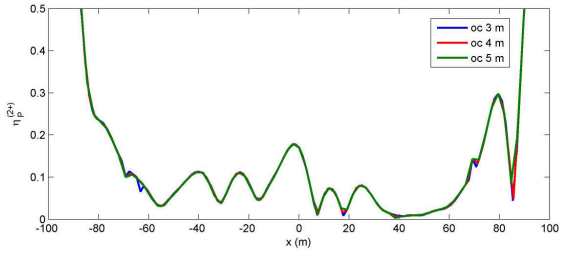

(b) Body cell 3 m, outer surface cell varies, outer radius 300 m

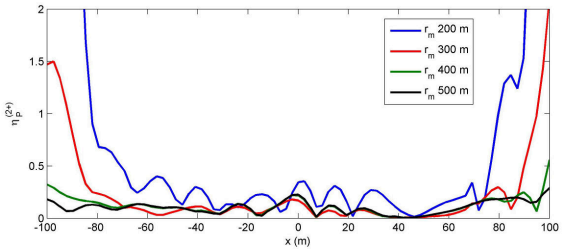

(c) Body cell 3 m, outer surface cell 5 m, outer radius varies

Figure 4.2: Investigating the effect of (a) body cell width, (b) outer surface cell width, and (c) outer surface radius on the convergence of the potential sum QTF along the x-axis for $(\omega_1, \omega_2) = (1.0725, 0.8259)$ rad/s $((T_1, T_2) = (5.858, 7.608)$ s).

amplitude incident waves but with three different meshes on the outer surface. The green line represents an outer surface mesh with average cell width 5 m, the red line an outer surface mesh with average cell width 4 m, and the blue line an outer surface mesh with average cell width 3 m. The body mesh for all three cases has an average cell width of 3 m and the outer surface meshes for all three cases have a shorter outer radius of 300 m to save computation time. The three different outer surface meshes give very similar results for this pair of incident waves, with a slightly larger gap between the green and red lines than between the red and blue lines. This shows that with an average outer surface cell width of 5 m, convergence has been reached to a satisfactory level.

Figure 4.2(c) plots the potential sum QTFs along the x-axis for the same pair of unit-amplitude incident waves but with four different meshes on the outer surface. The blue line represents an outer surface mesh with an outer radius of 200 m, the red line an outer surface radius of 300 m, the green line an outer surface radius of 400 m, and the black line an outer surface radius of 500 m. The body mesh for all three cases has an average cell width of 3 m and the outer surface meshes for all four cases have an average cell width of 5 m. The four different outer surface meshes give fairly similar results near the origin

but with much more variation further from the origin. This shows the importance of using a large radius outer surface mesh relative to both the water depth and the wavelength of the incident components. The 500 m radius mesh shows sufficient convergence, particularly within the range of ±70 m which includes the immediate area around the Thunder Horse structure. In this region it is almost exactly the same as the 400 m radius mesh. For this pair of frequencies, a mesh with body cell width 3 m, outer surface cell width 5 m, and outer surface radius 500 m was chosen.

4.3 Validation

As mentioned in Section 2.1.1, DIFFRACT has been well validated against published data for forces and surface elevations at both first- and second-order. However, it was once again deemed prudent for the author to perform his own validation simulations to ensure that the results presented in this chapter are accurate. This thesis focuses on surface elevation rather than body forces and so the results shown in this section are for surface elevations.

The results presented in the rest of this chapter require confidence in the author's ability to use DIFFRACT to calculate converged solutions for surface elevation to second-order with bichromatic, unidirectional waves incident on an array of closely spaced columns. Three validation examples are included in this section to cover these requirements. The first looks at runup around a square array of closely spaced circular columns for unidirectional monochromatic incident waves and can be compared to the semi-analytical results of Malenica et al. (1999). The second looks at surface elevation in the vicinity of a single column, rather than simply runup, for monochromatic incident waves and can be compared to semi-analytical results of Eatock Taylor and Huang (1997). Finally, results are presented for bichromatic waves incident on a single column and can be compared to the results of Kim and Yue (1990).

The first example examines the runup around a square array of four circular bottom-seated columns with radius a, depth $d = 3a$, incident wavenumber $ka = 0.468$, wave direction $\beta = 45°$, and column centres at $(\pm 2a, \pm 2a)$. These results are plotted in Figure 4.3 and can be compared to the semi-analytical results of Malenica et al. (1999), Figure 13, page

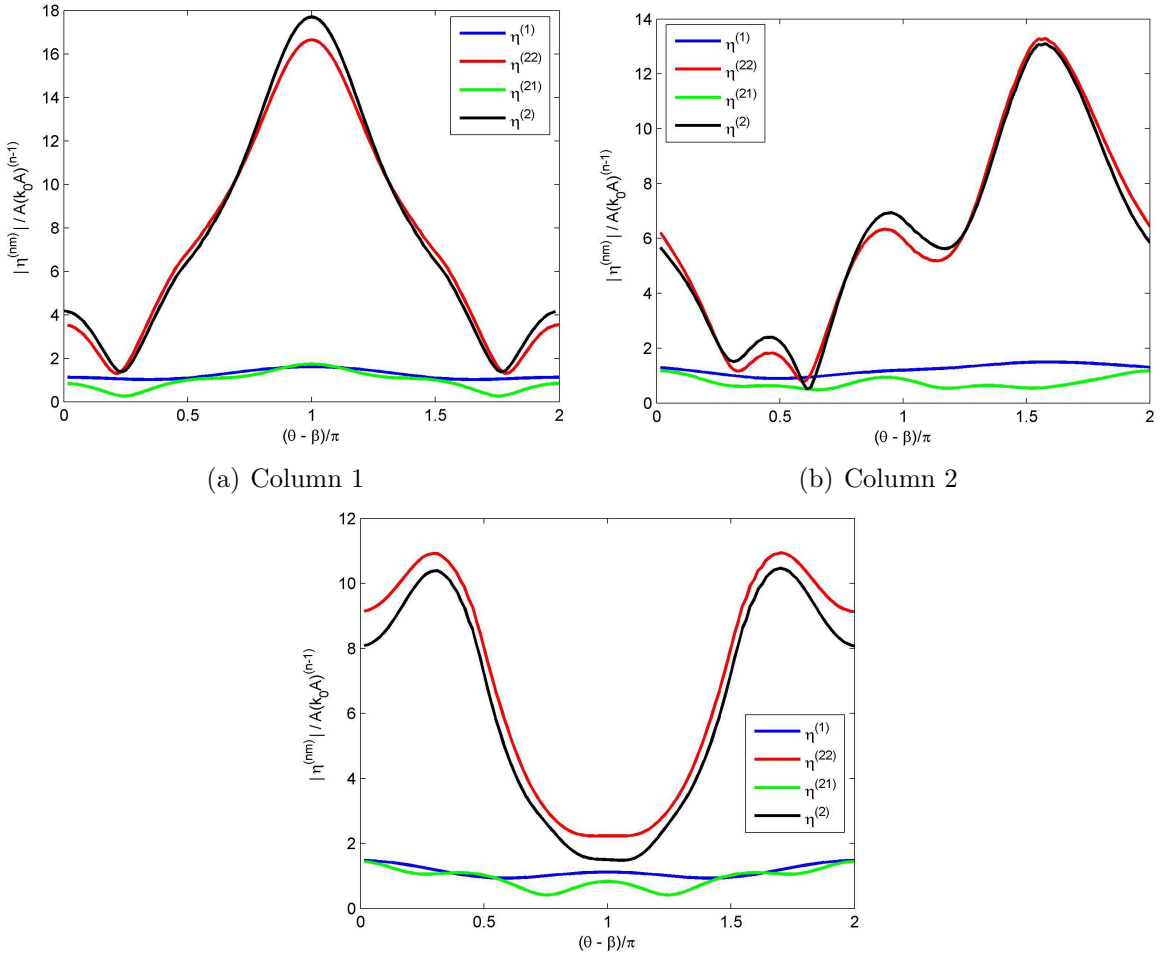

(a) Column 1

(b) Column 2

(c) Column 3

Figure 4.3: Normalised runup $|\eta^{(nm)}|/A(k_0A)^{(n-1)}$ around columns (a) one, (b) two, and (c) three for $ka = 0.468$, $\beta = 45\,^{\circ}$, and $d/a = 4$. The runup is split into the following components: first-order (blue line), second-order potential sum (red), second-order quadratic sum (green), and total second-order (black).

369. Figure 4.3(a-c) show runup around Columns 1-3 respectively, with the columns labelled as defined in Chapter 2. Each figure plots the linear (blue line), second-order potential sum (red), second-order quadratic sum (green), and total runup against the position on the column, measured anti-clockwise from the downstream point of each column. The quadratic difference component was not considered by Malenica et al. (1999). The results given in Figure 4.3 show excellent agreement with those of Malenica et al. and were also used to validate the work of Walker (2006).

Having established that runup can be calculated accurately to second-order, one can look at surface elevation away from the column. The next example looks at surface elevation around a single circular bottom-seated column with radius a, depth $d/a = 4$, incident wave

amplitude $A/a = 0.1$, wavenumber $ka = 0.8$, and wave direction $\beta = 0°$. The results are plotted in Figure 4.4 with each plot showing the following components: (a) linear, (b) total second-order sum, (c) second-order potential sum, and (d) second-order quadratic sum. These results show excellent agreement with the semi-analytical results of Eatock Taylor and Huang (1997), Figures 7 and 8, pages 1533 and 1534.

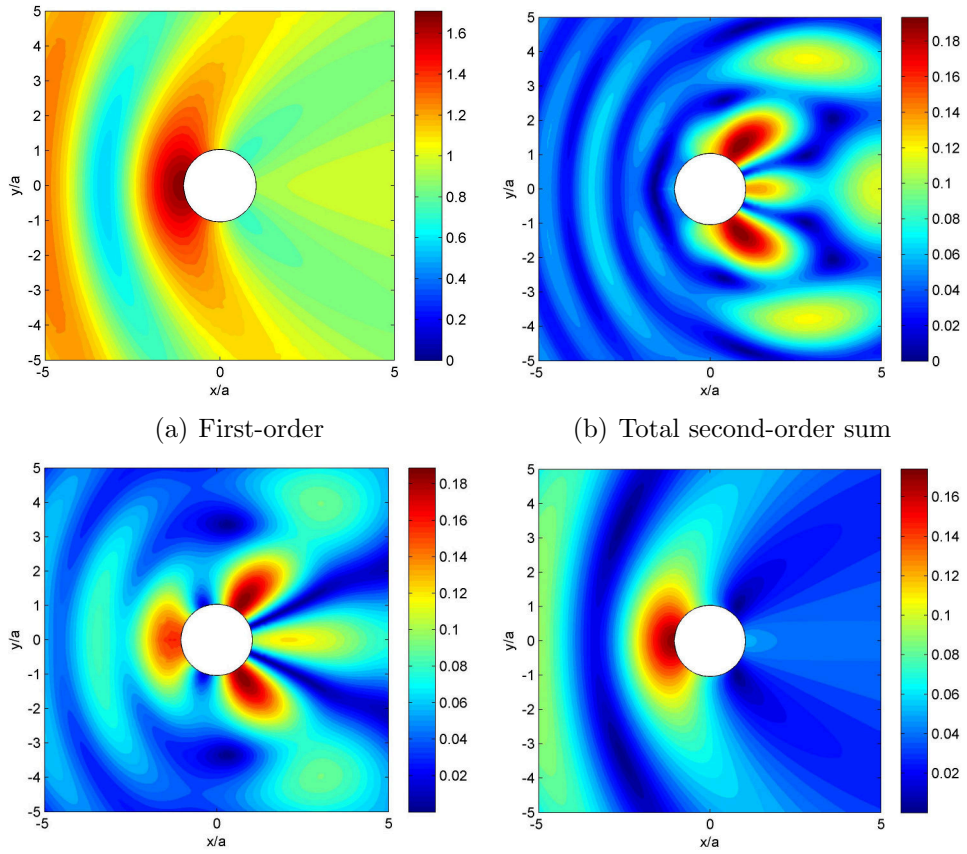

(a) First-order (b) Total second-order sum

(c) Second-order potential sum (d) Second-order quadratic sum

Figure 4.4: Surface elevation normalised by incident amplitude $|\eta|/A$ for $ka = 0.8$, $\beta = 0°$, $A/a = 0.1$, and $d/a = 4$. $|\eta|/A$ is split into the following components: (a) first-order, (b) total second-order sum, (c) second-order potential sum, and (d) quadratic sum.

Finally, we look at a bichromatic incident wave example as considered by Kim and Yue (1990). A pair of waves are incident on a single column of radius a, depth $d/a = 1$, with a wave direction of $\beta = 0°$ and wavenumbers $(k_1 a, k_2 a) = (1.536, 1.709)$, or as Kim and Yue define them with deep water wavenumbers, $(\nu_1 a, \nu_2 a) = (1.4, 1.6)$. Kim and Yue calculated the second-order sum and difference runup around the column using a ring source boundary integral approach. The DIFFRACT results show good agreement with Kim and Yue and are plotted in Figure 4.5. Figure 4.5(a) shows the sum components and Figure 4.5(b) shows the difference components, with potential terms in black and quadratic terms in grey.

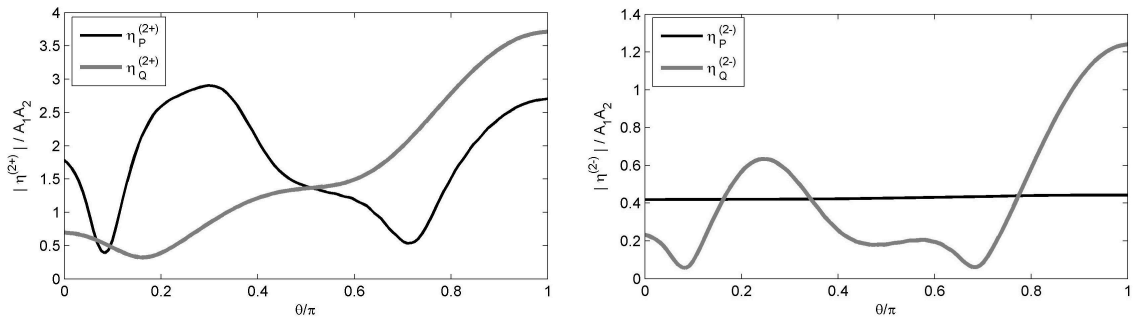

(a) Second-order sum (b) Second-order difference

Figure 4.5: Potential and quadratic components of (a) second-order sum and (b) second-order difference runup for a single bottom-seated circular column with radius a, depth $d/a = 1$, $\beta = 0\,^\circ$, and wavenumbers $(k_1a, k_2a) = (1.536, 1.709)$.

4.4 Effect of geometry

Chapter 2 looked at the effect of structure geometry on the linear diffraction of incident regular waves. This section looks at how structure geometry affects the second-order diffraction of regular waves. The effect on the diffracted field of both column cross-sectional shape and their proximity to other columns will be investigated. Three column cross-sections will be used in arrays of one, two, and four columns. The three column shapes investigated are circular, intermediate, and almost square. The circular and intermediate columns are the same as for Chapter 2 with circular radius a and water depth $d/a = 2.43$. The intermediate column is square with rounded edges, where the cross-sectional area and the radius of curvature on the corners are the average values for the Thunder Horse semi-submersible. The radius of curvature for the average Thunder Horse intermediate case is equal to 32.9 % of the column width, and for exact dimensions of the Thunder Horse structure see Appendix A. The almost square column has the same cross-sectional area as the other two column shapes but the rounded corners have a radius equal to 8.95 % of the column width. This gives a normalised radius of curvature of $r/a = 0.16$, which is much smaller than for the intermediate case with a ratio of $r/a = 0.62$. Second-order calculations can be very intensive computationally and so an almost square column is used to allow simpler meshes than an exactly square column by removing the sharp edges of a perfect square. For convenience, this column shape will be referred to as the square column for the rest of this section.

4.4.1 Single columns

Figure 4.6 shows the potential sum, quadratic sum, and quadratic difference components for a single bottom-seated circular column with a unit-amplitude incident regular wave of $\omega = 0.490$ rad/s ($T = 12.816$ s), $\beta = 0°$. The potential sum component has a much higher maximum amplitude than the other two components and the diffraction pattern is far more complex. In the interest of avoiding repetition, this section will focus on results for the potential sum component when investigating the effect of geometry on the surface elevation patterns.

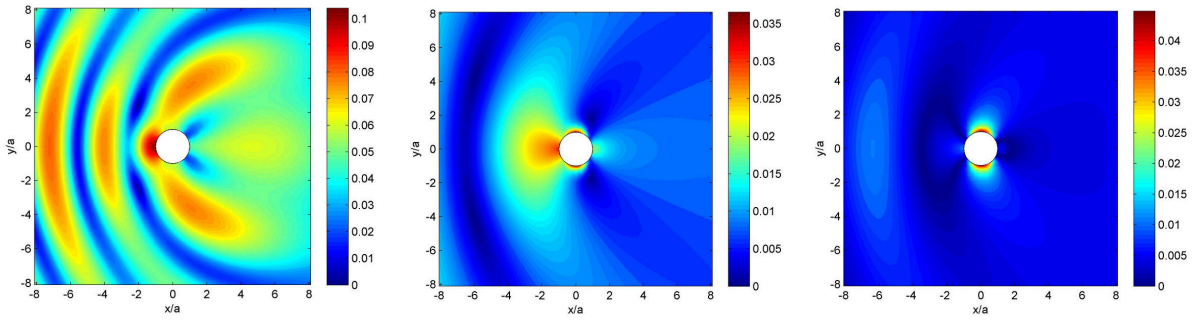

(a) Potential sum (b) Quadratic sum (c) Quadratic difference

Figure 4.6: Second-order components of the surface elevation for an isolated circular bottom-seated column with $\omega = 0.490$ rad/s ($T = 12.816$ s), $\beta = 0°$.

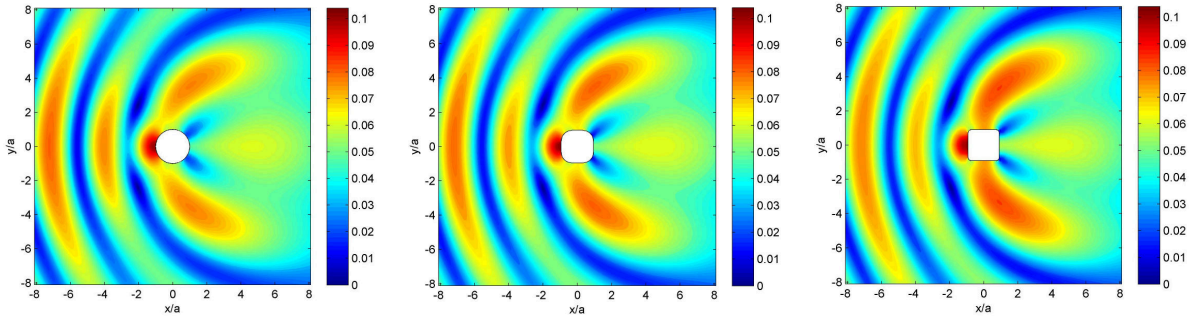

(a) Circular (b) Intermediate (c) Square

Figure 4.7: Second-order potential sum surface elevation for isolated bottom-seated columns of varying cross-section with $\omega = 0.490$ rad/s ($T = 12.816$ s), $\beta = 0°$.

Figure 4.7 plots the magnitude of the surface elevation potential sum component in the vicinity of a single column for the unit-amplitude incident regular wave with $\omega = 0.490$

rad/s ($T = 12.816$ s) and wave direction $\beta = 0°$. This incident period and wave direction were chosen so that the second-order sum response would excite a near-trapped mode in the four column arrays, as predicted by Section 2.5. There are few differences in the general surface elevation pattern between the three different column shapes. As the column gets more square, the maximum amplitude increases slightly and the high amplitude lobes either side of the column connect to the side faces of the column rather than the peak just upstream of the leading face.

4.4.2 Multiple columns

Figure 4.8 plots the magnitude of the surface elevation second-order potential sum component in the vicinity of pairs of bottom-seated columns for the same incident wave as the previous example. The general pattern is again very similar for all three column shapes but there is now a 12 % increase in maximum amplitude between the circular and square columns. The peak located between the columns increases in amplitude and extends further downstream as the columns become more square. This shows that at second-order, column shape is still important, as are the interactions between closely spaced columns.

# Columns	Circular	Intermediate	Square
One	0.1011	0.1028	0.1039
Two	0.1214	0.1293	0.1359
Four	0.2468	0.2510	0.2250

Table 4.1: Maximum $|\eta_P^{(2+)}|$ for arrays of one, two, and four bottom-seated columns with circular, intermediate or square cross-sections and an incident wave of $\omega = 0.490$ rad/s ($T = 12.816$ s), $\beta = 0°$.

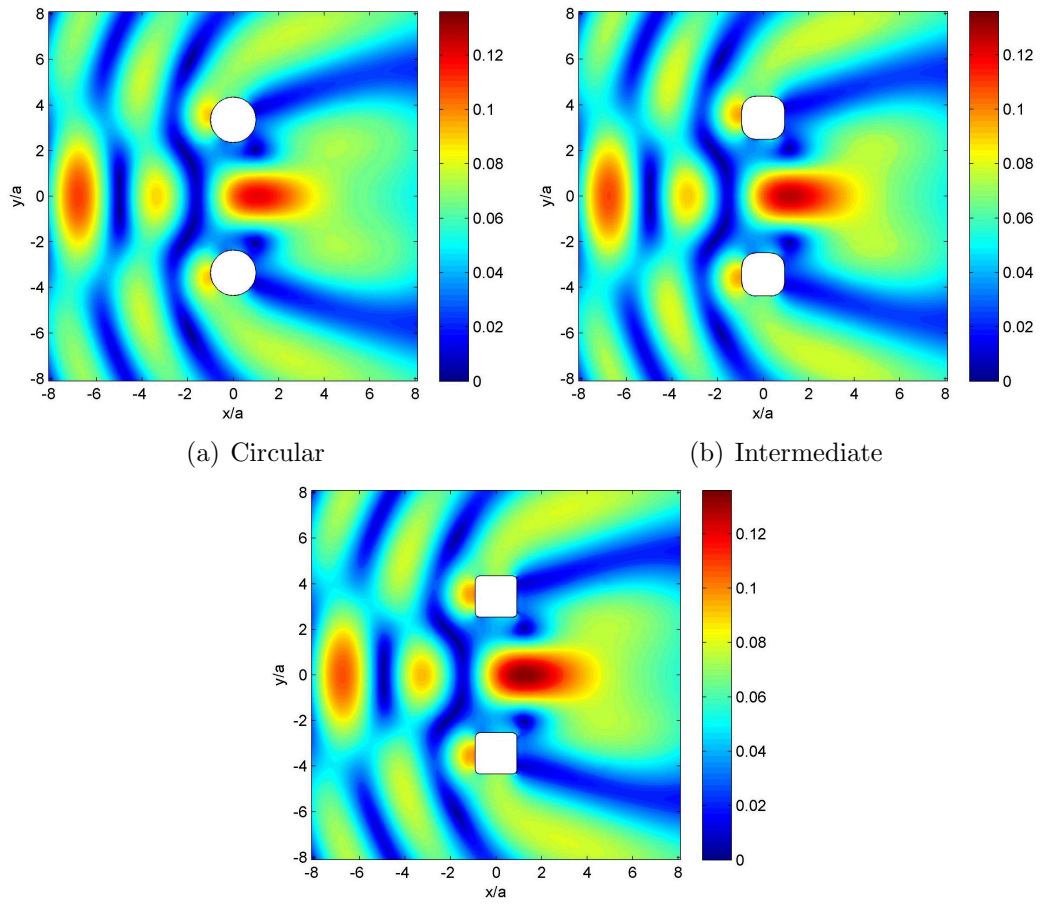

(a) Circular

(b) Intermediate

(c) Square

Figure 4.8: Second-order potential sum surface elevation for pairs of bottom-seated columns of varying cross-section with $\omega = 0.490$ rad/s ($T = 12.816$ s), $\beta = 0\,^{\circ}$.

Table 4.1 shows the maximum amplitude of the $\eta_P^{(2+)}$ elevation component for each of the structures under study. For each column shape, the maximum amplitude increases as the number of columns in the array increases. For both the isolated columns and pairs of columns, the maximum amplitude increases as the squareness of the column cross-section increases. However, for the arrays of four columns, the maximum amplitude in each case is found between the upstream columns, and the case with the highest value is with the intermediate column cross-section. A value of 0.251 for the maximum $\eta_P^{(2+)}$ elevation component with a unit-amplitude regular wave is rather large. Second-order components are proportional to the square of the incident amplitude. For an incident regular wave of amplitude 8 m, the $\eta_P^{(2+)}$ elevation component would be double the incident linear elevation with the intermediate columns in water of finite depth.

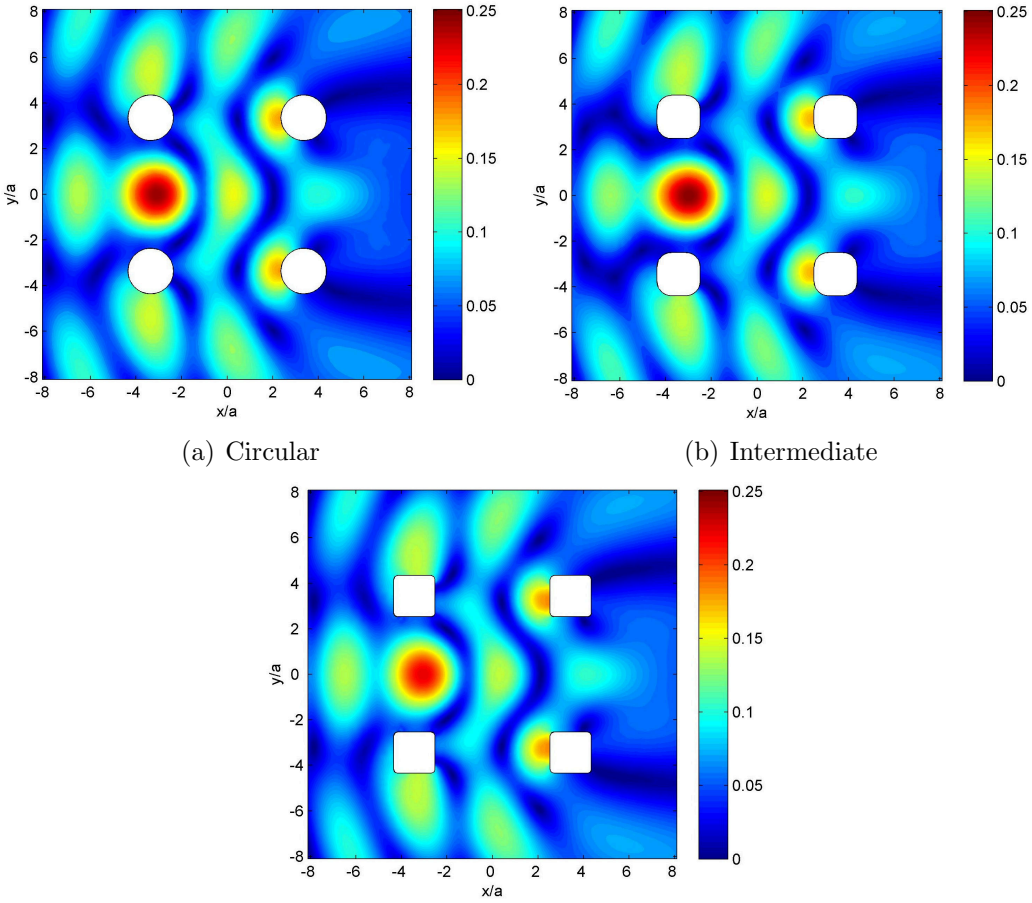

(a) Circular

(b) Intermediate

(c) Square

Figure 4.9: Second-order potential sum surface elevation for square arrays of four bottom-seated columns of varying cross-section with $\omega = 0.490$ rad/s ($T = 12.816$ s), $\beta = 0°$.

Figure 4.9 plots the magnitude of the $\eta_P^{(2+)}$ elevation component in the vicinity of square arrays of four bottom-seated columns for the same incident waves as the previous examples. The general pattern differs very little between the three column shapes but the maximum amplitude varies far more, as shown in Table 4.1. The circular and intermediate column cases have a similar maximum amplitude of approximately 0.25 but the maximum amplitude in the square case is around 10 % less at 0.225.

4.4.3 Multiple columns with pontoons

Figure 4.10 looks at the effect on $\eta_P^{(2+)}$ of extending the water depth and adding pontoons to the now floating structure, though the results presented here assume that the structure does not move but is a locked in place version of Thunder Horse. Figure 4.10(a) shows $\eta_P^{(2+)}$ around four bottom-seated intermediate shaped columns, which was introduced in Chapter 2 as Model 1. Figure 4.10(b) shows $\eta_P^{(2+)}$ around the more realistic Model 3, which is in deep

water and has pontoons. The increase in water depth and addition of pontoons obviously has a large effect on the second-order surface elevation. The main peak is in a similar position for both models but has been reduced in maximum amplitude from 0.225 to 0.174 between Models 1 and 3 respectively. The backwards 'C' shaped peak in the centre of Model 1 has split into three separate peaks with Model 3, and the peaks immediately upstream of the downstream column are almost completely gone.

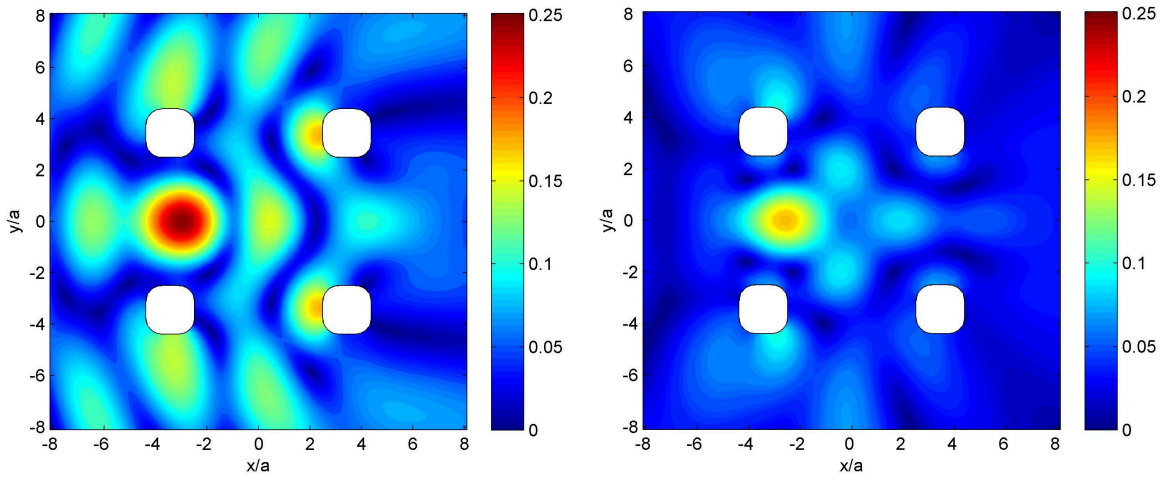

(a) Model 1 (b) Model 3

Figure 4.10: Second-order potential sum surface elevation for Thunder Horse Model 1 in (a) and Model 3 in (b), both with $\omega = 0.490$ rad/s ($T = 12.816$ s), $\beta = 0°$.

One of the aims of this research is to investigate whether linear results can be used to predict more computationally intensive second-order results. Figure 4.11 therefore compares the second-order $\eta_P^{(2+)}$ response of Model 3 for the $\omega = 0.490$ rad/s ($T = 12.816$ s), $\beta = 0°$ case used so far with the linear elevation at the second-order response frequency, $\omega = 0.980$ rad/s ($T = 6.408$ s), $\beta = 0°$. Near-trapped modes for second-order waves are associated with free waves. Free waves obey the dispersion relation and travel at the phase velocity associated with its frequency (for deep water phase velocity $c_p = \frac{g}{2\pi f}$ m/s). Bound waves are the higher harmonic waves formed by wave-wave interactions and generally don't obey the dispersion relation. They travel at the phase velocity of the 0^{th} harmonic, moving with the wave group rather than with their free phase velocity. During wave-structure interactions, free scattered waves at second-order sum frequencies can lead to near-trapping if that sum

frequency corresponds to an incident wave that would linearly excite a near-trapped mode.

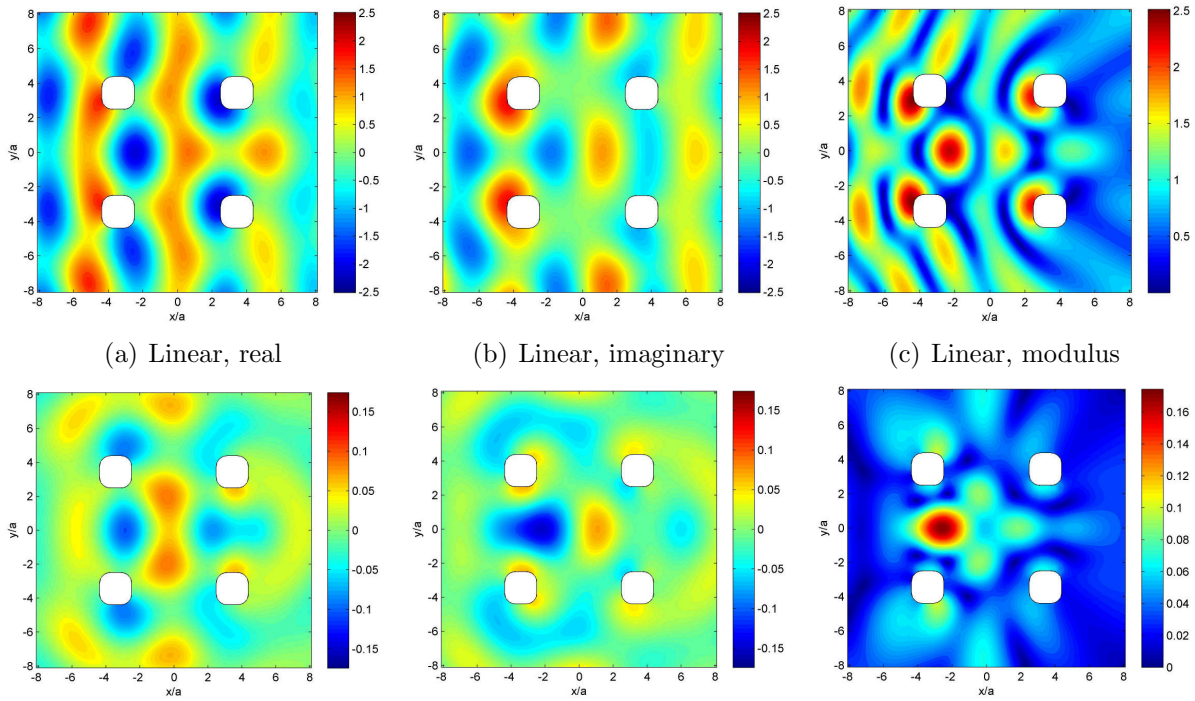

(a) Linear, real (b) Linear, imaginary (c) Linear, modulus

(d) Second-order, real (e) Second-order, imaginary (f) Second-order, modulus

Figure 4.11: Linear (a-c) and second-order potential sum (d-f) excitation of a near-trapped mode with Thunder Horse Model 3 and $\omega_R = 0.980$ rad/s ($T = 6.408$ s), $\beta = 0°$.

Figure 4.11(a-c) shows the real and imaginary components, and the modulus of these, of the linear elevation for an incident wave of $\omega = 0.980$ rad/s and Figure 4.11(d-f) shows the real and imaginary components, and the modulus of these, of the $\eta_P^{(2+)}$ elevation for an incident wave of $\omega = 0.490$ rad/s. There are definite similarities between the linear and second-order excitation cases shown here but the introduction of pontoons obviously had a much greater effect at second-order than at first-order. The linear excitation pattern is very similar to the equivalent second-order results for the bottom-seated column cases shown in Figure 4.9.

Figure 4.12 shows a second comparison between linear and second-order excitation of near-trapped modes, now at a lower near-trapped frequency of $\omega_R = 0.829$ rad/s ($T = 7.582$ s) and wave direction $\beta = 45°$. These figures are more similar for the two excitation frequencies, particularly within the array, although there are still obvious differences between

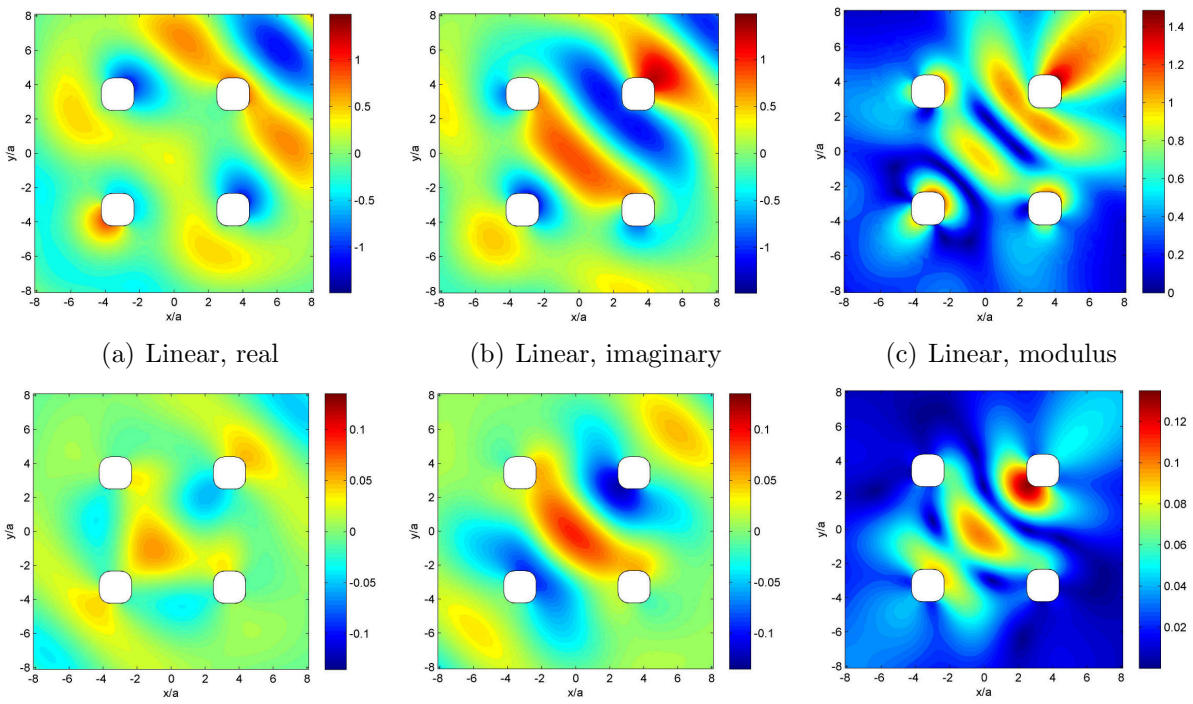

(a) Linear, real (b) Linear, imaginary (c) Linear, modulus

(d) Second-order, real (e) Second-order, imaginary (f) Second-order, modulus

Figure 4.12: Linear (a-c) and second-order potential sum (d-f) excitation of a near-trapped mode with Thunder Horse Model 3 and $\omega_R = 0.829$ rad/s ($T = 7.582$ s), $\beta = 45°$.

them. These figures show that linear results can be useful in giving predictions of where the largest second-order responses will be and in giving a general idea of the expected second-order diffraction pattern, but for a structure as complicated as Thunder Horse they cannot be relied upon to give an accurate description of the spatial structure of the local wave field.

Near-trapped mode excitation

The results presented so far in this section have all been at the same frequency when making comparisons between the different column shapes and arrays, and the same response frequency was used for comparisons between linear and second-order results. However, it was shown in Chapter 2 that the different geometries lead to slightly different near-trapped frequencies. This section investigates whether the geometrical differences that changed the linear near-trapped frequencies for each column shape will cause greater differences at second-order or whether the near-trapped mode response frequency will be fixed for each column shape regardless of how it is excited. Figure 4.13 looks at finding the near-trapped frequency through both linear and second-order excitation for the Thunder Horse type Model 3 at the highest near-trapped mode where convergence was achieved. These high frequencies were

used because it was shown in Chapter 2 that for lower frequencies the effect of structure geometry has less of an effect.

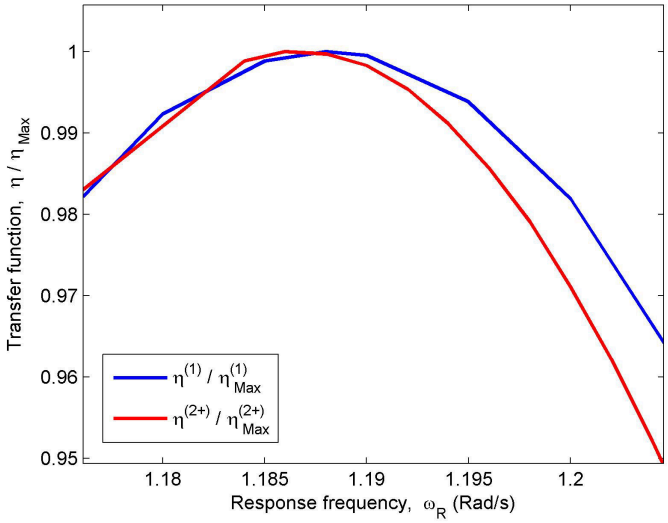

Figure 4.13: Linear and second-order potential sum transfer functions versus response frequency with $\beta = 45\,^{\circ}$. Each transfer function is normalised by its maximum value.

The response frequency for the near-trapped mode is extremely close in both cases with values of 1.189 rad/s and 1.187 rad/s for linear and second-order excitation respectively. This confirms that the geometry determines the response frequency for near-trapped modes but the method of excitation has no effect. These two near-trapped frequencies are a little different from the value of 1.205 rad/s predicted with four bottom-seated circular columns but considering the change in column shape, the addition of pontoons, and the extension to deep water, the simple analytical prediction gives a very good approximation.

4.5 Second-order mode shapes

The near-trapping phenomenon for arrays of closely spaced columns and methods of predicting their associated mode shapes were discussed in Chapter 2. In this section, comparisons are made between the shapes of modes that are excited linearly and through second-order interactions. The aim of this comparison is to determine whether linear calculations, that are quick and cheap computationally, can be used to predict the shape of responses at second-

order, which are far more computationally intensive. The modes that were excited linearly in Section 2.6 are now excited through second-order interactions and the results are compared. The simple model of four bottom-seated columns is used to allow direct comparison with the results of Section 2.6.

Incident waves with angular frequencies equal to half those of the linear cases were used. For a second-order sum response to these new incident waves, frequency doubling would lead to an excitation at the same response frequency as the identified near-trapped modes. For example, the first case looked at in Section 2.6 (Figure 2.18) was excited linearly by an incident wave of $\omega = 0.980$ rad/s, $\beta = 0°$. Second-order excitation by incident waves of $\omega = 0.490$ rad/s ($T = 12.816$ s), $\beta = 0°$ would lead to a response at the same frequency as the

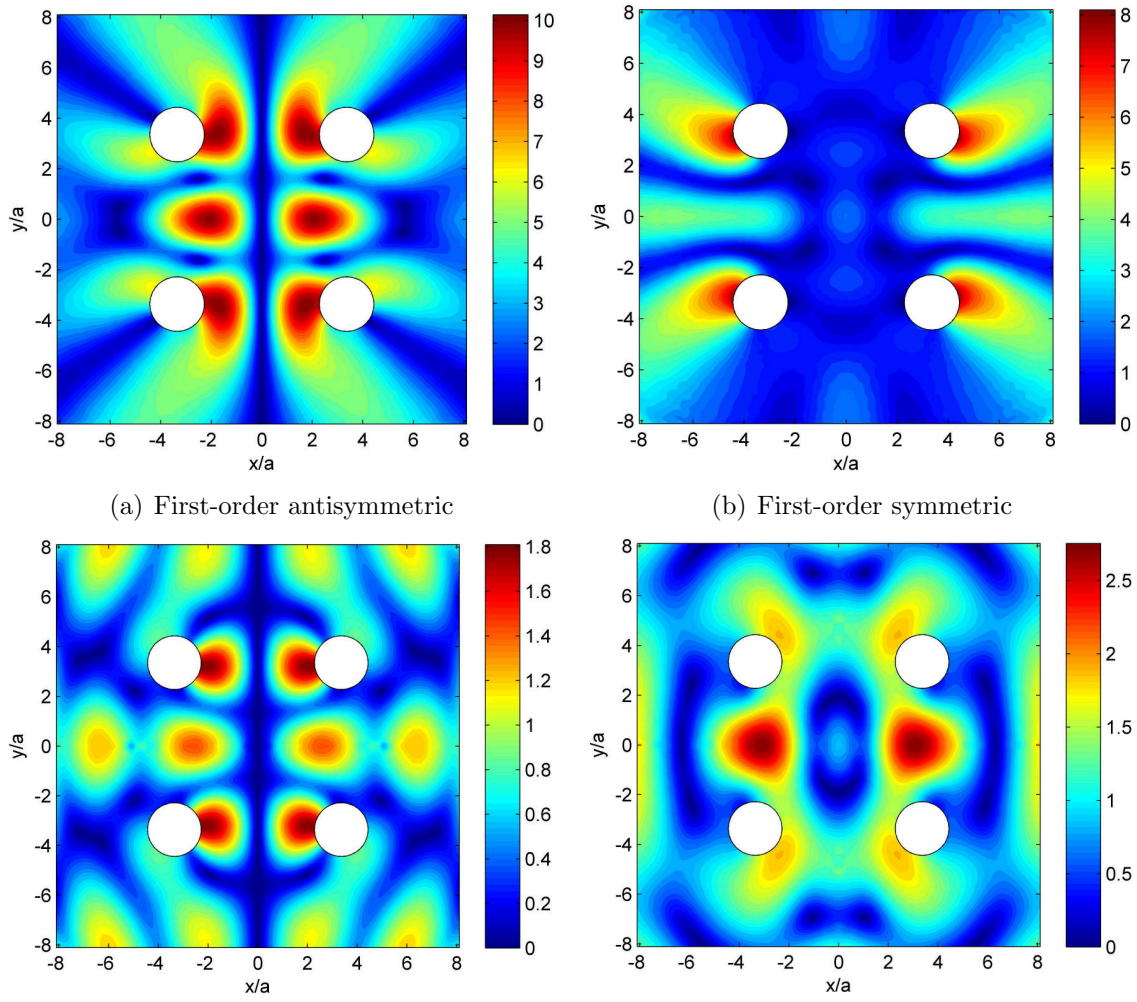

(a) First-order antisymmetric

(b) First-order symmetric

(c) Second-order antisymmetric

(d) Second-order symmetric

Figure 4.14: Comparison of symmetric and antisymmetric diffraction patterns for a near-trapped mode with first- and second-order excitation and four bottom-seated circular columns for a response angular frequency $\omega = 0.980$ rad/s ($T = 6.408$ s), $\beta = 0°$.

first case, $\omega = 0.980$ rad/s ($T = 6.408$ s).

Figure 4.14 compares the symmetric and antisymmetric components of both the first- and second-order excitation of this mode. For this second-order case it is less obvious as to whether a symmetric or antisymmetric standing wave dominates. Figures 4.14(c) and 4.14(d) show the antisymmetric and symmetric components respectively with both having complicated response patterns within the array. On first glance it appears that a combination of the antisymmetric and symmetric components would generate a pattern very similar to that excited linearly in Figure 4.14(a). Figure 4.14(c) seems a little closer to the linear pattern than the symmetric Figure 4.14(d) but the symmetric plot has a 50 % larger maximum response than the antisymmetric plot. Given the antisymmetric nature of the mode shape when excited linearly, perhaps Figure 4.14(d) represents some excitation of a different mode. One of the reasons that makes this method approximate is that all modes are excited to some extent by an incident wave and so the method is reliant on the response at peak frequency being sufficiently dominant to render any responses due to modes with peak responses at other frequencies negligible.

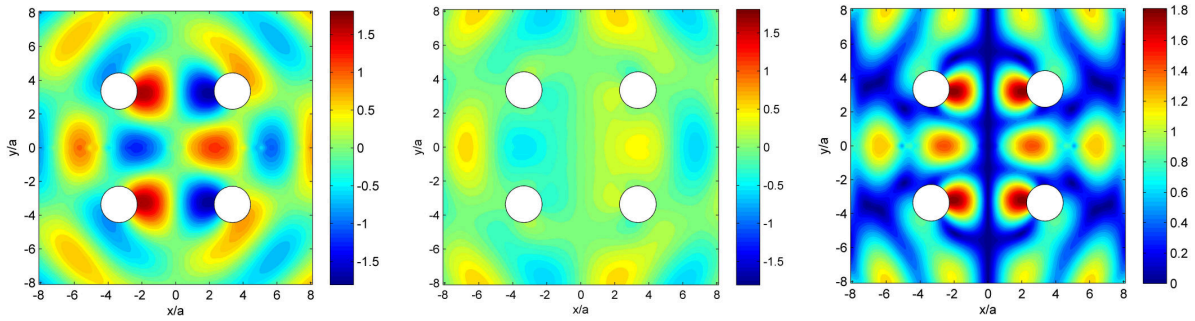

(a) Real (b) Imaginary (c) Modulus

Figure 4.15: Antisymmetric diffraction pattern for a near-trapped mode with second-order excitation and four bottom-seated circular columns for an incident angular frequency $\omega = 0.490$ rad/s ($T = 12.816$ s), $\beta = 0°$.

Figures 4.15 and 4.16 show the real and imaginary components, and the modulus of these, of the antisymmetric and symmetric components of the second-order response to incident waves of $\omega = 0.490$ rad/s, $\beta = 0°$. Figure 4.15 looks closest to the linear response but with reduced amplitude in the middle pair of peaks and larger radiated pulses along the positive and negative x-axes.

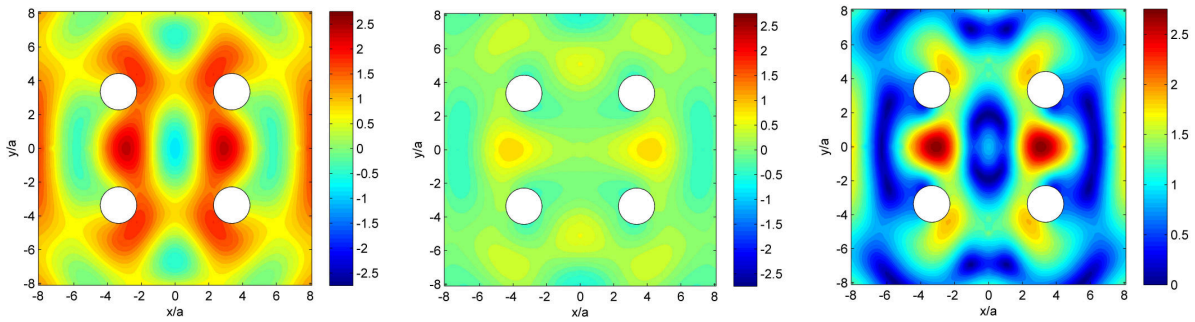

(a) Real (b) Imaginary (c) Modulus

Figure 4.16: Symmetric diffraction pattern for a near-trapped mode with second-order excitation and four bottom-seated circular columns for an incident angular frequency $\omega = 0.490$ rad/s ($T = 12.816$ s), $\beta = 0°$.

Figure 4.17 plots the real and imaginary components, and the modulus of these, of the mode shape for a near-trapped mode with an incident angular frequency of $\omega = 0.414$ rad/s ($T = 15.164$ s) at $\beta = 45°$ and shows a very similar ($\mp\pm$) oscillating pattern to the linear results in Figure 2.23, which was excited by an incident wave with $\omega = 0.829$ rad/s ($T = 7.582$ s). Within the array, the two mode shapes are almost identical. The main differences are that the pulses being radiated away from the array are increased in amplitude relative to the inner peaks and have merged from the pairs of pulses in the linear case into single elongated pulses in the second-order case.

Figure 4.18 shows the mode shape excited by a wave with an incident angular frequency of $\omega = 0.713$ rad/s ($T = 8.818$ s) at $\beta = 45°$. This mode shape is not as close to its first-order equivalent as seen in the previous simpler case. This is to be expected for such a complicated pattern. On first appearances Figures 4.18(a) and 2.24(a) seem quite different. However,

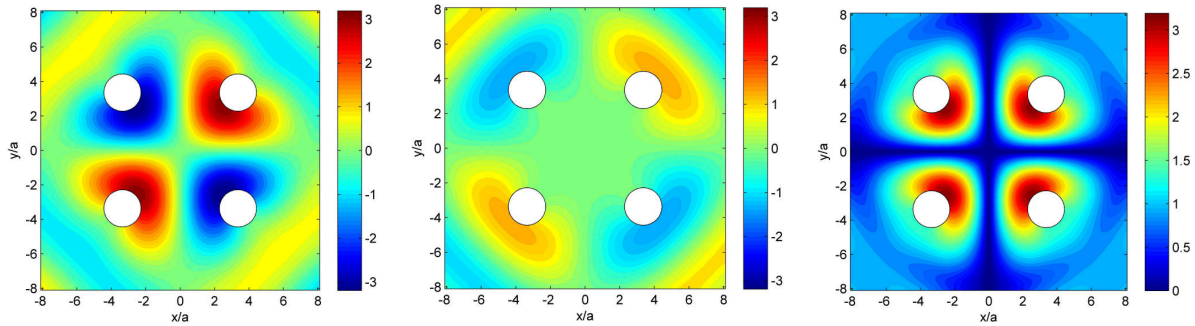

(a) Real (b) Imaginary (c) Modulus

Figure 4.17: Mode shape for a near-trapped mode with second-order excitation and four bottom-seated circular columns for an incident angular frequency $\omega = 0.414$ rad/s ($T = 15.164$ s), $\beta = 45°$.

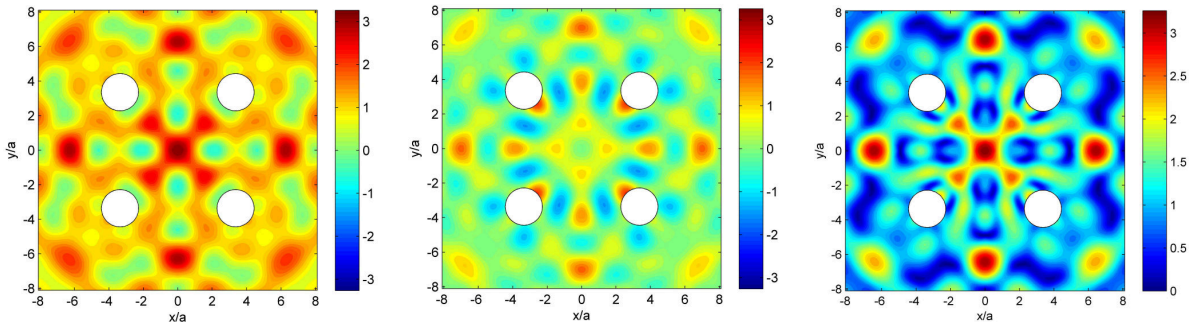

(a) Real (b) Imaginary (c) Modulus

Figure 4.18: Mode shape for a near-trapped mode with second-order excitation and four bottom-seated circular columns for an incident angular frequency $\omega = 0.713$ rad/s ($T = 8.818$ s), $\beta = 45\,°$.

on closer inspection the patterns still show some similarities. There is a high central peak surrounded by four peaks and four troughs in the centre of the array, and there are peaks on the inside edges of the four columns that are 180° out of phase with the central peak and a 'C' shaped band surrounding the inside of each column. The mean level in Figure 4.18(a) is higher than the first-order case and the pulses radiating out along the x- and y-axes are higher than in the first-order case.

Figure 4.19 compares the modulus field plots of first- and second-order excitations of four near-trapped mode shapes with incident angles of $\beta = 45\,°$. The four pairs of plots represent modes with response angular frequencies increasing by approximately 0.2 rad/s for each pair, starting and ending with the two modes discussed previously that have the smallest predicted imaginary wavenumber component. Looking at just the linear responses, Figure 4.19(a,c,e,g), there is a clear progression in the mode patterns as frequency increases. This is to be expected as they are all exciting a standing wave within the same geometry but for decreasing wavelengths. When looking at the first- and second-order pairs with the same response frequency there are definite similarities between each pair of plots but the level of similarity seems to decrease with frequency. This is also to be expected given the highly complex nature of the mode shapes at the higher frequencies. For low frequency near-trapped modes, linear calculations can give a good prediction of the second-order sum response pattern for arrays of circular columns.

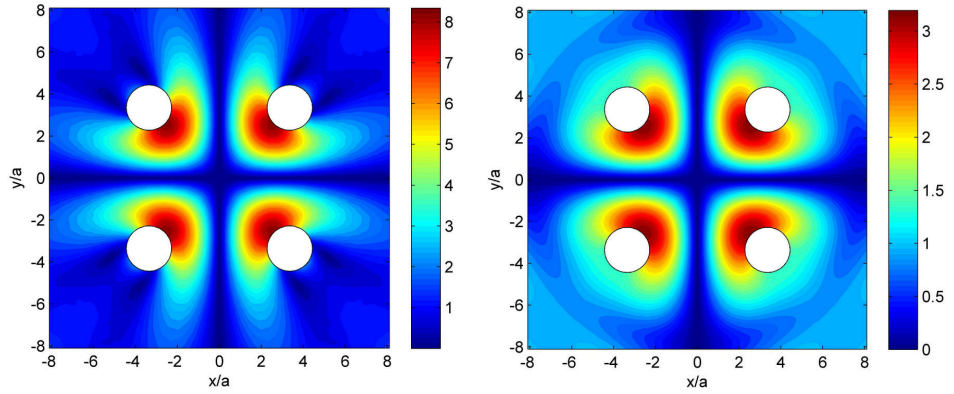

(a) 1st-order, Incident ω =0.829 rad/s (b) 2nd-order, Incident ω =0.414 rad/s

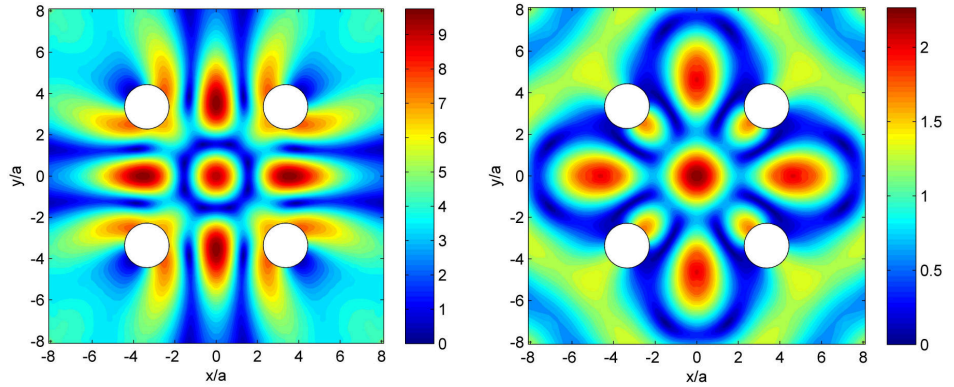

(c) 1st-order, Incident ω =1.072 rad/s (d) 2nd-order, Incident ω =0.5036 rad/s

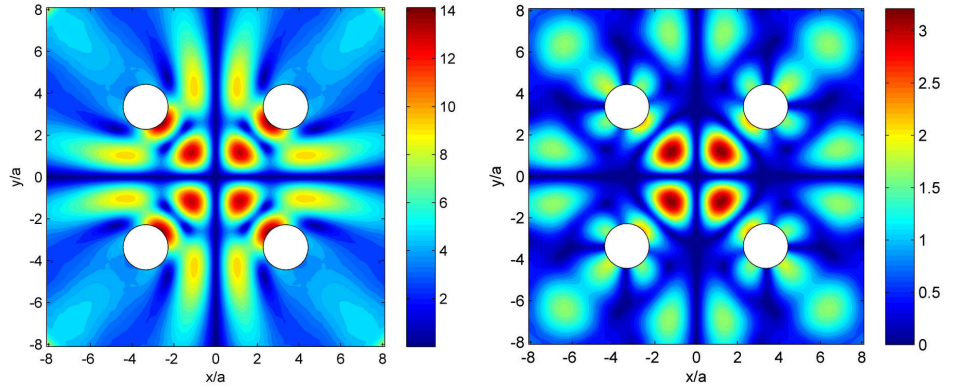

(e) 1st-order, Incident ω =1.205 rad/s (f) 2nd-order, Incident ω =0.602 rad/s

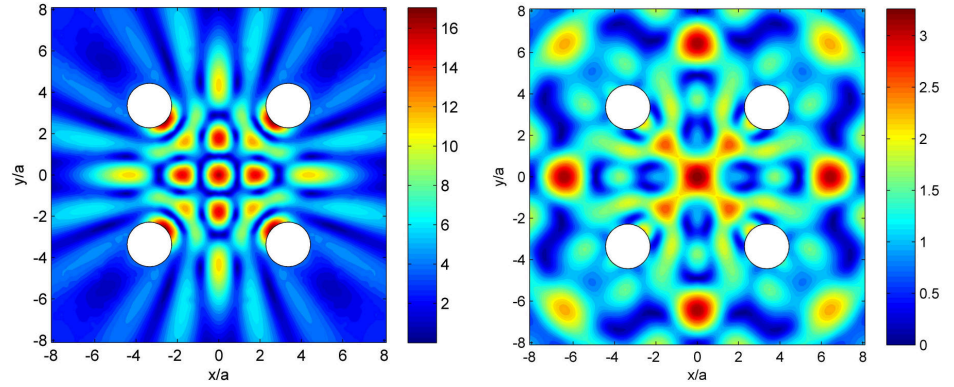

(g) 1st-order, Incident ω =1.425 rad/s (h) 2nd-order, Incident ω =0.713 rad/s

Figure 4.19: Comparison of first- and second-order excitation of mode shapes for near-trapped modes of increasing frequency with four bottom-seated circular columns, $\beta = 45°$.

4.6 QTF structure

The calculation of QTFs can be very computationally intensive, requiring a calculation at all frequency pairs, (ω_i, ω_j), needed to model a random sea state. Due to the high computation time of each calculation one can find the minimum number of frequency components to characterise the QTF behaviour, e.g. N = 10-15, and then interpolate between these. One can use symmetry in the QTF structure to reduce the number of calculations from N^2, where N is the number of frequency components in the incident spectrum, to $N(N+1)/2$. This is because for the second-order sum terms, $QTF(\omega_i, \omega_j) = QTF(\omega_j, \omega_i)$, and for second-order difference terms, $QTF(\omega_i, \omega_j)$ is the complex conjugate of $QTF(\omega_j, \omega_i)$. One therefore only needs to calculate the terms on, and to one side of, the leading diagonal. If $N = 13$ then the number of calculations can be reduced from 169 to 91 with use of the QTF symmetry. By making certain assumptions one can then reduce this even further to just N calculations.

This can be done by assuming that for each pair of frequencies adding to the same response frequency the QTF is constant. For a frequency pair (ω_i, ω_j) the second-order sum response frequency is at $\omega_R = \omega_i + \omega_j$. With the flat QTF approximation, the QTF for this pair would be equal to the QTF at $(\omega_R/2, \omega_R/2)$ which is on the leading diagonal. Therefore when QTFs are plotted against the two incident frequency components, this method of approximation would make the QTFs flat perpendicular to the leading diagonal. Taylor et al. (2007) showed why this is a good approximation at low frequencies. The following figures plot QTFs for the Thunder Horse Model 3 and suggest that these approximations are reasonable.

Figure 4.20 plots the potential sum surface elevation QTFs for each pair of incident frequency components in the range $0.12 \leq \omega_i, \omega_j \leq 0.6$ for a wave direction of $\beta = 45°$. QTFs are calculated at two locations within the array, both of which have previously been shown to give large responses at certain near-trapped modes. The locations used are (12,12) m and (32,32) m, where the origin is at the centre of the array and $\beta = 45°$ for both cases. Figure 4.20(a) shows the QTFs at a location of (12,12) m within the array, which has been shown to have a large response at the linear near-trapped period of $T = 7.582$ s, and Figure

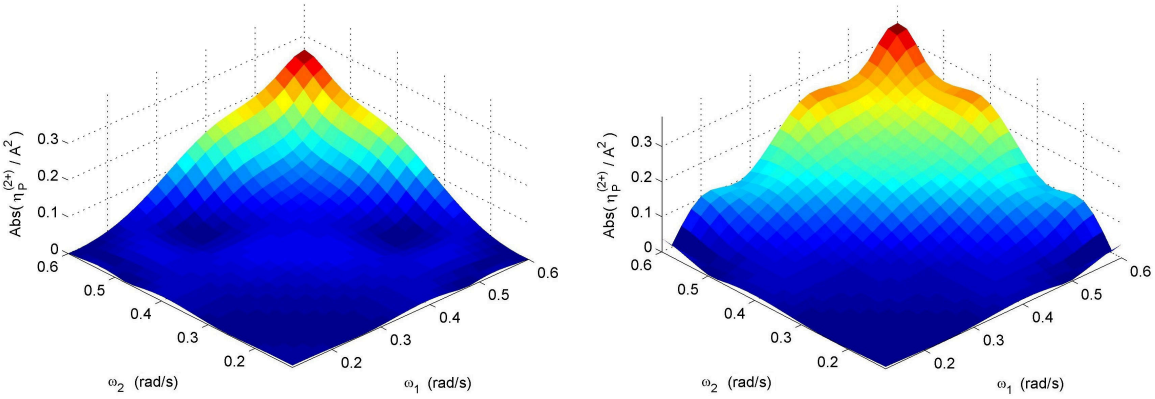

(a) $x = 12$ m, $y = 12$ m (b) $x = 32$ m, $y = 32$ m

Figure 4.20: Magnitude of the potential sum surface elevation QTFs against incident frequencies for Model 3 with $0.12 \leq \omega_i, \omega_j \leq 0.6$ rad/s, $\beta = 45°$, and (a) $x = 12$ m, $y = 12$ m, (b) $x = 32$ m, $y = 32$ m.

4.20(b) shows the QTFs just upstream of the downstream column at a location of (32,32) m, which has been shown to have a large response at the linear near-trapped period of $T = 5.215$ s. Both modes should be excited at second-order within the range of frequencies covered in Figure 4.20.

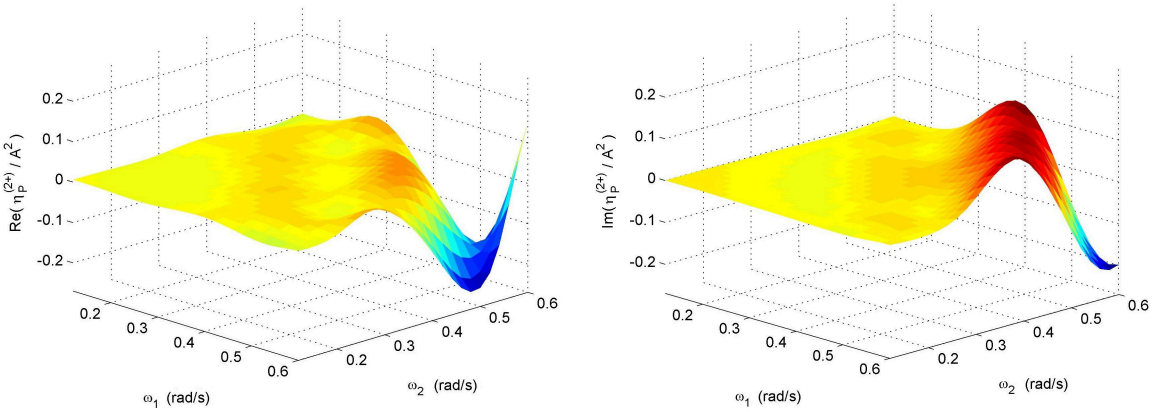

(a) Real (b) Imaginary

Figure 4.21: Components of the potential sum surface elevation QTFs against incident frequencies for Model 3 with $0.12 \leq \omega_i, \omega_j \leq 0.6$ rad/s, $\beta = 45°$, and $x = 12$ m, $y = 12$ m.

Figure 4.21 plots the real and imaginary components of the $x = 12$ m, $y = 12$ m case. Plotting the components shows clearly a ridge of high amplitude running perpendicular to the leading diagonal at a response frequency around 0.85 rad/s corresponding to the near-trapped mode of $T = 7.582$ s. There is perhaps another less obvious excitation of a

near-trapped mode at the lower response frequency of 0.75 rad/s, which matches a near-trapped mode at $T = 8.330$ s. Within the frequency range shown it is clear that assuming QTFs are flat perpendicular to the leading diagonal is a reasonable approximation.

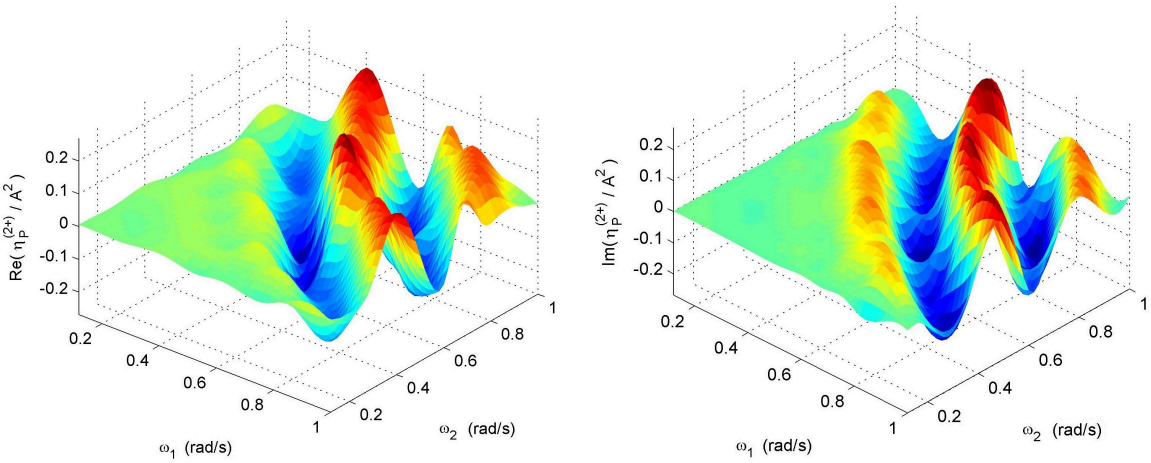

(a) Real

(b) Imaginary

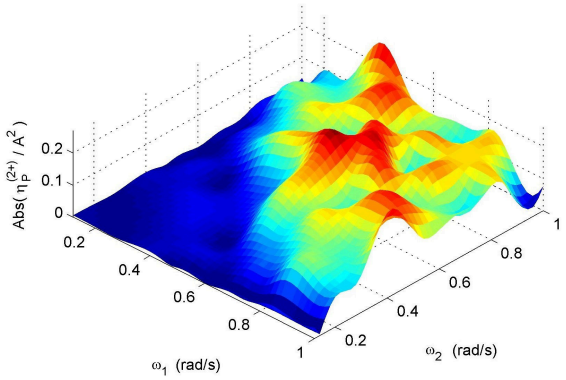

(c) Modulus

Figure 4.22: Components of the potential sum surface elevation QTFs against higher incident frequencies for Model 3 with $0.12 \leq \omega_i, \omega_j \leq 1$ rad/s, $\beta = 45°$, and $x = 12$ m, $y = 12$ m.

Figure 4.22 now extends the range of frequencies covered to $0.12 \leq \omega_i, \omega_j \leq 1$ rad/s for the real and imaginary components, and the modulus of these, of the potential sum QTF. It is immediately clear that at the higher frequencies there is more variation perpendicular to the leading diagonal. However, there are still very distinct ridges in the real and imaginary components, showing a further two near-trapped modes being excited at response frequencies around 1.4 rad/s and 1.8 rad/s. The 1.4 rad/s near-trapped mode matches well with the 5.215 s mode identified for the structure and the 1.8 rad/s mode goes beyond the predictions

made in Chapter 2. The approximation of assuming flat QTFs perpendicular to the leading diagonal is clearly less accurate at higher frequencies but can still be a reasonable alternative to the lengthy process of calculating the full QTF matrix.

It has been shown so far that for low frequencies and the Thunder Horse Model 3, the surface elevation QTFs for wave-structure interactions were approximately constant perpendicular to the leading diagonal. Further away from the leading diagonal and at higher frequencies this approximation becomes less reliable, but a JONSWAP spectrum has a high concentration of energy around the peak frequency. For second-order responses, the QTFs such as those shown in Figure 4.22 are used to modify the product of each pair of incident spectral components. By multiplying the incident spectral components the concentration of energy around the spectral peak is increased, and as one moves away from this spectral peak the amount of spectral energy quickly decreases. This is shown in Figure 4.23 which plots the spectral energy distribution, $S_i S_j$, for each frequency pair, (ω_i, ω_j), in an incident JONSWAP spectrum with a peak period of $T = 15.164$ s.

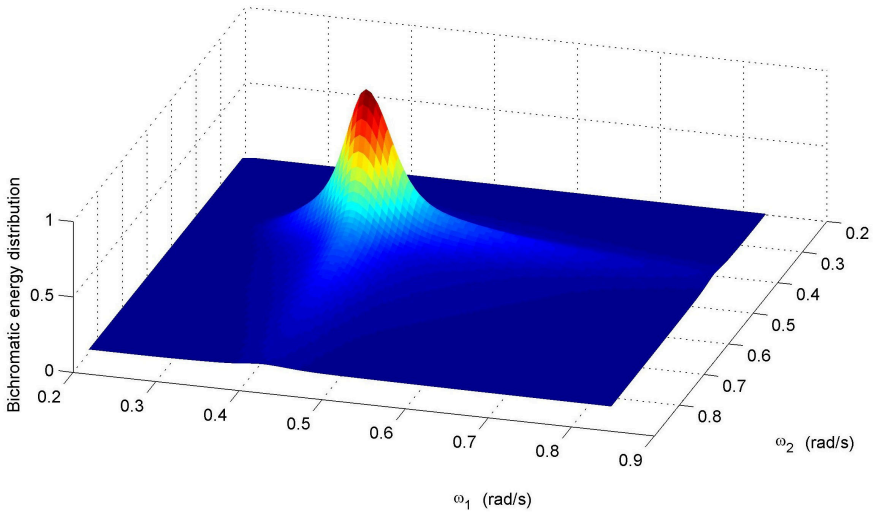

Figure 4.23: Spectral energy distribution at second-order for an incident JONSWAP wave with a peak period of $T = 15.164$ s.

The distribution has been normalised by the maximum amplitude to give a peak of unit amplitude at $\omega_i = \omega_j = 0.414$ rad/s. At frequencies 10 % either side of the peak the spectral energy has dropped by approximately 50 %. Further away from the peak there is an 'x'

shape of increased amplification along the two lines $\omega_1 = \omega_p$ and $\omega_2 = \omega_p$. By the edge of the plot, these lines of increased energy have been reduced to less than 3 % of the peak energy and away from those lines of increased amplitude the spectral energy has been reduced to less than 1 %. The weighting is so strong near the peak frequency that pairs only a short distance away from the peak will have little effect.

To further illustrate that only the QTFs close to the peak frequency are important, Figure 4.24 combines the spectral energy distribution from Figure 4.23 with the potential sum QTF magnitude at (12,12) m from Figure 4.22. The white areas in Figure 4.24 represent frequency pairs where the spectral energy is less than 5 % of the maximum value. The coloured areas show contours of the magnitude of the potential sum QTF where the spectral energy is greater than 5 % of the maximum value. The number of frequency pairs with more than 5 % of the maximum spectral energy is fairly small. Most of these pairs are centred about the peak, (ω_p, ω_p), with two extensions of the plotted area along the lines $\omega_1 = \omega_p$ and $\omega_2 = \omega_p$. This shows that assuming the QTFs are completely flat perpendicular to the leading diagonal can be a useful approximation to save time on the computationally intensive calculation of QTFs if the peak frequency is fairly low. It also shows that when using incident JONSWAP spectra, a cutoff at $\omega_{max} = 2\omega_p$ can be used without too much loss of spectral energy. Compared to the total energy in a spectrum with a cutoff at $\omega_{max} = 10\omega_p$, the loss in energy is less than 5 %.

4.7 Conclusions

Conclusions drawn from the results presented in this chapter are briefly summarized below.

- Changing column cross-section shape causes similar effects to second-order response elevation patterns as it did at first-order.
- For a given column cross-section, mode shape response frequencies are very similar for both first- and second-order excitation.
- The addition of pontoons can have a large effect on the second-order potential sum response pattern.

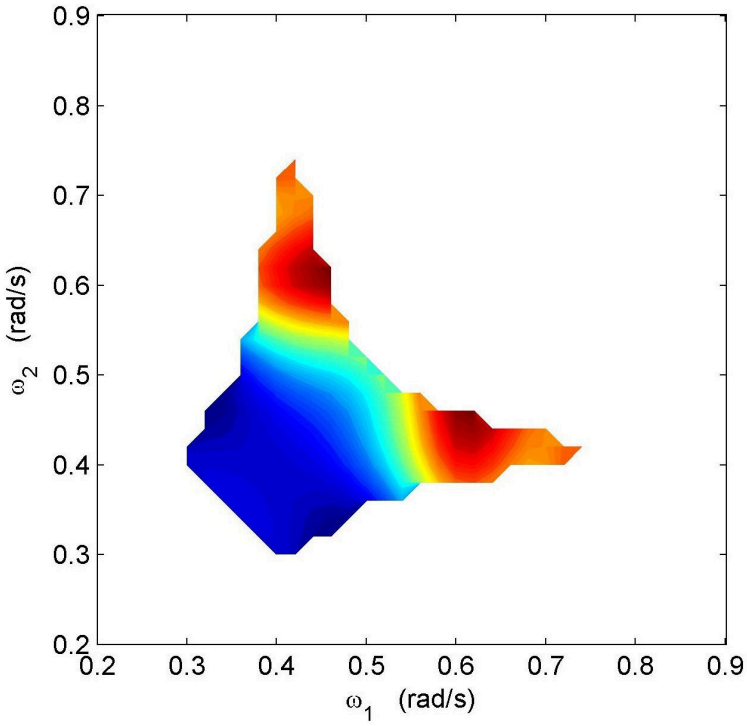

Figure 4.24: Second-order potential sum QTFs at frequency pairs with more than 5 % of the maximum spectral energy for an incident JONSWAP wave with a peak period of $T_p = 15.164$ s.

- Linear mode shape calculations give a good approximation of the second-order sum response for low frequency near-trapped modes and four circular bottom seated columns.
- Assuming QTFs are flat perpendicular to the leading diagonal is a reasonable approximation for use with a JONSWAP spectrum if the peak frequency is low and only the first few of the near-trapped modes are excited.

Chapter 5

Second-order statistics of response

5.1 Introduction

This chapter aims to build on the work of Chapter 3 by extending the collection of statistics of response to include both linear and second-order interactions. It has been shown previously that second-order components can contribute a significant proportion of the total surface elevation during wave-structure interaction. This chapter aims to present more accurate predictions for the maximum expected water projection than would be achieved by limiting the results to linear components. An assessment will be made of how far the predictions are changed by the inclusion of second-order results.

There are various possible approaches to obtain these statistics, including those proposed by Tromans, Winterstein, and Naess. The Tromans method, see Tromans et al. (1992), incorporates a weakly non-linear wave model into a spectral response surface method for broadbanded, unidirectional, deep-water sea states. To avoid lengthy time-domain simulations, all of the calculations are performed in the probability domain. A transfer function is found to account for the presence of the structure, relative to open ocean, and its effect on wave surface elevation. This transfer function is then applied to the open ocean surface elevation pdf to transform it into a pdf describing the response surface elevation. A numerical search is then carried out in probability space to find the Fourier representation of the most probable time history for the specified level of system response. (This is a first-order

reliability FORM method). The Winterstein method, see Jha and Winterstein (2000), uses water-depth dependent analytic formulae to predict the skewness and kurtosis of nonlinear random waves. The Hermite model is used to predict the wave elevation and crest heights with specified return periods. The Naess method, see Naess (1985), expresses extreme responses in terms of a second-order Volterra series (including a linear and a quadratic term). The mean upcrossing frequency is then found, and asymptotic expressions are used to obtain closed-form solutions to the extreme-value problem.

A brute force method is also possible using the linear and quadratic transfer functions (LTFs and QTFs) discussed previously. Until recently, a purely brute force method has been considered impractical for regular use (Naess et al. (2008), Sagrilo et al. (2011)) but definitely of use in validating any other method used. Since a linear brute force method was developed for validation in Chapter 3, it seemed logical to adapt this method for second-order calculations. It was found that given the nature of the statistics being obtained, the majority of calculations can take place in the frequency domain with just a single inverse FFT to then obtain the associated time history. This meant that once the LTFs and QTFs had been calculated for a structure, the computation time needed for a brute force method might not be much less efficient than some of the other methods suggested above. On a PC with a 2.2GHz processor with 6Gb RAM it takes approximately one hour to generate 10^7 s of random response time history. It therefore seemed more efficient to use the brute force method than to take the time to implement one of the more complex methods mentioned above for only a small reduction in computation time.

5.2 Second-order response

The generation of linear random spectra based on a specified sea state was validated and discussed in Chapter 3. These spectra were then used as the incident field for investigations into wave-structure interactions by convoluting them with linear transfer functions (LTFs). This chapter extends the analysis to second-order by modifying the incident waves with quadratic transfer functions (QTFs) and adding these responses to the linear component. To validate the extension of this method to second-order, a variety of spectra with known

responses were used as incident waves in the open ocean and the QTFs were based on second-order wave-wave interactions. These incident wave transfer functions were found using the method of Forristall (2000) (see also Sharma and Dean (1979) and Dalzell (1999)).

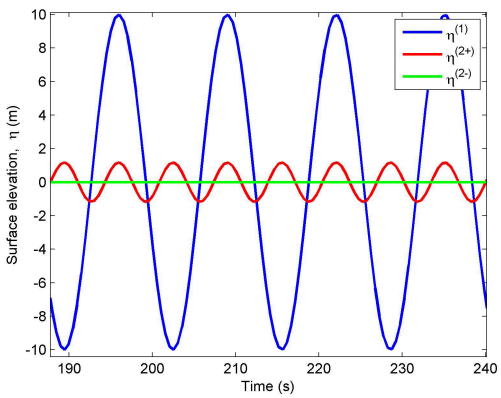

(a) One sine wave

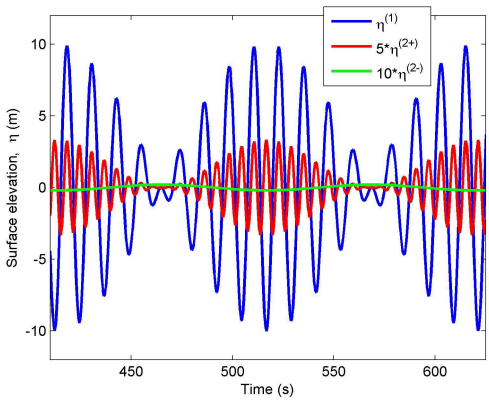

(b) Two sine waves

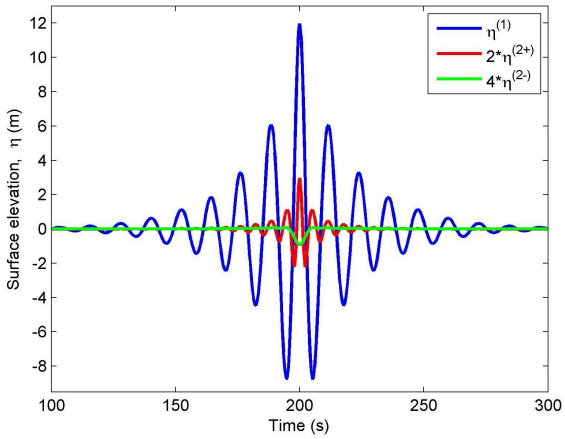

(c) NewWave focused at time $t = 200$ s

Figure 5.1: Surface elevation time histories for three spectra: (a) one sine wave with amplitude 10 m and $\omega = 0.4803$, (b) two sine waves each with amplitude 5 m and $\omega = 0.4803$ and 0.5411 rad/s, (c) a NewWave with $\omega_p = 0.5236$ rad/s, focused at time $t = 200$ s. The blue lines are $\eta^{(1)}$, red lines are $\eta^{(2+)}$, and the green lines are $\eta^{(2-)}$.

Figure 5.1 shows surface time histories for three incident spectra. In Figure 5.1(a) there is a single linear sine wave with amplitude 10 m and $\omega = 0.4803$ rad/s, and in Figure 5.1(b) there is a pair of linear sine waves with $\omega = 0.4803$ & 0.5411 rad/s and amplitude 5 m each. In Figure 5.1(c) there is a NewWave with peak frequency $\omega_p = 0.5236$ rad/s ($T_p = 12$ s) focused at time $t = 200$ s. In each figure the blue line shows the first-order surface elevation, the red line shows the second-order sum component, and the green line shows the second-

order difference component. The second-order components have been scaled up (see figure legends) to aid comparison with the first-order time history.

The second-order sum component in Figure 5.1(a) is at double the frequency of the linear component, with an amplitude that matches up with the Stokes expansion value of $\frac{1}{2}k_pA^2$, where A is the amplitude of the linear component and k_p is the wavenumber at the peak of the spectrum. For the pair of sines (Figure 5.1(b)), the second-order sum response is again at double the frequency of the linear elevation and the second-order difference term shows a long sine wave with a period of 103.3 s. This gives a frequency of 0.0608 rad/s which is equal to the difference in the incident linear components. Figure 5.1(c) shows that the second-order sum elevation is a NewWave shaped packet and that the second-order difference term is a set down centred at the same time as the other two components, $t = 200$ s. The amplitude of the second-order component is close to the Stokes approximation of $\frac{1}{2}k_pA^2$, as expected.

After verifying the accuracy of second-order terms found for simple spectra such as those in Figure 5.1, the code could then be used to analyse random spectra that were produced using the method of Section 3.4.1. Figure 5.2(a) shows an example of a time history generated from a random spectrum. The random spectrum was based on a JONSWAP spectrum with a peak period of 12 s and a ramp down to zero at three times the peak frequency. The blue line plots the linear component of the surface elevation, the red line is the second-order sum component, and the green line is the second-order difference term.

Figure 5.2(b) highlights a few periods of this time history with the second-order sum and difference components scaled by factors of four and six respectively. This section of the time history shows two NewWave like packets. On the left there is a packet similar to a sine wave based NewWave focused at time $t = 478$ s, and on the right there is a packet similar to a cosine based NewWave trough focused at time $t = 520$ s. The second-order sum components are also NewWave like packets, trough focused on the left and crest focused on the right. This phase difference is to be expected because a sine wave based NewWave is 90° out of phase with a cosine based one. The second-order sum response will then add this 90°

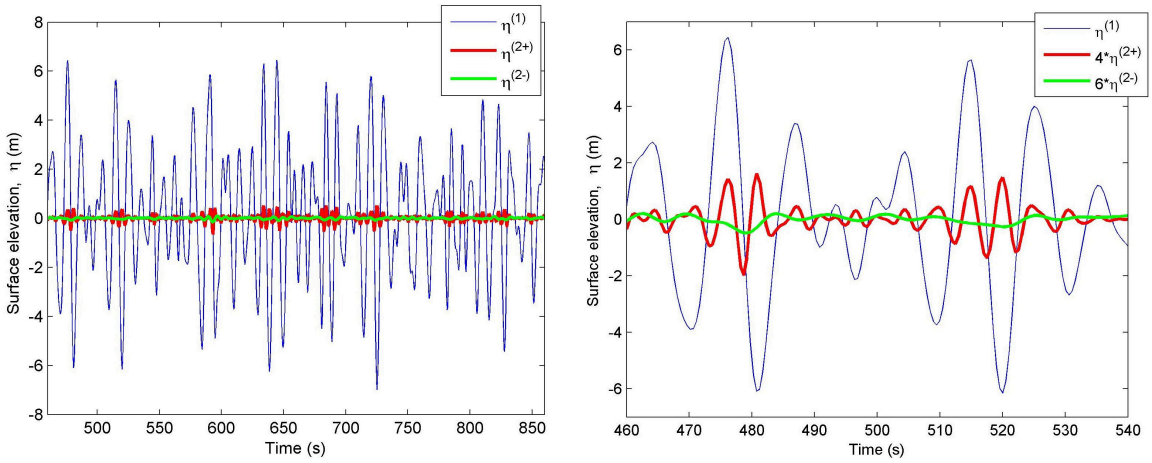

(a) Actual size (b) Scaled second-order components

Figure 5.2: Surface elevation time histories for a random spectra: (a) $t = 460 - 860$ s with no scaling, (b) $t = 460 - 540$ s with scaling (see legend). The blue line is $\eta^{(1)}$, the red line is $\eta^{(2+)}$, and the green line is $\eta^{(2-)}$.

phase difference twice, leading to a 180° phase difference between the two second-order sum packets. By the same reasoning, it makes sense that the second-order difference elevation is a set down for both packets because the two 90° phase shifts cancel out in the subtraction.

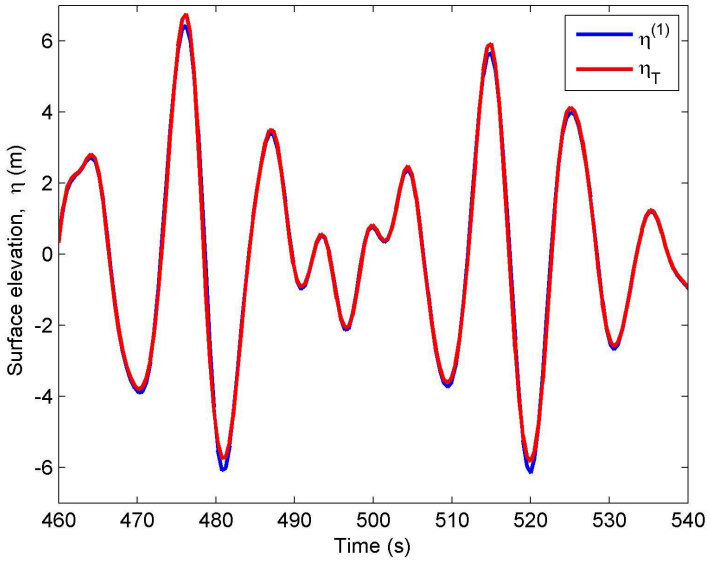

Figure 5.3: Surface elevation time histories with only the linear component, $\eta^{(1)}$ (blue line), and the total elevation, η_T (red line).

The linear component of the time history is compared to the total time history ($\eta_T = \eta^{(1)} + \eta^{(2+)} + \eta^{(2-)}$) in Figure 5.3, over the same section of time as Figure 5.2(b). The net

effect of the second-order components is to slightly increase the amplitude of the peaks and decrease the amplitude of the troughs.

5.3 Extreme events

The generation of random spectra was discussed earlier in Section 3.4.1. A target JONSWAP sea state spectrum was randomly sampled to give two sets of coefficients, a_n and b_n, where $n = 1 : N/2$ and N is the length of the signal being generated. The coefficients represent the amplitude of the cosine and sine components at each frequency in the spectrum and are defined as $a_n = z_n.\sqrt{S(\omega_n)d\omega}$, where z_n is a set of Gaussian distributed random numbers with zero mean and unit variance, and $S(\omega_n)$ is the spectral component of the target sea state at the n^{th} frequency, ω_n. Rather than generating one long time history from which to collect statistics, it was more convenient to generate a large number of short time histories that could then be combined. Sets of 10^6 waves were produced using 10^4 short time histories of length 1033 s with a sampling frequency of 1.98 Hz.

For each of these spectra, the total response to second-order was found for both undisturbed open ocean and in the presence of a Thunder Horse type structure. The QTFs for wave-wave interactions without a structure present were found using the method of Forristall (2000). For the Thunder Horse type structure, a symmetric array of four columns with the average Thunder Horse cross-section connected by pontoons was used. This was called Model 3 in Chapter 2, and the transfer functions were found using DIFFRACT. By calculating the response both in open ocean and in the vicinity of a structure one can find the change in surface elevation caused by the presence of the structure.

As mentioned previously, due to the limits of the computing power available, the author was unable to calculate converged QTFs above incident angular frequencies of 1.1 rad/s. Due to these limitations, the random spectra are generated based on a JONSWAP spectrum ramped down to zero at a maximum frequency of $\omega_{max} = 2\omega_p$. With the range of QTFs available and a spectrum truncated at $2\omega_p$, the peak frequency, ω_p, can be chosen to excite at second-order one of the first six near-trapped modes identified in Chapter 2. The random sea

state peak periods used in the results of this section are 19.578 and 15.164 s. These periods were selected so that second-order sum responses would occur at periods of 9.789 and 7.582 s respectively, which are the second and fourth near-trapped modes identified earlier.

5.3.1 NewWave in open ocean

As a further check that the extension of the method to second-order is reliable, one can use an artificially low H_s value and compare the largest events to a NewWave focused wave group. The size of a second-order component is proportional to the square of the H_s value and so at the value used, $H_s = 0.06$ m, the linear component dominates. If the method is working correctly then the results should be similar to those seen in Figure 3.12.

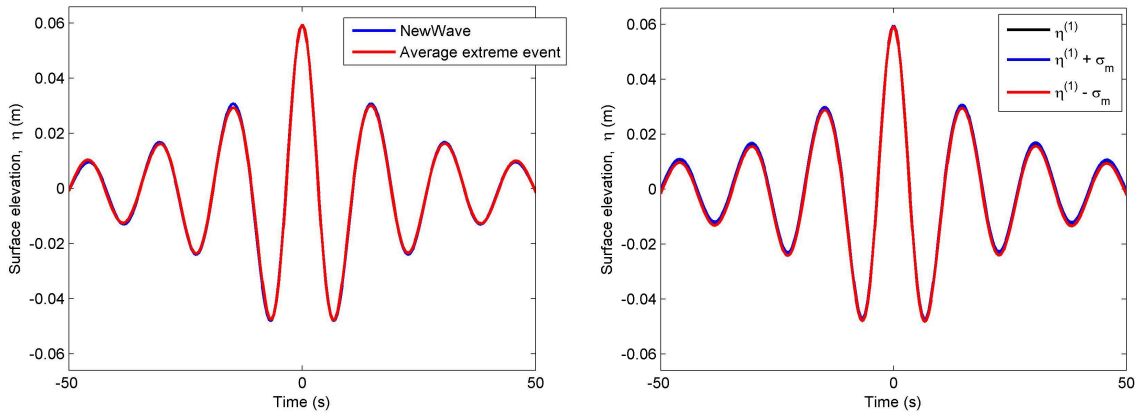

(a) Top 500 crests (b) Error bars

Figure 5.4: (a) Average surface elevation for the largest 500 crests in open ocean with $H_s = 0.06$ m and (b) the error bars one standard deviation either side of the mean.

Figure 5.4(a) shows a comparison between the average surface elevation for the largest 500 crests and an ideal NewWave in the same low steepness sea state. To find the average surface elevation for the largest crests, the zero upcrossing locations were found for each of the random time histories generated. The crest and trough between each pair of these zero upcrossings were then identified and the largest 500 crests were selected. For each of the 500 largest crests, the surface elevation time history 50 s either side of the largest crest was isolated and shifted in time so that the largest crest was at time $t = 0$ s. The time history ± 50 s was isolated because, when averaged, a NewWave like focused wave group is a short

event lasting only a few periods.

For the random sea states used in this section, averaging over the top 500 waves represents a one-in-1000 to one-in-1500 wave crest. A typical assumption is to model a peak storm duration as around 1000 waves, so the average extreme crests shown in these results are approximately the largest events one would expect to see in a typical storm with the stated sea states. One could argue that when looking at extreme events one should look at an event with a lower probability of occurrence, but it is the combined probability of sea state and event occurrence that is relevant. If the sea state has a probability of occurrence of say one-in-100 years then when looking at the events likely to occur in this storm a probability of one-in-1000 is perfectly reasonable.

The target random sea state is given by $H_s = 0.06$ m and $T_p = 15.164$ s which means that the wave group steepness is only $k_p H_s = 0.001$, ensuring that the linear component dominates if the code is behaving as expected. The results are very close to the ideal NewWave with some small differences. To check that these differences are within the expected tolerances, Figure 5.4(b) shows the error boundaries one standard deviation either side of the mean using the method discussed in the purely linear case of Section 3.4.3. The differences between the ideal NewWave and the average extreme crest elevation are within the expected range of values, given the number of time histories averaged over.

Figure 5.5 repeats this analysis but with the largest 500 troughs rather than crests. The average extreme trough elevation is very close to the ideal NewWave, with the differences between the two within the expected range of values. These figures suggest that the extension to second-order is working correctly for near-linear sea states.

5.3.2 Extreme crests and troughs

The previous section confirmed that the generation of random surface elevation time histories works in open ocean for near-linear sea states. This section begins by looking at the effect of second-order interactions for steeper sea states. Figure 5.6 plots the average components of the total surface elevation for the largest 500 crests and 500 troughs in open ocean with the

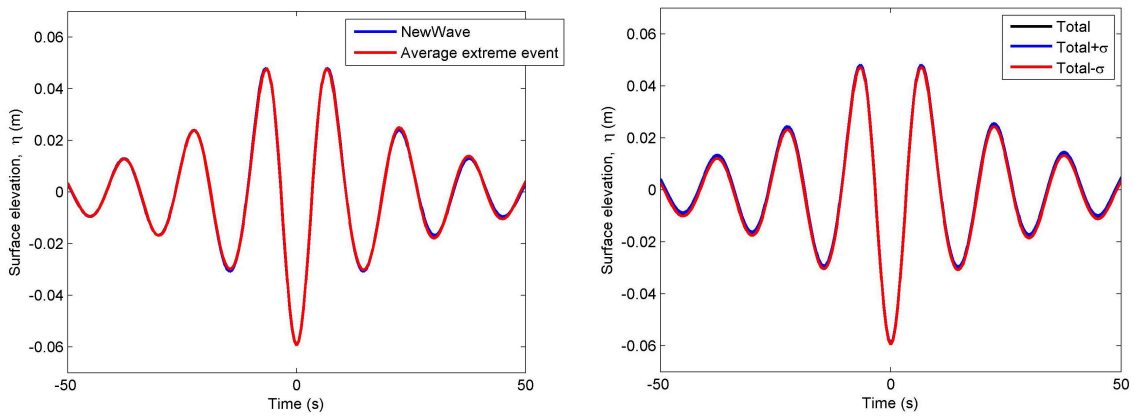

(a) Top 500 troughs (b) Error bars

Figure 5.5: (a) Average surface elevation for the largest 500 troughs in open ocean with $H_s = 0.06$ m and (b) the error bars one standard deviation either side of the mean.

same peak period as the previous example but now with $H_s = 12$ m. This gives a $k_p H_s$ value of 0.20, which combined with the peak period of 15.164 s gives a strong but not unrealistic storm sea state. The second-order interactions now provide a significant contribution to the total surface elevation, although still small relative to the linear component. The second-order component is almost identical in both the crest and trough figures. This is to be expected as there is no structure within the QTFs to introduce a phase change. The linear components of the trough focused signals are 180° out of phase with the crest focused signals and the quadratic nature of the second-order terms leads to this phase difference cancelling out. The overall effect of the second-order component is for the peaks in the total surface elevation to be slightly raised and the troughs slightly reduced relative to a linear NewWave.

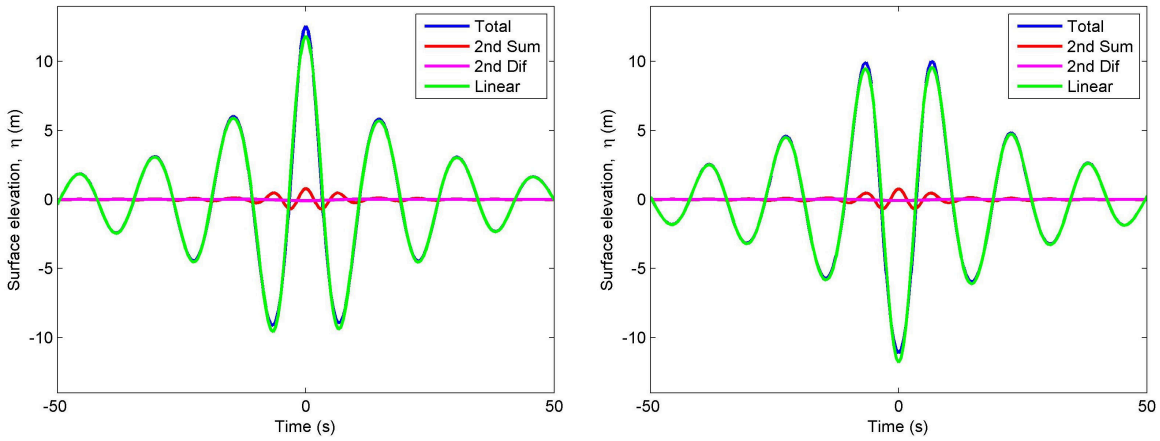

(a) Top 500 crests (b) Top 500 troughs

Figure 5.6: Average surface elevation for the largest 500 peaks and troughs in open ocean with $H_s = 12$ m.

Of more interest is the interaction of extreme waves with a structure. Figure 5.7(a) shows the components of the average of the top 500 crests in the total surface elevation with the Thunder Horse Model 3 present. The components shown are the total average surface elevation (blue line), second-order sum (red), second-order difference (magenta), and linear (green). These were calculated from random spectra based on a JONSWAP spectrum with $T_p = 15.164$ s and $H_s = 10.8$ m. The linear component is fairly symmetrical and NewWave in shape. The second-order component is also a NewWave like packet, but with double the frequency and an amplitude equal to 40 % of the linear amplitude. Figure 5.7(b) looks at the average of the incident waves from Figure 5.7(a) at the location of the structure but with the structure absent. Forristall coefficients were used instead of the DIFFRACT QTFs to find the open ocean surface elevation from the same incident linear spectra. This results in a 48 % reduction in the maximum amplitude and a delay of 8.6 s in the focus time. The ramp up in the open ocean case is slower than the ramp down. This is similar to, but not the same as, the shape of incident waves leading to large linear crests discussed in Section 3.3.

Figure 5.7(c) shows the components of the average of the largest 500 troughs in the total surface elevation with the structure present. The total average surface elevation is again a NewWave like packet with a maximum amplitude of 12.68 m. By selection of the largest responses we are effectively maximising the total trough depth, but there are two competing processes. The linear component needs to be large but the second-order component, which is bound to the wave group, must lead to minimal reduction of the trough depth. Two possible situations that allow this are by minimising the amplitude of the second-order envelope at the focus point or ensuring the phase is optimal. The second-order elevation in Figure 5.7(c) is an example of an occurrence of the first, with there being an obvious dip in the second-order envelope at the focus point. Figure 5.7(d) plots the open ocean surface elevation for the same incident wave as Figure 5.7(c), but without the structure present. The peak amplitude is -8.63 m which shows that the presence of the structure increases the peak amplitude by 47 %. It is interesting to note that the deepest trough in Figure 5.7(b) has a larger amplitude than the deepest trough in Figure 5.7(d), even though in Figure 5.7(b) the incident wave leads to the largest crest in the presence of the structure, rather than the deepest trough.

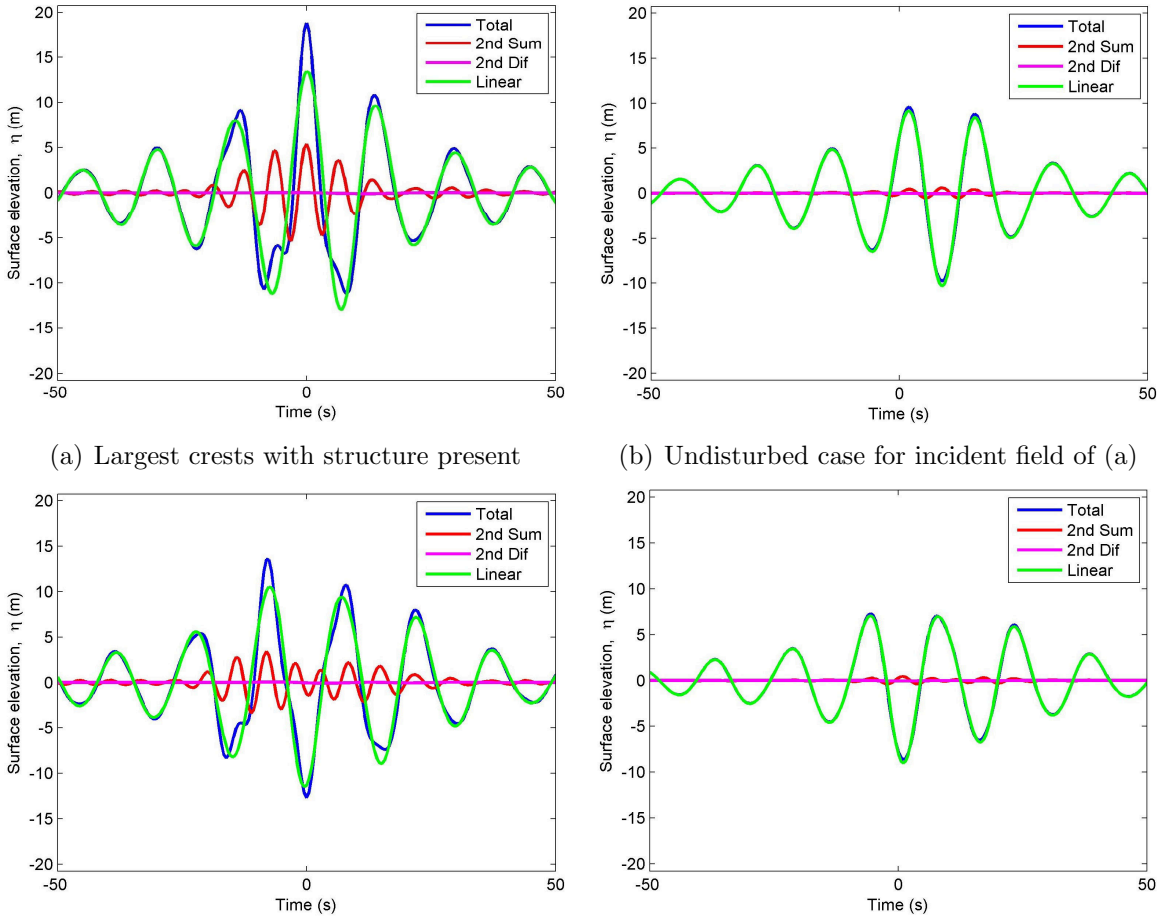

(a) Largest crests with structure present

(b) Undisturbed case for incident field of (a)

(c) Largest troughs with structure present

(d) Undisturbed case for incident field of (c)

Figure 5.7: Components of the average of the top 500 crests or troughs with the structure present along with the open ocean equivalent for each if there were no structure present.

5.3.3 QTF approximation

In Chapter 4, the approximation of assuming that QTFs are flat perpendicular to the leading diagonal was discussed as a possible method to reduce computation time. To investigate the accuracy of this approximation, a set of 10000 random spectra was generated with $H_s = 12$ m and $T_p = 15.164$ s. These spectra were then modified using either the full QTF matrix or a flat QTF matrix to give two sets of surface elevation spectra in the presence of the Thunder Horse Model 3. The inverse FFT was taken for each spectrum to give the associated time history, and the crests and troughs were identified between every zero-upcrossing location. When combined, these produced over 750000 crests for each of the QTF matrices used. The top 500 were isolated and used to give the average extreme wave elevation for the given sea state at a response level of approximately one-in-1500.

Figure 5.8(a) shows the average total surface elevation to second-order for the top 500

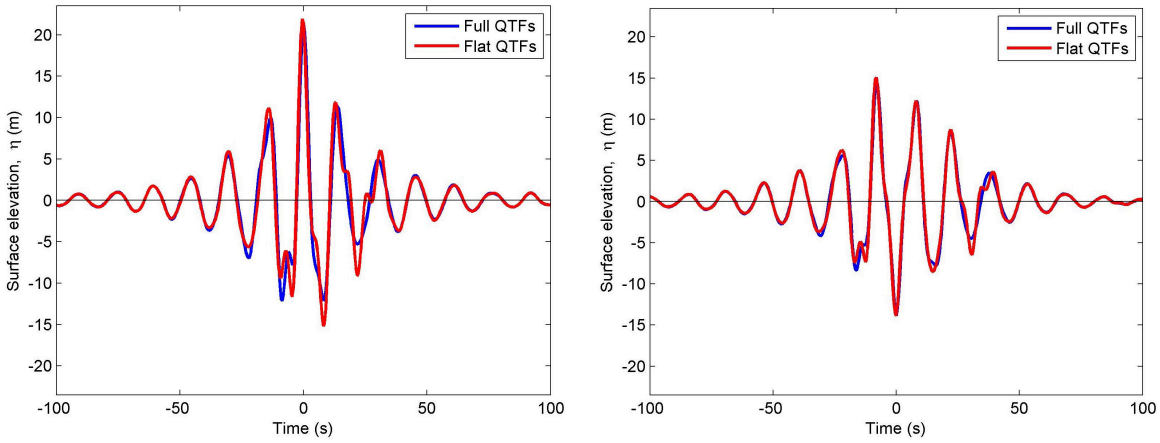

(a) Top 500 crests

(b) Top 500 troughs

Figure 5.8: Average surface elevation for the largest 500 peaks and troughs in the presence of a structure with $H_s = 12$ m, $T_p = 15.164$ s for a full QTF matrix (blue line) and a flat QTF matrix (red).

crests, with the full QTF matrix set in blue and the flat QTF approximation in red. Overall, the shape of the packet is very similar between the two signals with the full QTF matrix producing a maximum amplitude of 21.35 m and the flat approximation set producing a maximum amplitude of 21.94 m. This is just a 2.8 % difference between the two in what is a reasonably steep sea state. There are, however, some obvious differences between the two signals, particularly at the troughs either side of the largest crest. The differences between the two signals quickly become negligible after a few periods either side of the main crest, which is to be expected since the linear components are very similar in both sets and the differing second-order packets will be fairly compact. Figure 5.8(b) shows similar behaviour for the largest 500 troughs, with maximum amplitudes of 13.86 m and 13.82 m for the full and approximate QTF matrices respectively and the difference now being less than 1 %.

To gain a better understanding of exactly how the flat QTF approximation changes the shape of the second-order sum packet, Figure 5.9 shows the individual linear, second-order sum, and total elevation components for the crest case with each QTF matrix. The flat QTF second-order sum component has an increased maximum amplitude of 7.47 m, compared to 6.28 m for the full QTF component, and has been extended in duration to finish around 20 s after the full QTF component.

Overall, these results show that for this sea state the flat QTF approximation gives a

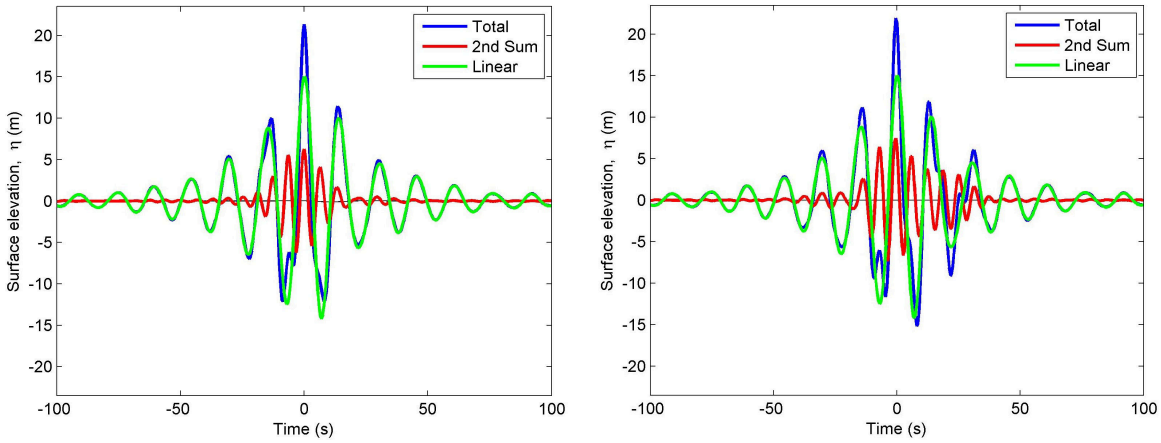

(a) Full QTFs (b) Flat QTFs

Figure 5.9: Components of the average surface elevation for the largest 500 peaks in the presence of a structure with $H_s = 12$ m, $T_p = 15.164$ s for (a) a full QTF matrix and (b) a flat QTF matrix.

fairly good approximation of the total maximum elevation reached for a given number of waves but the approximation of the complete time history of the second-order packet itself is not as good. As one of the aims of this research is to gain a better understanding of the physics behind extreme waves and the relative size of the individual harmonics within them, the rest of the results shown in this chapter will use the full QTF matrix.

5.3.4 Reciprocity

It is clear from Figure 5.7 that the incident fields leading to the largest crests and troughs with the structure present are not symmetrical NewWave groups like those seen for the largest events in open ocean. In Chapter 3 there were two types of NewWave solution under consideration, one in the undisturbed field and one in the response field. It was shown that there was a reciprocity between the deterministic scattered response when the open ocean NewWave was incident on a structure and the incident field in open ocean that would lead to the NewWave in response. A similar comparison can be extended to second-order for the extreme events identified in this section. The results can be split into two main cases: Case 1 contains the largest events in undisturbed open ocean surface elevation, and Case 2 contains the largest events in the scattered surface elevation with the Thunder Horse Model 3 present. Events from all 10000 time histories were analysed and for both Case 1 & Case 2, the highest 500 crests and the deepest 500 troughs were identified.

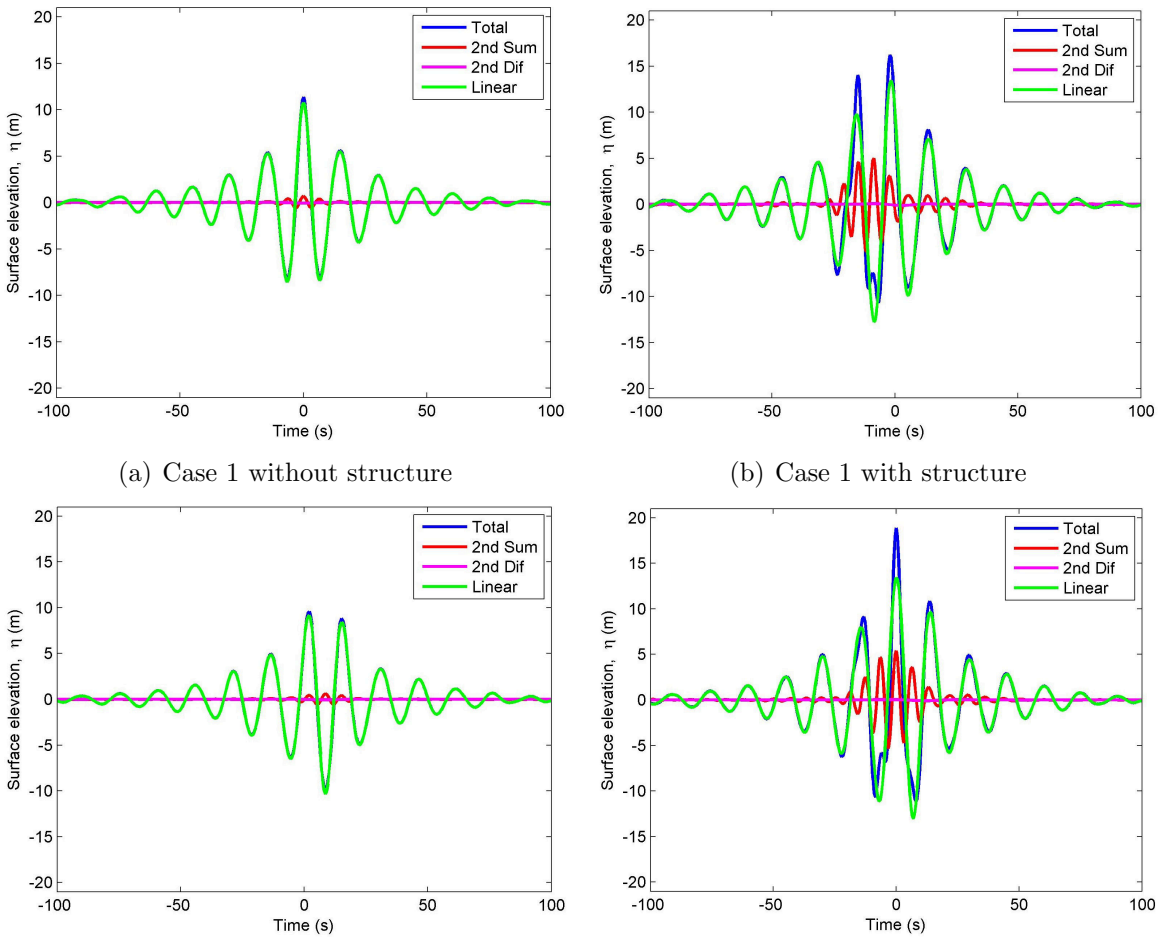

(a) Case 1 without structure

(b) Case 1 with structure

(c) Case 2 without structure

(d) Case 2 with structure

Figure 5.10: Average incident and response surface elevations for the top 500 crests in Case 1: open ocean, and the top 500 crests in Case 2: with the structure present.

Figure 5.10 shows four time histories found by averaging over 500 crests, with Figures 5.10(a) & 5.10(b) showing results for Case 1 and Figures 5.10(c) & 5.10(d) showing results for Case 2. Figure 5.10(a) plots the average surface elevation for the top 500 crests in open ocean and Figure 5.10(b) plots the average response when these top 500 undisturbed crests are instead incident on the four-columned structure. Figure 5.10(d) plots the top 500 crests in the scattered field and the average of the incident waves leading to these top crests are shown in Figure 5.10(c).

Figures 5.10(a) & 5.10(d) are both close to NewWave solutions in the linear components, with second-order sum packets adding to the crest amplitude. The maximum amplitude reached for the largest crests with the structure present is much higher than in open ocean. The peak amplitude in Case 2 with the structure present is 18.88 m whereas the maximum amplitude in open ocean for Case 1 is 11.36 m and this increases in the presence of the

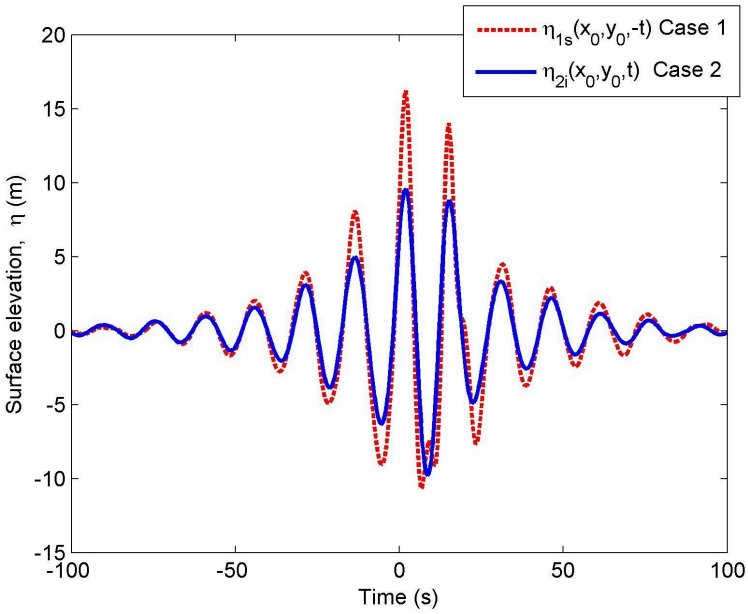

Figure 5.11: Average incident wave leading to the top 500 crests in Case 2 if the Model 3 were present (blue line) and the average deterministic response with the structure present for the top 500 open ocean crests in Case 1, inverted in time about $t = 0$ (red).

structure to 16.22 m. Figures 5.10(b) & 5.10(c) both have a shift in time for the focus point and a reduction in symmetry. However, Figures 5.10(b) & 5.10(c) do not show the same degree of reciprocity as shown at first-order in Section 3.3. In Figure 5.11, the total surface elevation time history from Figure 5.10(b) is mirrored in time by plotting against $-t$, rather than t, so that it can be compared directly with the total surface elevation from Figure 5.10(c). Although fairly close, the two signals are no longer separated by just a scaling factor, as was the case for linear interactions. This shows that simple reciprocity no longer holds at second-order, though there is not any reason why it should.

5.3.5 'Designer' wave

One of the aims of this section is to gain a better understanding of the physics of extreme waves and ask what kind of incident wave leads to an extreme event, rather than simply extracting examples of major events from a long data set. Figure 5.7 looked at the average components of the largest 500 crests and largest 500 troughs. For each of the top 500 crests and troughs, the incident wave field that led to these major events was identified. This was done by using the same incident spectra, but instead of using DIFFRACT QTFs to find the response in the presence of the structure, the method of Forristall (2000) was used to find

the surface elevation at the location of the structure but with the structure absent. The surface elevation for ±50 s was then isolated from this open ocean time history about the same focus time as the largest event from the response with the structure present. These incident surface elevation time histories were then collected together for two sets: one that led to the largest crests and one that led to the largest troughs. An average was then taken of each set of incident waves to give two 'designer' waves.

These 'designer' waves should lead to an extreme event if used as an incident field, with the total response field equal to the average total surface elevation seen in Figure 5.10(d). Figure 5.12 plots this 'designer' incident wave and the total surface elevation when it is incident on the structure. It is reassuringly similar to the plot seen in Figure 5.10(d), and this is confirmed by plotting both together in Figure 5.13. There are slight differences between the two which are down to the variation introduced by averaging over a finite set of random signals. A 'designer' wave such as this could be used instead of lengthy random time history generation for future analysis of extreme wave behaviour. In particular, one can use this for very careful experiments using a transient 'designer' wave to simulate an extreme event without worrying about the reflections associated with random wave tests. One can also use it for more detailed fluid loading calculations for structural design, and to look for areas where this method does not work such as third-order and higher harmonics.

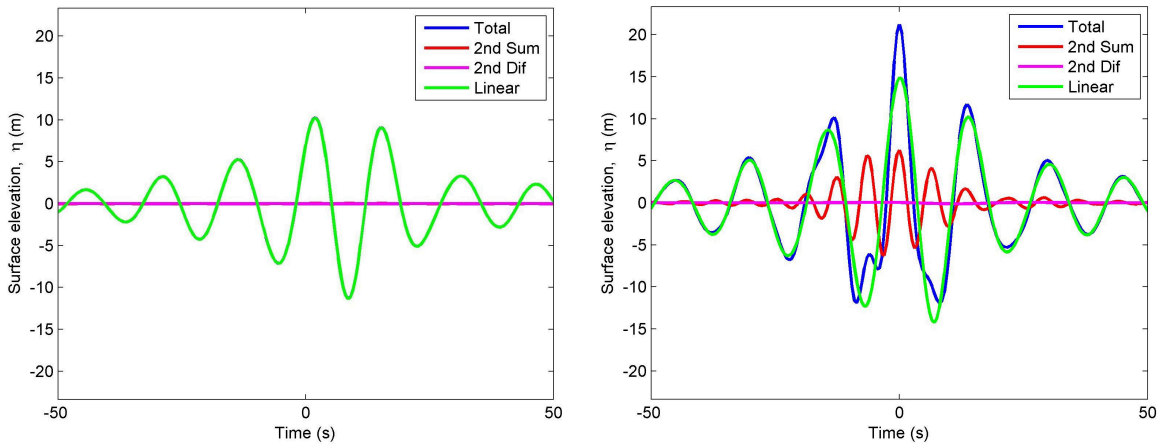

(a) 'Designer' incident wave

(b) Response to 'designer' incident wave

Figure 5.12: (a) The 'designer' incident wave and (b) the response to this wave when it is incident on the structure for $T_p = 15.164$ s and $\beta = 45°$.

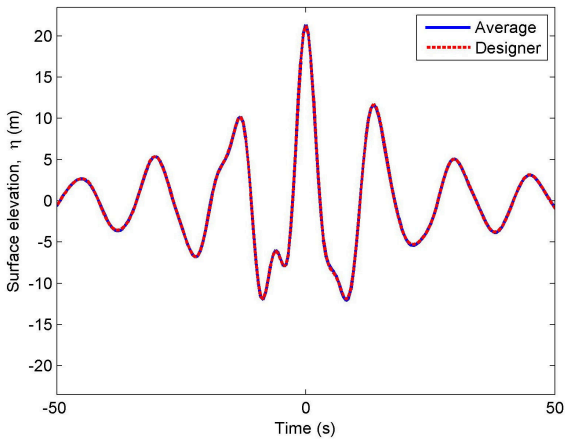

Figure 5.13: Comparing the average extreme responses to random incident waves and the 'designer' incident wave, both with the Model 3 present for $T_p = 15.164$ s and $\beta = 45°$.

Having shown for the largest crests that the average incident surface elevation at a one-in-N_w level can be used as a 'designer' wave for large crests, a similar one can be produced for the largest troughs. An example of the average of the largest 500 troughs and the average incident wave leading to them is given in Figure 5.7(c) and 5.7(d). It is then interesting to see if the 'designer' wave for a large crest is simply the inverse of the 'designer' wave for a large trough. To investigate this, the linear component of each incident time history for the largest crests and troughs was inverted and then used as a new incident field with the same structure present. Since only the linear incident wave field is being inverted, the second-order components in the response field will remain the same (as two negatives cancel out to become positive). This will likely have a large effect on the maximum elevations reached in the inverted cases as there will be a large positive second-order component reducing the amplitude of the troughs and a small second-order component contributing to the crests.

Figure 5.14(a) shows the average components of the total surface elevation for the incident waves that were the inverse of those leading to the 500 largest crests. Figure 5.14(b) shows the average components of the total surface elevation for the incident waves that were the inverse of those leading to the 500 largest troughs. The maximum elevation amplitude reached in Figure 5.14(a) is 10.87 m. This is significantly less than those reached in Figures 5.7(a & c) which are 18.88 m for the crests and 12.68 m for the troughs. The maximum amplitude in Figure 5.14(b) is 11.62 m, which is again a lot less than those reached in Figure 5.7. This shows that the incident waves leading to the largest events with the structure in place are

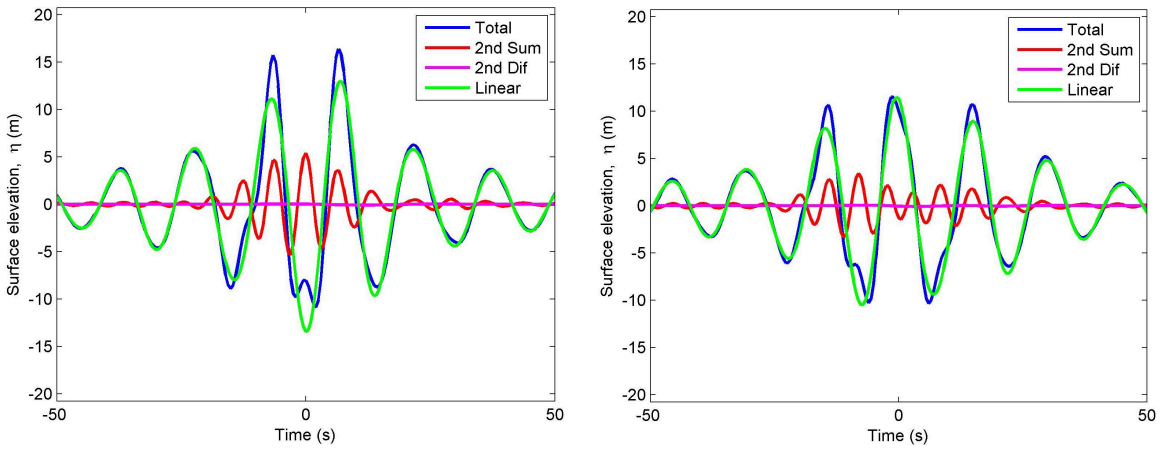

(a) Total η with inverted incident waves for the largest crests.

(b) Total η with inverted incident waves for the largest troughs.

Figure 5.14: Components of the average of the total surface elevation for the inverted incident fields from the top 500 crests and troughs with the structure present.

different for crests and troughs when the second-order interactions play a large part. This difference can be traced back to the fact that, even for the flat QTF approximation, the phase shifts of the QTFs are not simply two times those of the LTFs.

5.3.6 Varying return period

So far the analysis presented in this section has looked at the top 500 events in each case. The following results look at what happens when the return period is varied. The combination of storm return period and wave return period within a given storm was discussed earlier when modelling extreme waves. If a long return period storm is used with say a one-in-100 year probability of occurrence then the return period of the wave within a storm can be fairly low such as one-in-1000. A wave return period of one-in-1000 would be approximately the largest event seen in a typical storm duration, and so if this is coupled with a sea state with a long return period it represents an extreme wave. This section looks at the effect of varying the wave return period in a given storm while maintaining the same sea state. As the sea state return period lengthens, the peak period and significant wave height tend to increase, but when lengthening the wave return period within a storm, the peak period remains constant.

10000 random time histories were generated using the same method discussed earlier.

The crests and troughs were identified and then combined into one large data set. The sea state used to generate the random time histories was based on a JONSWAP spectrum with $H_s = 12$ m and $T_p = 15.164$ s. This sea state has a steepness value of $k_p H_s = 0.209$ which is steep but not unrealistic for a severe storm state. The peak period of 15.164 s is also within the range of typical values for a severe extra-tropical mid-latitude winter storm. For the Gulf of Mexico, the appropriate period is likely to be around 12-15 s. This sea state was chosen because it is both within the typical range for storms and should excite a near-trapped mode at second-order giving a large response.

Figure 5.15 shows four plots of crest surface elevation near the centre of the structure at (12,12) m against their probability of occurrence. The values at a probability of 10^{-4} therefore show the crest elevation for a one-in-10000 wave. The four coloured lines show the distribution of crest elevation to first- and second-order in open ocean (magenta and green lines respectively), and with the structure present (red and blue lines respectively). The dotted vertical lines show the starting probability for average surface elevations at four probabilities of occurrence per wave which will be plotted in Figure 5.18.

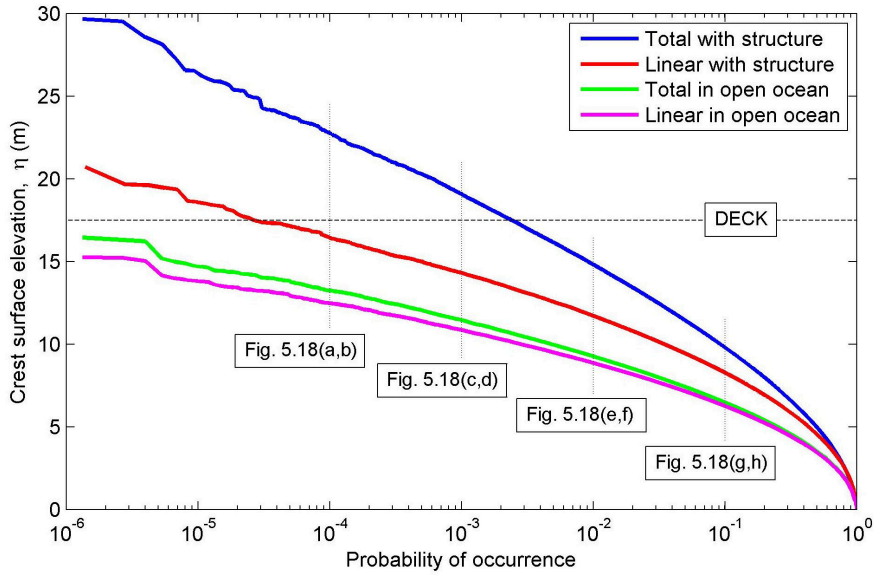

Figure 5.15: Crest height vs. probability of occurrence for $H_s = 12$ m, $T_p = 15.164$ s.

It is very clear from Figure 5.15 that second-order interactions contribute far more to the total elevation when the structure is present compared to open ocean. In open ocean,

the largest waves have a linear component of 15 m elevation and a second-order component of less than 2 m. However, with the structure present the linear component is increased to a maximum of 21 m and the second-order component to 9 m. This means that for the most extreme waves almost one third of the total surface elevation comes from second-order interactions. The highest elevations shown have a probability of occurrence of just over 10^{-6} per wave. Since a given storm lasts around 1000 waves on average it is very unlikely that the largest shown wave would occur in a typical storm. At the opposite end of the probability scale, wave surface elevations with probabilities greater than 10^{-1} per wave will inevitably occur in a typical storm. The range of crest elevations within the centre of the figure are of the most interest, as the maximum expected elevation in a given storm is likely to be in this range. It is interesting to see how the addition of second-order results has a large effect on the amplitude of this maximum expected crest elevation.

The maximum surface elevation reached of 29.7 m is huge given that the sea state has an H_s value of 12 m. Even the one-in-1000 wave elevation with the structure present is almost 20 m. To put this into context, the Thunder Horse platform has a steady state air-gap of 17.5 m, shown in Figure 5.15 as a black dashed line. If predictions are based on first-order results then the probability of water-deck impact in this sea state is approximately 2.5×10^{-5} per wave. If the results are extended to second-order then the probability of water-deck impact in this sea state is approximately 2.5×10^{-3} per wave. This suggests that if this sea state occurred for more than 400 waves (around 1.7 hours) one would expect there to be an impact on the deck, whereas linear predictions suggest it would take around 40000 waves for impact to occur. These results are dramatic but not necessarily representative of the actual structure, because Thunder Horse is a semi-submersible whereas the analysis so far is for a structure fixed vertically. A comparison will be made in Chapter 6 between diffraction of waves by identical hulls that are free to move or held fixed vertically.

Figure 5.16 looks at the distribution of trough height with probability of occurrence for the same data set as the previous figure. The pattern is similar to the crest distribution, with the four plots diverging at lower probabilities of occurrence. The presence of the structure causes a maximum increase of 34 % with the largest troughs being 14.69 m and 19.69 m in

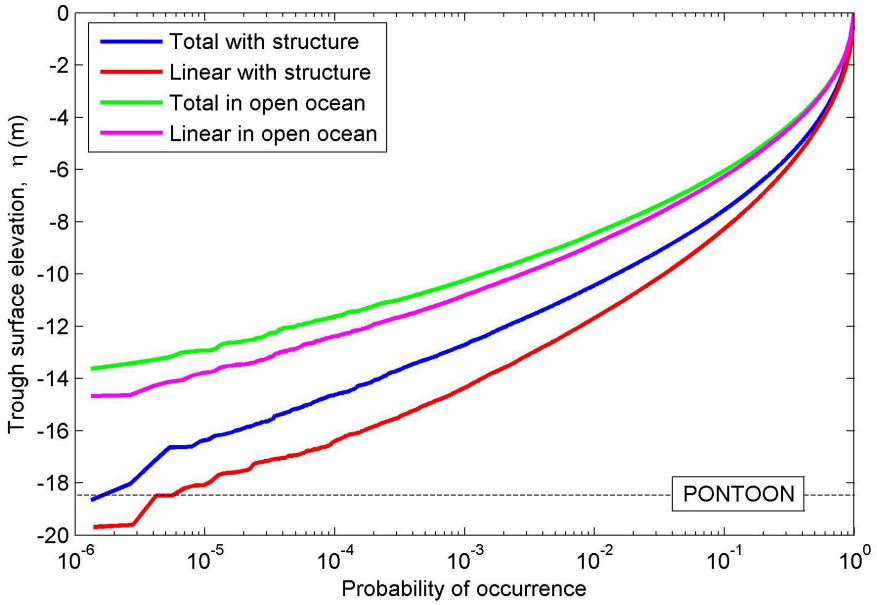

Figure 5.16: Trough height vs. probability of occurrence for $H_s = 12$ m, $T_p = 15.164$ s.

open ocean and with the structure present. The tops of the pontoons are 18.48 m below the surface, shown in Figure 5.16 as a black dashed line, so for this sea state there is a very low probability of the pontoons being exposed.

To compare the contribution to crest elevation from second-order in a less steep sea state, Figure 5.17 repeats the method of the previous case but this time for a sea state with $H_s = 6$ m, $k_p H_s = 0.105$. The maximum elevation reached with the structure present is still more than double the H_s value at 12.8 m. However, this time the second-order contribution is only 18 % of the linear component, compared to 43 % for the previous case. This is to be expected, as the second-order component has a squared relationship to the incident wave amplitude and the H_s has been halved.

Figure 5.18 looks at how varying return period changes the average extreme surface elevation response with the structure present and the 'designer' wave leading to each average extreme elevation response. The surface elevation is again taken near the centre of the structure at (12,12) m. Each pair of figures represents a different probability of occurrence per wave with Figure 5.18(a) and 5.18(b) representing the 'designer' wave and average response elevation at a probability of 0.0001 or one-in-10000 waves. The other pairs have probabilities of 0.001, 0.01, and 0.1 respectively (as shown on Figure 5.15), with the last pair almost certain to occur in a typical storm of 1000 waves. At each probability of occurrence, the

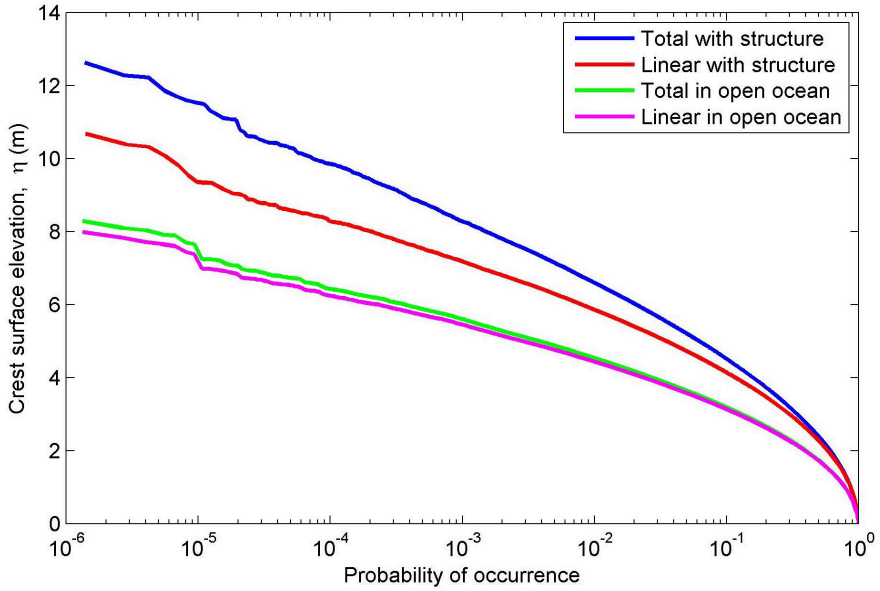

Figure 5.17: Crest height vs. probability of occurrence for $H_s = 6$ m, $T_p = 15.164$ s.

surface elevations are still averaged over 500 waves using the method discussed in Section 5.3.5, except previously the average was taken of the surface elevation ±50 s either side of the largest 500 crests. Instead of averaging over the largest crests, a sliding window of 500 events beginning at the stated probability of occurrence is used. For example, if a set contained 200000 waves then the 'designer' wave at a probability of occurrence of 0.001 would average over the 2000-2499 largest waves.

Figure 5.18 shows that the general shape of the signals is similar at each probability of occurrence but the level of non-linearity greatly increases as probability of occurrence decreases. The second-order component plays a much larger part at more extreme responses, as one would expect. The maximum elevation reached at a probability of occurrence of 0.0001 per wave is 20.66 m, and this is reduced to less than half at 9.79 m for a probability of 0.1 per wave. The ratio of second-order to linear components is 0.415 at the more extreme case of 0.0001 per wave, and this is reduced to 0.216 for the probability of 0.1 per wave case.

Tables 5.1 and 5.2 further emphasize these results by changing the return period of the first crest in the 500 being averaged over. Previously, for the largest 500 crests, the return period of the first crest is simply one-in-N_w waves. Now the return period is allowed to vary, with the 500 crest window sliding down to give an average crest that is more likely to occur. Table 5.1 shows crest heights in the presence of the structure and Table 5.2 in open ocean,

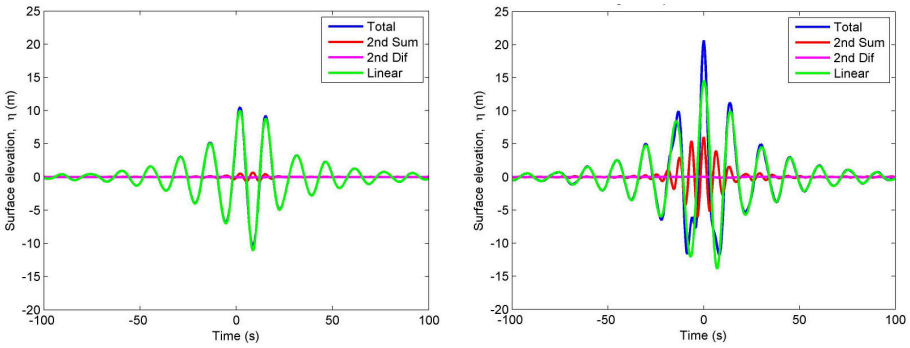

(a) Incident, $P = 0.0001$ (b) Response, $P = 0.0001$

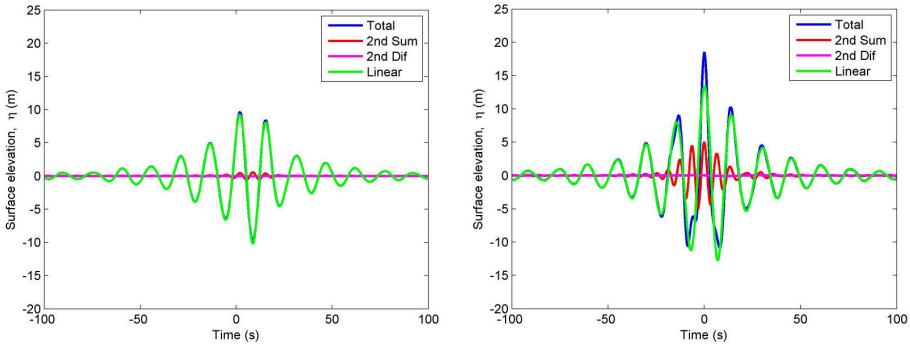

(c) Incident, $P = 0.001$ (d) Response, $P = 0.001$

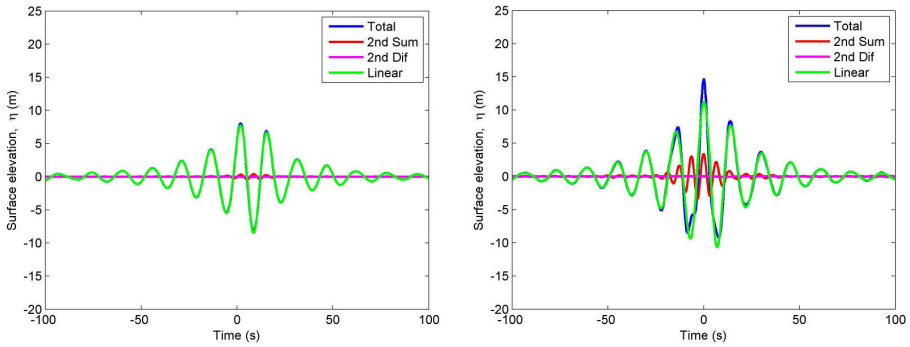

(e) Incident, $P = 0.01$ (f) Response, $P = 0.01$

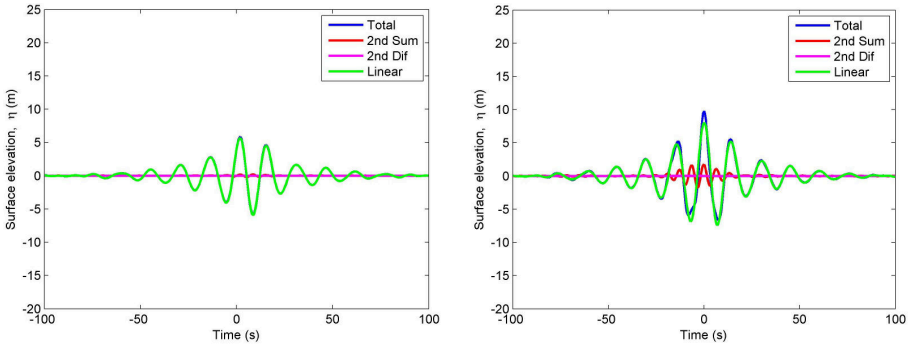

(g) Incident, $P = 0.1$ (h) Response, $P = 0.1$

Figure 5.18: 'Designer' incident wave and average crest response in the presence of the structure with varying probability of occurrence per wave. $H_s = 12$ m, $T_p = 15.164$ s, and $\beta = 45°$.

both for the $H_s = 12$ m data set. The first line in each table shows the top 500 crests, as discussed in the previous section. The following lines then show what happens when the sliding window moves down the data set. The 'Probability' column shows probability of occurrence of the crest at the start of the sliding window for each line. Since the data set used in this analysis had around 751000 crests, the second line of the two tables with a value of 0.0001 in the 'Probability' column represents a 500 crest window averaging over the 75^{th} to 574^{th} largest crests.

Probability	η_T (m)	$\eta^{(1)}$ (m)	$\eta^{(2)}$ (m)	$\eta^{(2)}/\eta^{(1)}$
0.0000013	21.35	14.90	6.41	0.430
0.0001	20.66	14.58	6.05	0.415
0.001	18.56	13.47	5.07	0.377
0.01	14.75	11.28	3.46	0.307
0.1	9.79	8.04	1.74	0.216
0.13	9.07	7.53	1.53	0.203
0.27	7.12	6.06	1.06	0.175
0.40	5.80	4.97	0.81	0.162
0.53	4.70	4.08	0.62	0.151
0.67	3.68	3.16	0.52	0.164
0.80	2.60	2.23	0.37	0.165
0.93	1.36	1.05	0.31	0.299

Table 5.1: Crest surface elevation at varying return periods for waves incident on the structure with $H_s = 12$ m and $T_p = 15.164$ s.

The maximum elevation given in the top line of Table 5.1 is greatly reduced from the maximum elevation of 29.7 m seen in Figure 5.15. This is because the results are for an average over 500 crests rather than just giving the largest value. The crests are fairly widely spaced at the low probability end of the figure, and a window covering 500 crests averages over a wide range of elevations. In both tables, the ratio of second-order to linear surface elevation decreases as the probability of occurrence increases. This holds until the last line in each table where there is a sudden increase in this ratio. This is because the destructive interference needed at first-order for such small crest heights to occur does not necessarily apply to second-order. For the smallest possible crests there would be total destructive interference in the linear component leading to an infinite ratio of second-order to linear.

Probability	η_T (m)	$\eta^{(1)}$ (m)	$\eta^{(2)}$ (m)	$\eta^{(2)}/\eta^{(1)}$
0.0000013	12.57	11.86	0.80	0.067
0.0001	12.24	11.57	0.76	0.065
0.001	11.20	10.63	0.63	0.056
0.01	9.22	8.82	0.44	0.050
0.1	6.46	6.25	0.23	0.037
0.13	6.04	5.85	0.20	0.034
0.27	4.88	4.75	0.14	0.029
0.40	4.05	3.95	0.10	0.025
0.53	3.35	3.28	0.07	0.022
0.67	2.68	2.63	0.05	0.019
0.80	1.97	1.94	0.03	0.016
0.93	1.27	1.25	0.02	0.019

Table 5.2: Crest surface elevation at varying return periods for waves in open ocean with $H_s = 12$ m and $T_p = 15.164$ s.

For a single Stokes wave expansion, the second-order component has an amplitude of $\frac{1}{2}kA^2$, where A is the amplitude of the linear component. For a JONSWAP spectrum wave group, the majority of spectral energy is focused around the peak frequency, and so one would expect the relationship between the second-order and linear components to still be approximately quadratic. Figure 5.19 plots the second-order vs linear components of crest elevation at varying probabilities of occurrence with log-log axes in open ocean (blue line) and with the structure present (red). To illustrate the relationship between the second-order and linear components, two arbitrary lines are plotted with linear and quadratic relationships between $\eta^{(1)}$ and $\eta^{(2)}$ for comparison. The dashed and dotted black lines show sample gradients for linear and squared relationships respectively between the two components, with an arbitrary y-intercept. At high crest elevations, the plots for both the open ocean case and with the structure present are approximately straight parallel lines on these log-log scales with a gradient matching the sample squared relationship (dotted line). At low crest elevations the Stokes scaling does not hold and the red and blue lines are no longer parallel to the black dotted line.

In Figures 5.15 and 5.17, the curves plotting crest height against probability lose their smoothness at high crest heights, with jumps in the data appearing due to sample variability. This is due to the randomness of the data set and the rarity of waves at such high elevations.

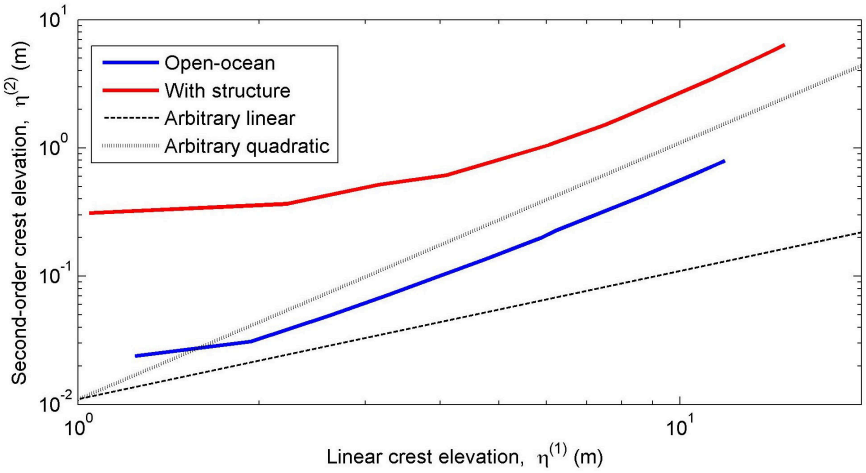

Figure 5.19: Second-order vs. linear components of surface elevation for $H_s = 12$ m, $T_p = 15.164$ s.

To confirm this, the method used to produce Figure 5.15 was repeated to give 10 data sets, each containing 10000 random spectra and an associated time history for each of length 1033 s. Crest elevation was then plotted against probability of occurrence for each data set, as shown in Figure 5.20(a). The mean of these 10 data sets was taken and plotted in Figure 5.20(b) in blue. This is a smooth curve and confirms that the steps in each data set at high elevations are due to the randomness of the data. The red lines plot error bars two standard deviations either side of the mean to show the confidence boundaries within which 95 % of values should lie.

To illustrate how the confidence boundaries diverge at high crest elevations, Table 5.3 looks at the mean and standard deviation at several probabilities of occurrence. It also gives the size of two standard deviations relative to the mean at each probability. At the far extremes of minimal probability of occurrence, the standard deviation is a large percentage of the mean. A single set of 10000 spectra can provide a wide variety of results in this range. For probabilities of occurrence greater than one-in-100000 waves, the spread of results is fairly compact.

5.3.7 NAF

In Chapter 3, the Net Amplification Factor was introduced as a useful tool for finding where in the vicinity of a structure a particular sea state is most likely to cause violent responses

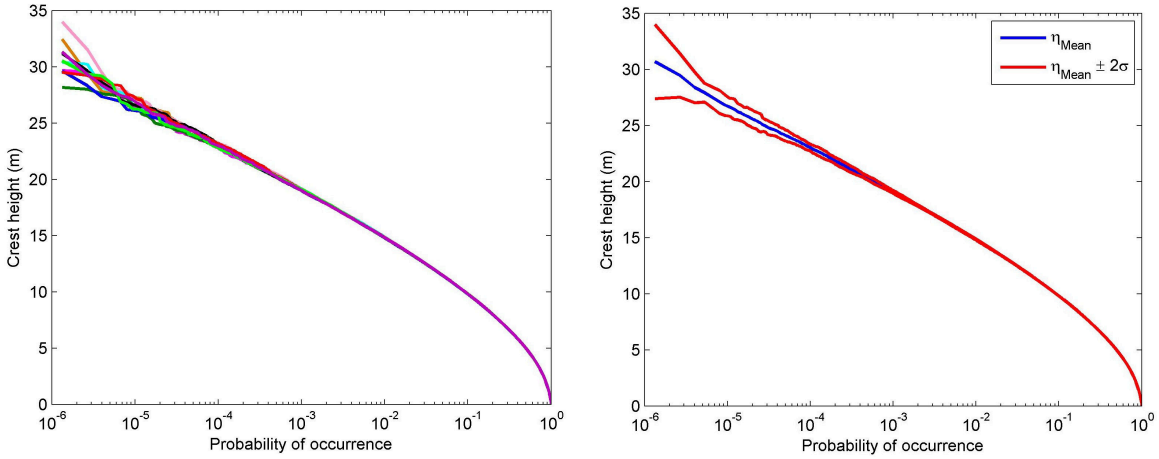

(a) Total crest elevation (b) Mean total crest elevation

Figure 5.20: (a) Total crest elevation against probability of occurrence for multiple data sets and (b) mean total crest elevation against probability of occurrence with 95 % confidence limits.

Probability	η_{mean}	2σ	$2\sigma/\eta_{mean}$ (%)
0.0000013	30.67	3.30	10.76
0.00001	26.71	0.86	3.22
0.0001	23.02	0.31	1.35
0.001	19.07	0.12	0.63
0.01	14.82	0.05	0.34

Table 5.3: Mean crest surface elevation, η_{mean}, and Standard Deviation, σ, at varying return periods for waves in open ocean with $H_s = 12$ m and $T_p = 15.164$ s.

and how large a response should be expected. The NAF shows the maximum linear surface elevation amplification expected due to the presence of a structure rather than in open ocean and this was validated in Section 3.4.4 using random linear statistics. However, it has also been shown that for extreme crests the second-order component makes a large contribution. To assess the usefulness of the NAF to predict responses at second-order, one can compare a NAF field plot with the statistical field plot of the previous linear validation extended to second-order.

At each location across the field, QTFs are used in addition to LTFs to give the total surface elevation in the presence of the structure for the same random time histories as in Section 3.4. These were 100 random time histories, each of length 1033 s. The crests are identified and sorted, with the top 500 being averaged as before. To normalise this average extreme crest elevation, the open ocean case is now extended to second-order using

the method of Forristall (see Forristall (2000)). The ratio of these average extreme crest elevations is then plotted across the field for the same sea state as used in Section 3.4.4, $T_p = 15.164$ s and $H_s = 12$ m. Figure 5.21(a) shows the NAF plot from Figure 3.15 with the colour bar rescaled to allow comparison with the field plot of the ratio of the statistical total surface elevation to second-order in Figure 5.21(b). The maximum amplification is still in front of the leading edge of the downstream column but this has now increased from 1.54 in the linear case to 1.79. Throughout the inside of the structure the maximum possible elevation amplification has been increased and the pattern has increased in complexity.

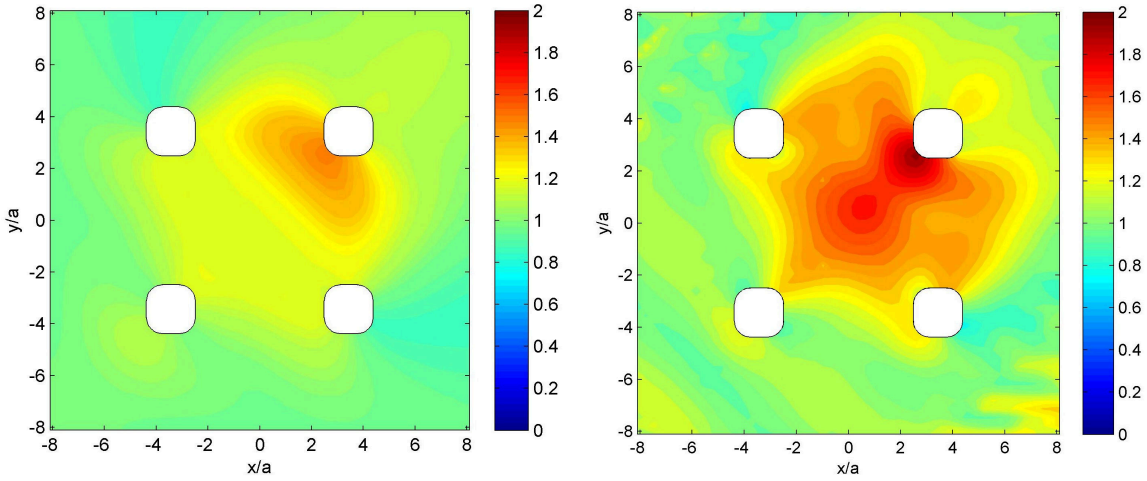

(a) NAF

(b) Average extreme crest amplification to second-order at a one-in-1500 wave level

Figure 5.21: (a) Net Amplification Factor and (b) average extreme crest amplification for $T_p = 15.164$ s, $\beta = 45°$, $H_s = 12$ m.

H_s	k_pH_s	Open ocean	With structure	Ratio
0.01	0.0002	0.0066	0.0101	1.5392
2	0.0348	1.3128	2.0207	1.5393
4	0.0695	2.6503	4.1353	1.5600
6	0.1043	4.0235	6.4518	1.6035
8	0.1391	5.4649	8.9401	1.6359
10	0.1738	6.7331	11.5169	1.7105
12	0.2086	8.2976	14.8381	1.7882
14	0.2434	9.7457	18.0951	1.8567

Table 5.4: Average extreme crest amplification to second-order for $T_p = 15.164$ s, $\beta = 45°$, and varying incident steepness values, all at a one-in-1500 level.

The size of the second-order component has a squared relationship with the linear am-

plitude. This means that at small incident wave amplitudes the second-order component is very small and the NAF gives a very good approximation of the total surface amplification in the vicinity of a structure. As the incident wave amplitude increases, the second-order component becomes more important and the NAF becomes less accurate as an approximation. Figure 5.22 shows how the average extreme crest amplification changes with increasing incident H_s. For each incident H_s, the maximum total surface elevations in open ocean and with the structure present are given in Table 5.4 along with the ratio of the two. At lower incident H_s values, this ratio converges on the linear value of 1.539. As H_s increases, the ratio of the maximum values increases and the area of high amplification spreads out from the downstream column across the inside of the array.

5.4 Conclusions

Conclusions drawn from the results presented in this chapter are briefly summarized below.

- Second-order contributions to free-surface elevation near an array of closely spaced columns are large in steep sea states.
- Summing in the frequency domain and using iFFT to find the response surface elevation is fast enough to be a realistic alternative to one of the other methods discussed, such as that of Winterstein (Winterstein and Sweetman (2001)).
- For lower frequency near-trapped modes, QTFs are fairly flat and the leading diagonal approximation is reasonable in realistic sea states.
- An average surface elevation can be found for an extreme event at a one-in-N_w level, along with a 'designer' incident wave that would lead to this average extreme event. The shape and amplitude of the 'designer' wave is dependent on the return period of the event.
- If Thunder Horse were a TLP (with vertical motions suppressed by tendon stiffness), there would be fairly regular water-deck impacts.

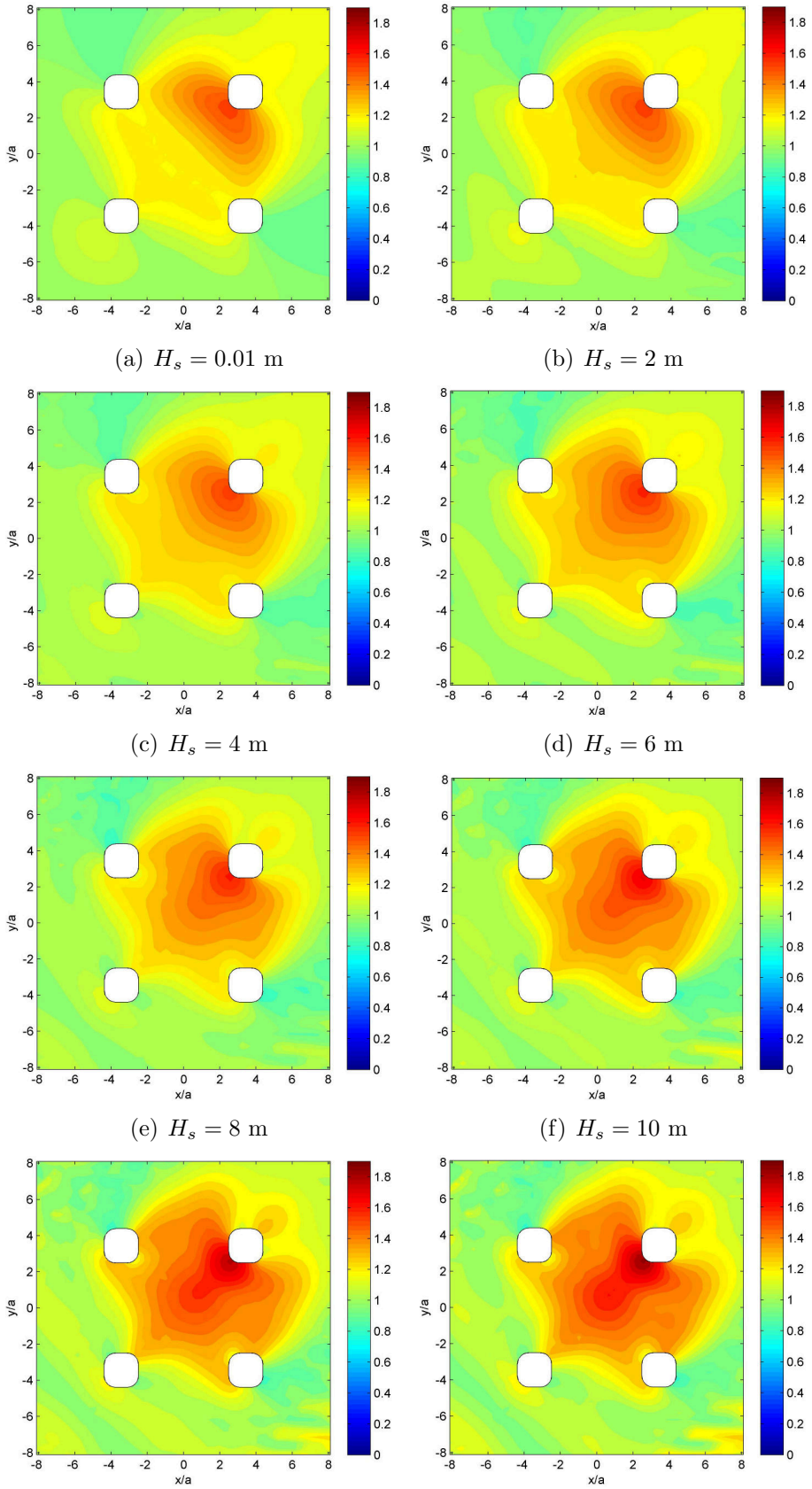

(a) $H_s = 0.01$ m (b) $H_s = 2$ m

(c) $H_s = 4$ m (d) $H_s = 6$ m

(e) $H_s = 8$ m (f) $H_s = 10$ m

(g) $H_s = 12$ m (h) $H_s = 14$ m

Figure 5.22: Average extreme crest amplification to second-order for $T_p = 15.164$ s, $\beta = 45°$, and varying incident steepness values, all at a one-in-1500 wave level in the appropriate sea state.

Chapter 6

Wave diffraction by a moving body

6.1 Introduction

The results presented so far have been for fixed structures. Fixed offshore structures constructed in the form of steel jackets or single towers tend to be economically viable in water depths up to around 500 m. Tension leg platforms (TLPs) can be used in water depths between around 150 - 1500 m. For water depths greater than this, freely floating structures restrained by soft moorings must be used. Both semi-submersibles and spars fall into this category. Although floating, TLPs can be approximated as fixed structures for the calculations presented in this thesis due to the minimal vertical movement allowed by the stiff tendons under high tension. However, this would not take into account horizontal movement, which would affect the second-order components of elevation amplification. The operational requirements of a TLP would lead to a rather different design from a semi-submersible with the same payload due to considerations such as buoyancy etc., but the general geometry of large TLPs and semi-submersibles are similar enough to allow a comparison between surface elevations in the vicinity of an identical hull that is held fixed or freely floating.

To predict accurately the likelihood of water-deck impact on semi-submersibles such as Thunder Horse, the model used in the calculations must be free to move. This chapter begins by presenting results to confirm that the motions of floating bodies can be accurately modelled. The next section then demonstrates that the hydrodynamic behaviour of Thunder

Horse can be modelled in a satisfactory manner using the Model 3 mesh discussed previously (see Section 2.9) and the hydro-restoring coefficients provided by BP p.l.c.

After confirming the ability to model a floating Thunder Horse like structure, the methods developed in the previous chapters are then applied to the now floating model and the behaviour is compared and contrasted to the equivalent fixed body results.

6.2 Validation

DIFFRACT has been well validated against published data for wave-excited forces, surface elevations, and body motions for a moving body. Eatock Taylor and Chamberlain (1993) compared DIFFRACT results to those of WAMIT and an axisymmetric boundary element analysis by Kim and Yue (1990) for a freely floating cylinder of radius a, draft a, in water of depth $10a$, with the centre of gravity $0.4a$ below the mean free surface. The results of DIFFRACT matched up well with those of WAMIT and Kim and Yue (1990). Tables 6.1 and 6.2 compare the author's results for first-order forces and body motions for this problem, with those designated 'Report' from Eatock Taylor and Chamberlain (1993). The forces are normalised by $F/\rho g a^2 A$ and moments are normalised by $M/\rho g a^3 A$ in Table 6.1, where ρ is the density of sea water, g is gravity, a is cylinder radius, and A is incident wave amplitude. The surge and heave motions in Table 6.2 are normalised as R/A and the pitch motion is normalised as Ra/A, where R is the relevant body displacement. The two sets of results match up well, with minor differences to be expected due to different surface meshes being used. The mesh used by Eatock Taylor and Chamberlain (1993) contained 96 elements per quadrant on the body, but the mesh used by the author has 256 elements per quadrant on the body. These results suggest that the author can accurately reproduce first-order results for diffraction about a moving body. DIFFRACT does not calculate second-order body motions and so for this study only linear body motions will be incorporated. For a typical storm wave with peak period in the range $T_p = 12 - 15$ s, a second-order sum body motion would likely be negligible as it will be shown in the next section that linear body motions for periods shorter than around 10 s are very small. Second-order difference body motions would have little energy near the heave resonant period with most high energy second-order

difference responses occurring with periods longer than around 40 s.

	Surge		Heave		Pitch	
ka	Report	Author	Report	Author	Report	Author
1.2	0.6519	0.6514	0.3208	0.3216	0.0564	0.0568
	-2.3212	-2.3202	-0.2678	-0.2683	-0.2007	-0.2021
	2.4110	2.4099	0.4179	0.4188	0.2085	0.2100
1.4	0.4727	0.4724	0.2006	0.2011	0.0425	0.0428
	-2.1066	-2.1057	-0.2336	-0.2341	-0.1894	-0.1906
	2.1590	2.1581	0.3079	0.3086	0.1941	0.1954
1.6	0.2482	0.2479	0.1170	0.1173	0.0235	0.0236
	-1.8988	-1.8981	-0.1963	-0.1968	-0.1794	-0.1804
	1.9150	1.9142	0.2285	0.2291	0.1809	0.1819

Table 6.1: Comparison of linear force results for a freely floating vertical cylinder calculated with DIFFRACT by Eatock Taylor and Chamberlain (1993) and the author. For each wavenumber the real and imaginary components, and the modulus of these, are given.

	Surge		Heave		Pitch	
ka	Report	Author	Report	Author	Report	Author
1.2	0.04400	0.0440	-0.1178	-0.1184	0.0172	0.0173
	0.4115	0.4114	0.1084	0.1089	0.1610	0.1616
	0.4138	0.4137	0.1601	0.1609	0.1619	0.1625
1.4	0.0567	0.0568	-0.0541	-0.0543	0.0216	0.0216
	0.3398	0.3397	0.0663	0.0667	0.1290	0.1294
	0.3445	0.3444	0.08559	0.0860	0.1307	0.1312
1.6	0.0682	0.0682	-0.0248	-0.0250	0.0259	0.0259
	0.2774	0.2773	0.0431	0.0433	0.1052	0.1055
	0.2856	0.2856	0.0497	0.0500	0.1083	0.1087

Table 6.2: Comparison of linear structure movement results for a freely floating vertical cylinder found with DIFFRACT by Eatock Taylor and Chamberlain (1993) and the author. For each wavenumber the real and imaginary components, and the modulus of these, are given.

6.3 Validation with Thunder Horse

The Thunder Horse mesh used in this section was introduced in Section 2.9 as Model 3. It is a slightly simplified version of Thunder Horse with dimensions averaged to make the model symmetrical about two planes of symmetry whilst maintaining the same displacement. It includes the pontoons and non-circular column cross-sections with the model in deep water. To allow the model to move rather than keeping it fixed, BP provided details on the displacement, centre of gravity, radii of gyration, etc. to allow calculation of the mass, hydro-restoring, and stiffness matrices that govern the body's motion in water.

A useful check to confirm that the DIFFRACT model is behaving as expected is to compare the predicted heave resonant period for the DIFFRACT model to the actual period for the real Thunder Horse structure. Thunder Horse has a heave resonant period of 26.2 s and Figure 6.1 plots the predicted amplitude of heave movement against incident wave period calculated for Model 3. Figure 6.1 shows a clear resonant frequency at 25.85 s, 0.35 s lower than the value given by BP. Model 3 is a simplified version of Thunder Horse so it is not surprising to see a small difference in the resonant frequency. It is close enough to support the use of Model 3 as a good approximation of Thunder Horse. It should be noted that the large amplitude of the predicted heave response at resonance is obviously not possible in real life. A 1 m incident wave could not cause a semi-submersible to move 67 m into the air. The reason for this gross overestimation is that the model used in DIFFRACT is damped only by wave radiation to infinity, and at the resonant peak this is clearly very small. The physical platform will have viscous damping from the submerged structure and a large number of mooring chains and cables, risers, and other equipment etc. attached to the platform that will provide a much higher level of viscous damping and restrict the motions to a large but physically possible magnitude.

To examine the heave response behaviour in more detail, Figure 6.2 plots the real and imaginary components, and the modulus of these, of the heave response versus period. When the period is very large, the phase of the heave response transfer function is approximately 0° and the amplitude of response asymptotes to one. This means that the structure simply

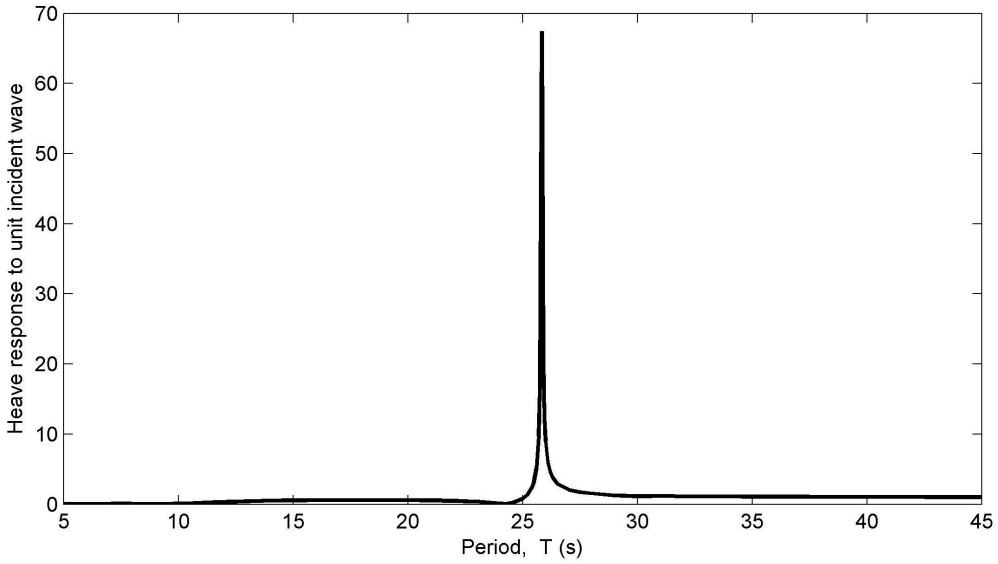

Figure 6.1: Heave motion vs. period for Thunder Horse Model 3 with pontoons in deep water and a unit-amplitude incident wave with $\beta = 45°$.

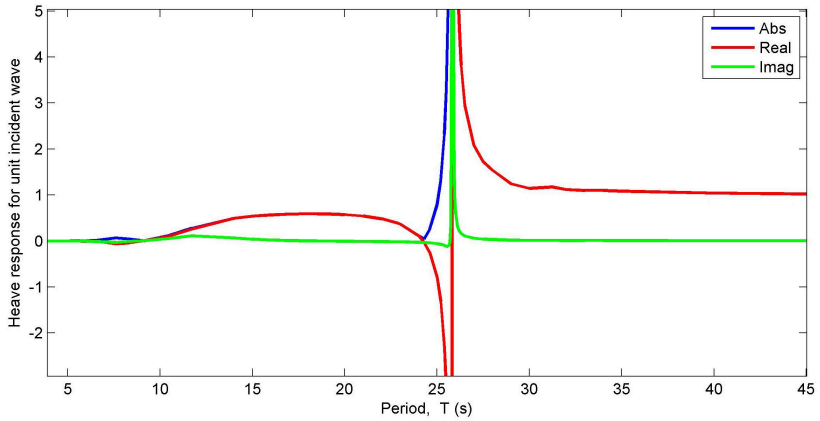

Figure 6.2: Real and imaginary components, and the modulus of these, of the structure's heave response vs. period, shown in blue, red, and green respectively for a unit-amplitude incident wave with $\beta = 45°$.

rides on top of the linear wave crest with no upwelling within the structure. As the period is decreased and approaches the resonant period the amplitude rapidly increases. There is a 180° phase shift across the resonant peak and then a short range of incident periods between 25.8-24.3 s where the structure would heave out of phase with the water surface elevation. The real part of the transfer function quickly increases after the resonant peak phase change, and for periods below $T = 24.3$ s the heave motion of the structure is again in phase with the incident wave crest.

For periods between approximately 4 s and 9 s, the structure moves out of phase with the incident wave but with very small amplitudes. For periods shorter than 4 s there is virtually

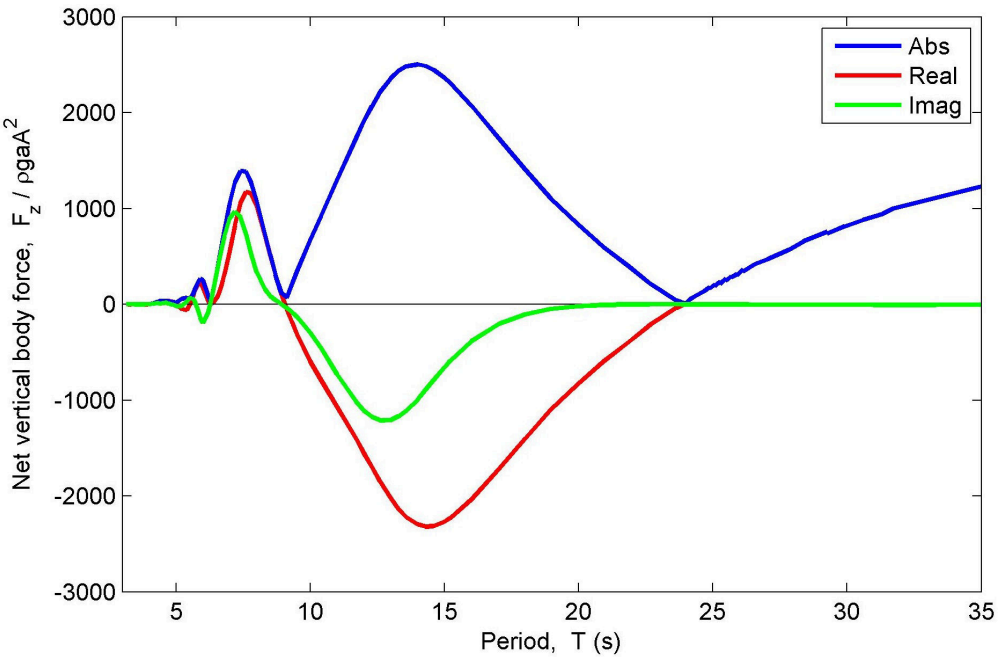

Figure 6.3: Real and imaginary components, and the modulus of these, of the net vertical force on the structure vs. period, shown in blue, red, and green respectively for a unit-amplitude incident wave with $\beta = 45°$.

no movement of the structure. The change in phase at a period of 25.85 s is due to crossing the resonant peak, but the changes in phase at periods of 4, 9, and 24.3 s correspond with a zero net vertical force on the structure. Pressure varies with depth at a decay rate dependent on incident wave frequency and when the net vertical force changes from positive to negative or vice versa, the heave response phase also changes. There would also be pressure variations across the pontoon at short periods with the length of pontoons determining the periods at which the phase changes. Figure 6.3 plots the real and imaginary components, and the modulus of these, of the vertical force to show the zero crossings match up with the heave response phase changes.

Figures 6.1 and 6.2 have shown that the heave response for periods shorter than 10 s is very small and approximately zero for periods below 4 s. The eigenperiods for surge, sway, roll, pitch, and yaw are all greater than 67 s. These are all sufficiently far from the peak periods of typical storm waves that, given the high inertia of the structure, it can be assumed there will be little response in any of these modes. This assumption combined with the minimal heave response for periods shorter than 10 s can be used as a further check to confirm that the model is behaving as expected. Local free surface motion between the

columns for a regular wave at periods shorter than 10 s should be very similar for fixed and moving models due to the negligible structure movement at these periods.

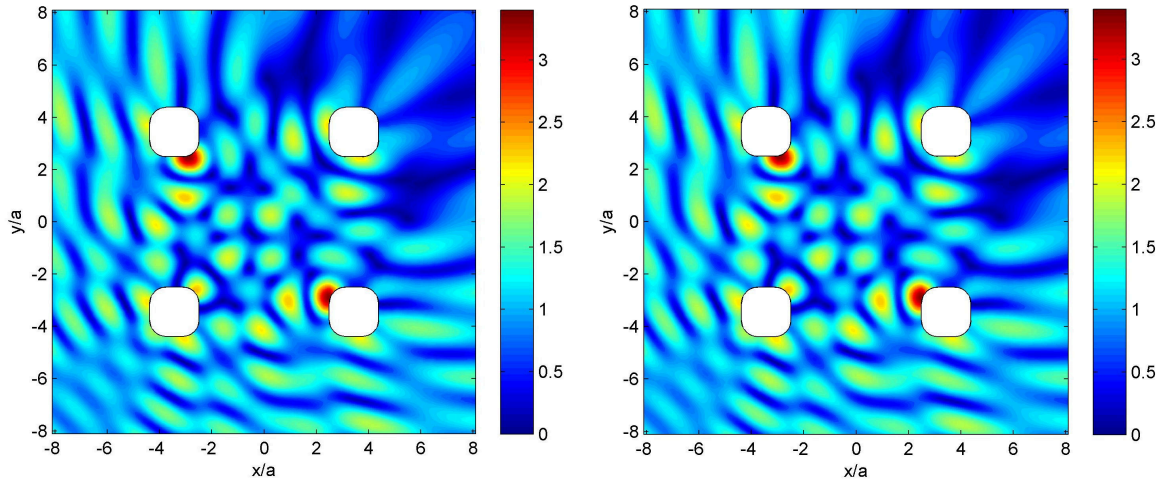

(a) Fixed (b) Moving

Figure 6.4: Modulus of the total surface elevation amplification for a unit-amplitude incident wave with $T = 4.409$ s, $\beta = 45°$ for (a) fixed and (b) moving structures.

Figure 6.4 compares the modulus of the surface elevation linear transfer function between a fixed and freely moving Model 3 type structure with a regular incident wave of $T = 4.409$ s, $\beta = 45°$. This is a near-trapped mode and so should lead to a strong wave-structure interaction. The plots for the two cases match extremely well, showing that the free surface motion around the moving model is behaving as expected at high frequencies. Overall, the results show that the model is behaving well and that it can be used to gain insight into the behaviour of Thunder Horse while using symmetry to minimise computation time.

6.4 Linear diffraction

Having shown that the moving model behaves as expected at very low and high frequencies, we can now look at how the model behaves in waves for typical storm wave periods. The surface elevations around this moving model can then be compared with equivalent results for the fixed model in an identical sea state. Figure 6.5 shows the modulus of the total surface elevation for a unit incident regular wave with $T = 7.582$ s and $\beta = 45°$, comparing

the results for fixed and moving structures. The overall pattern in the surface amplification is very similar for both the fixed and moving structures.

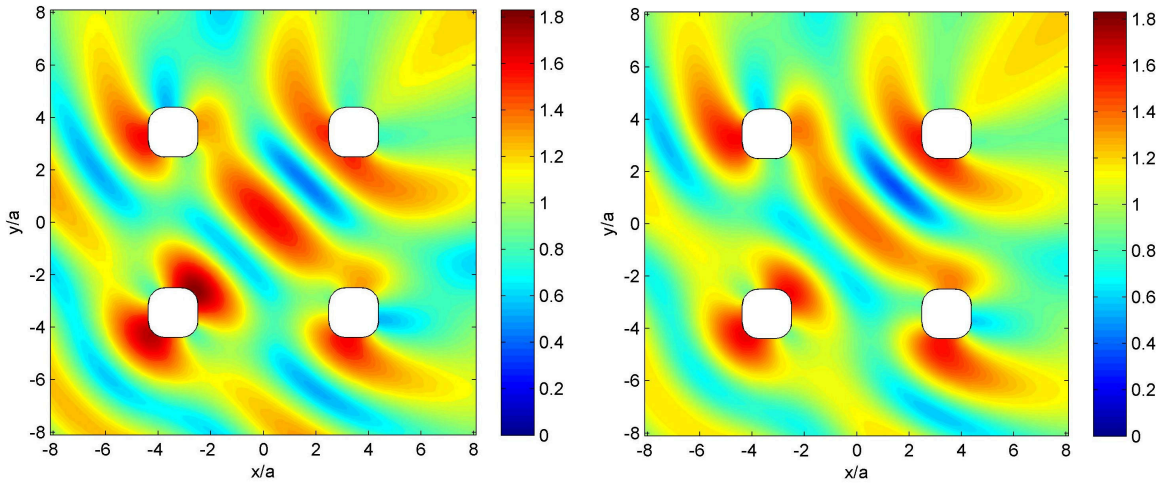

(a) Fixed (b) Moving

Figure 6.5: Modulus of the total surface elevation amplification for a unit incident wave with $T = 7.582$ s, $\beta = 45°$ for (a) fixed and (b) moving structures.

The main differences for the moving case are a reduction in amplitude of the peaks within the structure and a corresponding small increase in amplitude downstream. The surface elevation component caused by the movement of the structure interferes destructively with the diffraction pattern at this incident frequency. This causes the maximum free surface amplitude for a unit-amplitude incident regular wave to be reduced from 1.832 with a fixed structure to 1.649 with a moving structure. The differences between the fixed and moving cases are minimal, and so diffraction of the incident wave must be the dominant effect here. However, it may be useful to look at the radiation pattern caused by the movement of the structure separately.

Figure 6.6 shows the real and imaginary components, and the modulus, of the difference in total surface elevation amplification between the fixed and moving cases, where the difference is equal to $\eta_{Move} - \eta_{Fix}$. This should show the radiation pattern caused only by the movement of the structure. For periods shorter than around 10 s, the heave motion quickly decreases in amplitude. At short periods such as $T = 7.582$ s, the radiation surface elevations will contain contributions from surge and sway as well as heave. The surge and sway motions

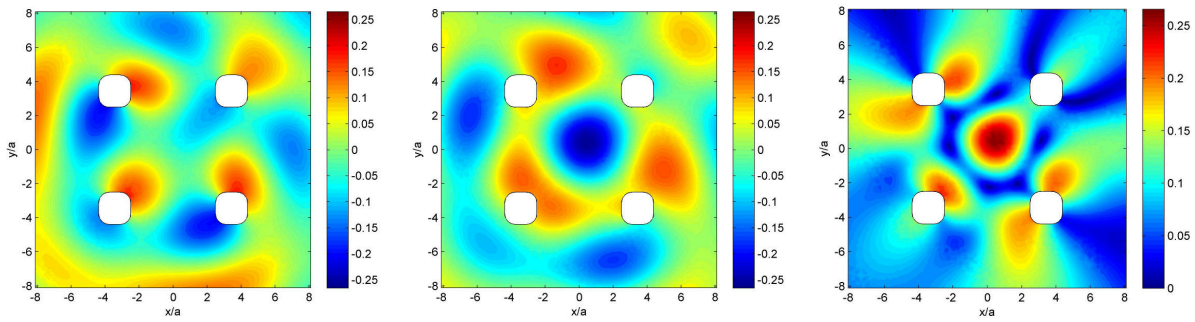

(a) Real (b) Imaginary (c) Modulus

Figure 6.6: Components of the difference in surface elevation amplification between fixed and moving structures for a unit incident wave with $T = 7.582$, $\beta = 45°$.

are still very small but decrease in amplitude more slowly with shortening period than heave motions. The maximum amplitude of the component due to structure movement is 0.266, significantly smaller than the fixed component with a maximum amplitude of 1.832. There is considerable antisymmetric surface radiation in the real component with runup upstream of each of the columns being 180° out of phase with the runup on the downstream side. There seems to be little correlation between the body motion radiation pattern and the near-trapped free surface mode shape (Figure 2.23) excited at this period.

The closest near-trapped mode to the one excited in Figure 6.6 has a period of 8.33 s, just 0.75 s longer than the previous case. The real and imaginary components, and the modulus, of the difference in total surface elevation amplification between the fixed and moving cases at this near-trapped mode are shown in Figure 6.7. The mode shape seen in Figure 6.7 is quite similar in shape to the previous case, with the imaginary component in Figure 6.7(b) being very similar to Figure 6.6(a) with a 180° phase difference. However, there are distinct differences which are highlighted when comparing the moduli for the two frequencies. The main difference is a strong peak in the centre of the array for the first case ($T = 7.582$ s) instead of a smaller peak upstream of the downstream column in the second case ($T = 8.33$ s). This could be interpreted as the antisymmetric mode seen in the second case being excited at both periods but for the first case there is a second local mode with a large central peak superimposed as well.

Figure 6.8 shows the real and imaginary components, and the modulus, of the difference in total surface elevation for the fixed and moving bodies at the next two near-trapped

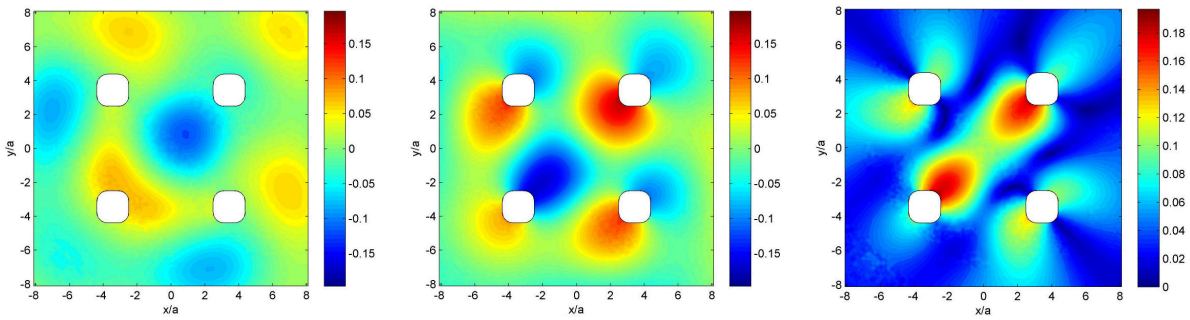

(a) Real (b) Imaginary (c) Modulus

Figure 6.7: Components of the difference in surface elevation amplification between fixed and moving structures for a unit incident wave with $T = 8.33$ s, $\beta = 45°$.

modes with smaller periods. Both cases are for $\beta = 45°$, and in Figure 6.8(a)-(c) $T = 6.408$ s, in Figure 6.8(d)-(f) $T = 5.865$ s. The surface elevation patterns quickly become more complicated, and the ratio of the maximum difference amplitude anywhere across the free surface, $|\eta_{Move} - \eta_{Fix}|_{Max}$, to the maximum elevation amplitude in the fixed case, $|\eta_{Fix}|_{Max}$, decreases. For the first nine near-trapped modes, Table 6.3 gives the maximum elevation amplitude for the moving and fixed cases, the amplitude of the maximum difference between the two cases, and the percentage of this relative to the maximum fixed case surface elevation. The surface elevations are normalised by the incident wave amplitude, and for all cases the wave direction is $\beta = 45°$.

Period, T (s)	Fixed	Moving	Difference	Ratio (%)
12.380	1.679	1.609	0.511	30.411
9.789	1.974	1.867	0.378	19.134
8.330	1.876	1.820	0.197	10.980
7.582	1.832	1.649	0.266	14.510
6.408	2.022	1.973	0.187	9.236
5.865	2.181	2.208	0.126	5.785
5.215	2.687	2.675	0.021	0.796
4.851	2.498	2.564	0.121	4.849
4.409	3.401	3.400	0.044	1.303

Table 6.3: Comparison of maximum surface elevation for fixed and moving cases and the ratio of the maximum difference and fixed elevations at near-trapped frequencies with $\beta = 45°$.

It is clear from the table that, at lower frequencies, the difference between the fixed and moving cases is much larger relative to the size of the fixed surface elevation. The lowest

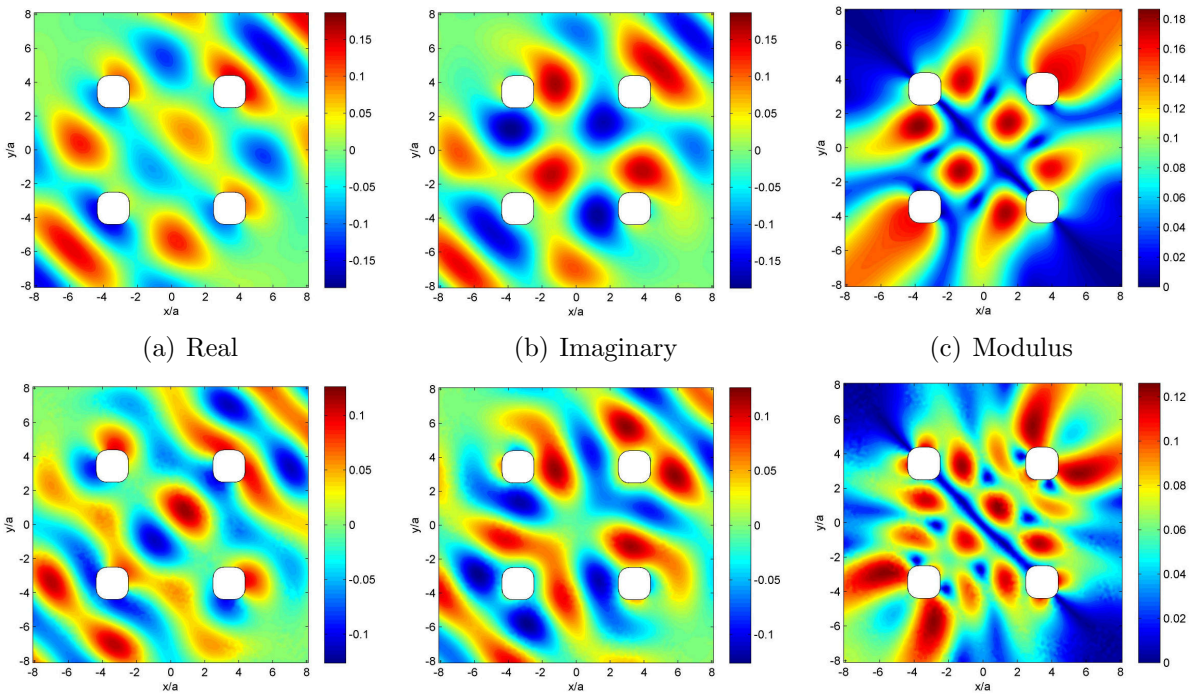

(a) Real (b) Imaginary (c) Modulus

(d) Real (e) Imaginary (f) Modulus

Figure 6.8: Components of the difference in surface elevation amplification between fixed and moving structures for a unit-amplitude incident wave with $\beta = 45\,^\circ$ and in (a)-(c) $T = 6.408$ s, in (d)-(f) $T = 5.865$ s.

near-trapped mode is important as this has a period of 12.38 s. This is within the range of likely storm periods and there are differences of up to 30 % between the two cases. At higher frequencies the difference is small but, as the majority of spectral energy is focused around the peak frequency in JONSWAP spectra, a moving Thunder Horse structure may experience rather different wave-structure interactions than for a fixed version of the same geometry.

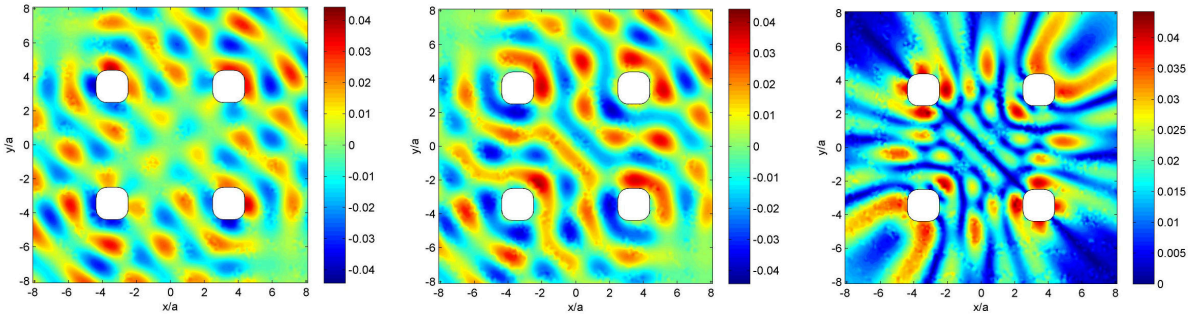

(a) Real (b) Imaginary (c) Modulus

Figure 6.9: Components of the difference in surface elevation amplification between fixed and moving structures for a unit incident wave with $T = 4.408$ s, $\beta = 45\,^\circ$.

In the previous section, the surface elevation was found at $T = 4.408$ s for the fixed and moving structures as a check to show that at low periods there is almost no movement. However, there is still some difference between the two, although very small compared to the fixed surface elevation amplitude, and this is shown in Figure 6.9. The maximum amplitude of the difference is just 1.3 % of the maximum fixed case surface elevation, and the pattern is extremely complex. When one looks at the figures for the difference in response between the fixed and moving models at the five periods shown, it seems there is a progression in the mode shape pattern as frequency increases. A similar progression was seen for near-trapped mode shapes but the mode shape patterns do not seem to match up with the moving body radiation patterns at the same frequencies.

6.5 Linear statistics of response

In Section 3.4.1, a method was discussed for generating a series of random time histories based on a given sea state to allow the collection of statistics of response. This method was applied to the now moving model and the results were compared with an equivalent fixed model. A modified time history is introduced where the vertical motion of the structure has been subtracted from the surface elevation. This ensures that a value of zero on the vertical elevation axis is 17.5 m below the platform deck, allowing a more direct comparison between the fixed and moving cases when one is interested in water-deck impact. The unrealistic response motions in heave at the resonant peak are avoided by cutting off spectra for periods longer than 24 s. Given the fairly sharp drop off in energy density for frequencies lower than the spectral peak in JONSWAP spectra, this cut-off should have a minimal effect for typical storm waves.

Figure 6.10 shows JONSWAP spectra with peak periods of (a) 15.164 s and (b) 19.578 s. The grey line in each shows the full spectrum and the black line shows the effect of ramping down the left hand side of the spectrum to remove components with periods below 24 s. The spectrum with a peak period of 15.164 s shows almost no loss in spectral energy when the cutoff is used. This is reassuring given the range of typical storm wave peak periods is 12-15 s. Figure 6.10(b) shows the spectra for a longer peak period of 19.578 s and there is now

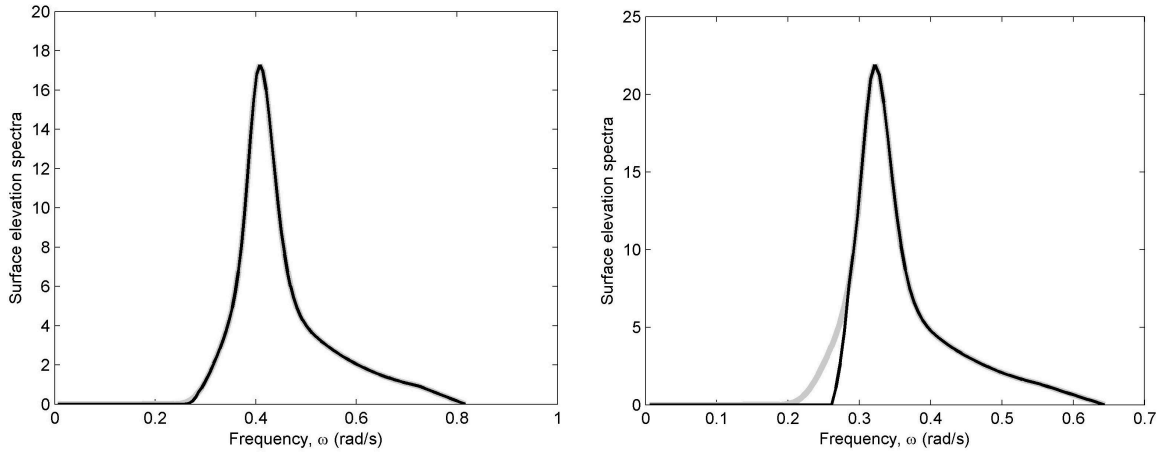

(a) $T_p = 15.164$ s (b) $T_p = 19.578$ s

Figure 6.10: JONSWAP spectra with peak periods of (a) 15.164 s and (b) 19.578 s, both with and without the cutoff for periods below 24 s (black line with the cutoff).

a larger, but still relatively small, loss of spectral energy. This must be taken into account when looking at low frequency wave groups but, since this is outside of the range of typical storm wave peak periods, these results are less important when investigating water-deck impact. Large low frequency drift responses may result in a small reduction in air-gap due to large horizontal movements and finite mooring cable lengths but this is likely to be very small relative to diffraction effects.

Figure 6.11 shows typical random surface elevation time histories at the geometric centre of the structure, (0 m, 0 m), for the fixed and moving models with the same incident wave in each case. This incident wave was based on a JONSWAP spectrum with $T_p = 15.164$ s, $H_s = 12$ m, and $\beta = 45°$. There are two time histories plotted for the moving case. The red line simply shows the total surface elevation about the mean level when the wave is incident on the moving structure. The green line shows the modified time history where the vertical motion of the structure has been subtracted from the surface elevation, giving the free surface elevation relative to the floating structure.

The difference in elevation above mean sea level for each crest and trough between the fixed model case (blue line) and the moving model (red line) is small relative to the total elevation. The plot for the moving case is generally within ±10 % of the fixed model time history. However, when the moving case is modified to take into account structure motion

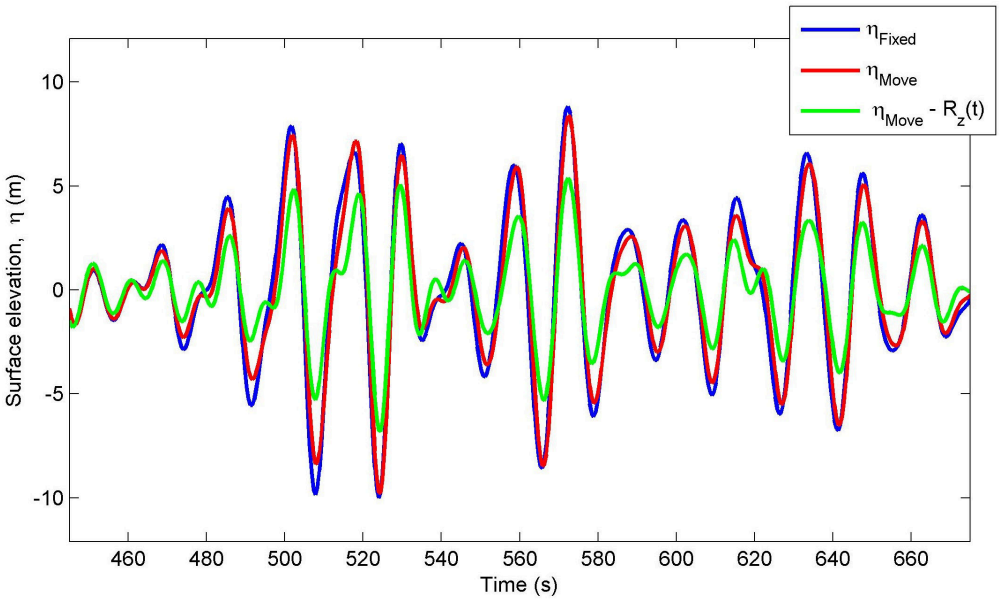

Figure 6.11: An example random surface elevation time history at the centre, ($x = 0$ m,$y = 0$ m), of a fixed and moving model with $T_p = 15.164$ s, $H_s = 12$ m and $\beta = 45°$.

(green line) the effective crest and trough amplitude is greatly reduced. This is because the structure motions are in phase with the surface elevation, as discussed in Section 6.3, and the structure effectively rides the crest of the longwave components with little change to the air-gap beneath the deck. The diffraction pattern seen between the columns is then made up of the higher frequency components, resulting in a smaller proportion of the total spectral energy contributing to the diffraction pattern.

To quantify the change in surface elevation relative to the deck caused by allowing the model to move, the method of Section 3.4.1 was used to generate 10000 random time histories in the sea state discussed above, and the average was taken of the time histories around the top 500 crests at the geometric centre of the moving model. The incident waves leading to the largest crests in the moving case were found and used as incident waves with the fixed structure. The average surface elevation for the responses with the fixed and moving models are shown in 6.12(a) with the fixed case shown in grey and the moving case in black. This method was then reversed so that the top 500 crests for the fixed model were found and the incident waves leading to these were used with the moving model. This reversed case is shown in Figure 6.12(b) for comparison. For 10000 spectra in this sea state, the average of the top 500 crests gives approximately the one-in-1500 wave case.

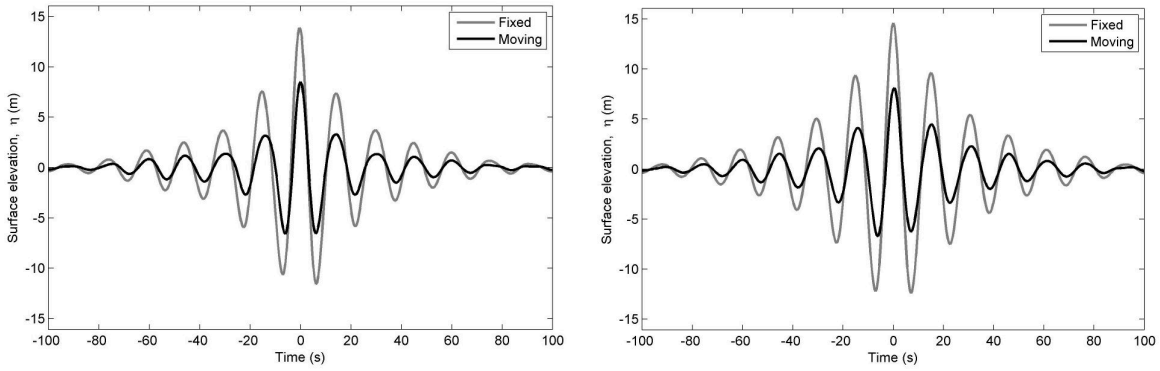

(a) Moving top 500 (b) Fixed top 500

Figure 6.12: Average of the top 500 crests at the geometric centre of (a) the moving body and (b) the fixed body with the equivalent results if incident on the other model. $T_p = 15.164$ s, $\beta = 45°$.

In Figure 6.12(a) with the moving model top 500, the average maximum elevation reached was 8.52 m, and this increased by 62.7 % to 13.86 m when the same incident waves interacted with the fixed model. However, if the top 500 crests are found for the fixed structure, these have an average maximum elevation of 14.6 m. The equivalent incident waves on a moving body then have an average maximum elevation of just 8.09 m. These results clearly show that allowing the structure to move greatly reduces the maximum surface elevation relative to the deck level for these sea states. Since the deck is 17.5 m above mean sea level, this means that the remaining air-gap for the one-in-1500 wave linear response is 2.9 m for the fixed model but 6.98 m in the moving case. This is a huge difference and confirms that when calculating the likelihood of water-deck impact for a given sea state, vertical body motions are very important.

The results also show that there are only fairly minor changes in the average extreme crest elevation if the incident wave is chosen to cause the largest crests with the fixed or moving models. This suggest that there are only minor differences between the 'designer' wave for fixed and moving structures in this sea state. Second-order 'designer' waves for extreme responses will be discussed in Section 6.7. Considering linear responses only, a version of reciprocity will hold for these two cases, similar to the case discussed in Section 3.3.3. Figure 6.13 compares the moving body surface elevation from Figure 6.12(b) with the fixed body surface elevation from 6.12(a) inverted in time. The red line with each datum marked by an asterisk plots the moving body surface elevation and the blue line plots the

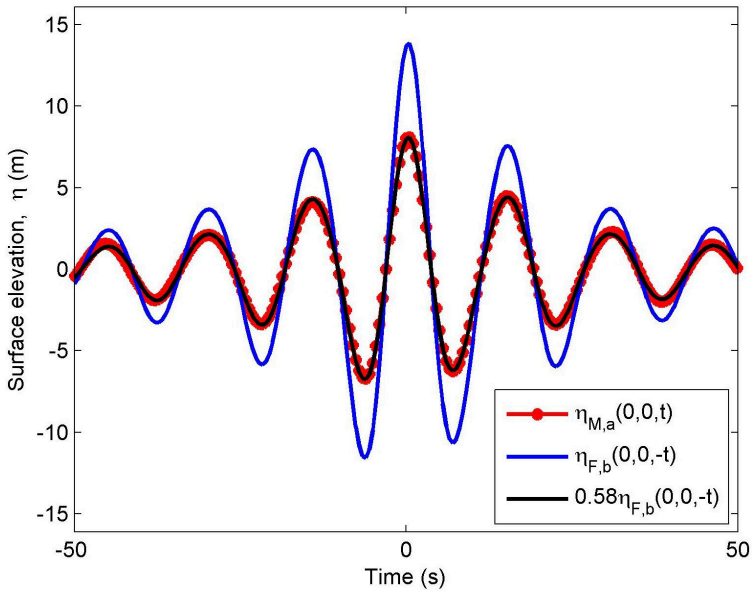

Figure 6.13: Reciprocity relationship between fixed and moving body surface elevation time histories. $T_p = 15.164$ s, $\beta = 45°$, η at the geometric centre of the structure.

fixed body surface elevation plotted against $-t$ rather than t. The shape of the two wave packets are extremely similar. To emphasize this, the black line shows a scaled down version of the fixed body elevation so that the maximum crest elevation is the same as that of the moving body case. The scaled fixed case surface time history shown in black matches the moving case time history very well.

The results given in previous chapters for fixed models are useful guides to frequencies and locations of interest, and the methods developed to produce those results are still valid and useful, but the predictions of surface elevation and likelihood of water-deck impact for the Thunder Horse semi-submersible need to be recalculated with a moving model. If Thunder Horse were a TLP then the fixed results of previous chapters would still be a good approximation because the vertical movement is very restricted in a TLP by the nature of the very stiff tendon system. However, for a semi-submersible, the catenary mooring system allows vertical movement which clearly needs to be taken into account.

At the lower end of the typical storm range periods, Figure 6.14 shows results for random incident JONSWAP waves with $T_p = 12.38$ s and $\beta = 45°$. Figure 6.14(a) shows an example of a random time history at the centre of the array with the body motions obviously having less effect on the maximum crest elevation relative to the deck. This is confirmed in Figure

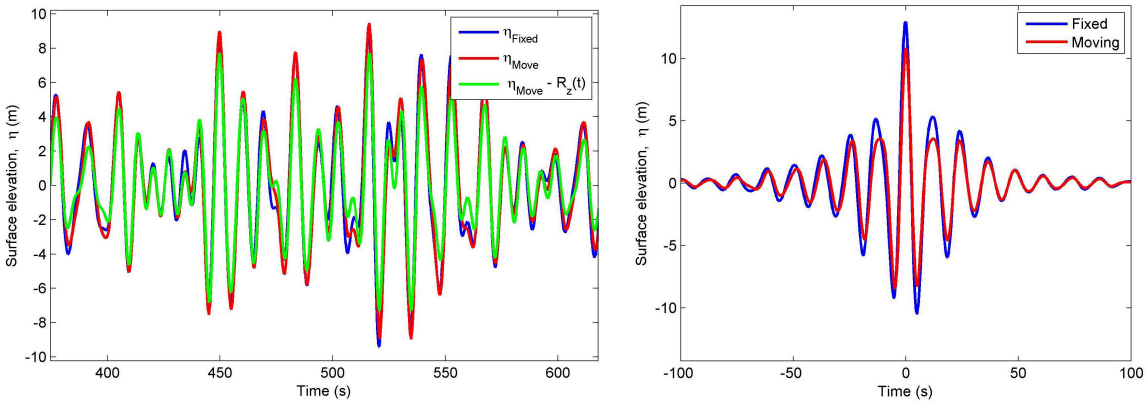

(a) Surface elevation (b) Top 500 crests

Figure 6.14: (a) An example random surface elevation time history and (b) the average of the top 500 crests in the moving case and the equivalent results if those waves were incident on the fixed model. $T_p = 12.38$ s, $\beta = 45°$.

6.14(b) which shows the average surface elevation for the top 500 crests in the moving case and the equivalent average elevation if the same incident waves interacted with the fixed structure. There is a much smaller increase of 19.4 % from the moving to the fixed case, with maximum elevations of 10.84 m and 12.94 m respectively. This reduction in the difference between the moving and fixed models is to be expected since the heave transfer function shown in Figure 6.1 was seen to have very low amplitude for periods shorter than around 10 s.

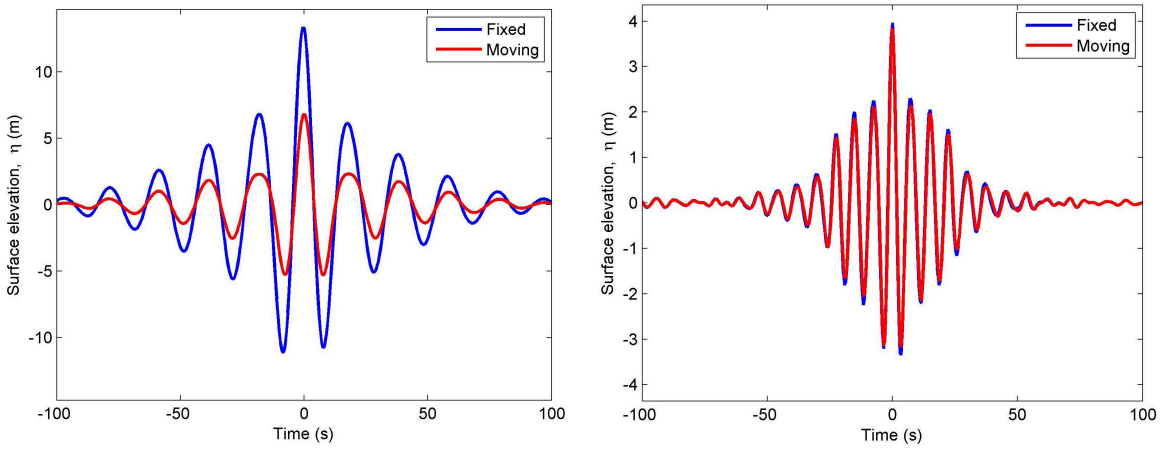

(a) $T_p = 19.6$ s, $H_s = 12$ m (b) $T_p = 7.58$ s, $H_s = 3$ m

Figure 6.15: Average of the top 500 crests in the moving case and equivalent fixed case results for $\beta = 45°$ and (a) $T_p = 19.578$ s, $H_s = 12$ m and (b) $T_p = 7.582$ s, $H_s = 3$ m.

Figure 6.15 shows the average surface elevation for the largest 500 crests at the centre

of the moving model for two rather artificial sea states: (a) $T_p = 19.578$ s, $H_s = 12$ m and (b) $T_p = 7.582$ s, $H_s = 3$ m. These emphasize the results found in the previous examples. The long period sea state of $T_p = 19.578$ s shows a very large difference in the maximum surface elevation between the fixed and moving models whereas the high frequency sea state of $T_p = 7.582$ s shows that there is very little difference between the fixed and moving models. These two examples are useful to illustrate the difference in fixed and moving model behaviour but lie outside the range of periods that one would expect for strong storm waves on the open sea.

6.5.1 NAF

In Section 3.3.1, a Net Amplification Factor (NAF) was introduced as a concept to illustrate where, in the vicinity of a structure, violent wave-structure interactions are most likely to occur. This was then validated by collecting statistics from random surface elevation simulations with and without a structure present. The NAF concept can also be used with a moving body by replacing the fixed model linear transfer functions (LTF) used in Section 3.3.1 with LTFs calculated for a moving model. If the moving LTF used does not include body motions then the moving NAF will not take into account the change in air-gap due to the model movement but it will illustrate how radiation due to movement of the body affects the wave-structure interaction relative to the mean water surface elevation. This NAF relative to the mean water level is shown in Figure 6.16(b), with a fixed model equivalent shown for comparison in Figure 6.16(a).

Figure 6.16 compares a NAF plot for fixed and moving models relative to the mean water level with a peak period of $T_p = 15.164$ s and wave direction $\beta = 45°$. This period was chosen because it is within the typical range of storm peak periods (around 12-15 s) and has been used with second-order calculations elsewhere in this research as it excites a near-trapped mode with frequency doubling. The pattern is very similar for both models but the moving case pattern is obviously reduced in amplitude. The maximum value reached in the moving case is 1.40, which is 8.3 % less than the fixed model with 1.53. The location of the maximum is the same in both cases, just upstream of the downstream column.

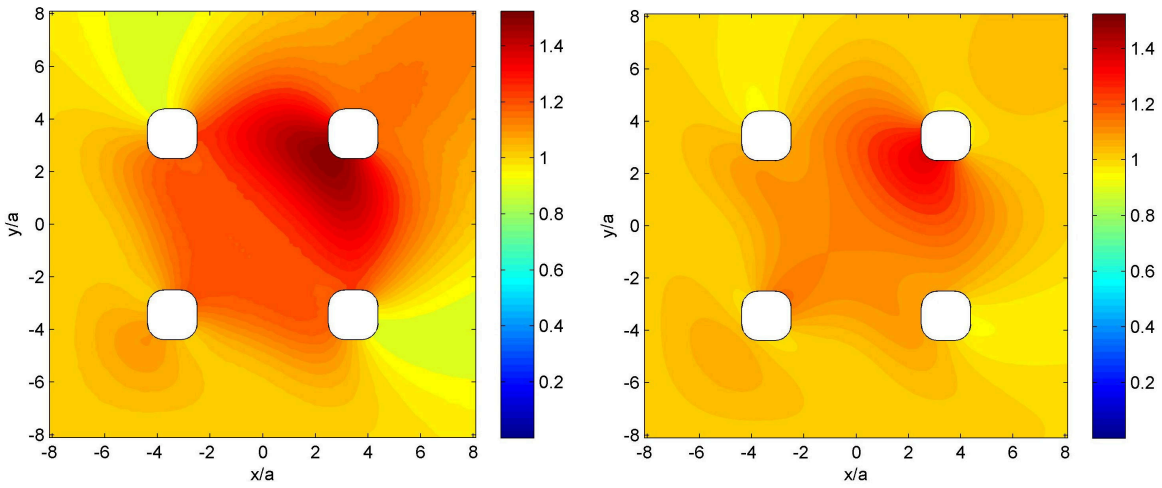

(a) Fixed (b) Moving

Figure 6.16: Net amplification factor for water surface relative to mean sea level for (a) fixed and (b) moving models with $T_p = 15.164$ s, $\beta = 45\,^\circ$.

The LTF used in the moving model NAF calculation can also include the body motions so that the surface elevation amplification value is then found relative to the platform deck. This is obviously of more practical use when calculating the air-gap needed for a structure. Figure 6.17(a) shows the NAF field plot relative to the deck height for the same conditions as the previous example: $T_p = 15.164$ s, $\beta = 45\,^\circ$. Figure 6.17(b) verifies this result through the collection of statistics from Monte Carlo simulations of random waves, as discussed in Section 3.4.

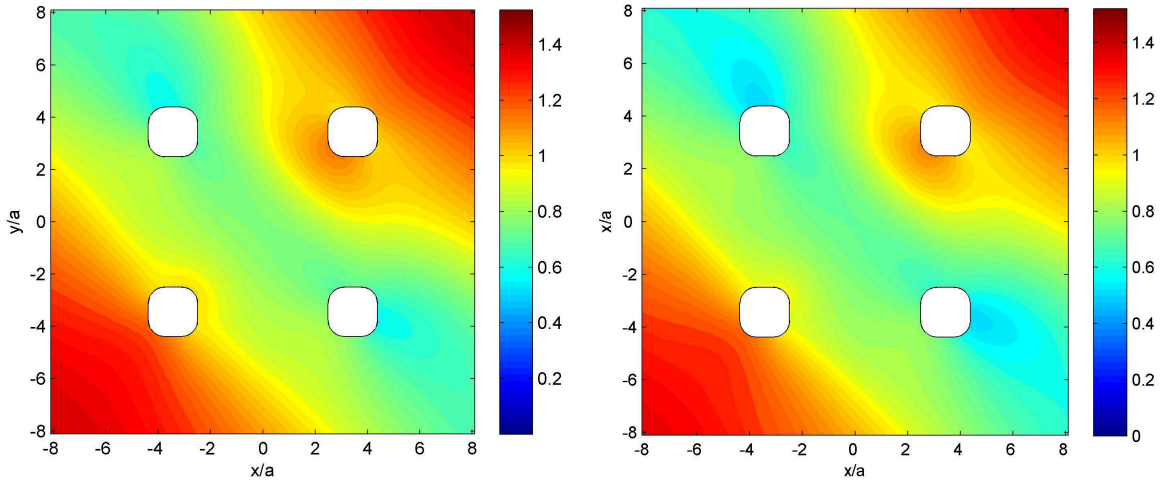

(a) NAF relative to deck (b) Collected statistics

Figure 6.17: Net amplification factor for water surface relative to platform deck found by (a) NAF and (b) Monte Carlo statistics with $T_p = 15.164$ s, $\beta = 45\,^\circ$.

The air-gap NAF has a reduced amplitude in the centre of the structure when compared with the fixed sea level NAF plots. There is still obviously runup upstream of the rear column with the highest elevations under the deck located there. However, this only has a maximum amplitude of 1.16 which is significantly less than the value of 1.53 in the fixed case. The air-gap NAF plot is dominated by a large band of reduced amplitude across the structure perpendicular to the incident direction and high amplitude areas upstream and downstream of the columns. This is because LTFs for diffraction and radiation effects vary with location but the body motion LTF does not. The body motion and surface elevation time histories are therefore in phase near the centre of rotation, reducing the relative surface amplification and causing the band of low amplitude across the centre of the plot. The largest component of the incident spectrum has a period of $T_p = 15.164$ s, which corresponds to a wavelength of around 360 m. The diagonal column spacing is 117 m and the area plotted has a diagonal distance of 283 m. It is therefore not surprising that at the corners upstream and downstream of the structure, the body motion and surface elevation time histories are out of phase and lead to increased surface elevation relative to deck height.

Figure 6.18 compares field plots of NAF with a lower period of 12.38 s for (a) a fixed body, (b) a moving model with NAF relative to mean water level (MWL), and (c) moving model with NAF relative to deck height. This period was chosen as it is at the other end of the typical range of storm peak periods and linearly excites the lowest near-trapped mode. The fixed body and moving body relative to MWL field plots are again very similar, with less difference in amplitude than the previous case. The maximum amplitude around the moving model is 1.61 which is only 1.3 % less than the fixed model with a maximum of 1.63. The moving body NAF calculation relative to deck height still shows obvious signs of the phasing difference between the body motion and surface elevation time histories outside of the array. However, it is easier to see the diffraction pattern showing through in this case. The maximum amplification within the array for the air-gap case is runup on the rear column with a value of 1.46. This is much closer to the other two models and shows that the effects of body motions are quickly reduced as periods become shorter.

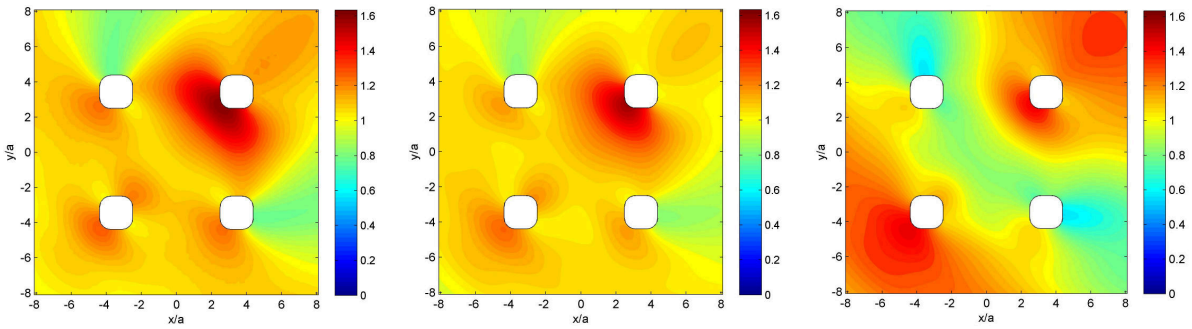

(a) Fixed body (b) Moving, relative to MWL (c) Moving, relative to deck

Figure 6.18: Net amplification factor for water surface elevation with (a) fixed model, (b) moving model relative to mean water level (MWL), and (c) moving model relative to deck height, all with $T_p = 12.38$ s, $\beta = 45\,^\circ$.

6.6 Second-order diffraction

Figure 6.19 shows the response at the near-trapped mode with $\omega_R = 0.980$ rad/s ($T_R = 6.408$ s), $\beta = 0^\circ$ for linear and second-order excitation with both fixed and moving versions of Thunder Horse Model 3. Figures 6.19(a) and 6.19(b) are for the fixed model, and Figures 6.19(c) and 6.19(d) are for the moving model. Figures 6.19(a) and 6.19(c) are for linear excitation of the near-trapped mode, and Figures 6.19(b) and 6.19(d) are the second-order potential sum response to an incident wave of $\omega = 0.490$ rad/s ($T = 12.816$ s).

The linear responses are almost identical for the fixed and moving models, with a maximum amplitude of the difference between the two being just 4 % of the fixed model maximum response. The second-order potential sum responses show a much greater difference between the fixed and moving cases in both amplitude and the diffraction pattern. The diffraction pattern of the moving case seems to be closer to the linear excitation pattern than for the fixed model second-order potential sum response. The large amplitude runup on the upstream columns and the reflections upstream of the array seen in the linear excitation case are not present in the moving second-order potential sum response, but within the array the pattern is fairly similar. Downstream of the array, the response at second-order is fairly high relative to the peaks within the array whereas the linear case shows more sheltering.

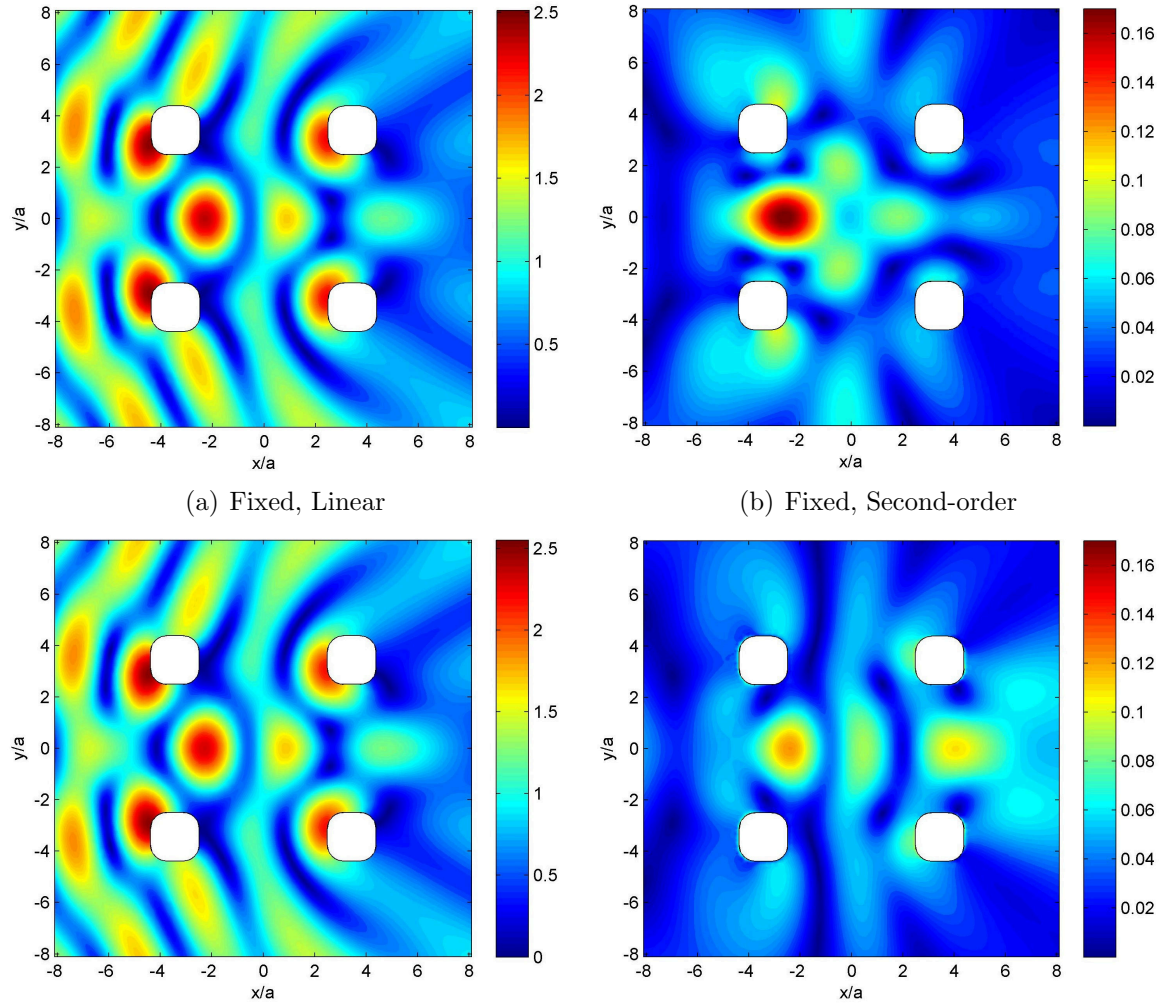

(a) Fixed, Linear

(b) Fixed, Second-order

(c) Moving, Linear

(d) Moving, Second-order

Figure 6.19: Linear and second-order potential sum excitation of a near-trapped mode with fixed and moving versions of Thunder Horse Model 3 and $\omega_R = 0.980$ rad/s ($T_R = 6.408$ s), $\beta = 0°$.

The moving case has a maximum potential sum response amplitude of 0.124 m for a unit-amplitude incident wave, which is 29 % less than for the fixed model case with 0.174 m. The magnitude of the difference in second-order potential sum between the moving and fixed models is given in Figure 6.20 and shows two large peaks within the centre of the array, a large difference in the runup on the downstream columns, and a fairly large difference in the amount of sheltering downstream of the array. The large amplitude of the maximum difference when compared to the maximum amplitude reached in the moving case shows that there must be a large phase difference between the two models. This is shown in Figure 6.21 which plots the real and imaginary components of the second-order potential sum response for the fixed and moving models. The imaginary part of the fixed model case shows a large trough between the upstream columns. In the imaginary part of the moving case there are

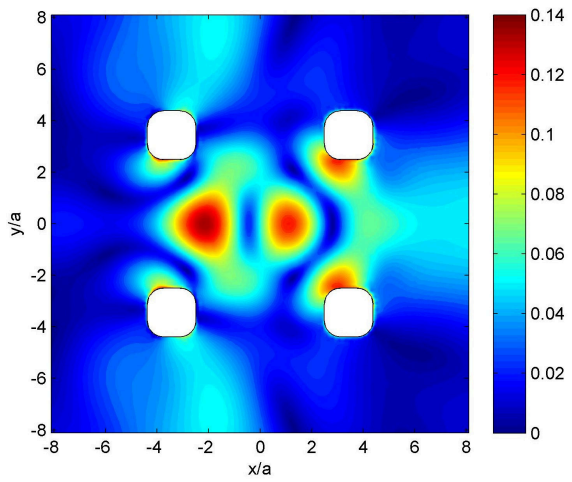

Figure 6.20: Difference in second-order potential sum excitation of a near-trapped mode between fixed and moving versions of Thunder Horse Model 3 with $\omega_R = 0.980$ rad/s ($T_R = 6.408$ s), $\beta = 0°$.

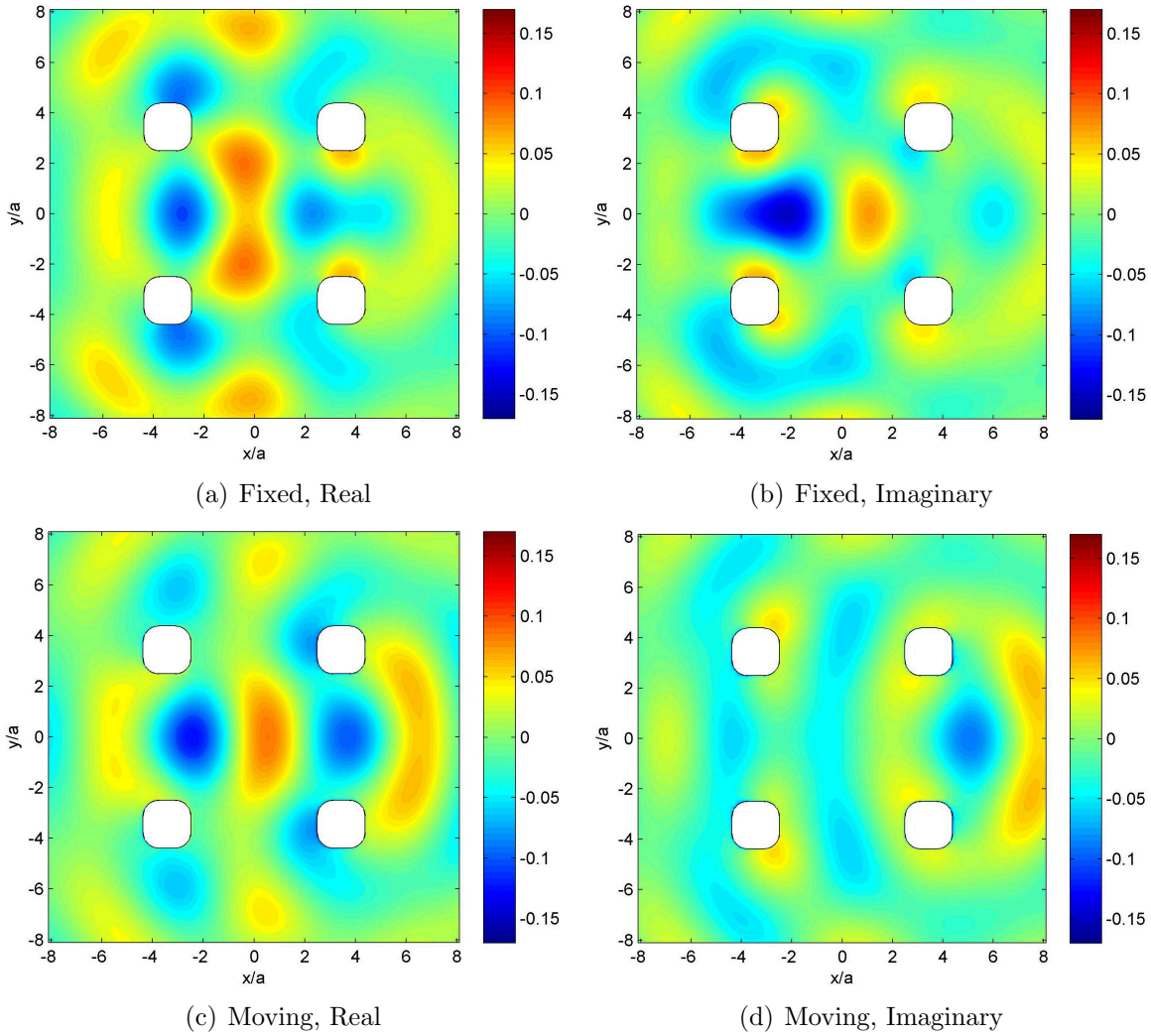

(a) Fixed, Real

(b) Fixed, Imaginary

(c) Moving, Real

(d) Moving, Imaginary

Figure 6.21: Components of the second-order potential sum excitation of a near-trapped mode with fixed and moving versions of Thunder Horse Model 3 and $\omega_R = 0.980$ rad/s ($T_R = 6.408$ s), $\beta = 0°$.

only minimal reductions in amplitude and a large trough appears 90° earlier in the real component.

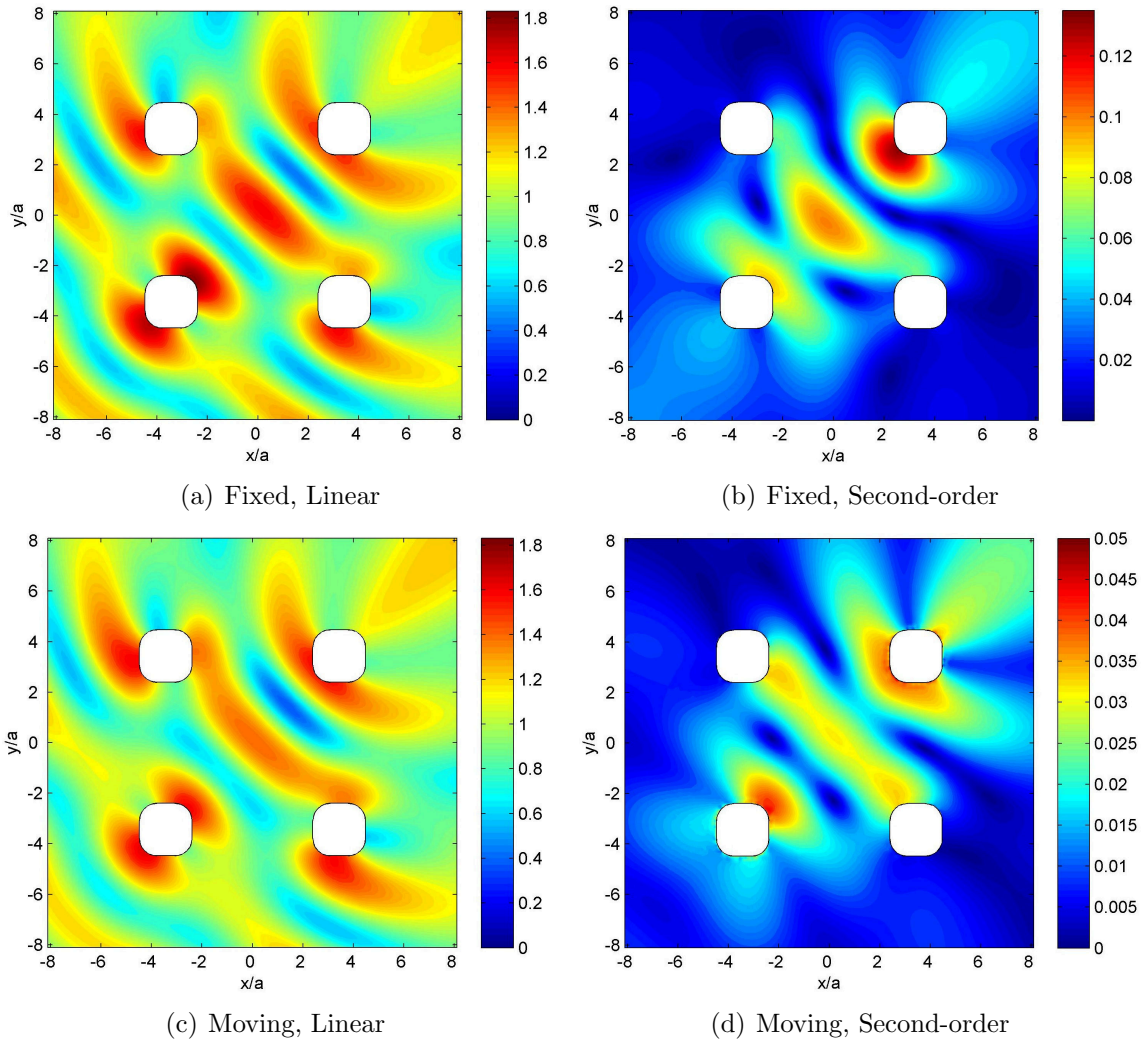

(a) Fixed, Linear

(b) Fixed, Second-order

(c) Moving, Linear

(d) Moving, Second-order

Figure 6.22: Linear and second-order potential sum excitation of a near-trapped mode with fixed and moving versions of Thunder Horse Model 3 and $\omega_R = 0.829$ rad/s ($T = 7.582$ s), $\beta = 45°$.

The differences between fixed and moving models with linear and second-order excitation are again studied, this time for a unit-amplitude incident wave at a near-trapped mode with $\omega_R = 0.829$ rad/s ($T_R = 7.582$ s), $\beta = 45°$. The results are shown in Figure 6.22 with Figures 6.22(a) and 6.22(c) showing linear excitation of the near-trapped mode, and Figures 6.22(b) and 6.22(d) showing second-order potential sum response to an incident wave of $\omega = 0.414$ rad/s ($T = 15.164$ s). Figures 6.22(a) and 6.22(b) are for the fixed model, and Figures 6.22(c) and 6.22(d) are for the moving model. The differences between the four plots

are rather similar to those discussed in Figure 6.19. The moving and fixed model responses are closer with first-order excitation than at second-order. The second-order moving case is closer to the linear diffraction pattern than the fixed second-order response within the array but the high runup upstream of the leading three columns and reflections upstream of the array that are seen in the linear cases are not present at second-order. There is an increase in the elevation downstream of the moving structure relative to the peaks in the centre and the maximum amplitude of the second-order potential sum response is greatly reduced in the moving model with a value of 0.04 m, down from 0.14 m in the fixed case.

6.7 Second-order statistics of response

The methods of generating random spectra discussed in Section 3.4.1 are used here, with both linear and quadratic transfer functions calculated for fixed and moving models, to see how body movement affects extreme wave-structure interactions to second-order. The modified time history is used again where the vertical motion of the structure has been subtracted from the surface elevation to ensure that a value of zero on the vertical elevation axis is 17.5 m below the platform deck. The spectral cut-off at periods longer than 24 s is used to remove the unrealistic body motions in heave at the resonant peak.

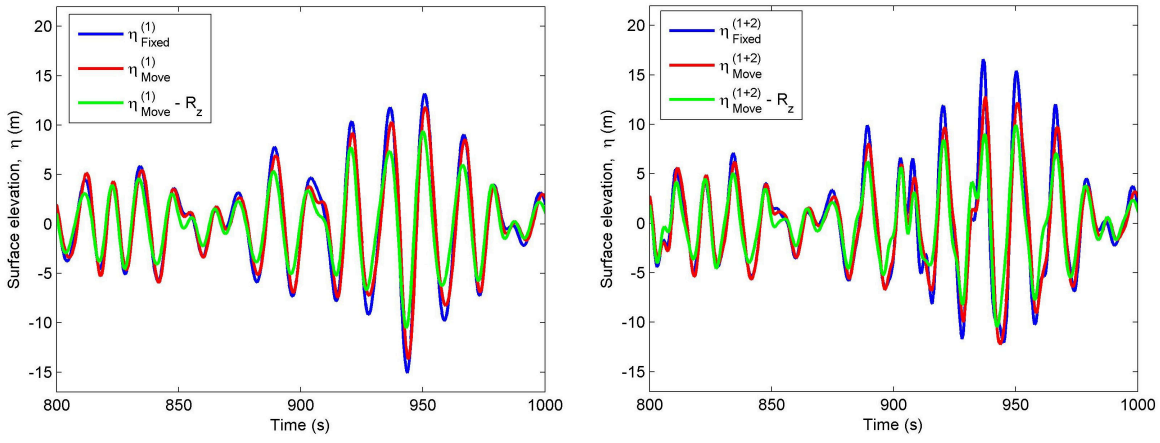

(a) First-order (b) Second-order

Figure 6.23: An example random surface elevation time history to (a) first-order and (b) second-order, both at the centre of a fixed and moving model with $T_p = 15.164$ s, $H_s = 12$ m, and $\beta = 45°$.

Figure 6.23 shows an example random time history to (a) first-order and (b) second-order for fixed and moving models in a sea state with peak period $T_p = 15.164$ s, significant wave height $H_s = 12$ m, and wave direction $\beta = 45°$. The blue line shows the water surface elevation at the centre of the array for a fixed model, the red line shows the surface elevation relative to mean water level at the centre of the moving model, and the green line shows the modified moving model surface elevation with the zero elevation fixed at 17.5 m below the deck. For the linear case, Figure 6.23(a), the fixed and unmodified moving cases are fairly close with only a small reduction in amplitude for the moving model. After taking into account body heave motions, the green line shows there is a larger difference relative to the fixed model with crest and trough amplitudes reduced by a fairly even amount.

Figure 6.23(b) shows a surface elevation time history from the identical segment of a random time history, but now to second-order. There is a larger difference in crest amplitude between the moving cases and the fixed model compared to first-order, and the troughs of the fixed, moving, and air-gap cases are now closer in amplitude. There is a substantial difference in maximum crest height between the fixed and moving models shown in this second-order time history, with the fixed model reaching a maximum elevation of 16.58 m compared to the maximum elevation in the modified moving case (green line) of 9.94 m. Figure 6.24 compares the average extreme crest elevation time histories for fixed and moving models at two locations in the array. The largest 500 crests relative to the deck at 17.5 m were identified in the fixed and modified moving cases and then, at each point in time, the average of these 500 elevation time histories was found. Figure 6.24(a) compares the average extreme crest elevations at the centre of the array, and Figure 6.24(b) compares the average extreme crest elevations just upstream of the downstream column.

At both locations, the average extreme crest elevations for the fixed and moving models show a similar NewWave type shape with a reduction in amplitude for the moving case. There is a larger reduction at the centre of the array with maximum average extreme crest elevations of 21.0 m and 11.8 m for the fixed and moving cases respectively. In Figure 6.24(b) there are larger maximum elevations and a smaller difference between the two with values of 24.8 m and 19.5 m respectively. To gain a better understanding of the physics behind these

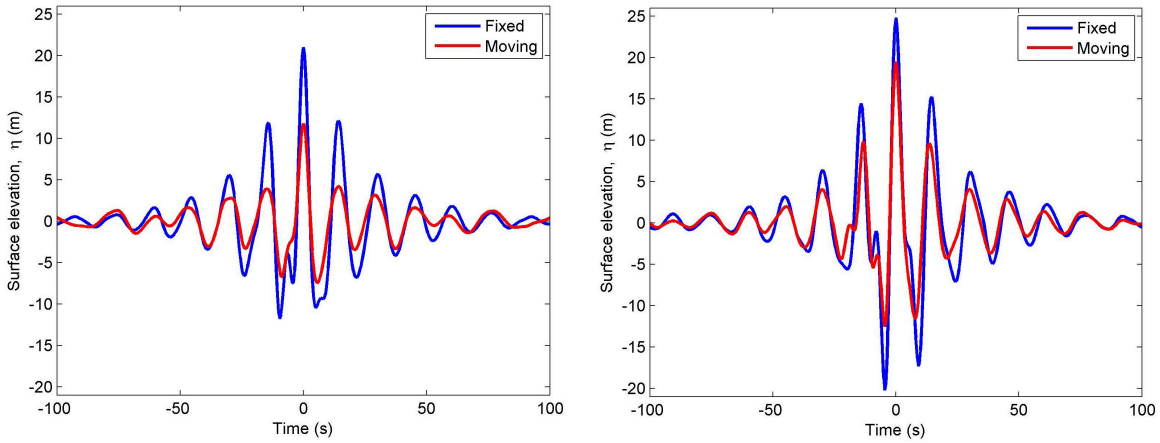

(a) Centre of the structure (b) Just upstream of the downstream column

Figure 6.24: Average of the top 500 crests to second-order for moving and fixed models at (a) the centre of the array and (b) just upstream of the downstream column with $T_p = 15.164$ s, $\beta = 45°$.

extreme wave-structure interactions the individual components contributing to these large elevations will be investigated.

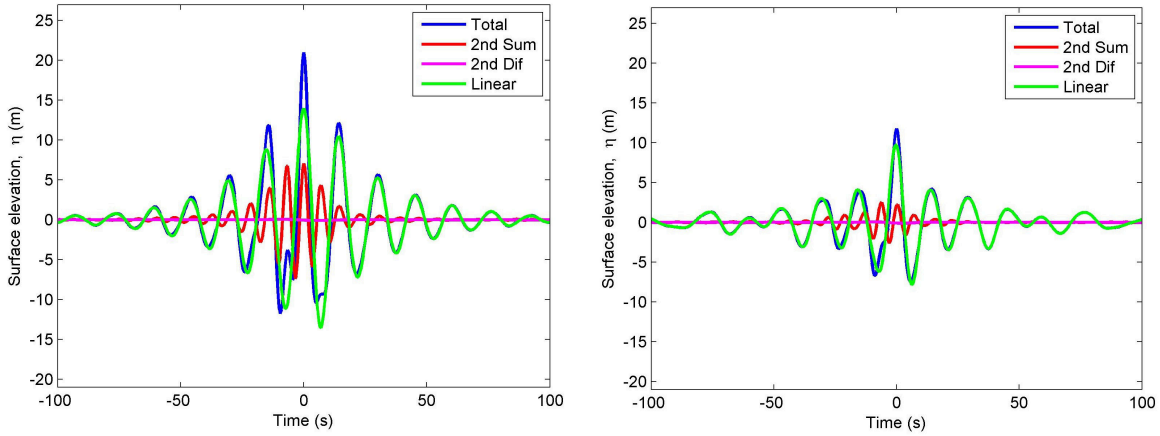

(a) Fixed (b) Moving

Figure 6.25: Components of the average of the top 500 crests to second-order for (a) fixed and (b) moving models at the centre of the array with $T_p = 15.164$ s, $\beta = 45°$.

Figure 6.25 shows the components of the average extreme crest time history at the centre of the (a) fixed and (b) moving models with the same sea state as the previous examples: $T_p = 15.164$ s, $H_s = 12$ m, and $\beta = 45°$. The fixed model case, Figure 6.25(a), has a large second-order sum component with a maximum amplitude of 7.39 m, 52.9 % of the linear component, which has an amplitude of 13.97 m. The moving model case, Figure 6.25(b),

has a much smaller second-order sum component with a maximum amplitude of 2.61 m, 26.8 % of the linear component, which has an amplitude of 9.74 m. There are differences in the focus times for the linear and second-order components in both models, with the second-order sum component reaching its maximum value 3-4 s before the linear component. This means that at time $t = 0$ s for the largest crest elevation, the contribution due to second-order sum interactions is less than the maximum value. For the fixed case the second-order sum contribution at $t = 0$ s is 7.07 m and for the moving case it is 2.17 m. The second-order difference component is very small compared to the other components in both cases.

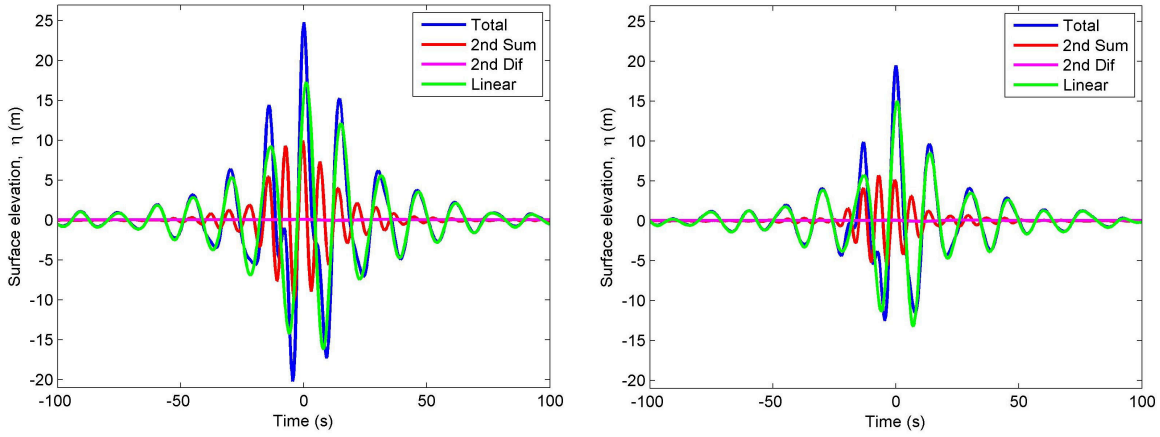

(a) Fixed (b) Moving

Figure 6.26: Components of the average of the top 500 crests to second-order for (a) fixed and (b) moving models at a point just upstream of the downstream column with $T_p = 15.164$ s, $\beta = 45°$.

Figure 6.26 shows the components of the average extreme crest time history just upstream of the downstream column with (a) fixed and (b) moving models, and the same sea state as the previous examples: $T_p = 15.164$ s, $H_s = 12$ m, and $\beta = 45°$. The fixed case has a maximum linear amplitude of 17.32 m and a maximum second-order sum component of 10.14 m. The moving case has linear and second-order sum maximum amplitudes of 15.05 m and 5.69 m respectively. The linear components are fairly similar for the two models but the second-order sum elevation in the moving case is just over half that of the fixed case. As with the last example there is a difference in focus time between the linear and second-order sum components, in this case around 5.5 s. There is a smaller reduction in the contribution of the second-order component to maximum crest elevation relative to the previous example

as the shape of the second-order sum packet is more rounded with a slower drop in amplitude either side of the focus time.

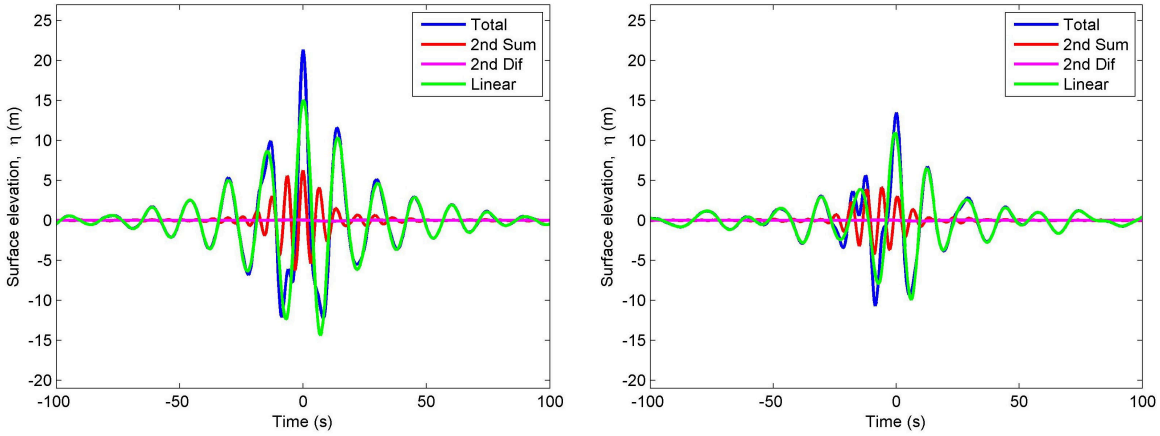

(a) Fixed (b) Moving

Figure 6.27: Components of the average of the top 500 crests to second-order for (a) fixed and (b) moving models near the centre of the array at (12,12) m with $T_p = 15.164$ s, $\beta = 45°$.

Figure 6.27 shows the components of the average extreme crest time history near the centre of the array at (12 m, 12 m), where the origin is at the centre, with (a) fixed and (b) moving models, and the same sea state as the previous examples: $T_p = 15.164$ s, $H_s = 12$ m, and $\beta = 45°$. The focus time of the second-order sum component is much earlier in the moving case than for the fixed case, and this leads to a large reduction in the maximum crest elevation reached. The moving case second-order sum component is focused around $t = -8.5$ s, and for the fixed case at around $t = -1.5$ s. The phasing of the two second-order sum packets results in a crest lining up with the maximum linear elevation to give the highest total crest at $t = 0$ s, but the moving case contributes a smaller fraction of the maximum amplitude than the fixed case. This difference in focus times along with the reduction in amplitude of the components results in the maximum average extreme elevation being reduced from 21.38 m in the fixed case to just 13.49 m in the moving case.

Figure 6.28 shows the components of the average extreme trough time history near the centre of the array at (12,12) m with (a) fixed and (b) moving models, and the same sea state as the previous examples: $T_p = 15.164$ s, $H_s = 12$ m, and $\beta = 45°$. The fixed model

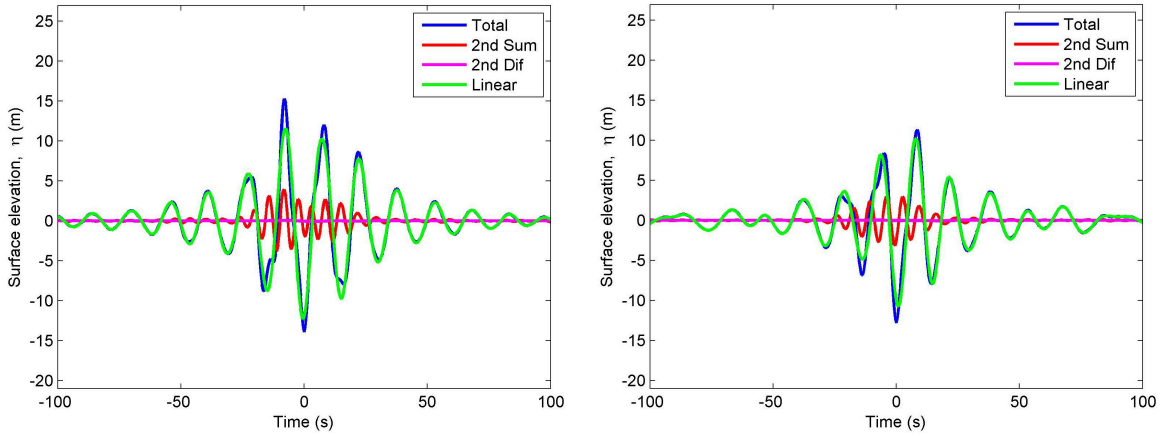

(a) Fixed (b) Moving

Figure 6.28: Components of the average of the top 500 troughs to second-order for (a) fixed and (b) moving models near the centre of the array at (12,12) m with $T_p = 15.164$ s, $\beta = 45°$.

case shows a reduction in the amplitude of the second-order sum envelope at the focus point, resulting in a small deepening of the trough (-1.96 m) at time $t = 0$ s. For the moving case, the second-order sum envelope does not have a dip in amplitude. Instead, it has a slightly longer build up than ramp down and, more importantly, a maximum value at $t = 0$ s (-3.15 m). This causes a larger increase to the maximum trough amplitude and so the maximum average extreme trough in the moving case is only a little less than in the fixed case, with values of -12.81 m and -13.92 m respectively. This is in spite of the linear component being smaller for the moving model than the fixed model, with values of -10.68 m and -12.30 m respectively.

6.7.1 'Designer' wave

In Section 5.3.6, a 'designer' wave was introduced where the average of the incident waves leading to the largest 500 events in response was found. This method will be repeated for both fixed and moving bodies to see how the 'designer' wave differs between the two cases. Before this is discussed, the average response to a NewWave-type solution in the incident field will be investigated. Figures 6.29(a) and 6.29(d) show the average of the largest 500 crests and largest 500 troughs respectively in open ocean for random time histories sampled from a sea state with $T_p = 15.164$ s, $H_s = 12$ m, and $\beta = 45°$. Both are in the form of a NewWave wave group focused at time $t = 0$ s, with maximum elevation 12.61 m and 11.21 m for the

average extreme crests and troughs respectively. The difference between these two is mostly due to the second-order sum component which increases the maximum crest amplitude but decreases the maximum trough amplitude. However, there will also be some differences due to the random sampling process. The linear components have very similar amplitudes of 11.89 m and 11.91 m respectively, with the difference caused by random sampling.

Figures 6.29(b) and 6.29(e) show the average response in the presence of the fixed structure when the linear component of the incident waves from Figures 6.29(a) and 6.29(d) respectively are incident on the structure. The second-order sum components are very similar for both the crest and trough cases. This is to be expected as the incident waves are almost identical apart from a phase difference of 180°, and for second-order sum interactions this phase difference will double to give a phase difference of 360° or 0°. The maximum amplitude reached in the trough case is larger than for the crest case as the second-order sum component adds to the largest linear component rather than subtracting from it. The focus points of the two responses are shifted a few seconds earlier than the equivalent open ocean case, and the ramp down is a little slower than the ramp up.

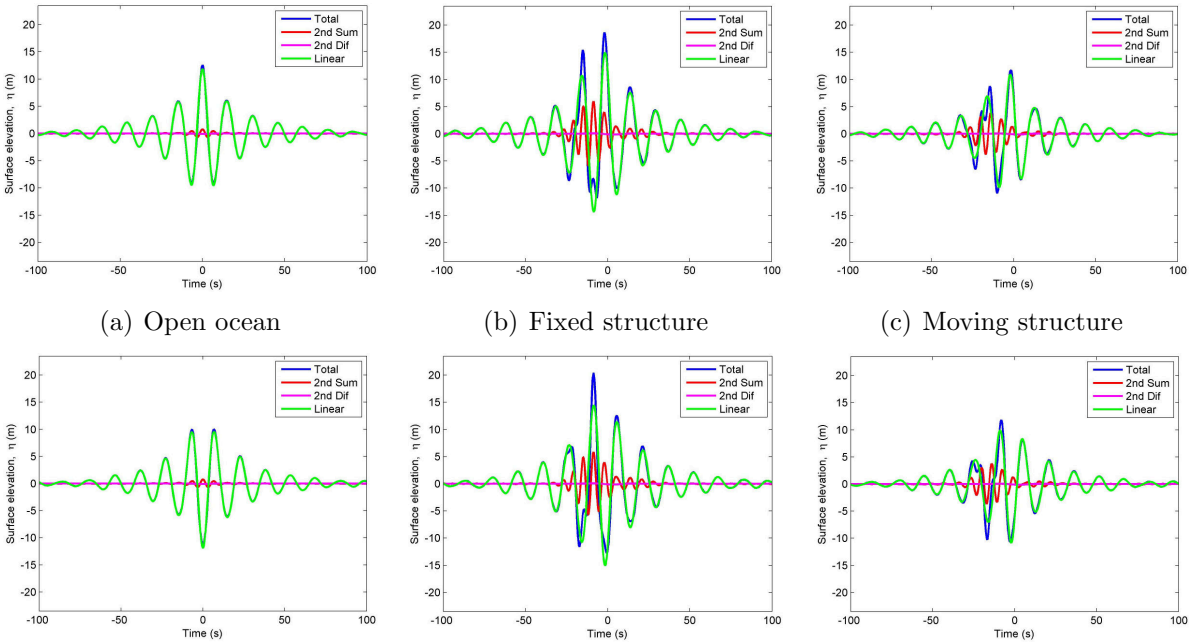

(a) Open ocean (b) Fixed structure (c) Moving structure

(d) Open ocean (e) Fixed structure (f) Moving structure

Figure 6.29: Average of the top 500 crests and troughs to second-order in open ocean (a,d) along with the responses when incident on fixed (b,e) and moving (c,f) models, taken near the centre of the array at (12,12) m with $T_p = 15.164$ s, $\beta = 45°$.

Figures 6.29(c) and 6.29(f) plot the average response in the presence of the moving rather than fixed structure, with the surface elevation modified by the body movement so that $\eta = 0$ m is always 17.5 m below the deck. Similar behaviour to the fixed case is seen with very similar second-order sum components, focus points shifted earlier in time, and a ramp down that takes a little longer than the build up. The biggest difference between the fixed and moving cases is the greatly reduced amplitude. The maximum surface elevation amplitudes reached in the moving cases are 11.68 m and 11.83 m, crest and trough cases respectively. These are very close to the open ocean amplitudes of 12.61 m and 11.21 m. For the incident crest focused NewWave case there is actually a higher maximum amplitude in open ocean than the maximum modified elevation with a moving structure present.

Having looked at how the fixed and moving structures behave when a NewWave type group is incident on them, one can now look at the average incident wave group leading to the largest events with a structure present. All results are taken near the centre of the array, at (12,12) m, with $T_p = 15.164$ s, $H_s = 12$ m, and $\beta = 45°$. Figure 6.30 shows the average of the largest 500 crests in the presence of (a) the fixed model and (c) the moving model, with the average incident surface elevations leading to these extreme responses, (b) and (d), at the same location but with the structure absent. The average incident surface elevations in open ocean (Figures 6.30(b) and 6.30(d)) are very similar for both the fixed and moving cases with a focus point a few seconds later than with the structure present, and a ramp up that takes a little longer than the ramp down. These incident groups are compared more closely in Figure 6.31(a).

Figure 6.31(a) plots the average total incident wave elevation that leads to the largest 500 crests with the fixed structure present (blue line) and the average total incident wave elevation that leads to the largest 500 crests with the moving structure present (red line). These are the same as the blue lines in Figures 6.30(b) and 6.30(d) respectively. The 'designer' waves for the largest crests with fixed and moving models present are very similar. There is a sharper rise and fall in amplitude either side of the maximum elevation for the moving case, which results in differences between the crests and troughs a few periods either side of the focus point, but overall they are very similar. The maximum amplitudes are

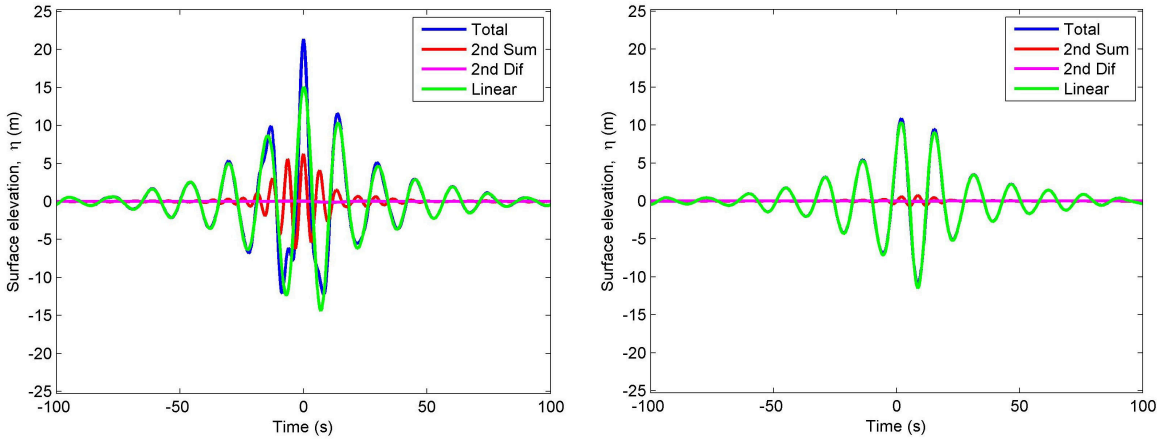

(a) Fixed structure

(b) Open ocean

(c) Moving structure

(d) Open ocean

Figure 6.30: Average of the top 500 crests to second-order with (a) a fixed model and (b) the average incident wave leading to this in open ocean. Average of the top 500 crests to second-order with (c) a moving model and (d) the average incident wave leading to this in open ocean. All results taken near the centre of the array at (12,12) m with $T_p = 15.164$ s, $\beta = 45°$.

10.84 m and 10.08 m for the fixed and moving models respectively, and yet the difference in maximum elevation in response from these incident groups is far greater.

Figure 6.31(b) plots the average total incident wave elevation that leads to the largest 500 *troughs* with the fixed structure present (blue line) and the average total incident wave elevation that leads to the largest 500 *troughs* with the moving structure present (red line). These incident groups have less in common. The incident wave for the fixed case is similar to a trough focused NewWave with a focus time only a little later than $t = 0$ s, but the moving case is similar to a crest focused NewWave with a focus time a little over half a period later. The maximum amplitude for the incident wave leading to the largest troughs in the presence of a moving body is greater than for the equivalent fixed body incident wave group.

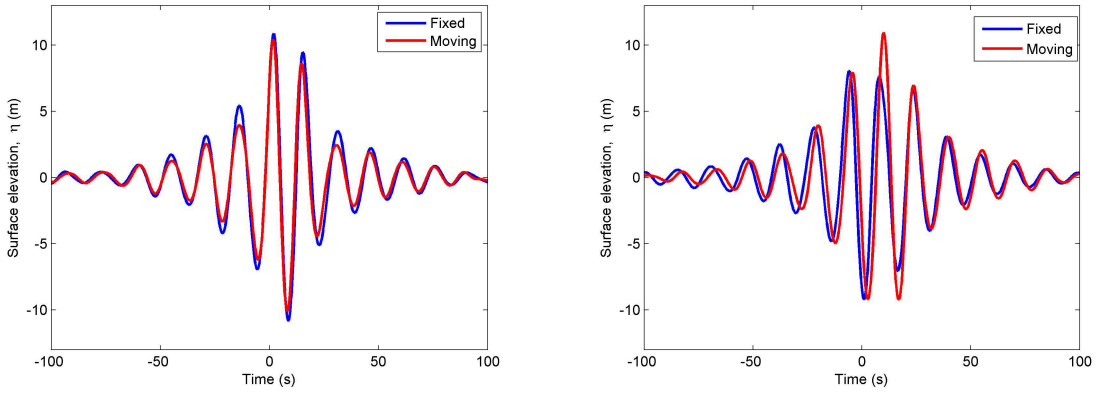

(a) Crest (b) Trough

Figure 6.31: Average incident wave groups leading to the largest 500 (a) crests and (b) troughs with a fixed (blue line) or moving (red line) model present. All results taken near the centre of the array at (12,12) m with $T_p = 15.164$ s, $H_s = 12$ m, and $\beta = 45°$.

6.7.2 Varying return period

Figure 6.32 plots crest elevation against probability of occurrence per wave for both fixed and moving models in a sea state with peak period $T_p = 15.164$ s, significant wave height $H_s = 12$ m, and wave direction $\beta = 45°$. The moving model case has had the vertical body motions subtracted from the wave elevation so that a relative crest height of 17.5 m in the moving model still indicates impact on the deck. Frequency doubling at the peak frequency will lead to second-order excitation of a near-trapped mode. The red and blue lines show the crest elevation to first- and second-order respectively for the fixed model, and the purple and green lines show the crest elevation to first- and second-order respectively for the moving model.

At each probability of occurrence the total crest height to second-order with the moving model is less than the linear crest elevation with the fixed model. For the moving model, the total crest elevation versus probability shows that there is a 7.25×10^{-6} probability of water impacting on the deck. For the fixed model, the total crest elevation shows a probability of 2.5×10^{-3} for water-deck impact. This suggests that for the moving model in this sea state one would expect water deck impact approximately every 140,000 waves but with the fixed model one would expect it to occur every 400 waves. This is clearly a huge difference, and similar differences are seen with the distribution of trough elevation against probability, as shown in Figure 6.33. However, it is interesting to note that troughs calculated to second-

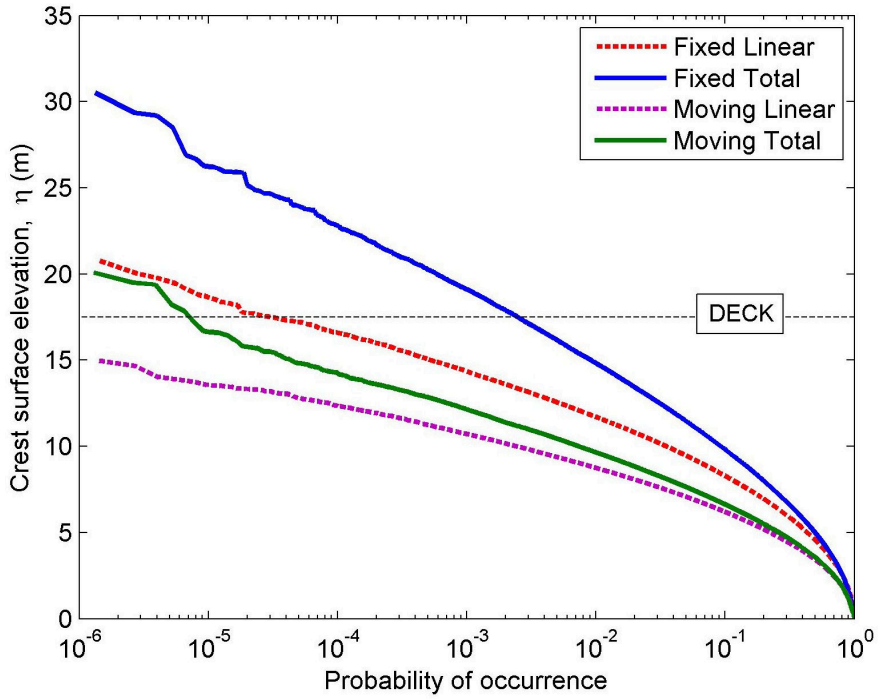

Figure 6.32: Crest height vs. probability of occurrence per wave to first- and second-order for fixed and moving models with $H_s = 12$ m, $T_p = 15.164$ s.

order are deeper than linear results for a moving body but shallower for a fixed body.

An example of a large TLP (with restricted vertical motion) is Ursa in the Gulf of Mexico, which is constructed using four large circular columns connected at the base by pontoons. Ursa is fairly similar in its overall dimensions to Thunder Horse, with a column width of 25.9 m, column centre-centre spacing of 65.5 m, and a draft comparable to Thunder Horse. Thus, it is not unreasonable to compare the same hull shape for fixed and moving cases. These figures show that when designing an offshore structure in deep water, the choice of structure type is very important. For an identical hull shape that is fixed vertically or allowed to move freely, the freely moving structure is predicted to experience far fewer water-deck impacts. For a fixed body, this could lead to a greater risk to the lives of staff on the platform and also a greater chance of financial loss due to downtime caused by damage from water-deck impact.

6.8 Conclusions

Conclusions drawn from the results presented in this chapter are briefly summarized below.

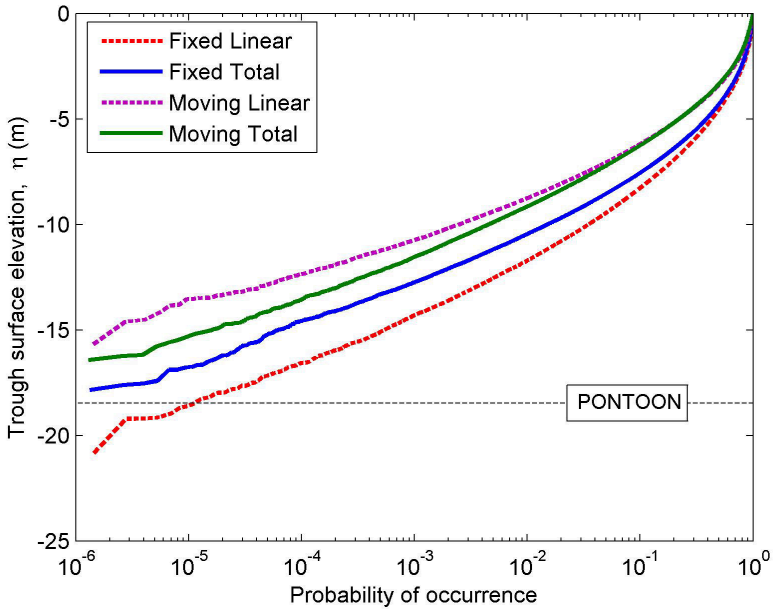

Figure 6.33: Trough height vs. probability of occurrence per wave to first- and second-order for fixed and moving models with $H_s = 12$ m, $T_p = 15.164$ s.

- At periods shorter than around 10 s, there is little body movement or change in diffraction pattern.

- At periods longer than around 10 s, there is usually a reduction in diffraction LTFs and QTFs of surface elevation for the moving body relative to the fixed body. The difference pattern between plots of the modulus of fixed and moving diffraction transfer functions shows little correlation with near-trapped mode shapes.

- NAF is easily modified to give useful information on the likelihood of water-deck impact across the field.

- Second-order excitation of near-trapped modes for a moving body show diffraction patterns that are closer to linear near-trapped modes at the same response frequency than when the body is fixed.

- Surface elevations modified to take into account body motions show that the risk of water-deck impact in a typical storm sea state is much lower for a moving body compared to the same body fixed vertically.

Chapter 7

Violent wave interactions with a vertical cylinder - experimental results

7.1 Introduction

A series of experiments was carried out to investigate the interactions of steep waves with a vertical bottom-seated circular column, see Zang et al. (2010). The wave surface elevation was measured by nineteen wave gauges around the column, and ADV (acoustic Doppler velocimetry) data were collected on the wave kinematics adjacent to the column. The total force on the column was measured through strain gauges at its mount, along with pressures recorded at several locations on the front of the column. The majority of the results obtained were for the interaction of focused wave groups with the column, rather than just regular or random waves. Regular waves give a poor representation of real ocean waves, and random waves, although capturing the broadbanded nature of storm wave spectra, are an inefficient method for generating extreme waves experimentally and suffer problems due to reflections in a finite sized wave tank. The author does not know of other multi-column wave tank experiments using NewWave focused wave groups as a control signal, which means the data collected contained a uniquely large number of high quality measurements of extreme wave-structure interactions.

The main purpose of these experiments was to investigate 'ringing' - a dynamic response at the natural frequency of the column excited by high frequency components of the focused wave group. To obtain a clearer understanding of the high frequency components that lead to ringing, a complete Stokes expansion type representation of the applied force was sought. This meant extracting the individual components of the applied force, including linear, second-order double-frequency sum and difference, third-order triple-frequency sum etc. terms from the measured total force. To separate out the individual components, the separation method from Hunt et al. (2002), Zang et al. (2006), and Borthwick et al. (2006) was implemented, see Section 7.3, and will be referenced as the Taylor separation method hence forth.

The aim of this thesis is to improve our ability to predict wave surface elevation around arrays of large surface piercing columns. This section only looks at a single vertical column but one must fully understand wave-structure interactions for a single column before one can move on to the increased complexity that arrays of multiple columns introduce. It is also necessary to validate the software and methods used to predict surface elevations and body forces. The methods and techniques discussed in this chapter can be applied to single or multiple columns. Since a large volume of data from these extensive and thorough experiments was available, it was appropriate within the present project to analyse some of this data using the methodology developed here.

7.2 Experiments

The tests were carried out on a single vertical circular column in the shallow water basin at DHI (Dansk Hydraulisk Institut/Danish Hydraulic Institute). In the tests studied here, the shallow water basin was filled with water to a constant depth of 0.505 m above a flat bed. There were 32 connected paddles along one side of the tank, each measuring 0.5 m in width, with the column placed 7.8 m in front of the centre of these paddles. The column was attached to a stiff triangular frame via a load cell at the top of the column, with a 1 mm gap between the column base and the basin floor. Figure 7.1(a) shows the column attached to the frame without water present. It is surrounded by the wave surface elevation gauges, and

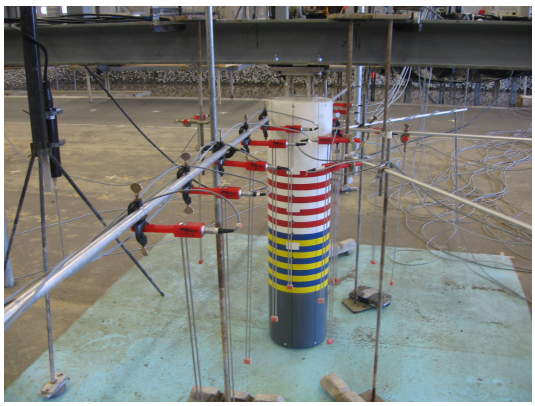

(a) Experimental setup

(b) Incident wave group

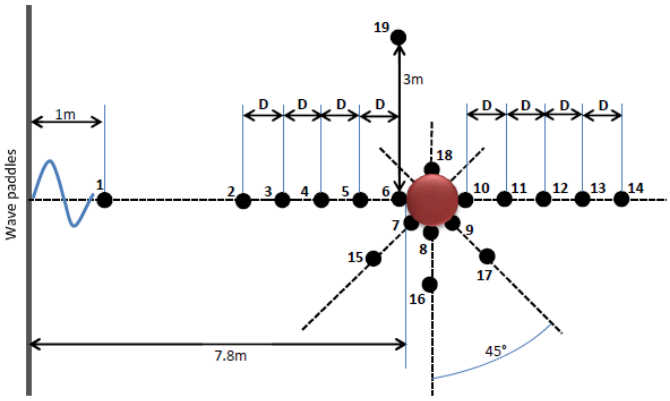

(c) Apparatus layout

Figure 7.1: DHI experimental set up.

the stripes on the column are clearly visible. The transition from blue and yellow to red and white stripes coincides with the mean water level. Figure 7.1(b) shows a plunging breaker about to impact on the column, with set down at the column causing the blue and yellow stripes below the mean water level to be clearly visible. Figure 7.1(c) shows the layout of the column and wave gauges relative to the paddles.

Some regular wave tests were carried out but the majority of experiments were for NewWave focused wave groups based on a JONSWAP spectrum ($\gamma = 3.3$). These experiments covered a range of wave conditions including small amplitude, near linear waves up to violent bidirectional plunging breakers. All wave groups were approximately focused at the front of the column but there was some trial and error in this focusing due to the non-linear dispersion of the wave groups. Some of the recorded wave groups are therefore focused better than others. Each wave group was run in a matching pair, where two groups were run separately but with the same amplitude and centre frequency. The first of these

groups was crest focused, with a large amplitude peak at the focus point. The second of these groups was generated by multiplying the paddle control signal by -1, meaning there was a large amplitude trough at the focus point. The phase difference between these matching crest and trough pairs is the basis for the Taylor method of separating out the Stokes expansion harmonics.

The basic method used to analyse each set of experiments contains the nine steps shown below. These steps are looked at in more detail in the following sections.

1. Find the hydrodynamic force from the measured total force signal transmitted through the load cell by removing the dynamic structure response. Do this for both the crest and trough focused signals.

2. Align the crest and trough focused signals in time.

3. Separate the odd and even harmonics using Taylor separation for both the hydrodynamic force and surface elevation signals.

4. Fourier transform each of the (C-T)/2 and (C+T)/2 signals to find their respective spectra.

5. Check that the crest and trough signals are correctly aligned and that leakage is minimised. Repeat the previous steps if necessary.

6. Filter out the individual harmonics.

7. Inverse FFT the individual harmonic spectra to find the force and surface elevation time histories associated with each harmonic.

8. Use DIFFRACT transfer functions to reconstruct the force time histories from the measured surface elevation signals for the linear, second-order sum, and second-order difference terms based on classical diffraction theory.

9. Use the Hilbert transform to find the fundamental envelope and approximations for higher order harmonics.

7.2.1 Natural frequency

A simple 'twang' test was carried out to find the resonant characteristics of the column model. A displacement was applied at the base of the column, and then the column was released and allowed to oscillate in otherwise still water until the motion ceased. The total force on the column was measured during this test and Figure 7.2(a) shows the recorded force time history in grey. The spectrum shown in Figure 7.2(b) was found by taking the Fourier transform of this time history, and it clearly shows a large resonant peak at a frequency of 3.88Hz. A decay curve of the form $Ce^{-\zeta\omega_0 t}$ (shown in bold black on Figure 7.2(a)) was then fitted to the time history. This was found to fit best with a value of $\zeta = 0.009$, corresponding to a structural damping factor 0.9 % of critical.

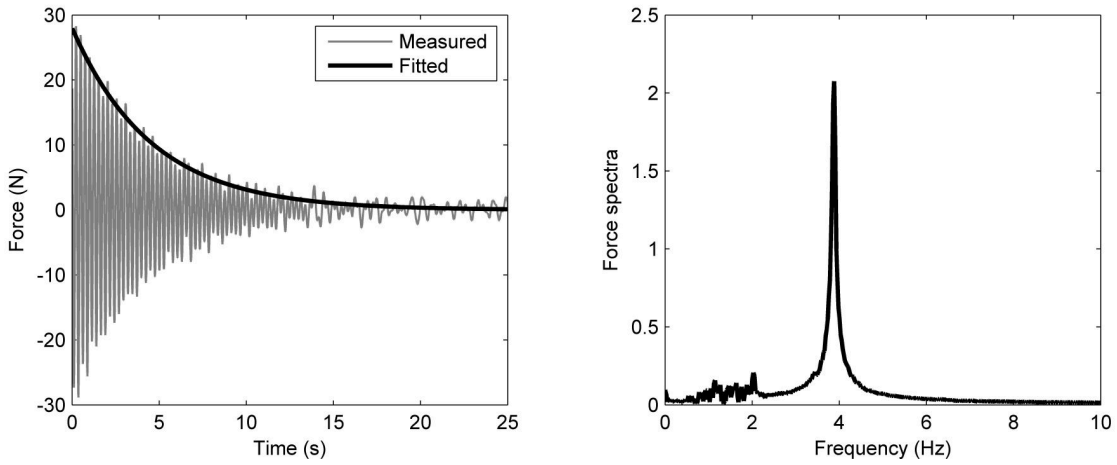

(a) Time history (b) Spectrum

Figure 7.2: Time history and spectrum of a 'twang' test to find the column's natural frequency and damping coefficient.

7.2.2 Hydrodynamic transfer function

One of the main purposes of the DHI experiments was to investigate the effect of ringing on columns in intermediate depth water. Ringing is a dynamic response excited by some of the higher frequency components of the incident wave group. The measured horizontal force at the support therefore has components driven by the hydrodynamic force from the incident wave but modified by the dynamic ringing response of the structure. The ringing

will cause a local magnification of the force at the high excitation frequencies, and this must be removed if the hydrodynamics of the wave-structure interaction are to be studied.

The high frequency components that excite ringing are of interest in the hydrodynamic analysis, so the local force magnification cannot simply be cut-off with a low pass filter. Instead, the hydrodynamic force can be found by modelling the column as a mass-spring-damper system, finding a transfer function for the dynamic response, and using this to remove the force response due to structural vibration without losing the high frequency hydrodynamic components. This is based on the assumptions that the measured force is horizontal only, that the column moves horizontally rather than bending, and that any non-linear structural dynamics can be neglected.

The governing equation for a mass-spring-damper system is given by Newton's second law:

$$\frac{d^2x}{dt^2} + 2\zeta\omega_0\frac{dx}{dt} + \omega_0^2 x = \frac{f}{m} \tag{7.1}$$

where ω_0 is the undamped natural frequency, ζ is the structural damping, x is the column displacement, and f is the hydrodynamic force applied to the structure. Fourier transforms are then applied to each side:

$$-\omega^2 X(\omega) + 2\zeta\omega_0\omega X(\omega)\mathrm{i} + \omega_0^2 X(\omega) = [\omega_0^2 - \omega^2 + 2\zeta\omega_0\omega\mathrm{i}]X(\omega) = \frac{F(\omega)}{m} \tag{7.2}$$

where $\omega/\omega_0 = (1-2\zeta^2)^{\frac{1}{2}}$. Since $m = k/\omega_0^2$, where k is the wavenumber, the above equation can be rearranged to give the following transfer function:

$$T(\omega) = \frac{F(\omega)}{X(\omega)} = 1 - \left(\frac{\omega}{\omega_0}\right)^2 + 2\zeta\left(\frac{\omega}{\omega_0}\right)\mathrm{i} \tag{7.3}$$

The damping factor and natural frequency used in this transfer function were found in the 'twang' test discussed earlier. The amplitude of the transfer function grows rapidly at high frequency which means it must be turned off before it starts to ramp up and amplify useless noise. The cut-off needed to prevent this can be well above any useful spectral information

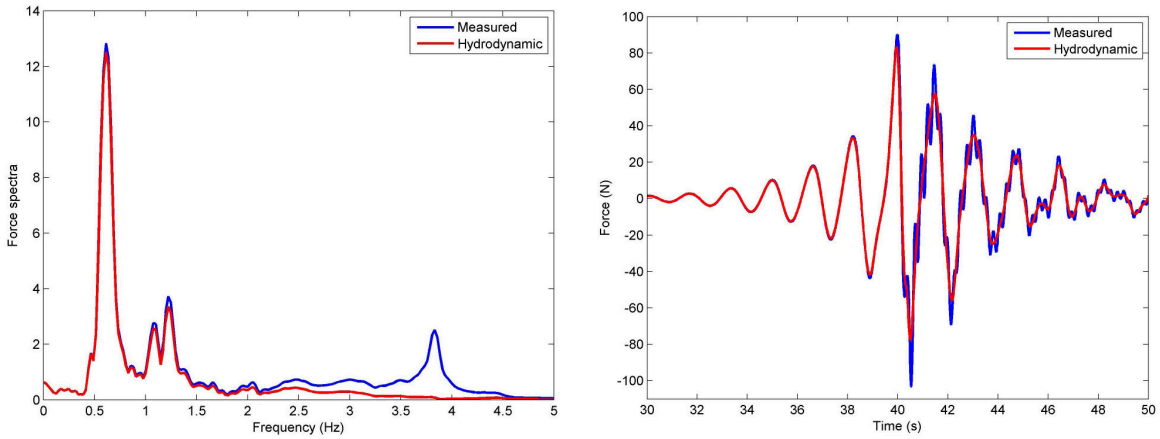

(a) Force spectra (b) Force time history

Figure 7.3: Spectra and time histories for a trough focused signal, before and after the transfer function is applied to remove the ringing response.

before the transfer function gets unacceptably high.

Figure 7.3(a) shows the force spectra for an incident focused wave group, both with and without the transfer function applied. The blue line shows the spectrum of the measured force and this is used with the transfer function to find the hydrodynamic force, shown by the red line. In the measured spectra there is an obvious resonant peak at 3.88Hz. In the hydrodynamic spectra this has clearly been removed using the structural response transfer function. The amplitudes of the harmonic peaks nearest to the resonant frequency have also been reduced. The effect of this on the time history is shown in Figure 7.3(b). The blue line shows the measured force time history and the red line shows the estimated hydrodynamic force. The oscillations in the data seen after time $t = 40$ s have been removed, leaving a much smoother signal.

7.2.3 Signal alignment

The Taylor method of separating the odd and even harmonics is based on the linear parts of the crest (C) and trough (T) focussed signals being exactly out of phase via the calculation of the time series $(C - T)/2$ and $(C + T)/2$. If the phase difference between these two signals is not 180°, then the effectiveness of the method will decrease as $|Phase - 180°|$ increases. Misalignment between the crest and trough signals will mean that the odd and

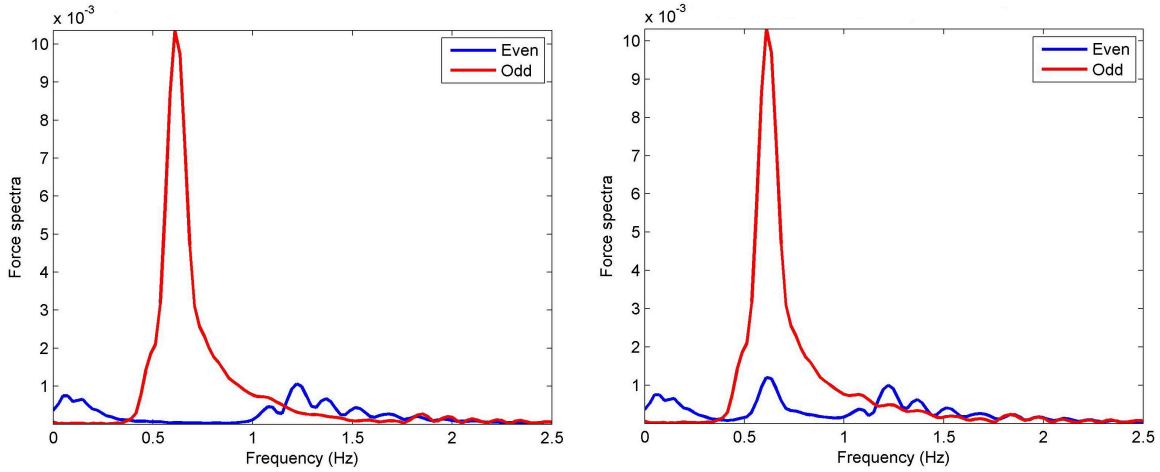

(a) Signals aligned, leakage minimised

(b) Signals misaligned, leakage obvious

Figure 7.4: Spectra of the odd, $(C-T)/2$, and even, $(C+T)/2$, components of surface elevation at the focus of a wave group with crest and trough signals (a) aligned and (b) misaligned by 0.06 s.

even harmonics will not be completely separated. Instead the odd and even harmonics will be partially combined with some leakage from the odd harmonics into the assumed even spectra components and vice versa. This is demonstrated in Figure 7.4 where the spectra of the separated odd and even harmonics are shown for two cases: Figure 7.4(a) shows minimal leakage, and Figure 7.4(b) shows leakage caused by a misalignment of 0.06 s in the crest and trough signals. This is most obvious at a frequency of 0.61Hz where there is a peak in the apparently even spectra for Figure 7.4(b), but not in Figure 7.4(a).

The importance of aligning the crest and trough signals has been shown. However, there was unfortunately no timing signal available at the DHI basin to indicate the start of testing, and so a robust method had to be found to ensure that the crest and trough signals were aligned. One possible method was to take the cross-correlation of the two signals. Since the trough control signal sent to the paddle is simply the negative of the crest control signal, the location of the minimum of the cross-correlation should indicate the shift in time needed to minimize leakage. Figure 7.5 plots the cross-correlation for a time shift of -4 to 4 s. The minimum is found at $\tau = 0.07$ s and should correspond to the minimum leakage.

To verify this, the amplitude of the leakage of predominantly linear components into the even harmonic spectra at 0.61Hz was found over the range of time shifts between $\tau = \tau_0 \pm 0.05$ s, where τ_0 is the shift predicted by cross-correlation. The results are shown in Table 7.1

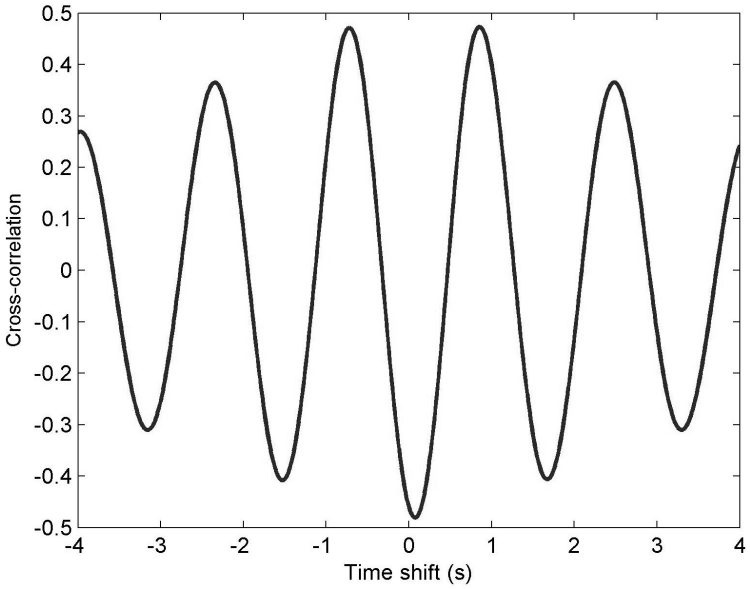

Figure 7.5: The cross-correlation of the crest and trough surface elevation signals to show the time shift needed to align them.

with the leakage given as both the amplitude of the peak and as a percentage of the first harmonic in the odd spectra. These results show that the cross-correlation method comes close to finding the minimal leakage, but the smallest value is actually at $\tau = \tau_0 - 0.01$ s. This is due to the linear nature of the signal controlling the paddle and the higher order error waves generated at the paddle as a result. Instead of having $\eta_{Control} = \eta_{Crest} = -\eta_{Trough}$, the signals are in fact $\eta_{Crest} = \eta_{Control} + \eta_{Error}$ and $\eta_{Trough} = -\eta_{Control} + \eta_{Error}$. Schäffer (1996) discussed full second-order wave-maker theory and its use in suppressing spurious free-wave generation and the generation of a wave field correct to second-order.

τ	-5	-4	-3	-2	-1	0	+1	+2	+3	+4	+5
Le (mm)	0.785	0.585	0.389	0.192	0.040	0.213	0.410	0.608	0.807	1.005	1.203
Le (%)	7.55	5.63	3.74	1.85	0.38	2.05	3.94	5.85	7.76	9.66	11.57

Table 7.1: Amount of leakage, Le, in the $(C+T)/2$ surface elevation spectra from the first harmonic due to misaligning the crest and trough signals by $\tau/100$ s.

The cross-correlation method can therefore only be used as an estimate of the time shift needed. A further example of the effect of misalignment, and a possible method of finding the correct alignment after using cross-correlation as an estimate, is shown in Figure 7.6.

The Taylor separation method was used to find the second-order difference elevation signal for a range of time shifts, between $\tau = \tau_0 \pm 0.05$ s again, and each of these signals was then plotted against time. A second-order signal was used because the signal amplitude is related to the square of the incident amplitude, A^2, and errors are therefore more obvious. Figure 7.6 clearly shows that misalignments as small as a few hundredths of a second can lead to leakage and large oscillations in the extracted signal. After close examination of the oscillations introduced, it was still hard to pick a time shift that minimised these oscillations. To the right of the focus point, the time shift to minimise oscillations seems to be between the black and yellow lines, therefore $\tau = \tau_0 - 0.015$. However, to the left of the focus point the time shift to minimise oscillations seems to be between the black and magenta lines, therefore $\tau = \tau_0 - 0.005$. Overall $\tau = \tau_0 - 0.01$ s, as plotted in the black line, seems to be the optimum time shift.

This is a rather inefficient method for finding the optimum time shift, but since this is a side project with only a few cases being studied it will suffice.

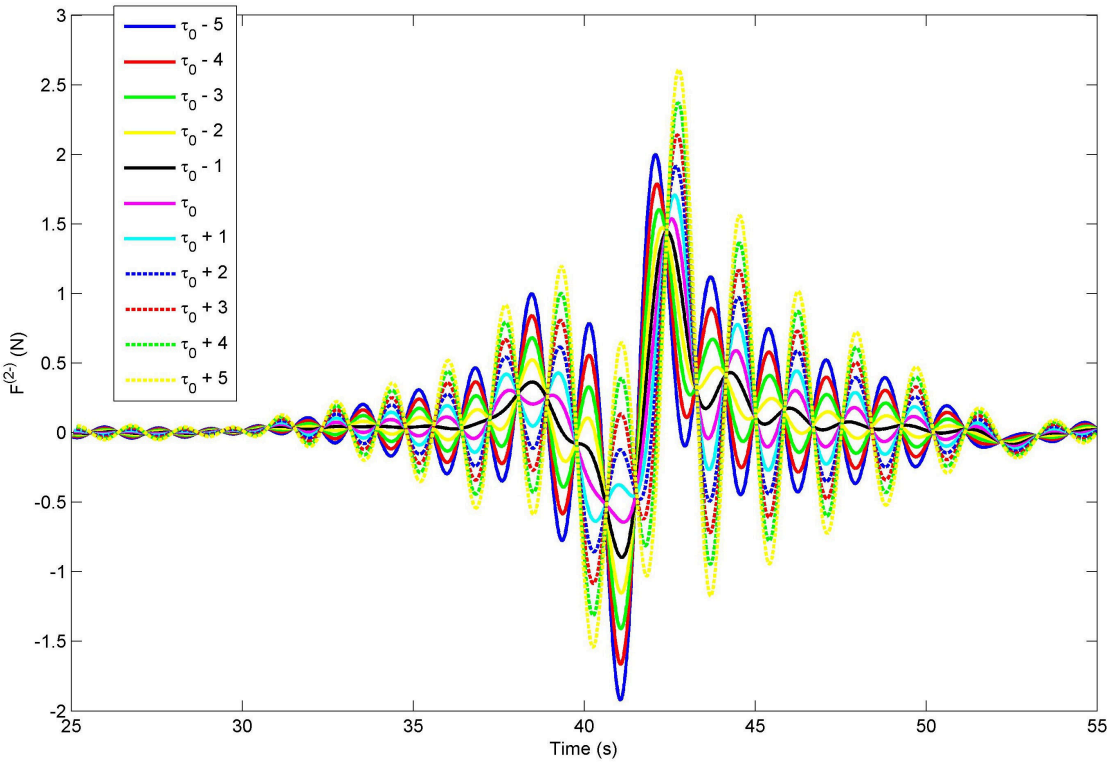

Figure 7.6: The variation of the longwave signal as the time shift τ varies.

7.3 Taylor separation method

A regular non-linear Stokes wave can be written in the following form

$$\eta_{Stokes} = a_1 A\, cos(\theta) + a_2 A^2 cos(2\theta) + a_3 A^3 cos(3\theta) + ... + a_n A^n cos(n\theta) \tag{7.4}$$

where A is the fundamental wave amplitude, $\theta = (\omega t - kz)$, z is distance along the wave direction, and a_n are coefficients. If this represents a crest at the focus point, $\eta_{Stokes} = \eta_{Crest}$, then multiplying the fundamental amplitude by -1 will generate the trough equivalent. This is described by the following equation:

$$\eta_{Trough} = -a_1 A\, cos(\theta) + a_2 A^2 cos(2\theta) - a_3 A^3 cos(3\theta) + ... + (-1)^n a_n A^n cos(n\theta) \tag{7.5}$$

These crest and trough equations can then be combined to separate out the odd and even harmonics:

$$\frac{C - T}{2} = \frac{\eta_{Crest} - \eta_{Trough}}{2} = a_1 A\, cos(\theta) + a_3 A^3 cos(3\theta) + ... \tag{7.6}$$

$$\frac{C + T}{2} = \frac{\eta_{Crest} + \eta_{Trough}}{2} = a_2 A^2\, cos(2\theta) + a_4 A^4 cos(4\theta) + ... \tag{7.7}$$

where (C-T)/2 represents the odd harmonics (linear, third sum etc.), and (C+T)/2 represents the even harmonics (second difference, second sum, fourth sum etc.). By separating out the odd and even harmonics, adjacent harmonics within each spectrum are now much further apart in frequency and can be cleanly filtered.

The above equations are for a regular Stokes wave expansion. For NewWave focused wave groups, the method is an approximation due to the broadbanded nature of the spectra. Since JONSWAP spectra are the basis for the NewWave groups used here, the bandwidth is narrow enough for the overlapping harmonics to be separated sufficiently by the Taylor separation method to ensure clean filtering. This method has been successfully applied to

surface elevation data around a simplified FPSO by Zang et al. (2006), and to shoaling waves on a plane beach by Hunt et al. (2002) and Borthwick et al. (2006).

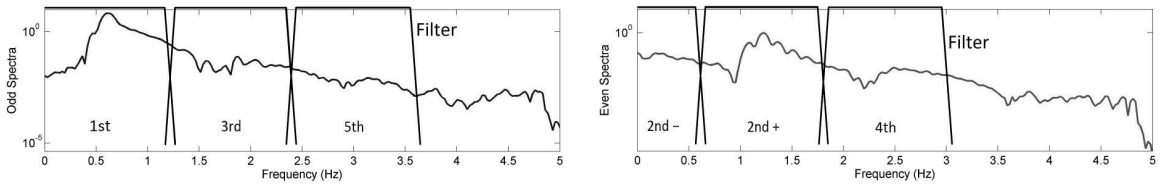

(a) Odd harmonics (b) Even harmonics

Figure 7.7: Force spectra for the odd, $(C - T)/2$, and even, $(C + T)/2$, harmonics with filters of width $2f_0$.

Figure 7.7 shows an example of the odd and even harmonics' spectra after separation, with the boundaries of a filter for each harmonic shown above. The n^{th} harmonic is filtered over a range of $2f_0$, centred about nf_0, where f_0 is the peak frequency of the fundamental harmonic. At each boundary between adjacent filters there is a simultaneous ramp down and ramp up to ensure that all spectral information is included in the decomposed harmonics. A disadvantage of these filters is that they are more susceptible to leakage.

Figure 7.8 shows an alternative type of filter, where the filters are more harsh. They have a width of f_0 and alternate between the odd and even harmonics, so that all the filters combine to a uniform band of height 1 across the frequencies of interest. This stricter form of filtering allows cleaner separation of the harmonics but leads to a small amount of loss in the total spectral information. This can be seen in Figure 7.9, which plots the original force time history and its recombination from the decomposed harmonics using the two forms of filtering. The broader filter (green line) matches the original signal almost exactly, whereas the narrow filters have some loss of amplitude at the peaks.

7.4 Fitting Envelopes

Once the harmonic components have been separated out, it is useful to fit an envelope to the signals. An envelope will give a better representation of the energy in the incident wave

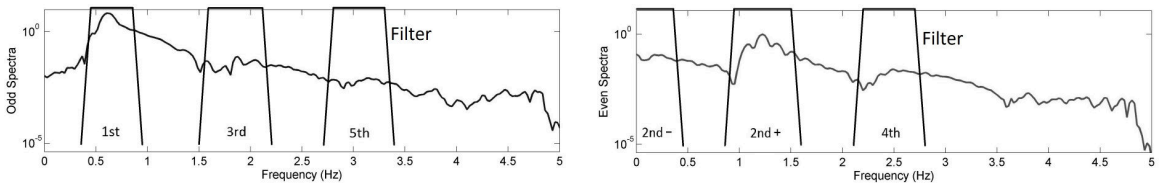

(a) Odd harmonics (b) Even harmonics

Figure 7.8: Force spectra for the odd, $(C-T)/2$, and even, $(C+T)/2$, harmonics with filters of width f_0.

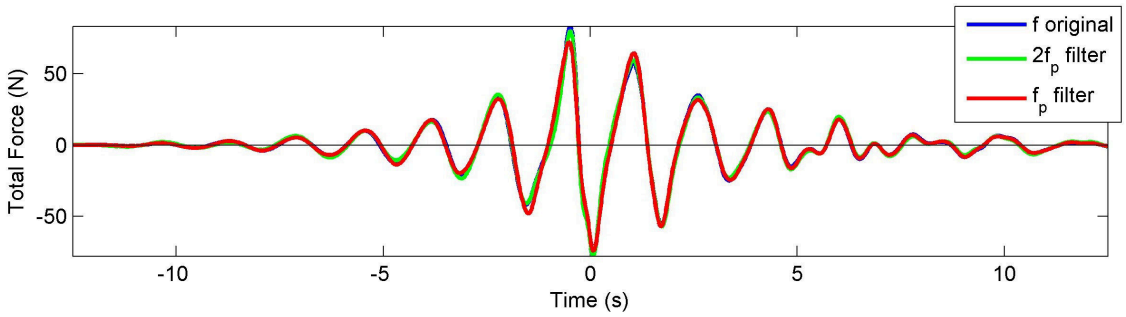

Figure 7.9: Total hydrodynamic force time history (blue line) and its recombination after decomposition into harmonics using filters of width f_0 (red line) and $2f_0$ (green line).

group and for poorly focused wave groups it will show when the peak of the wave group has passed. Fitting an envelope to the fundamental and then comparing the n^{th} power of this envelope (which is scaled to fit the n^{th} harmonic by a least squares method) to the n^{th} harmonic signal allows an assessment to be made of whether one can predict the shape of higher harmonics based only on the fundamental.

An envelope can be fitted to the fundamental using the Hilbert transform. The Hilbert transform is defined as follows:

$$Hilbert\{F(\omega)\} = F(\omega) \times \begin{cases} i = e^{\frac{i\pi}{2}},\ for\,\omega < 0 \\ 0,\ for\,\omega = 0 \\ -i = e^{\frac{-i\pi}{2}},\ for\,\omega > 0 \end{cases} \tag{7.8}$$

After finding the Hilbert transform of the fundamental force time history, the envelope can be found with this simple equation:

$$Envelope = \sqrt{F_L^{(1)^2} + F_{LH}^{(1)^2}} \tag{7.9}$$

where $F_L^{(1)}$ is the fundamental force component and $F_{LH}^{(1)}$ is the Hilbert transform of $F_L^{(1)}$.

An example of an envelope found by this method is shown in Figure 7.10. The Envelope fits the signal well and shows the location of the energy peak between the crest and trough at the centre of the wave group.

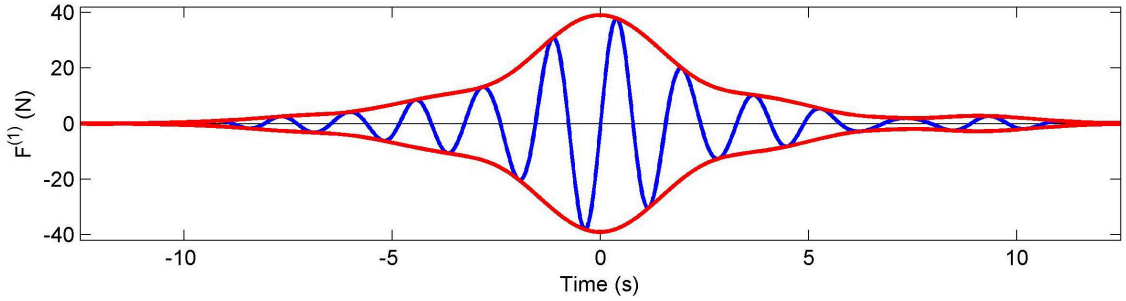

Figure 7.10: Envelope fitted to the fundamental force component.

7.5 Harmonic separation results

This section looks at some results for separating harmonic components using the method discussed above. Initially, the broader filters of width $2f_0$ were used to maximise the spectral information preserved. Unfortunately, the method proved too sensitive to the alignment of the crest and trough signals and so the results presented in this section use filters of width f_0. Figures 7.11, 7.12, and 7.13 show a Stokes style expansion of the extracted harmonic components for three different wave groups. These three wave groups are all NewWaves based on JONSWAP spectra with $\gamma = 3.3$ and $f_0 = 0.61$ Hz. Figure 7.11 is a unidirectional wave group with amplitude $A = 0.06$ m, Figure 7.12 is a unidirectional wave group with amplitude $A = 0.115$ m, and Figure 7.13 is a bidirectional wave group with a wave direction of $\beta = \pm 20°$ and each component group of amplitude $A = 0.115$ m, giving a combined amplitude of $A = 0.23$ m.

The first plot in each of the three figures is the measured total horizontal force for the crest and trough focused wave groups, realigned so that they focus at the same point in time. The succeeding plots are the harmonic components of the hydrodynamic force that are extracted from the measured crest and trough signals. These are the longwave or second-order difference component, first-order, second-order sum, third-order sum, fourth-order

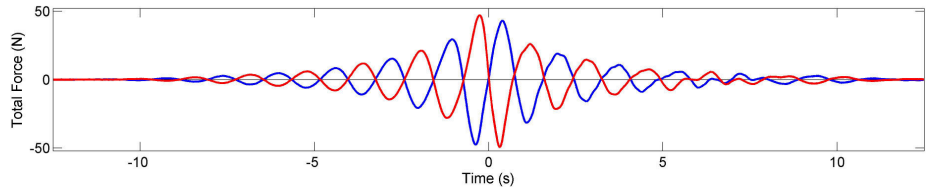

(a) Total crest and trough focused signals

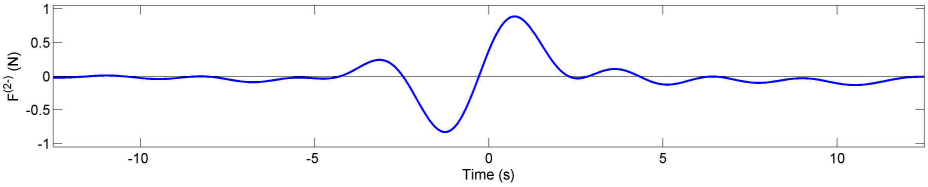

(b) Longwave

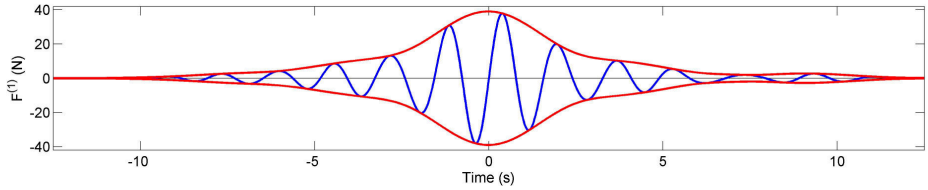

(c) Linear

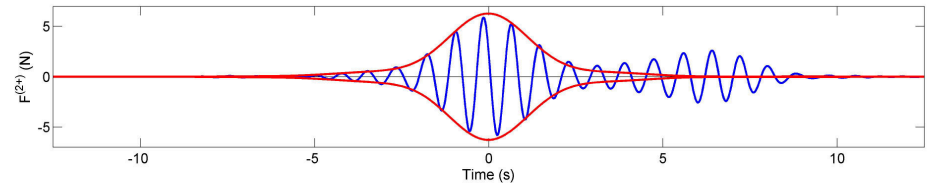

(d) Second sum

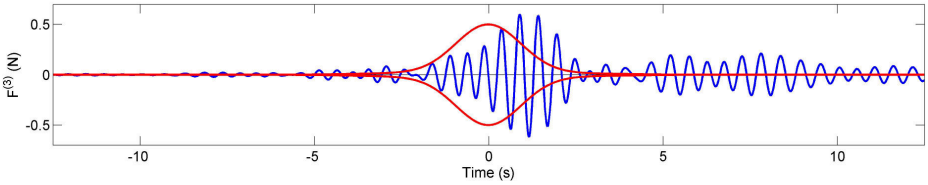

(e) Third sum

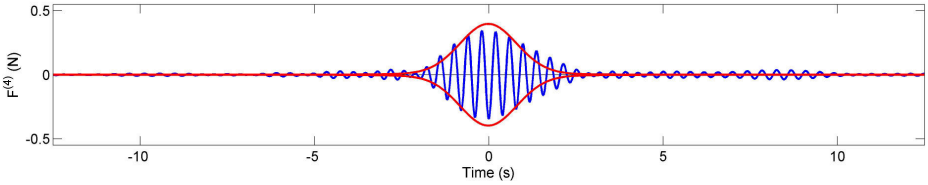

(f) Fourth sum

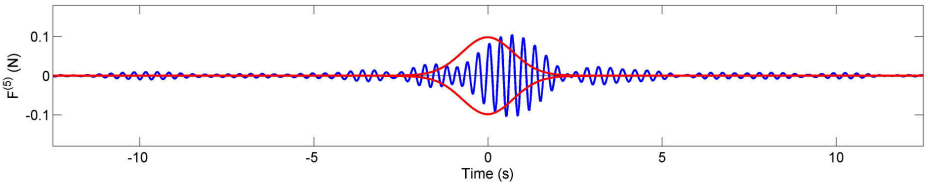

(g) Fifth sum

Figure 7.11: Harmonic components of the hydrodynamic force, extracted using the Taylor separation method, $A = 6$cm.

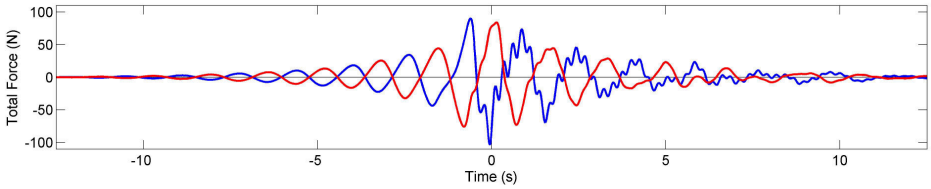

(a) Total crest and trough focused signals

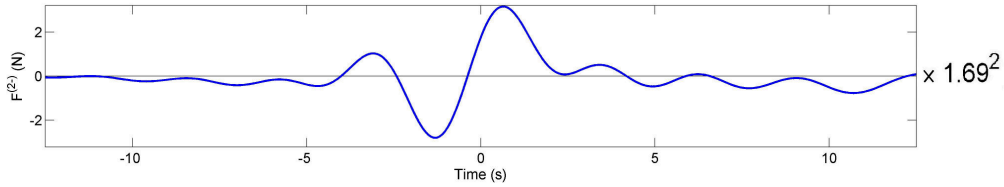

(b) Longwave

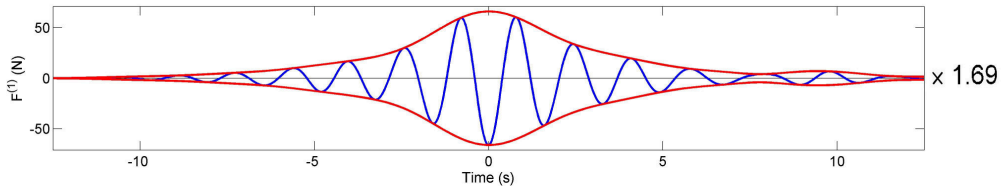

(c) Linear

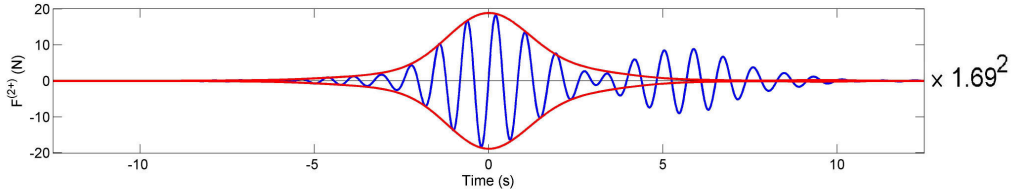

(d) Second sum

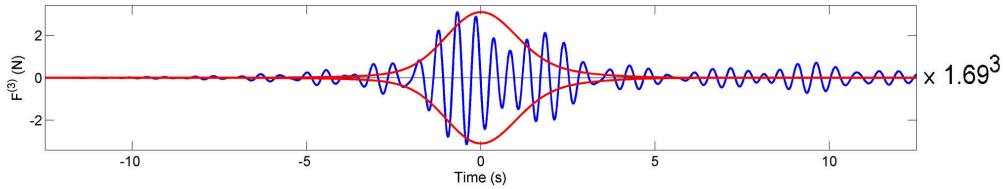

(e) Third sum

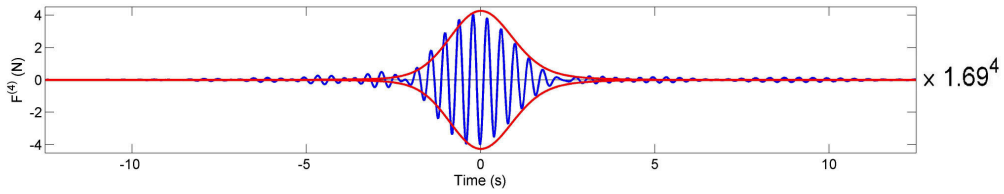

(f) Fourth sum

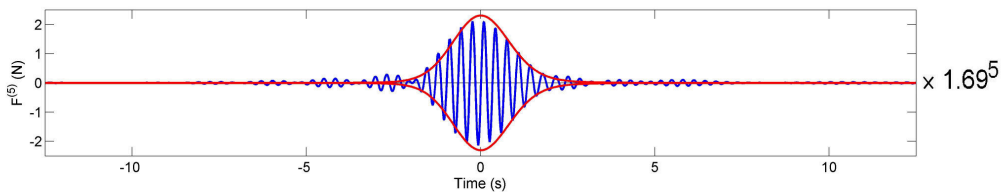

(g) Fifth sum

Figure 7.12: Harmonic components of the hydrodynamic force, extracted using the Taylor separation method, $A = 11.5$cm.

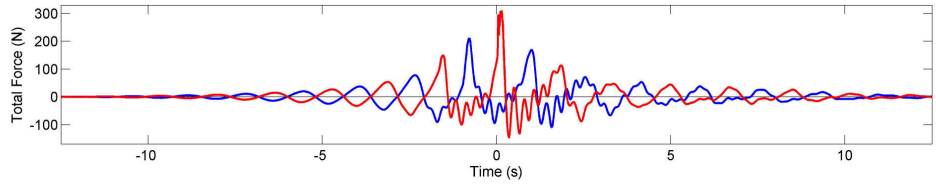

(a) Total crest and trough focused signals

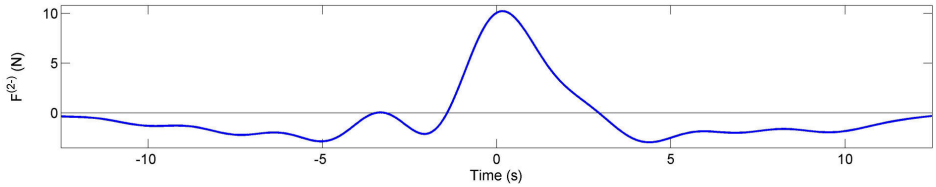

(b) Longwave

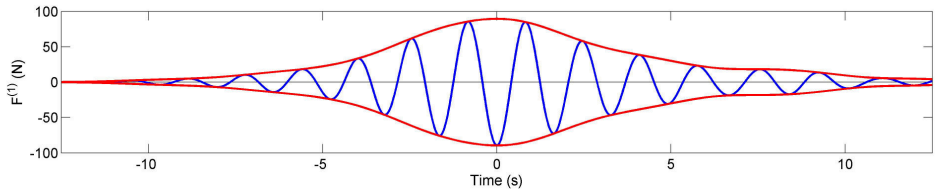

(c) Linear

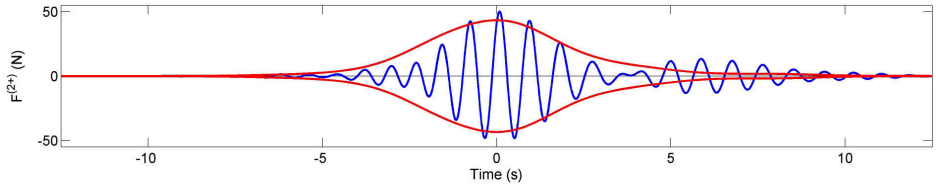

(d) Second sum

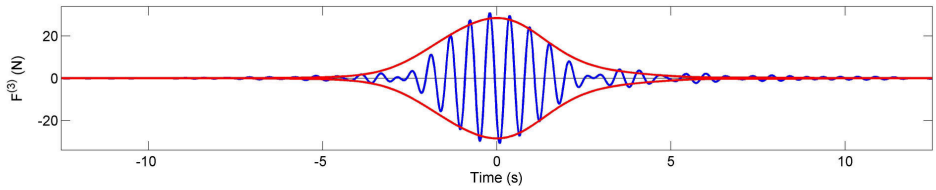

(e) Third sum

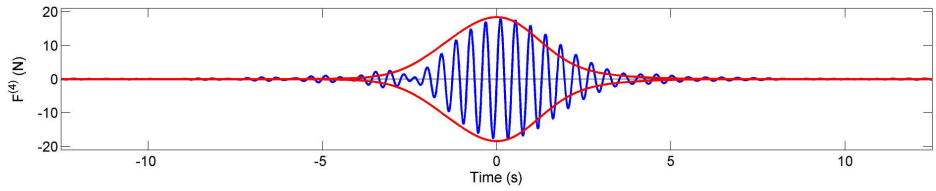

(f) Fourth sum

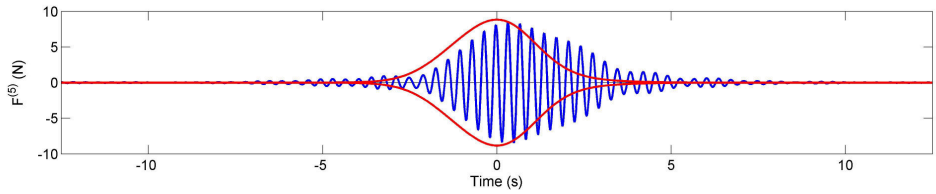

(g) Fifth sum

Figure 7.13: Harmonic components of the hydrodynamic force, extracted using the Taylor separation method, bidirectional with $A = 11.5$cm, $\beta = \pm 20\,^{\circ}$.

sum, and fifth-order sum respectively. For each of the fundamental components, the envelope plotted in red has been found using the Hilbert transform method discussed previously. This fundamental envelope is then raised to the n^{th} power and plotted on top of the n^{th} harmonic component for each of the sum components, after being scaled using a least squares method.

At first glance, all three of the wave group decompositions seem to give reasonable results, which is particularly impressive for the most violent biharmonic group. Figure 7.13(a) gives an indication of the large amount of violent local breaking and splashing that occurred during the test. The robustness of this method for successfully decomposing such a violent wave group is because the force is related to an integration of pressure across the whole cylinder surface. A single point pressure or wave elevation gauge would be more susceptible to the violent splashing and local breaking if it were used to decompose the signal into the harmonic components.

7.5.1 Approximate envelopes

It can be seen from the three figures that the approximate envelopes, found by taking the n^{th} power of the fundamental envelope, match the extracted harmonics fairly well. However, a secondary packet seen in all three of the second-order sum harmonic plots stands out as obviously not fitting the approximate envelope. This extra packet can be attributed to error waves from the paddle. The control signal sent to the paddle was linear, and yet the waves generated were non-linear. This meant that error waves were also generated instantaneously to cancel at the paddle with the true second-order components of the wave group. The error waves then freely propagate down the wave tank separately from the main group and can be seen in surface elevation data whether the column is in place or not.

After accounting for the extra packet at second-order, in the two unidirectional cases the third harmonic is the worst fit to the approximate envelope. These show both a timing difference in the third harmonic relative to the fundamental, and later error waves in addition to the main packet. The poor fit of the main packet could be due to several factors. The $u|u|$ term in Morison drag for regular waves can be Fourier decomposed into two terms related

to the fundamental and third harmonic frequencies. This third harmonic term of the fluid dynamic drag may be present in the extracted third harmonic component found using the Taylor separation method. In addition to this fluid dynamic drag term there could also be a contribution from nonlinear free-surface forces in potential flow, as discussed by Faltinsen et al. (1995) and Chaplin et al. (1997). Finally, there could also be a secondary load cycle due to short and steep waves propagating around the perimeter of the column, as observed by Huseby (2000).

7.5.2 Stokes scaling

The axes for Figures 7.11 and 7.12 are scaled to demonstrate the validity of Stokes scaling. If Stokes scaling is a valid assumption, then the linear scaling factor between the two fundamental force components should be the same as the ratio of the incident wave amplitudes. The factor between an equivalent component in each of the two cases at a higher n^{th} harmonic would then be the n^{th} power of this linear factor. The vertical axis in the n^{th} component of Figure 7.12 is therefore scaled by s^n, where $s = (\max(Envelope^{(1)}_{6cm}))/(\max(Envelope^{(1)}_{11.5cm}))$. This allows a direct comparison between the harmonic plots in the two figures discussed. The ratio of linear force components between Figures 7.11 and 7.12 is $s = 1.69$. On the right of each plot in Figure 7.12 the scaling factor for that harmonic is written, e.g. for the fourth harmonic the scaling factor is 1.69^4.

If Stokes scaling holds true then the scaled plot for each harmonic should be the same height for both wave groups. Figures 7.11 and 7.12 show that they are very close in amplitude and suggest that a simple Stokes-like expansion of a wave group into the harmonic components is a valid approximation. The slightly increased differences in amplitude at fourth- and fifth-order are to be expected, as the effect of any error due to misalignment increases with each harmonic. Higher orders are not shown here as their amplitude is very small and the transfer function to remove the structure dynamic response also attenuates these higher orders. The previous section showed that an approximate envelope could be found for each harmonic from only the fundamental component. This section now shows that these can then be scaled to give a reasonable approximation of the envelopes at each

harmonic for an incident wave group with the same peak period and an arbitrary amplitude.

The linear component time history can also be used to give an approximation of the actual time history at a higher harmonic, rather than just the envelope. Taking the Hilbert transform of the linear component gives a time history that is 90° out of phase with the original signal. These two time histories can then be combined to give an approximation for the time history of a higher harmonic using Stokes fifth-order wave theory, see Fenton (1985). For example, the second-order sum time history would be given by a combination of odd and even terms as shown in Equation 7.10.

$$F^{(2)} = a_1(2F_L F_{LH}) + a_2(F_L^2 - F_{LH}^2) \tag{7.10}$$

where F_L is the linear force component, F_{LH} is the Hilbert transform of the linear component, a_1 is the amplitude of the odd periodic terms ($2F_L F_{LH}$), and a_2 is the amplitude of the even periodic terms ($F_L^2 - F_{LH}^2$). Similar expressions can be derived at each harmonic using only the linear component and its Hilbert transform. The amplitudes, a_1 & a_2, can be found using the envelope amplitude and a phase angle. Since a reasonable approximation of each harmonic envelope can be found from the linear force signal, one then only needs a phase angle at each harmonic to reconstruct the time histories for the higher harmonics. It is remarkable that even for very violent interactions, such as the example shown in Figure 7.13, each force component to a high order can be entirely reconstructed to a reasonable approximation by just the linear signal and a phase angle at each harmonic.

7.6 Force reconstruction

One of the aims of this project is to reproduce accurately the hydrodynamic force on the column using measured surface elevation. This would be very useful in industry as surface elevation is far easier to measure than the forces experienced by a structure during its life. The surface elevation data used as a basis for the force reconstruction were measured by a wave gauge situated 3 m to the side of the column and at the same distance from the paddle as the column leading edge. This meant it was at the focus point of the NewWave wave

groups for unidirectional waves, whilst being far enough away from the column not to be affected by reflections.

7.6.1 Linear

Given the large amount of computing power required to generate a full set of QTFs (quadratic transfer functions), it seemed prudent to test the assumptions made in the method detailed above with some initial tests. First, Morison inertia transfer functions were used to modify the surface elevation for the extracted linear component. This Morison inertia time history matched the measured force well and a comparison of the time histories can be seen in Figure 7.14 (Morison - green, DHI measured - blue), and the spectra in Figure 7.15. Having established that the assumptions made in the method are reasonable, the next stage was to test the ability of DIFFRACT to produce the LTFs (linear transfer functions) and QTFs required. As a first step, a flat QTF matrix approximation was used to minimise computer time by assuming that the QTFs were flat perpendicular to the leading diagonal. This meant that the off-diagonal terms did not need to be calculated and was discussed in Chapters 4 and 5. The force reconstruction for the first harmonic using DIFFRACT and the flat QTF approximation are shown in red in Figures 7.14 and 7.15.

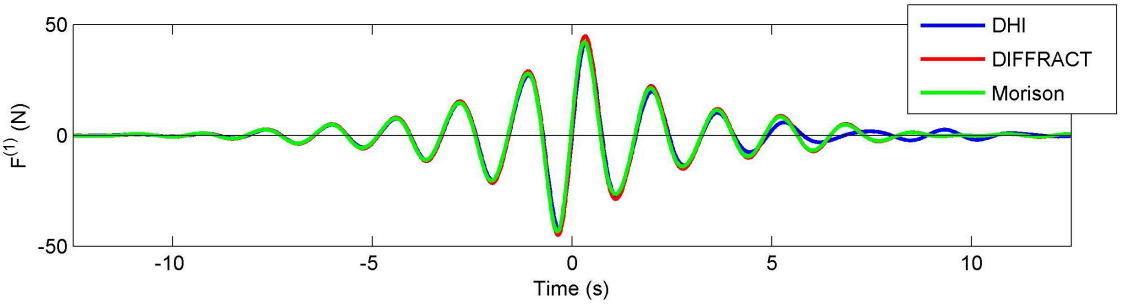

Figure 7.14: Time histories of the first-order force on the column, found by Taylor separation (blue), DIFFRACT reconstruction from the extracted DHI surface elevation (red), and Morison's inertia (green).

Both Morison and DIFFRACT overestimate the central peak of the linear spectrum, with Morison being roughly halfway between the two. However, this has little effect on the force time history, with all three plots being very close. The reconstructions are particularly

close at the lead up to the focus point, but are far less accurate beyond 5 s at the end of the packet. This could be due to some reflections from the column or the wave tank wall reaching the wave gauge before the wave group has completely passed.

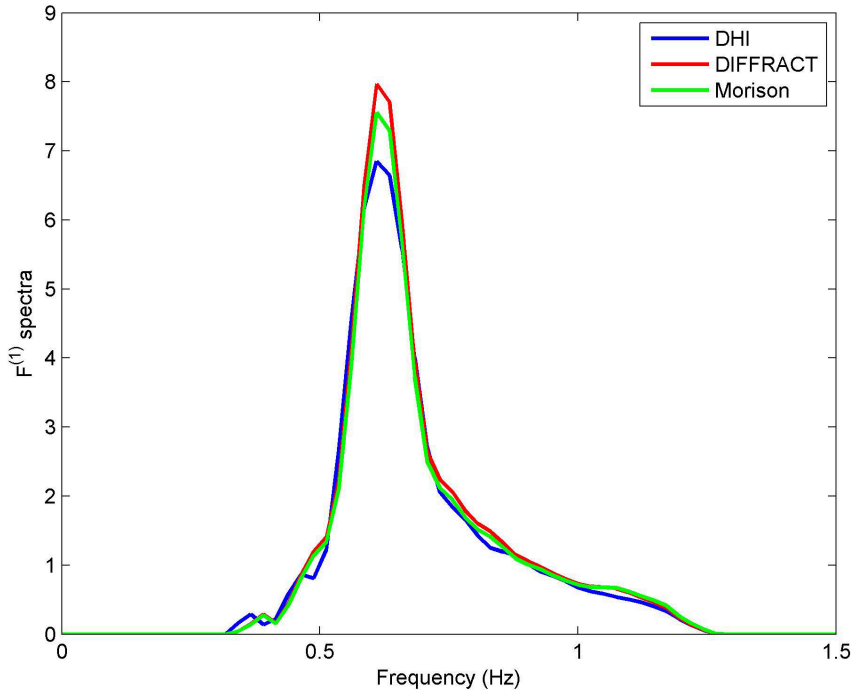

Figure 7.15: Spectra of the first-order force on the cylinder, found by Taylor separation (blue), DIFFRACT reconstruction from the extracted DHI surface elevation (red), and Morison's inertia (green).

7.6.2 Second-order sum

Flat QTF approximation

Having established that the linear force time history could be reproduced fairly closely, the second-order sum and difference terms were looked at next. Figure 7.16 shows the time histories of the second-order sum force, with the blue line showing the signal extracted from the measured data and the red line showing the DIFFRACT reconstruction, again using the flat QTF approximation. Figure 7.17(a) shows the spectra of the extracted DHI signal (blue) and the DIFFRACT reconstruction (red). The reconstruction is clearly not as accurate as it is for the linear case. The reason for the second peak in the time history, around 6 s after

the initial NewWave peak, is due to a second-order error wave from the paddle. The control signal sent to the paddle was linear and so second-order error waves are emitted in addition to the intended NewWave packet. Based on a peak frequency for the fundamental wave group, the group velocity for the main packet is 2.215 m/s, and for the second-order sum error wave it is 1.695 m/s. Since the cylinder is placed 7.8 m from the paddle this means that the second-order sum error wave should arrive around 5 s after the main packet.

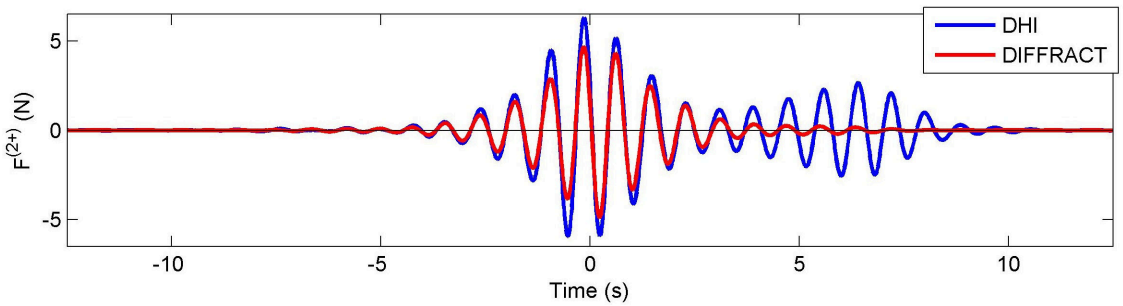

Figure 7.16: Time history of the second-order sum forces on the cylinder, found by Taylor separation (blue) and DIFFRACT reconstruction from the extracted DHI surface elevation (red).

Since the error wave is oscillating at a frequency very similar to the main second-order sum packet, it is reasonable to assume that this is the cause of such a large difference between the spectral peaks in Figure 7.17(a). An attempt to improve the reconstruction involved removing this error wave by applying a ramp down to zero between 2.5-6.5 s of the measured surface elevation data. The spectrum of this modified signal is shown in green in Figure 7.17(b), which now matches the DIFFRACT reconstruction far more closely.

The main difference between the DIFFRACT and modified DHI spectra is the hump before the main peak in the modified DHI spectrum. This hump is centred at 0.61Hz and so is most likely leakage from the first harmonic. It has an amplitude of 0.036, which is around 0.5 % of the first harmonic spectral peak. This is a very small amount of leakage relative to the fundamental but cannot be neglected at second-order. A high pass filter was therefore used to remove this leakage hump from the DHI spectrum, leaving just the second-order sum component. This final modified second-order sum force spectrum is shown in Figure 7.17(b) in black and matches the DIFFRACT reconstruction very closely. The time signals

associated with the modified DHI and DIFFRACT spectra are shown in Figure 7.18 with excellent results.

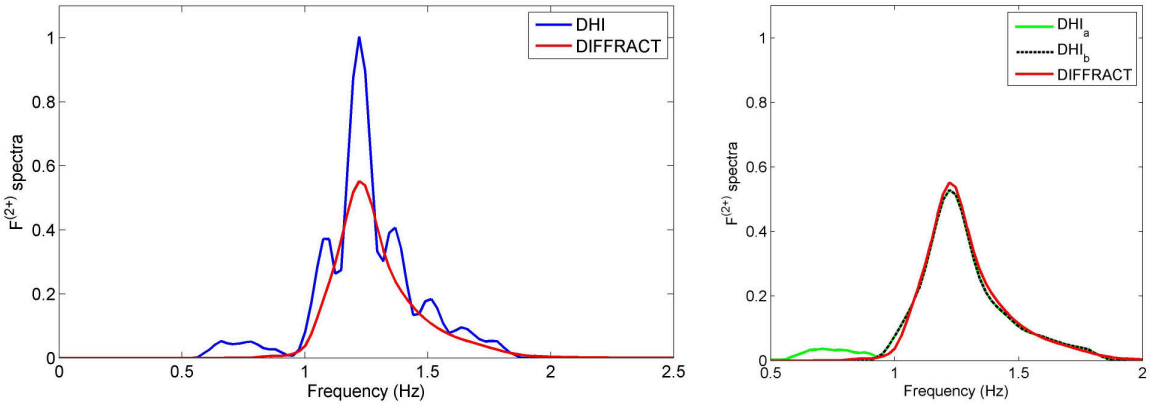

(a) Original extracted DHI signal (b) Modified DHI signals

Figure 7.17: Spectra of the second-order sum forces on the cylinder. In (a) the extracted DHI component is shown in blue, and the DIFFRACT reconstruction from the extracted DHI surface elevation in red. In (b) the DIFFRACT reconstruction again (red), the modified spectrum with error wave removed (green), and the modified spectrum after the first-order leakage was removed (dashed black).

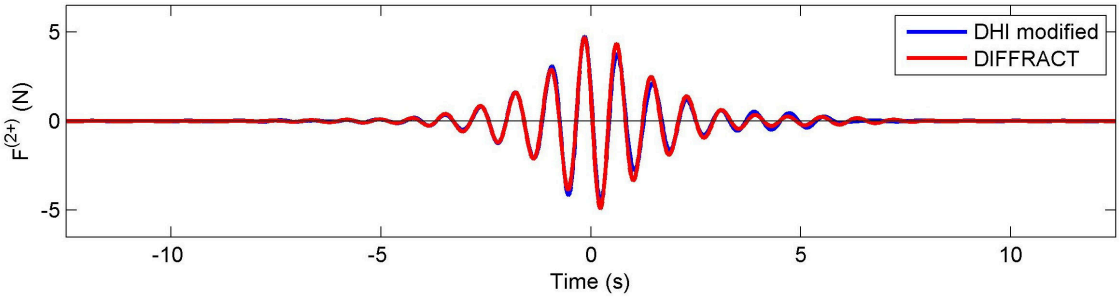

Figure 7.18: Time history of the second-order sum forces on the cylinder, with the blue line showing the modified component extracted from the DHI data and the red line showing the DIFFRACT reconstruction from the original extracted DHI surface elevation.

Full QTFs

Using DIFFRACT QTFs and the flat QTF approximation allowed a fairly accurate reconstruction of the second-order sum force time history. The next steps were to generate the full QTF matrix using DIFFRACT, and to repeat the force reconstruction. Figure 7.19 shows a comparison between the full QTF reconstruction and the extracted DHI results. The blue line is the DHI time history, as modified in the previous section with the error wave and leakage removed. The red line is the full QTF reconstruction and again shows excellent agreement with the extracted DHI results. There is very little difference between

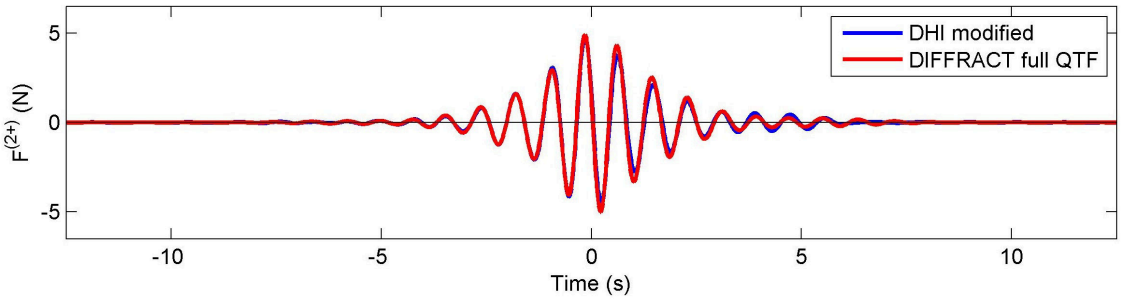

Figure 7.19: Time history of the second-order sum forces on the cylinder, with the blue line showing the modified component extracted from the DHI data and the red line showing the DIFFRACT reconstruction from the original extracted DHI surface elevation and a full QTF matrix.

the two reconstructions, which shows that the flat QTF approximation is a very useful tool for reducing the computational resources required for complex second-order calculations.

7.6.3 Second-order difference

The second-order difference term has proven more difficult to reconstruct. One possible reason for this is the small amplitude of the component relative to the total force signal. As the maximum amplitude of the second-order difference component is only 2 % of the full signal amplitude, any errors in the extraction, such as leakage from other harmonics or noise in the record, will have a large effect. The method used attempts to minimise these errors but there may still be some contamination. Another possible source of contamination is from higher harmonic difference terms. DIFFRACT can only calculate the second-order difference terms and not higher harmonics. The second-order term should dominate a longwave signal but there will be some contributions from higher order difference terms. Finally, there may also be error waves generated at the paddle due to the linear nature of the control signal. A second-order difference error wave generated at the paddle would be free to travel along the tank unbound from the focused wave group and would arrive at the column very close in time to the bound longwave signal.

Reconstruction of the second-order difference wave is not yet understood and requires further work. However, the amplitude of the second-order difference term is very small relative to the total force time history. It has been shown that the linear and second-order sum force time histories can be accurately reproduced from a surface elevation time

history. These are the two largest components and it has been shown that higher order harmonics can also be approximated using a Stokes-like fifth-order model. For an actual structure offshore it is far easier to measure surface elevations than body forces. The ability to reasonably approximate the force time history from surface elevation measurements could therefore be very useful in monitoring body forces during a structure's life and to improve our understanding of the structural requirements when designing an offshore platform.

7.7 Conclusions

Conclusions drawn from the results presented in this chapter are briefly summarized below.

- The Taylor separation method can be used to cleanly separate harmonic components of measured force time histories up to high orders, even for violent reactions with splashing.
- A Stokes expansion gives a good approximation to higher harmonics of the force time history. Finding the fundamental envelope and raising it to the n^{th} power gives a reasonable approximation of the shape of the envelope for the n^{th} harmonic.
- The linear force component can be used to reconstruct the time history of a higher harmonic using the Hilbert transform and a phase angle at the harmonic component. Only an amplitude and phase angle is needed at each harmonic to reconstruct the force time history from the linear component using the Stokes expansion.
- Linear and second-order sum components of body forces can be accurately reconstructed from surface elevation data using transfer functions found with a program such as DIFFRACT, or at first order by Morison's inertia calculations.
- The second-order difference component of the body force is harder to reconstruct but is very small relative to the linear and second-order sum components.
- For the most violent interactions with bidirectional wave groups, the force time history could be separated into harmonic components which matched the Stokes approximation surprisingly well for the first five harmonics.

Chapter 8

Analysis of damage to a TLP

8.1 Introduction

Data was made available to us concerning some storm damage that occurred to a floating concrete tension leg platform (TLP) in the North Sea. The minor damage occurred at a very high elevation: around 28 - 29 m above mean sea level. The following sea state parameters were recorded: significant wave height $H_s = 10.8$ m, zero mean crossing period $T_z = 10.4$ s, peak period $T_p = 13$ - 14 s, and average peak wave direction $\beta = 25^\circ$ relative to the platform north face. At the time of discussion it was not yet known to what extent the sea consisted of waves from two weather systems or not. After taking into account a possible platform set-down of up to 0.5 m, a tidal amplitude of up to 1 m, and storm surge of up to 0.5 m, the water projection must have been at least 26 m above the mean sea level in order to reach the level where damage occurred.

Based on the recorded peak wave direction, the damage occurred a short distance in front of the leading column. The geometry of the platform can be seen in Figure 8.1(a) below and is very similar in the basic dimensions to those of Thunder Horse. The centre-to-centre spacing of the columns is 80 m, compared to an average spacing of just over 80 m for Thunder Horse, and the radius of the columns is 15.5 m, compared to an equivalent average radius of 12.34 m for Thunder Horse. Thus, we have information on a real life situation with a somewhat similar geometry to Thunder Horse and actual storm data rather than average

expected responses. It therefore seemed a good opportunity to use the methods developed in this project. This chapter looks at the application of these methods in order to investigate what conditions could cause such violent water projections.

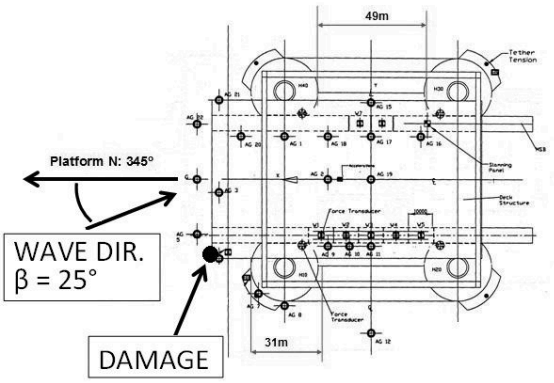

(a) Schematic of geometry with peak wave direction and location of damage

(b) Side view of platform

Figure 8.1: The floating concrete tension leg platform.

8.2 Linear analysis

8.2.1 Regular waves

Some initial linear analysis was carried out using the Linton and Evans analytical solution for a simplified model of four bottom-seated circular cylinders with centre-to-centre spacing 80 m, radius 15.5 m, depth 30 m, and no pontoons. Using the same method as discussed in Section 2.5, the linear near-trapped mode frequencies for the simplified model were found and can be seen in Table 8.1. The columns show the real and imaginary parts of the wavenumber normalised by the circular radius, $a = 15.5$ m, and the associated peak period.

The two near-trapped mode frequencies with the smallest imaginary component (which are therefore likely to be associated with the largest predicted responses and the most violent physical interactions, as explained earlier) are shown in Table 8.1 in bold. These are at $Re(ka) = 1.150$ and 3.626, with corresponding peak periods of $T_p = 7.365$ and 4.148 s respectively. These are very interesting results because period doubling of the first case and

Re(ka)	Im(ka)	T_p (s)
0.627	-0.217	9.977
0.883	-0.223	8.404
1.150	**-0.059**	**7.365**
1.452	-0.222	6.554
1.981	-0.188	5.612
2.234	-0.161	5.284
2.580	-0.135	4.917
3.011	-0.125	4.552
3.626	**-0.086**	**4.148**
4.030	-0.145	3.934
4.710	-0.115	3.639

Table 8.1: Near-trapped mode wavenumbers for the simplified damaged platform geometry.

period tripling of the second both lead to wave periods close to the average peak period recorded in the storm. This suggests that there could be some very violent second- and third-order effects as well as linear amplification. The possible third-order effects cannot be investigated using DIFFRACT, but second-order sum excitation of the near-trapped modes with periods of $T = 7.365$, 6.554, and 5.612 s will be investigated, along with the linear behaviour at $T = 4.148$ s.

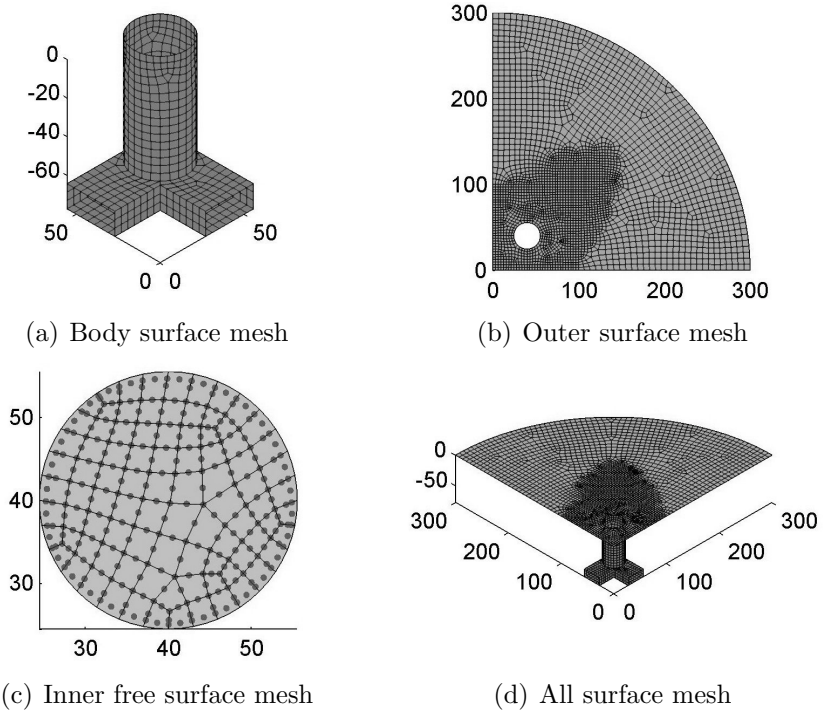

(a) Body surface mesh

(b) Outer surface mesh

(c) Inner free surface mesh

(d) All surface mesh

Figure 8.2: A more realistic model mesh for the damaged platform with pontoons and deep water.

Having established which frequencies are of interest using the simplified model, the runup was found around a more realistic diffraction model to check that the predicted near-trapped mode frequencies were similar for both the simple and more realistic models. Looking only at runup can miss upwelling peaks within the array, but it allows for a quick comparison and it seems a reasonable starting point since the damage occurred near to Column 3. The model used is shown in Figure 8.2, and is now in deep water with pontoons connecting the columns at their base.

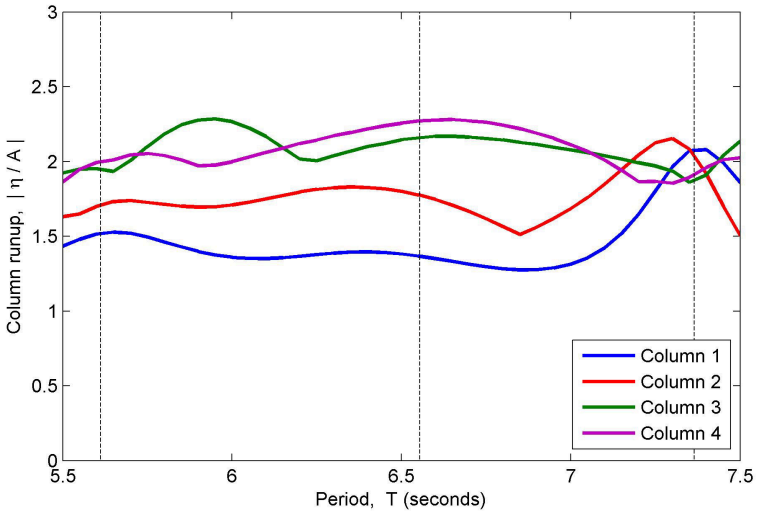

Figure 8.3: Maximum runup around each column with the more realistic model over the range of periods $T = 5.5 - 7.5$ s for a unit-amplitude incident wave and $\beta = 25°$.

Figure 8.3 shows the linear runup on all four columns between the periods of 5.5-7.5 s. Second-order sum responses at these periods correspond to incident waves with periods between 11-15 s, covering the range of likely values for the peak period of the storm wave that caused the damage. The three near-trapped modes with periods within this range are shown on the figure with the vertical dashed black lines. The peak runup amplitudes shown in Figure 8.3 match up reasonably well with the predicted near-trapped modes, allowing for some differences given that the plot only shows runup and a near-trapped mode could be associated with a maximum upwelling within the array rather than runup. The main exception to this is the peak in amplitude on Column 3 (the upstream column for $\beta = 25°$) at a period of 5.95 s. This has an elevation amplification of 2.29, which is the largest within

the range investigated. The damage recorded was located just upstream of Column 3, so this period will be investigated as well as the near-trapped modes.

Having confirmed that the near-trapped mode frequencies are similar for both the simple and more realistic models, Figures 8.4(a) and 8.4(b) show plots of the response to monochromatic waves at $T = 7.365$ and 4.148 s respectively, with the recorded peak wave direction of $\beta = 25°$ to the platform north. The northern face on this plot is the left hand side and so the wave direction is coming from the bottom left corner towards the upper right corner at an angle of 25° anticlockwise from the horizontal axis. Both cases show fairly large runup in front of Column 3 (upstream column) but the largest values are runup on Column 1 (downstream column) with maximum amplifications relative to the incident wave of 2.09 and 2.81 for (a) and (b) respectively. There is fairly significant runup on Column 3 nearest the area of damage, but the damage occurred approximately 15 m in front of the column. This would suggest up-welling rather than column runup.

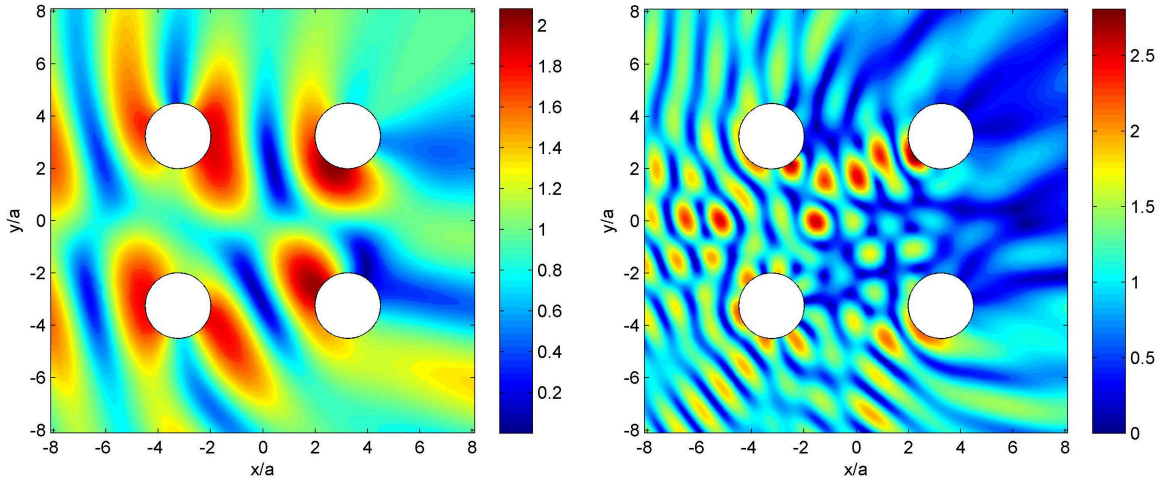

(a) $T = 7.365$ s (b) $T = 4.148$ s

Figure 8.4: Modulus of the total linear surface elevation for unit-amplitude regular waves with $\beta = 25°$ at near-trapped mode periods (a) $T = 7.365$ s and (b) $T = 4.148$ s.

Two other possible modes of interest are at periods $T = 6.554$ and $T = 5.612$ s, which if excited by second-order sum terms will correspond to incident waves of period $T = 13.108$ and $T = 11.224$ s respectively. Given the estimated peak period range of 13-14 s, a component at 11.224 s may not have enough energy to be of interest but will be included for

completeness. Figures 8.5(a) and 8.5(b) show plots of the total linear surface amplification for regular waves at $T = 6.554$ and $T = 5.612$ s respectively, with the recorded peak wave direction of $\beta = 25°$ anticlockwise from the horizontal axis. Both of these near-trapped modes show peaks in the surface elevation very close to where the damage occurred. At these higher wavenumbers, the majority of surface amplification takes place between the leading columns and in front of the structure, with sheltering occurring behind. This suggests that one of these modes is more likely to be responsible for the recorded damage, rather than the mode with the smallest imaginary part.

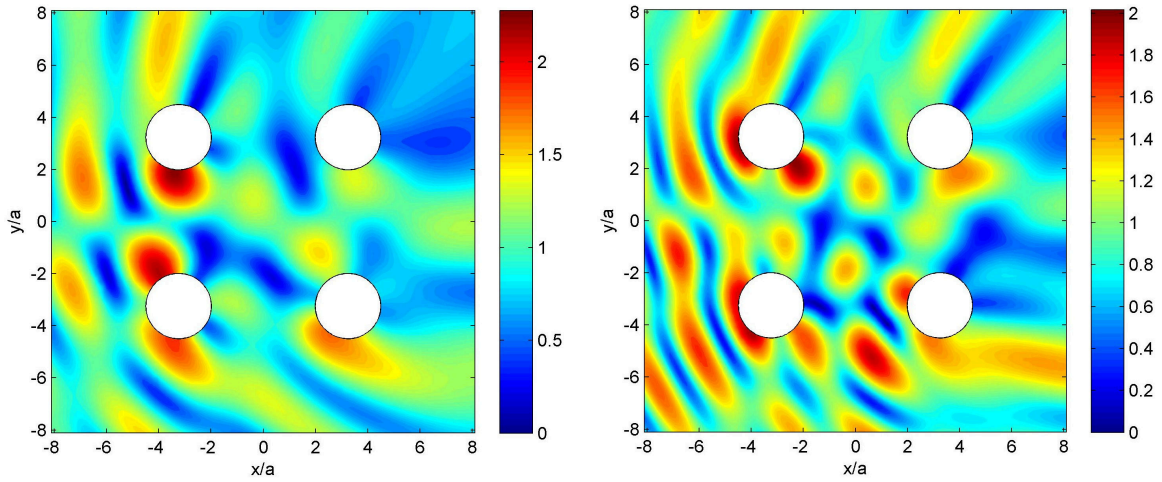

(a) $T = 6.554$ s (b) $T = 5.612$ s

Figure 8.5: Modulus of the total linear surface elevation for regular waves with $\beta = 25°$ at near-trapped mode periods (a) $T = 6.554$ s and (b) $T = 5.612$ s.

The runup analysis in Figure 8.3 showed a particularly high elevation at an incident period of $T = 5.95$ s. This could be excited through second-order sum interactions by an incident wave of $T = 11.9$ s, which is close enough to the measured peak period range to be worth investigating. Figure 8.6 shows the total surface elevation for incident regular waves with the measured wave direction and both the period of maximum runup, $T = 5.95$ s, and the incident period leading to second-order sum excitation, $T = 11.9$ s. There are numerous peaks on the leading edges of the array, with sheltering behind the structure and also to some extent in the centre of the array.

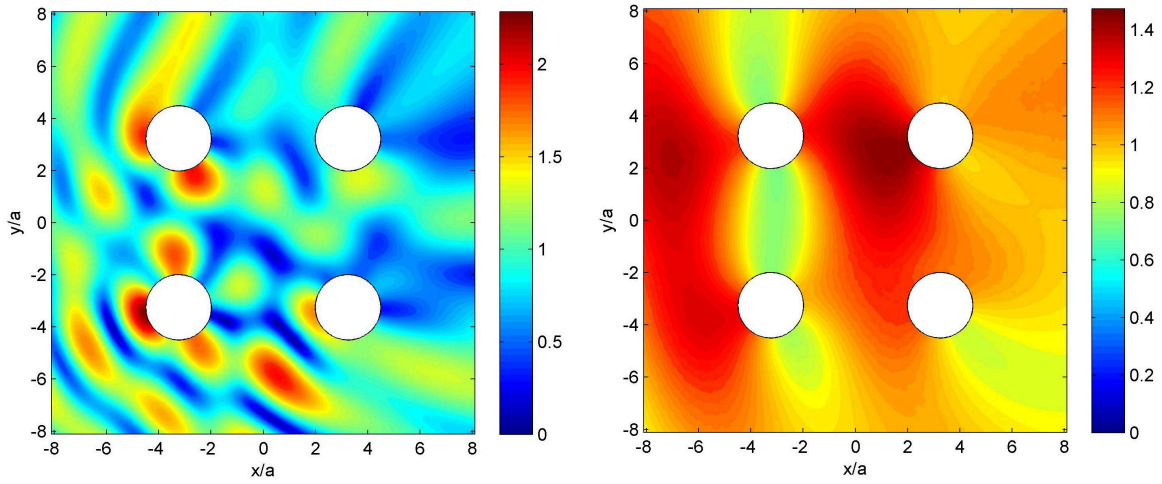

(a) $T = 5.95$ s (b) $T = 11.9$ s

Figure 8.6: Modulus of the total linear surface elevation for regular waves with $\beta = 25°$ at periods (a) $T = 5.95$ s and (b) $T = 11.9$ s.

8.2.2 Net Amplification Factor

The results of the previous section were for monochromatic incident waves, which are unrealistic models of storm waves. Rather than monochromatic waves, an incident sea state based on a JONSWAP spectrum is far more appropriate when predicting responses during a strong storm. The Net Amplification Factor introduced in Chapter 3 can therefore be used to give a more accurate prediction of where violent linear responses are most likely to occur. The Net Amplification Factor is based on incident waves with a JONSWAP spectrum and gives the amplification for a given number of waves caused by the presence of a structure relative to open ocean. Figure 8.7 shows field plots of the Net Amplification Factor for four JONSWAP peak periods, $T_p = 11.224$, 11.9, 13.108, and 14.73 s, all with $\beta = 25°$. All four plots are similar, which is to be expected given that the peak periods are fairly close. The first plot, with a peak period of $T_p = 11.224$ s, gives the largest amplification with a value of 1.57. The largest amplification in the first two cases is located upstream of Column 4 (top left column) and in the second two cases this shifts to upstream of Column 1 (top right column). All four cases show reasonably high amplification around the location of the damage given the incident peak periods.

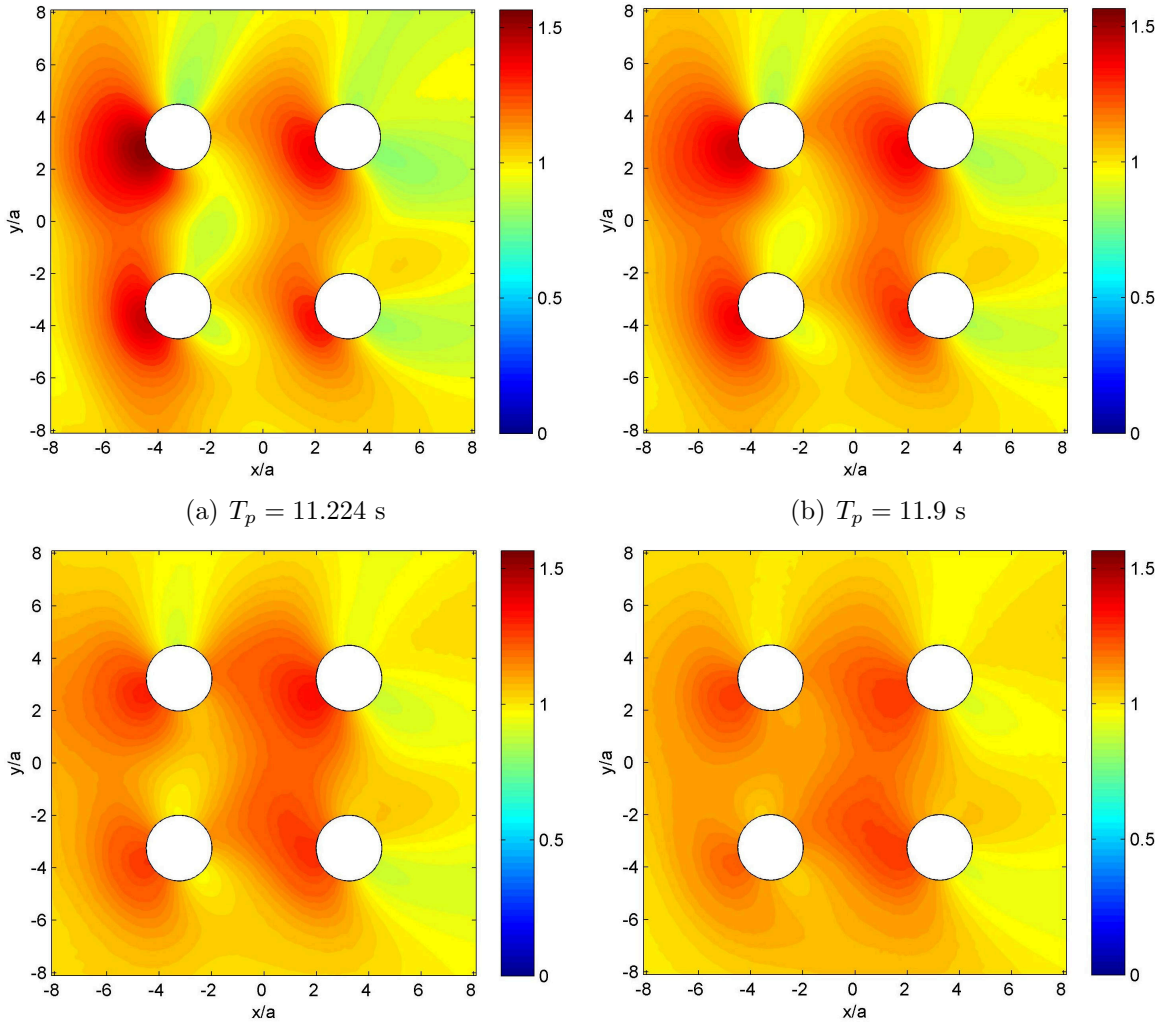

(a) $T_p = 11.224$ s

(b) $T_p = 11.9$ s

(c) $T_p = 13.108$ s

(d) $T_p = 14.73$ s

Figure 8.7: NAF with $\beta = 25°$ and period (a) $T_p = 11.224$, (b) $T_p = 11.9$, (c) $T_p = 13.108$, and (d) $T_p = 14.73$ s.

8.3 Second-order analysis

Building on the work done at first-order, second-order simulations were run to see if the extra elevation needed for water to reach the damage location could be successfully predicted. Figure 8.8 plots the modulus of the second-order sum QTFs across the field for incident wave periods of $T = 11.224$, 11.9, 13.108, and 14.73 s. For a response as violent as the one recorded, both the linear and second-order components must be large and in phase. Comparison of the second-order sum QTF and linear NAF field plots can highlight locations where this might be the case. Given the spectral nature of incident storm waves, a large second-order component will also need large QTFs at other frequencies in the spectra, but the peak period is the largest contribution and therefore a good indication.

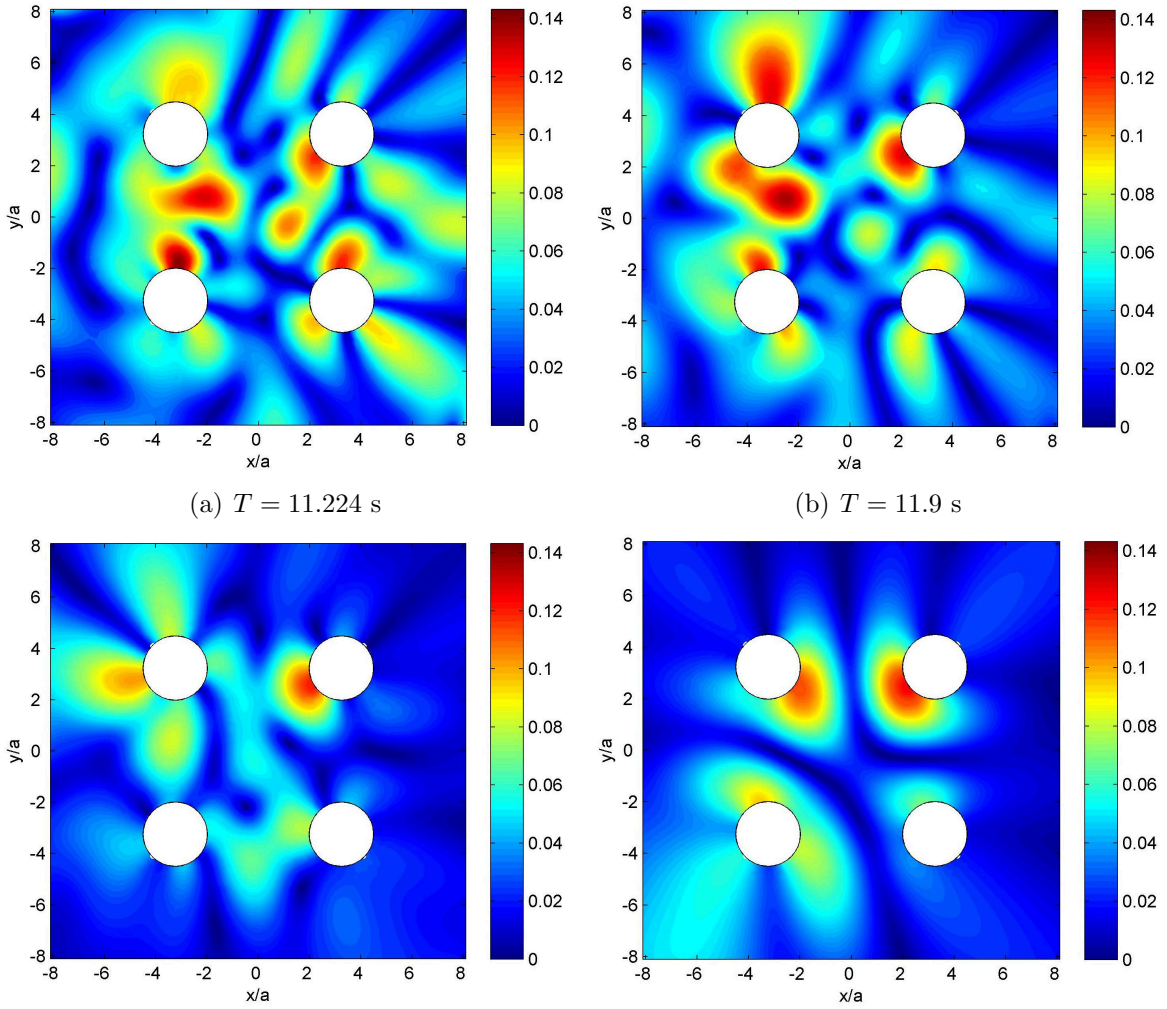

(a) $T = 11.224$ s

(b) $T = 11.9$ s

(c) $T = 13.108$ s

(d) $T = 14.73$ s

Figure 8.8: Modulus of the second-order sum surface elevation QTF for an incident regular wave with $\beta = 25°$ and period (a) $T = 11.224$, (b) $T = 11.9$, (c) $T = 13.108$, and (d) $T = 14.73$ s.

There is quite a lot of change between the four plots, despite the response frequencies being separated by less than two seconds. This suggests it may be hard to find a location with a very large second-order component for an incident sea state with a JONSWAP spectrum. The only location with a large QTF amplitude in each of the four cases is just upstream of the downstream column. The QTF amplitude at the location of the recorded damage is relatively low for all four cases.

Figure 8.9 shows the modulus of the total surface elevation, including first and second-order interactions, for two near-trapped modes of interest. Figure 8.9(a) has an incident regular wave with $T = 13.108$ s, and Figure 8.9(b) with $T = 11.224$ s, both of which will excite a near-trapped mode through second-order sum interactions. Both cases have a wave

amplitude of 10.06 m and a wave direction of $\beta = 25°$. A wave amplitude of 10.06 m was chosen by assuming a time period of three hours (fairly typical for a storm duration) and by using the measured significant wave height of 10.8 m to find the standard deviation of the wave amplitudes. Equation 3.6 was then used to find the most probable extreme wave amplitude in the chosen time period.

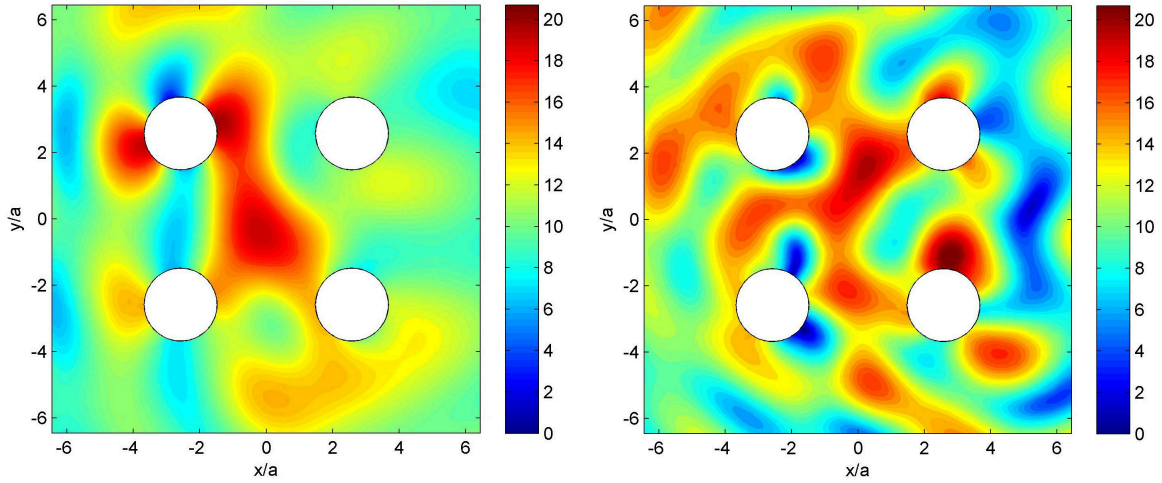

(a) $T = 13.108$ s (b) $T = 11.224$ s

Figure 8.9: Modulus of the total surface elevation including first- and second-order interactions for an incident regular wave with amplitude $A = 10.06$ m, $\beta = 25°$, and (a) $T = 13.108$ s, (b) $T = 11.224$ s.

Both figures show large projections within the centre of the array and large runup on some of the columns. The maximum predicted elevations in these cases are 19.3 m and 21.2 m respectively, which are both well below the required 26 m. These results are for monochromatic incident waves and so it is likely that this maximum elevation will be reduced for a wave group with an incident JONSWAP spectrum of the same peak period. Also, the location of the projections with the maximum amplitudes in these two cases are within the array and not where the damage was recorded.

As there was some doubt as to whether the storm waves were uni-directional or if there were two weather systems present, it seemed worth looking briefly into the effect of changing the incident direction. First-order runup was found on all four columns for an incident wave direction of $\beta = 0°$ (moving horizontally from left to right on the figures) across the same

range of periods as Figure 8.3. The maximum runup occurred at a period of 6.2 s, which could be excited at second-order by an incident period of 12.4 s. Figure 8.10(a) shows the modulus of the total surface elevation for an incident wave period of $T = 12.4$ s with an incident wave amplitude of 10.06 m and wave direction $\beta = 0°$.

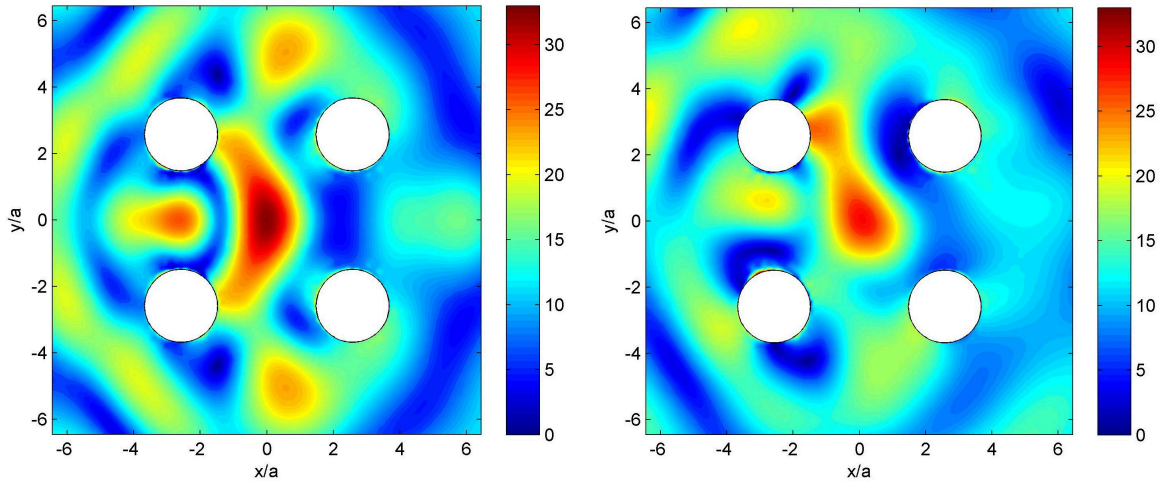

(a) $T = 12.4$ s, $\beta = 0°$ (b) $T = 12.4$ s, $\beta = 25°$

Figure 8.10: Modulus of the total surface elevation including first- and second-order interactions for an incident regular wave with amplitude $A = 10.06$ m, period $T = 12.4$ s, and (a) $\beta = 0°$, (b) $\beta = 25°$.

This clearly shows a huge projection in the centre of the array with an amplitude of 33.1 m above mean sea level. This projection will not cause the damage recorded in front of the leading column but it shows that a very large elevation can be predicted in sea states with a slightly different wave direction. Figure 8.10(b) shows an equivalent plot to Figure 8.10(a), but this time with a wave direction equal to the mean measured wave direction, $\beta = 25°$. The effect of this is to reduce the maximum elevation to 28.7 m and change the position of some of the smaller elevation peaks.

8.4 Second-order statistics of response

The method of generating random spectra discussed in Section 3.4.1 was then applied to this problem. Several target JONSWAP sea state spectra were selected so that second-order sum interactions at the peak period would excite one of the predicted near-trapped modes close

to the parameters recorded during the storm damage. Rather than calculating statistics across the entire field, which would take a lot of resources, locations of interest were selected for each of the spectra using the NAF plots discussed earlier. All of the spectra used had a significant wave height of $H_s = 10.8$ m and an incident wave direction of $\beta = 25°$. Statistics were not collected at other wave directions, despite the high predictions shown at $\beta = 0°$ because of the lengthy computation time for QTF calculations and limited resources for this case study.

The target spectra were each randomly sampled to give two sets of coefficients, a_n and b_n, where $n = 1 : N/2$ and N is the length of the signal being generated. These coefficients represent the amplitude of the cosine and sine components at the n^{th} frequency in the spectrum and are defined as $a_n = z_n.\sqrt{S(\omega_n)d\omega}$, where z_n is a set of Gaussian distributed random numbers with zero mean and unit variance and $S(\omega_n)$ is the spectral component of the target sea state at the n^{th} frequency, ω_n. Rather than generating one long time history with which to collect statistics, it was more convenient to generate a large number of short time histories that could then be combined. Sets of 10^6 waves were produced using 10^4 short time histories of length 1033 s with a sampling frequency of 1.98 Hz.

The linear and quadratic transfer functions calculated for the more realistic model of the damaged platform were used to modify the random incident spectra in the frequency domain. An inverse FFT was then taken to find the response surface elevation to second-order with the structure present. For the response time histories, each zero upcrossing was found and the crest and trough within each period identified. These crests and troughs were then combined into a single large data set. The average expected extreme crest surface elevation for approximately a one-in-2000 wave was found by averaging the surface elevation of the largest 500 crests.

Figure 8.11(a) is based on an incident spectrum with a peak period of $T_p = 11.9$ s and the transfer coefficients were calculated at a location of $x = -56$ m, $y = -30$ m, which is just upstream of Column 3 and close to where the damage occurred. There is a fairly large second-order sum component with an amplitude of 4.24 m but a low linear component.

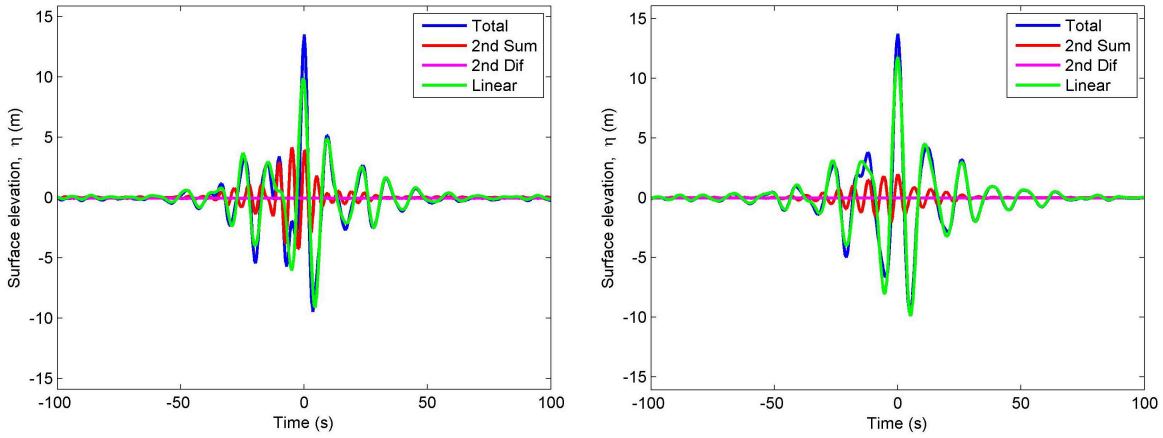

(a) $T_p = 11.9$ s at (-56 m,-30 m)

(b) $T_p = 13.108$ s at (-60 m,-40 m)

Figure 8.11: Average extreme crest elevation with $\beta = 25\,^\circ$ for (a) $T_p = 11.9$ s at (-56 m,-30 m) and (b) $T_p = 13.108$ s at (-60 m,-40 m).

This frequency was chosen to maximise the response from second-order sum interactions. However, the linear response is fairly close to the elevation in open ocean. When combined, the total one-in-2000 wave elevation is 13.53 m. This is barely half of the recorded damage height. When crest elevation is plotted against probability of occurrence, the one-in-10^6 wave elevation is predicted to be just under 20 m.

When the same method was applied for a base incident spectrum with a peak period of $T_p = 13.108$ s at the same location, the results were similar with a maximum crest elevation of 12.51 m and a second-order sum component with a maximum amplitude of 4.08 m. However, if the location is moved around 10 m to (-60 m,-40 m), which is closer to the damage location, then the second-order component is much smaller. Figure 8.11(b) is based on an incident spectrum with a peak period of $T_p = 13.108$ s, and the transfer coefficients were calculated at the new location of $x = -60$ m, $y = -40$ m. The maximum elevation for the average expected one-in-2000 crest is 13.71 m, with 11.78 m contributed from linear interactions. The maximum second-order sum amplitude of 1.96 m is very small considering the small change in location. The maximum elevation reached is very similar to Figure 8.11(a) except the second-order sum component is smaller and the linear component is larger.

Figure 8.12 plots the average extreme crest elevation and crest vs. period for $T_p = 11.224$ s, $\beta = 25^\circ$ at $x = -57$ m and $y = 34$ m, which is just upstream of Column 4 (top left). This is still on the same face as the recorded damage but much closer to the other column.

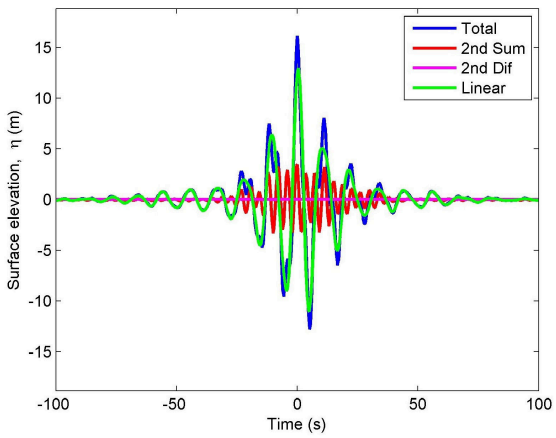

(a) Average extreme crest elevation

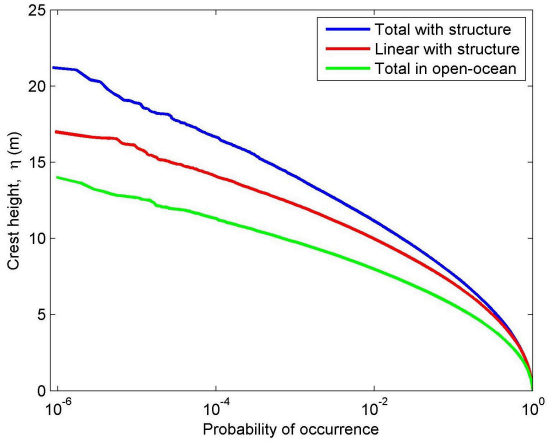

(b) Crest vs. Probability of occurrence

Figure 8.12: (a) Average of the top 500 crests and (b) crest amplitude vs. probability of occurrence per wave with $T = 11.224$ s, $\beta = 25°$ at $x = -57$ m and $y = 34$ m.

The maximum crest elevation for the average one-in-2000 wave is 16.13 m, almost 10 m short of the damage elevation. Figure 8.12(b) shows the crest elevation against probability of occurrence and the maximum elevation shown of 21.22 m for a one-in-1.2×10^6 wave is still at least five meters short of the target height.

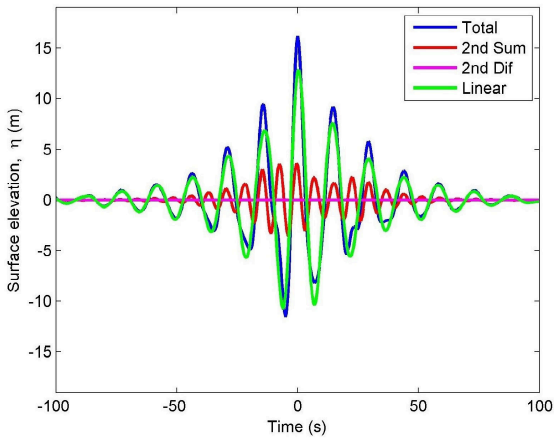

(a) Average extreme crest elevation

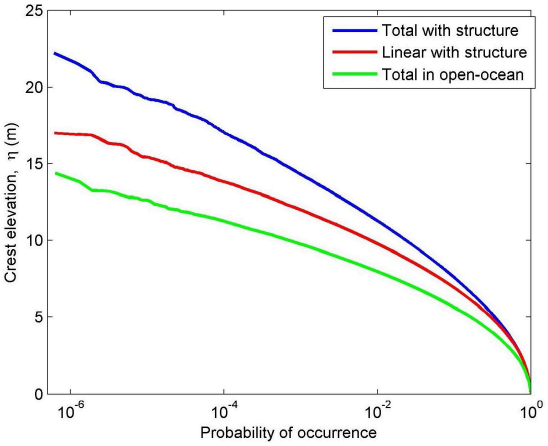

(b) Crest vs. Probability of occurrence

Figure 8.13: (a) Average of the top 500 crests and (b) crest amplitude vs. probability of occurrence per wave with $T = 14.73$ s, $\beta = 25°$ at $x = 27$ m and $y = 30$ m.

Figure 8.13 shows the average extreme crest elevation and crest vs. period for $T_p = 14.73$ s, $\beta = 25°$ at $x = 27$ m and $y = 30$ m, which is just upstream of the downstream column. This location had the most consistently large amplitude second-order sum component in Figure 8.8 and a fairly high linear elevation in Figure 8.7. Figure 8.13(a) shows that the

average one-in-2000 crest surface elevation reaches a maximum amplitude of 16.14 m, which is well below the target value of 26 m. Figure 8.13(b) plots crest elevation against probability of occurrence per wave and shows that at probabilities as low as one-in-1.6×10^6 waves, the elevation predicted is still below the target with a value of 22.19 m. Given the difficulty in finding large elevation predictions close to the location of the damage or any elevation predictions within the array at the same height as the damage location, perhaps a two weather system is a more plausible explanation. More work could be done on investigating other wave direction results but the interactions between two crossing weather systems would be more likely to produce such a large response given the measured significant wave height. It is also possible that the interaction cannot be accurately modelled by second-order theory. A near-trapped mode was predicted at $T = 4.148$ s so there could also be a strong third-order triple frequency interaction occurring.

8.5 Conclusions

Conclusions drawn from the results presented in this chapter are briefly summarized below.

- Near-trapped modes were predicted at periods that suggest, given the recorded peak period, there could be violent second- and third-order effects.
- Statistics of response to second-order predicted maximum elevations that were all well below the elevation of the damage for the sea states examined.
- It is possible strong third-order triple frequency interactions occurred in which case second-order theory could not accurately model the interaction.
- It is also possible that waves from two weather systems interacted with the structure rather than just one. Unidirectional waves cannot accurately model the interaction in crossing seas.
- Further work would need to be done to understand how damage occurred so high above mean water level.

Chapter 9

Conclusions and recommendations

The main aims of this research were to improve our understanding of extreme wave-structure interactions, and develop a screening process to aid in air-gap design for new structures. This chapter reviews the main conclusions drawn from the research presented in this thesis and discusses possible future work.

9.1 Conclusions

The research began by looking at the diffraction of monochromatic waves and how body shape affects this. The cross-sectional shape of surface piercing columns was shown to need careful consideration when designing new structures. Fresnel diffraction effects due to sharp corners were shown to extend across the whole face of the column. Interactions between closely spaced columns lead to higher wave-structure interactions than for an isolated column, with all the column cross-sections studied. Comparing the diffraction pattern between columns with different cross-sections showed that, although the overall pattern was very similar for the different cross-sections, there were distinct changes in the pattern geometry, in peak amplitudes, and in the position of maximum amplification at a given frequency. The near-trapping phenomenon was investigated and shown to contribute significantly to the largest wave-structure interactions. Changing the column cross-section led to small changes in the excitation frequency for a given near-trapped mode. Perturbing the structure geometry by moving one column relative to the others or changing the radius of one of the

columns could lead to large changes in both the diffraction pattern and the maximum amplitude reached at a given frequency. The largest reduction in maximum amplitude for the near-trapped mode studied was for the case of moving a column towards the centre of the array by 10 % of the centre spacing. If symmetry perturbation were to be used to minimise water-deck impact for a real structure one would have to look at the effects across all frequencies in the expected range to ensure that it did not increase the risk of water-deck impact at another frequency. One would also have to balance any benefits gained from reduced water-deck impact with increased cost and complexity in construction of a non-symmetrical structure.

Regular waves are not realistic models for extreme storm waves, so random waves consistent with a spectrum such as JONSWAP should be used instead. Diffraction of waves from a JONSWAP spectrum is rather different from that of waves at a single frequency due to several near-trapped modes being excited at once. For a NewWave focused wave group there is also the consideration of where to focus the wave group. Statistical tools such as the Net Amplification Factor can be used to show which locations within an array are most likely to give a violent response for a given storm approach direction and spectral content. This can be used to target simulations and analysis on the locations where water-deck impact is most likely to occur. It was also shown that large numbers of random surface elevation time histories can be generated for a sea state efficiently by performing diffraction transfer function calculations in the frequency domain. This allows a much cheaper alternative to wave-tank model testing for the calculation of statistics which could then lead to targeted wave-tank model experiments rather than general random wave simulations. Collection of random linear statistics in this way was used to verify the Net Amplification Factor as a tool for analysing water-deck impact.

Second-order diffraction patterns were compared to the first-order results seen earlier, and it was found that the diffraction pattern and mode shape excitation frequency were similar at second-order double frequency to the linear behaviour at the same response frequency. Changing column shape and placement do not make large changes to the general diffraction pattern but do make distinct local changes and can change the amplitude and position of the

maximum surface amplification predicted. For a given geometry, the response frequency for a near-trapped mode is independent of whether it is excited linearly or by second-order sum interactions. For the simple geometry of four circular columns, one can use linear results to give reasonable approximations of low frequency near-trapped mode shapes excited by second-order sum interactions. At higher frequencies, the second-order and first-order mode shapes become less similar. More complex geometries, such as adding pontoons, can lead to larger changes at second-order, which can result in poorer approximations of second-order mode shapes from linear results. It was also shown that at low frequencies one can approximate the QTF sum-interaction matrices as being flat perpendicular to the leading diagonal, which allows the number of lengthy second-order calculations necessary (N^2) to be reduced to just N along the leading diagonal. At higher frequencies there is more variation and a flat QTF approximation becomes less reasonable, but it was shown when the real and imaginary components of the elevation QTFs were plotted that there is still distinct structural behaviour indicating the frequencies of near-trapped modes.

The statistical methods introduced with linear transfer functions were then extended to include second-order results. It was shown that second-order components could make a large contribution to the total surface elevation, particularly in steep sea states. Statistics were collected on random waves using a brute force method in which incident spectral components were multiplied by LTFs, and pairs of incident spectral components were multiplied together and then by QTFs, to find the response spectrum in the vicinity of a structure. Only a single inverse FFT was then needed to find to second-order the surface elevation time history associated with the response spectrum. Using QTFs to modify the incident spectra in the frequency domain allowed a fast, efficient method of calculating surface elevation time histories to second-order, without needing to implement the complex methods of Naess or Winterstein. Comparison of surface elevation time histories calculated using both the full QTF matrix and the flat QTF approximation showed that the results for the approximation were fairly close to the full matrix elevations. This showed that the flat QTF approximation can be used to greatly reduce the number of lengthy QTF calculations needed for second-order results without significantly compromising the quality of results, although for highly accurate second-order elevations one must still use the full matrix. The average surface

elevation for a one-in-N_w wave can be found along with the average incident wave that would cause it. These average incident waves or 'designer' waves could be used in targeted wave-tank model testing rather than general random wave simulations. They require far less time and have the added benefit of minimal interference from side and end wall reflections in a real wave tank. The comparison of first- and second-order water-deck impact predictions also showed that first-order predictions greatly underestimated the likelihood of violent responses. The second-order results suggest that if the Thunder Horse platform were a TLP with minimal vertical movement there would be fairly frequent water-deck impacts.

Comparison of fixed and freely floating bodies shows that, despite the large size and inertia of a platform such as Thunder Horse, allowing the structure to move can have a dramatic effect on the prediction of water-deck impact. One must be very careful to accurately model the movement of a structure when assessing the required air-gap during the design phase. The resonant periods of Thunder Horse in all motions except heave are very long compared to typical storm wave peak periods. It is likely that the spectral energy at these resonant periods would be minimal. In heave, the resonant period of 26.2 s is close enough to typical storm peak periods that body motions must be modelled. At low periods, there are negligible differences between diffraction coefficients for fixed and moving bodies. However, for periods between approximately 10 to 24 s there are significant differences. Both linear and quadratic transfer functions of free surface elevation tend to be smaller in amplitude for the moving model relative to the fixed model. There are also some differences in the surface elevation amplification diffraction patterns between the fixed and moving models. The linear NAF can be easily modified to give useful information on air-gap requirements for a moving body. The difference patterns at near-trapped modes between the fixed and moving models form a progression in the geometric pattern similar to that seen in the fixed model near-trapped mode shapes, although the patterns themselves do not match up with the fixed model near-trapped mode shapes. Second-order diffraction patterns for moving models are closer in shape to linear excitation at the same response frequency than is the case with the fixed model. The statistics collected for extreme wave-structure interactions showed that there was usually a small reduction in wave crest level above mean water level for the moving model relative to the fixed model, with larger reductions at second-order than

at first-order. When body motions are taken into account in addition to the slightly reduced wave elevation, the probability of water-deck impact occurring in the sea states studied is greatly reduced for the moving model. When designing a new structure, the type of mooring system (stiff or soft moorings) must be very carefully considered. For the model considered here, stiff tendons would lead to far more water-deck impacts and therefore a greater risk to personnel and equipment. Thus, semi-submersibles would seem to have distinct advantages over TLPs in terms of the risk of wave-deck impacts (although one major advantage of TLPs – dry tree steel conductors – is lost).

Analysis of the DHI data showed that the Taylor separation method can give clean separation of body force harmonic components to high orders for a single surface piercing column. This separation method for force is still possible despite large amounts of splashing and violent breaking. The separation method is, however, very sensitive to the correct line-up of the focus points in the crest and trough signals. The use of NewWave focused wave groups rather than random wave simulations proved a very efficient method of recording extreme wave-structure interactions, and allowed a huge number of targeted experiments to be carried out in the allotted tank time. Comparison of the harmonic components between incident waves with different H_s values shows that Stokes scaling gives a reasonable approximation of the nonlinear harmonic behaviour in steeper seas. The ratio between envelope amplitudes at the n^{th} order is approximately equal to the ratio between the fundamental envelope amplitudes raised to the power n. The shape of the envelope for the n^{th} harmonic can also be approximated by finding the envelope of the fundamental component and raising this to the power n. Filtering can be used to remove high frequency structural response 'ringing' effects without significant loss of spectral energy in the hydrodynamic force data. A good approximation of the linear and second-order sum components of the body forces can be reconstructed from measured surface elevation data in the vicinity of the structure along with transfer functions found using DIFFRACT. This could be very useful in practice as it is far easier to measure surface elevation than body force on a structure in operation offshore. The second-order difference component proved more difficult to reconstruct, largely due to second-order error waves from the paddle, but is very small. The only important sum harmonic for which the Stokes decomposition does not work well is the triple frequency

third-order sum term. The physical reason for this is unknown at present.

Analysis of wave-structure interactions with the damaged platform showed that there were several near-trapped modes that could have been excited by second-order sum interactions of large components in the incident wave group. However, surface elevations large enough to cause the recorded damage were not predicted in the analysis with the average peak wave direction. Large responses were shown to be possible at other wave directions and it is likely that a different wave direction from the average recorded direction or waves from a second weather system not known at the time of the case study were responsible for the damage.

9.2 Recommendations for future work

It has been shown that structure geometry can have a large effect on wave-structure interactions and that by perturbing the geometry or changing column shape one can alter the position and amplitude of the maximum wave surface amplification. One could build on the research presented here by carrying out a study across a range of frequencies for one or two cases of perturbed geometries to investigate the feasibility of using a perturbed geometry to minimise water-deck impact and to show whether benefits at one frequency would then lead to increased probability of a violent response at another frequency. It would also be of interest to investigate whether it would be at all practical to construct a perturbed geometry structure. If carried out, these investigations should include both second- and first-order results as it has been shown that second-order results can contribute a large part of the total surface elevation. Although DIFFRACT has been thoroughly validated over the years, extensive use of symmetry has been made both to reduce DIFFRACT computation time and to find an approximate mode shape from surface elevation field plots. It would be useful to validate these methods against experimental data in addition to the more elegant analytical method of Meylan and Eatock Taylor (2009).

It was shown that random surface elevation time histories could be generated efficiently using frequency domain calculations. An automated procedure could be created by collecting

the methods discussed in this research that would generate large numbers of random time histories across a range of possible storm wave spectra and then calculate statistics on the generated data sets. This automated procedure would mean that once diffraction transfer functions were generated for a model, one could simply set the program going and output results on the sea states most likely to cause water-deck impact, the locations within the array where this would likely occur, and the expected probability of occurrence for water-deck impact with this structure. 'Designer' incident waves could also be generated automatically that would lead to the largest expected wave-structure interactions, so that further numerical analysis and wave-tank model testing could then be planned based on the overview generated by the automatic procedure.

Large differences were predicted in the probability of water-deck impact between fixed and moving models. It would be useful to be able to compare experimental data for a model fixed vertically and then allowed to move freely with incident NewWave focused wave groups at the predicted near-trapped modes for the structure. It was shown in Chapters 2 and 4 that there is a geometric progression in the shape of fixed model near-trapped modes with shortening period. It was suggested in Chapter 6 that there could also be a similar geometric progression in the shape of the surface elevation difference between moving and fixed models. It would be worth spending some time investigating whether there is a relationship between these two geometric progressions. If a relationship were found it could then be used to give approximations of the surface elevation about a moving body based on fixed body simulations. Fixed body simulations require fewer computer resources to calculate than an equivalent moving body simulation.

It was shown that, for periods shorter than 10 s, the differences between fixed and moving models were fairly minimal with little heave motion. It would be interesting to assess the effect of changing the heave resonant period by plus or minus a few seconds, given that the typical range of storm peak periods is 12-15 s and the period of 10 s, below which there is little difference between the current fixed and moving models, is very close to this range. However, this may be more of academic interest than practical use as heave resonance is dependent on many parameters such as structure stability and the positioning of equipment

on the deck etc. which could not necessarily be changed.

Building on the analysis of the DHI data, it would be interesting to apply the methods discussed in this research to the data recorded for wave-structure interactions with a column on a sloping bed. The results presented in this research were only for the flat bed case and it would be useful to investigate whether the presence of the sloping bed changed the wave-structure interactions. It was shown that the Taylor separation method is very sensitive to accurate lining up of the focus points for the crest and trough signals. Misalignment of just a few hundredths of a second can lead to a large amount of leakage between the odd and even harmonics. If similar experiments were carried out in the future it would be very helpful to have a timing signal or automated recording procedure to ensure that the recorded data signals could be lined up in time exactly. Using a paddle signal that included second-order corrections could lead to more accurate reconstructions of body forces from recorded surface elevations. This is particularly true for the second-order difference term which arrives at the body at approximately the same time as a freely propagating second-order difference error wave. It would also be of great interest if experiments such as these were carried out on an array of four closely spaced columns rather than just an isolated column. This could provide much useful information on the physics behind extreme wave-structure interactions for closely spaced arrays of surface piercing columns.

Further study of the damaged platform data with statistics collected for other wave directions would be of interest to gain insight into the cause of the damage. Extending the wave-structure interaction analysis discussed in this research to bi- or multi-directional sea states would allow further opportunities to accurately model extreme wave-structure interactions.

Bibliography

Adcock, T.A.A., Taylor, P.H., Yan, S., Ma, Q.W., and Janssen, P.A.E.M. (2011) Did the Draupner wave occur in a crossing sea? *Philosophical Transactions of the Royal Society of London, Series A: Mathematical, Physical, and Engineering Sciences*, Vol. 467(2134), p3004-3021.

Bai, W. and Eatock Taylor, R. (2006) Higher-order boundary element simulation of fully nonlinear wave radiation by oscillating vertical cylinders. *Applied Ocean Research*, Vol. 28(4), p247-265.

Bai, W. and Eatock Taylor, R. (2007) Numerical simulation of fully nonlinear regular and focused wave diffraction around a vertical cylinder using domain decomposition. *Applied Ocean Research*, Vol. 29(1-2), p55-71.

Bai, W. and Eatock Taylor, R. (2009) Fully nonlinear simulation of wave interaction with fixed and floating flared structures. *Ocean Engineering*, Vol. 36(3-4), p223-236.

Baldock, T.E., Swan, C., and Taylor, P.H. (1996) A laboratory study of nonlinear surface waves on water. *Philosophical Transactions of the Royal Society of London, Series A: Mathematical, Physical, and Engineering Sciences*, Vol. 354, p649-676.

Berek, E.P., Cooper, C.K., Driver, D.B., Heideman, J.C., Mitchell, D.A., Stear, J.D., and Vogel, M.J. (2007) Development of Revised Gulf of Mexico Metocean Hurricane Conditions for Reference by API Recommended Practices. *Offshore Technology Conference*, 2007, Houston, Texas.

Bingham, H.B. and Zhang, H. (2007) On the accuracy of finite-difference solutions for nonlinear water waves. *Journal of Engineering Mathematics*, Vol. 58, p211-228.

Boccotti, P. (1983) Some new results on statistical properties of wind waves. *Applied Ocean Research*, Vol. 5, p134-140.

Boo, S.Y. (2002) Linear and nonlinear irregular waves and forces in a numerical wave tank. *Ocean Engineering*, Vol. 29, p475-493.

Borthwick, A.G.L., Hunt, A.C., Feng, T., Taylor, P.H., and Stansby, P.K. (2006) Flow kinematics of focused waves on a plane beach in the U.K. Coastal Research Facility. *Coastal Engineering*, Vol. 53, p1033-1044.

Büchman, B., Ferrant, P., and Skourup, J. (2000) Runup on a body in waves and current. Fully nonlinear and finite-order calculations. *Applied Ocean Research*, Vol. 22, p349-360.

Buldakov, E.V., Eatock Taylor, R., and Taylor, P.H. (2004) Diffraction of a directionally spread wave group by a cylinder. *Applied Ocean Research*, Vol. 25, p301-320.

Callan, M., Linton, C.M., and Evans, D.V. (1991) Trapped modes in two-dimensional waveguides. *Journal of Fluid Mechanics*, Vol. 229, p51-64.

Chakrabarti, S.K. (1978) Comments on second-order wave effects on a large diameter vertical cylinder. *Journal of Ship Research*. Vol. 22, p266-268.

Chaplin, J.R., Rainey, R.C.T., and Yemm, R.W. (1997) Ringing of a vertical cylinder in waves. *Journal of Fluid Mechanics*, Vol. 350, p119-147.

Chau, F.P. (1989) *The second order velocity potential for diffraction of waves by fixed offshore structures*. Ph.D. thesis, University College London.

Chau, F.P. and Eatock Taylor, R. (1992) Second-order wave diffraction by a vertical cylinder. *Journal of Fluid Mechanics*, Vol. 240, p571-599.

Dalzell, J.F. (1999) A note on finite depth second-order wave-wave interactions. *Applied Ocean Research*, Vol 21(3), p105-111.

Davies, E.B. and Pamovski, L. (1998) Trapped modes in acoustic waveguides. *Quarterly Journal of Mechanics and Applied Mathematics*, Vol. 51, p477-492.

Dean, R.G. and Dalrymple, R.A. (1991) *Water wave mechanics for engineers and scientists*, World Scientific.

Douglas-Westwood (2012) The World Floating Production Market Forecast 2013-2017. http://www.douglas-westwood.com/

Drake, K.R., Eatock Taylor, R., Taylor, P.H., and Bai, W. (2009) On the hydrodynamics of bobbing cones. *Ocean Engineering*, Vol. 36(15-16), p1270-1277.

Ducrozet, G., Bingham, H.B., Engsig-Karup, A.P., and Ferrant, P. (2010) High-order finite difference solution for 3D nonlinear wave-structure interaction. 9^{th} *International Conference on Hydrodynamics*, Shanghai, China.

Eatock Taylor, R., Bai, W., Wu, G.X., and Hu, Z.Z. (2005) Numerical wave tanks based on finite element and boundary element modelling. *In Proceedings of the International Conference on Offshore Mechanics and Arctic Engineering - OMAE*, Vol. 67508, Haldiki, Greece.

Eatock Taylor, R. and Chamberlain, P.G. (1993) High frequency TLP responses, Managed programme on behaviour of fixed and compliant offshore structures. *Final report on Project FLU80*.

Eatock Taylor, R. and Chau, F.P. (1992) Wave diffraction theory - some developments in linear and non-linear theory. *Transactions of ASME, Journal of Offshore Mechanics and Arctic Engineering*, Vol. 114, p185-194.

Eatock Taylor, R. and Fonquernie, G. (2001) Second-order diffraction in a focused wave group. *Hydrodynamics in ship and ocean engineering*, RIAM, Kyushu University, p57-84.

Eatock Taylor, R. and Huang, J.B. (1996) Practical computation of non-linear wave diffraction effects in offshore structures. *Proceedings of International Symposium on Offshore Engineering*, Bandung, Indonesia.

Eatock Taylor, R. and Huang, J.B. (1997) Second-order wave diffraction by an axisymmetric body in monochromatic waves. *Philosophical Transactions of the Royal Society of London, Series A: Mathematical, Physical, and Engineering Sciences*, Vol. 453, p1515-1541.

Eatock Taylor, R. and Hung, S. M. (1987) Second-order diffraction forces on a vertical cylinder in regular waves. *Applied Ocean Resarch*, Vol. 9, p19-30.

Eatock Taylor, R. and Sincock, P. (1989) Wave upwelling effects in TLP and semisubmersible structures. *Ocean Engineering*, Vol. 16(3), p281-306.

Eatock Taylor, R., Taylor, P.H., and Sun, L. (2008) Efficient second-order diffraction method for multiple bodies in waves. *SAFE OFFLOAD Report*.

Engsig-Karup, A.P., Bingham, H.B., and Lindberg, O. (2009) An efficient flexible-order model for 3D nonlinear water waves. *Journal of Computational Physics*, Vol. 228, p2100-2118.

Enright, D., Fedkiw, R.P., Ferziger, J.H., and Mitchell, I. (2002) A hybrid particle level set method for improved interface capturing. *Journal of Computational Physics*, Vol. 183, p83-116.

Evans, D.V., Levitin, M., and Vassiliev, D. (1994) Existence theorems for trapped modes. *Journal of Fluid Mechanics*, Vol. 261, p21-31.

Evans, D.V. and Porter, R. (1997) Near-trapping of waves by circular arrays of vertical columns. *Applied Ocean Research*, Vol. 1187, p83-99.

Evans, D.V. and Porter, R. (1999) Trapping and near-trapping by arrays of columns in waves. *Journal of Engineering Mathematics*, Vol. 35, p149-179.

Faltinsen, O.M., Newman, J.N., and Vinje, T. (1995) Nonlinear wave loads on a slender vertical cylinder. *Journal of Fluid Mechanics*, Vol. 289, p179-198.

Fenton, J.D. (1985) A fifth-order Stokes theory for steady waves. *Journal of Waterway, Port, Coastal, and Ocean Engineering*, Vol. 111(2), p216-234.

Ferrant, P., Le Touzé , D., and Pelletier, K. (2003) Nonlinear time-domain models for irregular wave diffraction about offshore structures. *International Journal of Numerical Methods in Fluids*, Vol. 43, p1257-1277.

Forristall, G.Z. (2000) Wave Crest Distributions: Observations and second-order theory. *Journal of Physical Oceanography*, Vol. 30, p1931-1943.

Ghalayini, S.A. and Williams, A.N. (1991) Nonlinear wave forces on vertical cylinder arrays. *Journal of Fluids and Structures*, Vol. 5, p1-32.

Gibson, R., Swan, C., and Tromans, P.S. (2007) Fully nonlinear statistics of wave crest elevation calculated using a spectral response surface method: Applications to unidirectional sea states. *Journal of Physical Oceanography*, Vol. 37(1), p3-15.

Gingold, R.A. and Monaghan, J.J. (1977) Smoothed particle hydrodynamics: theory and application to non-spherical stars. *Monthly Notices of the Royal Astronomical Society*, Vol. 181, p375-389.

Hasselmann, K., Barnett, T.P., Bouws, E., Carlson, H., Cartwright, D.E., Eake, K., Euring, J.A., Gicnapp, A., Hasselmann, D.E., Kruseman, P., Meerburg, A., Mullen, P., Olbers, D.J., Richren, K., Sell, W., and Walden, H. (1973) Measurements of wind-wave growth and swell decay during the joint North Sea wave project (JONSWAP). *Ergänzungsheft zur Deutschen Hydrographischen Zeitschrift Reihe*, Vol. 8(12), p1-95.

Havelock, T.H. (1940) The pressure of water waves upon a fixed obstacle. *Philosophical Transactions of the Royal Society of London, Series A: Mathematical, Physical, and Engineering Sciences*, Vol. 175, p409-421.

Hazard, C. and Lenoir, M. (1993) Determination of scattering frequencies for an elastic floating body. *SIAM Journal of Mathematical Analysis*, Vol. 24(4), p1458-1514.

Hazard, C. and Lenoir, M. (2002) Surface water waves. *Scattering*, Editors Pike, R. and Sabatier, P., p618-636.

Hirt, C.W. and Nichols, B.D. (1981) Volume of fluid (VOF) method for the dynamics of free boundaries. *Journal of Computational Physics*, Vol. 39(1), p201-225.

Hogben, N., Miller, B.L., Searle, J.W., and Ward, G. (1977) Estimation of fluid loading on offshore structures. *Proceedings of the Institution of Civil Engineers*, Part 2, Vol. 63, p515-562.

Hu, C. and Kashiwagi, M. (2004) A CIP-based method for numerical simulation of violent free-surface flows. *Journal of Marine Science and Tecnology*, Vol. 9(4), p143-157.

Huang, J.B. and Eatock Taylor, R. (1996a) Semianalytical solution for second-order wave diffraction by a truncated circular cylinder in monochromatic waves. *Journal of Fluid Mechanics*, Vol. 319, p171-196.

Huang, J.B. and Eatock Taylor, R. (1996b) Application of second-order diffraction analysis to TLP design. *Final Report on Project A4, Managed Programme on Uncertainties in Loads on Offshore Structures*, Department of Engineering Science, University of Oxford.

Huang, J.B. and Eatock Taylor, R. (1996c) Second-order interaction between waves and multiple bottom-mounted vertical circular cylinders. *Proceedings of the* 11^{th} *International Workshop on Water Waves and Floating Bodies*, Hamburg, Germany.

Huang, Z. and Lin, P. (2012) Numerical simulation of propagation and breaking processes of a focused waves group. *Journal of Hydrodynamics*, Vol 24(3), p399-409.

Hunt, A.C., Taylor, P.H., Borthwick, A.G.L., and Stansby, P.K. (2002) Focused waves onto a plane beach. 7^{th} *International Workshop on Wave Hindcasting and Forecasting*, Banff, Canada.

Hunt-Raby, A.C., Borthwick, A.G.L., Stansby, P.K., and Taylor, P.H. (2011) Experimental measurement of focused wave group and solitary wave overtopping. *Journal of Hydraulic Research*, Vol. 49(4), p450-464.

Huseby M., Jensen A., and Grue A. (2000) An experimental investigation of ringing loads on a vertical cylinder in transient waves. *Proceedings of the* 15^{th} *International Workshop on Water Waves and Floating Bodies.*

Ihmsen, M., Akinci, N., Gissler, M., and Teschner, M. (2010) Boundary handling and adaptive time-stepping for PCISPH. *Workshop on Virtual Reality Interaction and Physical Simulation, VRIPHYS.*

Jacobsen, N.G., Fuhrman, D.R., and Fredse, J. (2012) A wave generation toolbox for the open-source CFD library : OpenFoam. *International Journal for Numerical Methods in Fluids*, Vol. 70, p1073-1088.

Jha, A. and Winterstein, S.R. (2000) Non-linear random ocean waves: prediction and comparison with data. *Proceedings of ETCE/OMAE2000 Joint Conference.*

Johannessen, T. and Swan, C. (2001) A laboratory study of the focusing of transient and directionally spread surface water waves. *Philosophical Transactions of the Royal Society of London, Series A: Mathematical, Physical, and Engineering Sciences*, Vol. 457, p971-1006.

Jonathan, P. and Taylor, P.H. (1997) On irregular, nonlinear waves in a spread sea. *Journal of Offshore Mechanics and Arctic Engineering*, Vol. 119(1), p37-41.

Jones, D.S. (1953) The eigenvalues of $\Delta^2 u + \lambda u = 0$ when the boundary conditions are given on semi-infinite domains. *Proceedings of the Cambridge Philosophical Society*, Vol. 49, p668-684.

Kagemoto, H. and Yue, D.K.P. (1986) Interactions among multiple three-dimensional bodies in water waves: an exact algebraic method. *Journal of Fluid Mechanics*, Vol. 166, p189-209.

Kagemoto, H., Murai, M., Saito, M., Molin, B., and Malenica, Š. (2002) Experimental and theoretical analysis of the wave decay along a long array of vertical cylinders. *Journal of Fluid Mechanics*, Vol. 456, p113-135.

Kaiser, M.J., Dismukes, D.E., Yu, Y. (2008) Field redevelopment economics and storm impact assessment. *Oil and Gas journal*, Vol. 106(25), p42-50.

Kernot, M.P. (1989) *The second-order forcing and response of offshore structures in irregular seas*. D.Phil. thesis, University of Oxford.

Kim, J.W., Kyoung, J.H., Ertekin, R.C., and Bai, K.J. (2006) Finite-element computation of wave-structure interaction of steep Stokes waves and vertical cylinders. *Journal of Waterway, Port, Coastal, and Ocean Engineering*, Vol. 132, p337-347.

Kim, M.H. and Yue, D.K.P. (1989) Slowly-varying wave drift forces in short-crested irregular seas. *Applied Ocean Research*, Vol. 11, p2-18.

Kim, M.H. and Yue, D.K.P. (1990) The complete second-order diffraction solution for an axisymmetric body. Part 2. Bichromatic incident waves and body motions. *Journal of Fluid Mechanics*, Vol. 211, p557-593.

Kleefsman, K.M.T., Fekken, G., Veldman, A.E.P., and Iwanowski, B. (2004) Improved Volume-of-Fluid Method for Wave Impact Problems. *ISOPE 2004*, p334-341.

Korsemeyer, F.T., Lee, C.-H., Newman, J.N., and Sclavounos, P.D. (1988) The analysis of wave interactions with tension leg platforms. *Proceedings of the International Conference on Offshore Mechanics and Arctic Engineering - OMAE*, Houston, Texas, USA.

Kriebel, D.L. (1990) Nonlinear wave interaction with a vertical circular cylinder - Part I: Monochromatic incident waves. *Ocean Engineering*, Vol. 17, p345-377.

Kriebel, D.L. (1992) Nonlinear wave interaction with a vertical circular cylinder - Part II: Wave runup. *Ocean Engineering*, Vol. 19, p75-99.

Langley, R.S. (1987) A statistical analysis of low frequency second-order forces and motions. *Applied Ocean Research*, Vol. 9, p163-170.

Lee, C.-H., Newman, J.N., Kim, M.-H., and Yue, D.K.P. (1991) The computation of second order wave loads. *Proceedings of the International Conference on Offshore Mechanics and Arctic Engineering - OMAE*, Stavanger, Norway.

Lee, C.-H. and Newman, J.N. (1994) Second-order wave effects on offshore structures. *Conference on the Behaviour of Offshore Structures, BOSS 1994*, MIT, p133-145.

Lee, C.-H. and Newman, J.N. (2004) Computation of wave effects using the panel method. *Numerical models in fluid-structure interaction*, Editor S. Chakrabarti, WIT Press, Southhampton.

Li, J., Wang, Z., and Liu, S. (2012) Calculations of Wave Runup on Cylinder in Multi-Directional Focused Waves. *Proceedings of the* 22^{nd} *International Offshore and Polar Engineering Conference*, Greece.

Lighthill, J. (1979) Waves and hydrodynamic loading. *Proceedings of the* 2^{nd} *International Conference on the Behaviour of Offshore Structures*, Vol. 1, p1-40.

Lindgren, G. (1970) Some properties of a normal process near a local maximum. *Annals of Mathematical Statistics*, Vol. 41, p1870-1883.

Lindgren, G. (1980) Extreme values and crossings for the cai squared process and other functions of multidimensional Gaussian processes, with reliability applications. *Advances in Applied Probability*, Vol. 12(3), p746-774.

Linton, C.M. and Evans, D.V. (1990) Interaction of waves with arrays of vertical circular cylinders. *Journal of Fluid Mechanics*, Vol. 215, p549-569.

Linton, C.M. and Evans, D.V. (1993) The interaction of waves with a row of circular cylinders. *Journal of Fluid Mechanics*, Vol. 251, p687-708.

Longuet-Higgins, M.S. (1952) On the statistical distribution of the heights of sea waves. *Journal of Marine Research*, Vol. 11(3), p245-266.

Lucy, L.B. (1977) A numerical approach to the testing of the fission hypothesis. *The Astronomical Journal*, Vol. 82, p1013-1024.

Ma, Q.W., Wu, G.X., and Eatock Taylor, R. (2001a) Finite element simulation of fully non-linear interaction between vertical cylinders and steep waves - Part 1: methodology and numerical procedure. *International Journal for Numerical Methods in Fluids*, Vol. 36, p265-285.

Ma, Q.W., Wu, G.X., and Eatock Taylor, R. (2001b) Finite element simulation of fully non-linear interaction between vertical cylinders and steep waves - Part 2: numerical results and validation. *International Journal for Numerical Methods in Fluids*, Vol. 36, p287-308.

Macklin, M. and Müller, M. (2013) Position Based Fluids. *ACM Transactions on Graphics (SIGGRAPH 2013)*, Vol. 32(4), Article 104.

MacLaurin, R.A. (1909) *Light: Columbia University Lectures*, Columbia University Press, Chapter VII.

Malenica, Š. (1997) Second-order interaction of water waves with arrays of vertical circular cylinders. *In Proceedings of the* 2^{nd} *Congress of the Croation Society of Mechanics*, p599-606.

Malenica, S., Eatock Taylor, R., and Huang, J.B. (1999) Second-order water wave diffraction by an array of vertical cylinders. *Journal of Fluid Mechanics*, Vol. 390, p349-373.

Maniar, H.D. and Newman, J.N. (1997) Wave diffraction by a long array of cylinders. *Journal of Fluid Mechanics*, Vol. 339, p309-330.

McCamy, R.S. and Fuchs, R.A. (1954) Wave forces on piles: A diffraction theory. *US Army Corps of Engineers, Technical Memo*, Washington, DC.

McCormick, M.E. and Kraemer, D.R.B. (2002) Polynomial approximations for Fresnel integrals in diffraction analysis. *Journal of Coastal Engineering*, Vol. 44, p261-266.

McIver, P. and Evans, D.V. (1984) Approximation of wave forces on cylinder arrays. *Applied Ocean Research*, Vol. 6(2), p101-107.

McIver, M. (1996) An example of non-uniqueness in the two-dimensional water wave problem. *Journal of Fluid Mechanics*, Vol. 315, p257-266.

McIver, M. (2000) Trapped modes supported by submerged obstacles. *Philosophical Transactions of the Royal Society of London, Series A: Mathematical, Physical, and Engineering Sciences*, Vol. 456, p1851-1860.

McIver, P. and McIver, M. (1997) Excitation of trapped water waves by the forced motion of structures. *Journal of Mechanics and Applied Mathematics*, Vol. 50, p165-178.

McIver, P. and McIver, M. (2006) Trapped modes in the water-wave problem for a freely-floating structure. *Journal of Fluid Mechanics*, Vol. 558, p53-67.

Mei, C.C. (1989) *The applied dynamics of ocean surface waves*, World Scientific.

Meylan, M.H. and Eatock Taylor, R. (2009) Time-dependent water-wave scattering by arrays of cylinders and the approximation of near trapping. *Journal of Fluid Mechanics*, Vol. 631, p103-125.

Meylan, M.H. and Gross, L. (2003) A parallel algorithm to find the zeros of a complex analytic function. *ANZIAM Journal*, Vol. 44(E), p216-234.

Molin, B. (1979) Second-order diffraction loads upon three-dimensional bodies. *Applied Ocean Research*, Vol. 1, p197-202.

Molin, B., Jamois, E., Lee, C.H., and Newman, J.N. (2005) Non-linear wave interaction with a square cylinder. *Proceedings of the* 20^{th} *International Workshop on Water Waves and Floating Bodies*, Longyearbyen, Norway.

Molin, B., Remy, F., and Kimmoun, O. (2006) Second-order wave interaction with a vertical plate. *Journal of Engineering Mathematics*, Vol. 58, p109-119.

Monaghan, J.J. (1988) An introduction to SPH. *Computer Physics Communications*, Vol. 48(1), p89-96.

Monaghan, J.J. and Kos, A. (1999) Solitary waves on a Cretan Beach. *Journal of Waterway, Port, Coastal, and Ocean Engineering*, Vol. 125(3), p145-154.

Monaghan, J.J., Kos, S., and Issa, N. (2003) Fluid Motion Generated by Impact. *Journal of Waterway, Port, Coastal, and Ocean Engineering*, Vol. 129(6), p250-259.

Mori, N. and Janssen, P.A.E.M. (2006) On kurtosis and occurrence probability of freak waves. *American Meterological Society*, Vol. 36(7), p1471-1483.

Morris-Thomas, M.T. and Thiagarajan, K.P. (2004) The runup on a cylinder in progressive surface gravity waves: Harmonic components. *Applied Ocean Research*, Vol. 26(3-4), p98-113.

Moubayed, W.I. and Williams, A.N. (1995) Second order hydrodynamic interactions in an array of vertical cylinders in bichromatic waves. *Journal of Fluid and Structures*, Vol. 9, p61-98.

Naess, A. (1985) Statistical analysis of second-order response of marine structures. *Journal of Ship Research*, Vol. 29(4), p270-284.

Naess, A. (1990) Statistical analysis of nonlinear, second-order forces and motions of offshore structures in short-crested random seas. *Probabilistic Engineering Mechanics*, Vol. 5(4), p192-203.

Naess, A. and Karlsen, H.C. (2004) Numerical calculation of the level crossing rate of second-order stochastic Volterra systems. *Probabilistic Engineering Mechanics*, Vol. 19(2), p155-160.

Naess, A., Karlsen, H.C., and Teigen, P.S. (2006) Numerical methods for calculating the crossing rate of high and extreme response levels of compliant offshore structures subjected to random waves. *Applied Ocean Research*, Vol. 28, p1-8.

Naess, A., Gaidai, O., and Teigen, P.S. (2008) Extreme response prediction for nonlinear floating offshore structures by Monte Carlo simulation. *Applied Ocean Research*, Vol. 29, p221-230.

Newman, J.N. (1977) *Marine hydrodynamics*, Cambridge, MA: MIT Press.

Newman, J.N. and Lee, C.-H. (1992) Sensitivity of wave loads to the discretization of bodies. *Conference on the Behaviour of Offshore Structures (BOSS 1992)*, London, UK.

Ning, D.Z., Zang, J., Liu, S.X., Eatock Taylor, R., Teng, B., and Taylor, P.H. (2009) Free-surface evolution and wave kinematics for nonlinear uni-directional focused wave groups. *Ocean Engineering*, Vol. 36(15-16), p1226-1243.

Noh, W.F. and Woodward, P. (1976) SLIC (Simple Line Interface Calculation). *Proceedings of 5th International Conference of Fluid Dynamics*, Lecture Notes in Physics, Vol. 59, p330-340.

Ochi, M.K. (1973) On prediction of extreme values. *Journal of Ship Research*, Vol. 17, p29-37.

Ochi, M.K. (1998) Ocean waves: The Stochastic approach. *Cambridge Ocean Technology*, Series 6.

Ohl, C.O.G., Taylor, P.H., Eatock Taylor, R., and Borthwick, A.G.L. (2001) Water wave diffraction by a cylinder array - Part 1: Regular waves. *Journal of Fluid Mechanics*, Vol. 442, p1-32.

Ohl, C.O.G., Taylor, P.H., Eatock Taylor, R., and Borthwick, A.G.L. (2001) Water wave diffraction by a cylinder array - Part 2: Irregular waves. *Journal of Fluid Mechanics*, Vol. 442, p33-66.

Onorato, M., Residori, S., Bortolozzo, U., Montina, A., and Arecchi, F.T. (2013) Rogue waves and their generating mechanisms in different physical contexts. *Physics Reports*, Vol. 528(2), p47-89.

Osher, S. and Sethian, J.A. (1988) Fronts propagating with curvature-dependent speed: Algorithms based on Hamilton-Jacobi formulations. *Journal of Computational Physics*, Vol. 79 p1249.

Osher, S.J. and Fedkiw, R.P. (2002) *Level Set Methods and Dynamic Implicit Surfaces*, Springer-Verlag. ISBN 0-387-95482-1.

Pierson, W.J. and Moskowitz, L. (1964) A proposed spectral form for fully developed wind seas based on the similarity theory of S.A. Kitaigorodskii. *Journal of Geophysical Research*, Vol. 69, p5181-5190.

Rapp, R.J. and Melville, W.K. (1990) Laboratory measurements of deep-water breaking wave [J]. *Philosophical Transactions of the Royal Society of London, Series A: Mathematical, Physical, and Engineering Sciences*, Vol. 331(1622), p735-800.

http://www.rigsworld.com/Offshore-Accidents.htm

Sagrilo, L.V.S., Gao, Z., Naess, A., and Lima, E.C.P. (2011) A straightforward approach for using single time domain simulations to assess characteristic extreme responses. *Ocean Engineering*, Vol. 38(13), p1464-1471.

Schäffer, H.A. (1996) Second-order wavemaker theory for irregular waves. *Ocean Engineering*, Vol. 23(1), P47-88.

Sethian, J.A. (1999) *Level Set Methods and Fast Marching Methods : Evolving Interfaces in Computational Geometry, Fluid Mechanics, Computer Vision, and Materials Science*, Cambridge University Press, ISBN 0-521-64557-3.

Sharma, J.N. and Dean, R.G. (1979) Development and evaluation of a procedure for simulating a random directional second-order sea surface and associated wave forces. *Ocean Engineering Rep. 20*, University of Delaware.

Simon, M.J. (1982) Multiple scattering in arrays of axisymmetric wave-energy devices - Part 1: A matrix method using a plane wave approximation. *Journal of Fluid Mechanics*, Vol. 120, p1-25.

Solenthaler, B. and Pajarola, R. (2009) Predictive-corrective incompressible SPH. *ACM Transactions on Graphics (SIGGRAPH 2009)*, Vol. 28(3), Article 40.

Spring, B.H. and Monkmeyer, P.L. (1974) Interaction of plane waves with vertical cylinders. *Proceedings of* 14^{th} *International Conference on Coastal Engineering*, Chap. 107, p1828-1845.

Stokes, G.G. (1847) On the theory of oscillatory waves. *Transactions of the Cambridge Philosophical society*, Vol. 8, p441-455.

Sun, L., Teng, B., and Liu, C.F. (2008) Removing irregular frequencies by a partial discontinuous higher order boundary element method. *Ocean Engineering*, Vol. 35, p920-930.

Takewaki, H., Nishiguchi, A., and Yabe, T. (1985) The cubic-interpolated pseudo-particle (CIP) method for solving hyperbolic-type equations. *Journal of Computational Physics*, Vol. 61, p261-268.

Takewaki, H., Nishiguchi, A., and Yabe, T. (1987) Cubic-interpolated pseudo particle (CIP) method - application to nonlinear or multi-dimensional problems. *Journal of Computational Physics*, Vol. 70, p355-365.

Tayfun, M.A. (1980) Narrow-band non-linear sea waves. *Journal of Geophysical Research*, Vol. 85(C3), p1548-1552.

Tayfun, M.A. and Fedele, F. (2007) Expected shape of extreme waves in storm seas. *Proceedings of the International Conference on Offshore Mechanics and Arctic Engineering - OMAE*, Vol. 2, p53-60.

Taylor, P.H. and Williams, B.A. (2004) Wave statistics for intermediate depth water: NewWaves and symmetry. *Journal of Offshore Mechanics and Arctic Engineering*, Vol. 126(1), p54-59.

Taylor, P.H., Zang, J., Walker, D.A.G., and Eatock Taylor, R. (2007) Second order near-trapping for multi-column structures and near-flat QTFs. 22^{nd} *International Workshop on Water Waves and Floating Bodies*, Croatia.

Tromans, P.S., Anaturk, A.H.R., and Hagemeijer, P.M. (1991) New model for the kinematics of large ocean waves - application as a design wave. *Proceedings of the* 1^{st} *International Offshore and Polar Engineering Conference*, p64-71.

Tromans, P.S., Hagemeijer, P.M., and Wassink, H.R. (1992) The statistics of the extreme response of offshore structures. *Ocean Engineering*, Vol. 19(2), p161-181.

Tulin, M.P. and Landrini, M. (2000) Breaking waves in the Ocean and around Ships. *Proceedings of the* 23^{rd} *ONR Symposium on Naval Hydrodynamics*, Val de Reuil, France.

Twersky, V. (1952) Multiple scattering of radiation by an arbitrary configuration of parallel cylinders. *Journal of the Acoustics Society of America*, Vol. 24, p42-46.

Ursell, F. (1951) Trapping modes in the theory of surface waves. *Proceedings of the Cambridge Philosophical Society*, Vol. 47, p347-358.

Vinje, T. (1983) On the statistical distribution of second-order forces and motions. *International Shipbuilding Progress*, Vol. 30, p58-68.

Walker, D.A.G. (2006) *Interaction of extreme ocean waves with offshore structures*. D.Phil. thesis, University of Oxford.

Walker, D.A.G. and Eatock Taylor, R. (2005) Wave diffraction from linear arrays of cylinders. *Journal of Ocean Engineering*, Vol. 32(17-18), p2053-2078.

Walker, D.A.G., Eatock Taylor, R., Taylor, P.H., and Zang, J. (2008) Wave diffraction and near-trapping by a multi-column gravity-based structure. *Journal of Ocean Engineering*, Vol. 35(2), p201-229

Wang, Z., Yang, J., and Stern, F. (2008) Comparison of Particle Level Set and CLSVOF Methods for Interfacial Flows. 46^{th} *AIAA Aerospace Sciences Meeting and Exhibit*, January 2008, Reno, Nevada, AIAA-2008-530.

Wang, Z., Yang, J., and Stern, F. (2009) An improved particle correction procedure for the particle level set method. *Journal of Computational Physics*, Vol. 228(16), p5819-5837.

Winterstein, S. (1988) Nonlinear vibration models for extremes and fatigue. *Journal of Engineering Mechanics*, Vol. 114(10), p1769-1787.

Winterstein, S. and Sweetman, B. (2001) Airgap response of floating structures: statistical predictions versus observed behavior. *Journal of Offshore Mechanics and Arctic Engineering*, Vol. 123(3), p118-123.

Wu, G.X. and Eatock Taylor, R. (1995) Time stepping solutions of the two-dimensional nonlinear wave problem. *Ocean Engineering*, Vol. 22, p785-798.

Wu, G.X. and Eatock Taylor, R. (2003) The coupled finite element and boundary element analysis of nonlinear interactions between waves and bodies. *Ocean Engineering*, Vol. 30, p387-400.

Yabe, T., Xiao, F., and Utsumi, T. (2001) The Constrained Interpolation Profile Method for Multiphase Analysis. *Journal of Computational Physics*, Vol. 169(2), p556-593.

Yabe, T., Ishikawa, T., Wang, P. Y., Aoki, T., Kadota, Y., and Ikeda, F. (1991) A universal solver for hyperbolic-equations by cubic-polynomial interpolation. II. Two- and three-dimensional solvers. *Computer Physics Communications*, Vol. 66(2-3), p219-232.

Yang, Q. and Qiu, W. (2012) Numerical Solution of 3-D Water Entry Problems With a Constrained Interpolation Profile Method. *Journal of Offshore Mechanics and Arctic Engineering*, Vol. 134(4), p1-8.

Yeung, R.W. (1982) Numerical methods in free surface flows. *Annual Review of Fluid Mechanics*, Vol. 14, p395-442.

Zang, J., Taylor, P.H., and Eatock Taylor, R. (2003) Hydrodynamics of ship-shaped floating bodies. *REBASDO progress report*, Department of Engineering Science, University of Oxford.

Zang, J., Gibson, R., Taylor, P.H., Eatock Taylor, R., and Swan, C. (2006) Second order wave diffraction around a fixed ship-shaped body in unidirectional steep waves. *Journal of Offshore Mechanics and Arctic Engineering*, Vol. 128, p89-99.

Zang, J., Gibson, R., Eatock Taylor, R., and Taylor, P.H. (2009) Wave runup and response spectrum for wave scattering from a cylinder. *International Journal of Offshore and Polar Engineering*, Vol. 19(2), p1-6.

Zang, J., Taylor, P.H., Morgan, G., Tello, M., Grice, J., and Orszaghova, J. (2010) Experimental study of non-linear wave impact on offshore wind turbine foundations. *Proceedings of the 3rd International Conference on the Application of Physical Modelling to Port and Coastal Protection.*

Appendix A

Thunder Horse geometry

This appendix details the specifics of the actual Thunder Horse geometry and describes the different models used in this research to approximate it. The draft of Thunder Horse is 30 m and the pontoons are 11.52 m tall, leaving 18.48 m of water between the top of the pontoon and the water free surface at steady state. The width of the pontoons is determined by the columns it attaches to, and so of the four pontoons there are two of width 21.76 m, one of width 25.6 m, and one of with 23.04 m. The corners of the pontoons are rounded so that they are flush with the column at that corner. There are two pairs of columns with matching cross-sections. The northern pair have a column cross-section with dimensions 21.76 m $\times$ 25.6 m and a radius of curvature on the rounded corners of 8.32 m. The southern pair have column cross-section dimensions of 21.76 m $\times$ 23.04 m and a radius of curvature of 7.04 m. The long edges of the pontoons between each of the columns have a chamfer rather than a right angled edge.

Thunder Horse has a total displacement of 129,626 tons and its centre of mass is located at (-0.783, 0.012, 10.046) m. The radii of gyration are $G_x = 42.95$ m, $G_y = 46.60$ m, and $G_z = 49.65$ m, and the eigenperiods of the structure, including the horizontal stiffness of the mooring system, are given in Table A.1.

Mode	Eigenperiod (s)
Surge	161.7
Sway	248.6
Heave	26.2
Roll	87.8
Pitch	67.9
Yaw	77.1

Table A.1: Eigenperiods of Thunder Horse in all six degrees of freedom.

When creating a model for use with DIFFRACT one can use 2 planes of symmetry to minimise computation time, and just mesh one quadrant of the structure. This meant that

the Thunder Horse models created used the average dimensions of the actual structure and four identical columns placed on four corners of a square, rather than the slightly rectangular positioning in the actual structure. The average cross-sectional area of the columns is 478 m^2, which with an average radius of curvature of 7.68 m gives an average column width of 23.0 m. The columns are centred at $(\pm 41.42 \text{ m}, \pm 41.42 \text{ m})$. The draft and pontoon height are as stated above for the actual Thunder Horse structure.

Figure A.1 shows an example mesh used for second-order QTF calculations at low frequencies. The cells on the body mesh, inner surface mesh, and the 100 m × 100 m free surface mesh for which QTF results are output are approximately 3 m × 3 m. The outer radius of the free surface mesh is 1550 m and the outer cell size is approximately 25 m × 25 m, which means that the range of incident frequencies that are likely to give converged results is approximately 0.2-0.56 rad/s.

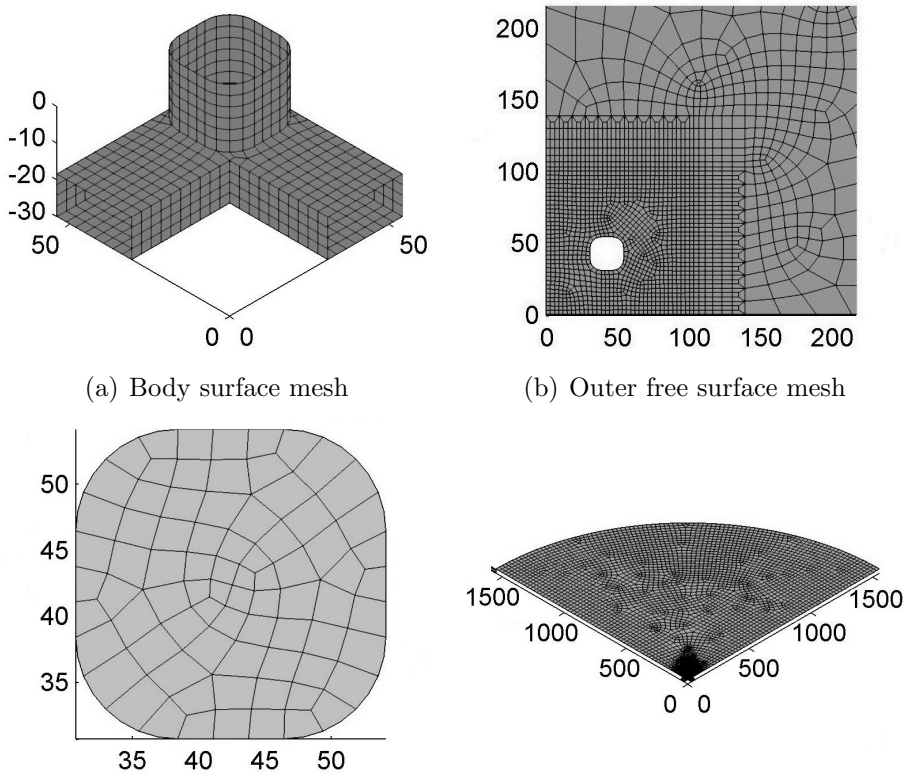

(a) Body surface mesh

(b) Outer free surface mesh

(c) Inner free surface mesh

(d) All surface meshes

Figure A.1: An example mesh with views of the body and inner meshes, the outer free service zoomed in around the structure, and all three meshes together.